

KYOTO UNIVERSITY

TOPOLOGY OPTIMIZATION
FOR THE MICRO- AND MACROSTRUCTURE DESIGNS
IN ELECTROMAGNETIC WAVE PROBLEMS

BY
MASAKI OTOMORI

A DISSERTATION SUBMITTED IN PARTIAL FULFILLMENT
OF THE REQUIREMENTS FOR THE DEGREE OF DOCTOR OF ENGINEERING

IN THE
GRADUATE SCHOOL OF ENGINEERING
DEPARTMENT OF MECHANICAL ENGINEERING AND SCIENCE

MARCH 2013



京都大学 博士学位論文

電磁波問題におけるマイクロおよびマクロ構造の
トポロジー最適化

乙守 正樹

工学研究科機械理工学専攻

2013年3月



© Copyright by Masaki Otomori, 2013.
All Rights Reserved

Abstract

The capabilities and operation of electromagnetic devices can be dramatically enhanced if artificial materials that provide certain prescribed properties can be designed and fabricated, provided that the structure of electromagnetic devices can be properly designed. This thesis describes how topology optimization can be used for the microstructure design of electromagnetic materials that exhibit desirable electromagnetic properties, and for the macrostructure design to enhance the response of the electromagnetic devices. In addition, in the practical design of mechanical and electromagnetic devices, manufacturability is a crucial concern, as are several design requirements such as the maximum volume of the material used, the prevention of mechanical interference, the maximum allowable stress, and so on. Optimization methods that can effectively deal with these requirements are also discussed. This thesis consists of three main parts.

The first part (Chapters 3 and 4) discusses two topology optimization methods that take into account manufacturability and the design requirements of compliant mechanisms and normal structures. In Chapter 3, a new formulation for reducing the number of design variables in a multiple phase projection method (MPPM) is discussed that can impose a minimum length scale in the topology optimization. Chapter 4 deals with a level set-based topology optimization using mathematical programming that is applied to several optimization problems that include a mean compliance constraints, a mutual mean compliance constraint, and a stress constraint.

The second part (Chapters 5 and 6) deals with the microstructure design of electromagnetic materials. In Chapter 5, a level set-based topology optimization is applied for the design of dielectric metamaterials that have negative permeability. The effective permeability minimization problem and effective permeability design problems are formulated and applied for two- and three-dimensional problems to demonstrate that the presented method successfully finds clear configurations that have the desired negative effective permeability. Chapter 6 discusses the microstructure design of dielectric materials that exhibit set degrees of effective permittivity. An energy-based homogenization method is used to obtain the effective permittivity tensor and isotropic and anisotropic materials are designed using density-based topology optimization procedures. The theoretical bounds of the two- and three-dimensional anisotropic effective property in the principal direction when the effective property in the other principal direction(s) is/are set to a prescribed value are derived, to evaluate the effective permittivity values obtained by the optimization.

The third part (Chapter 7) addresses the macrostructure design of electromagnetic devices. An electromagnetic cloak and a metallic waveguide design problem are considered, both using a ferrite material. Ferrite materials exhibit a frequency-dependent degree of permeability, due to a magnetic resonance phenomenon that can be influenced by applying an external DC magnetic field. Thus, the use of an appropriately designed ferrite material for the electromagnetic cloaking device and metallic waveguide is expected to result in novel functions, such as on-off operation

in response to on-off application of an external magnetic field, or a tunable frequency range under which the cloak or waveguide operates. The level set-based topology optimization method is used to design the configurations of the ferrite material and the results show that the presented method yields appropriate optimization results.

Acknowledgements

First, I would like to thank my three supervisors, Professors Shinji Nishiwaki, Kazuhiro Izui, and Takayuki Yamada, for their invaluable support and advice throughout my doctoral research, and for providing me with an ideal environment for conducting creative research.

I am also very grateful to Professor Osamu Tabata in the Department of Micro-engineering at Kyoto University, and Professor Masahiro Hasuo in the Department of Mechanical Engineering and Science, also at Kyoto University, for their support and thoughtful advice.

I also would like to thank several individuals at AISIN AW Co., LTD. : Mr. Mutsumi Kawamoto, president; Mr. Kazumasa Tsukamoto, executive vice president; Mr. Kozo Yamaguchi, executive vice president; Mr. Kazuhisa Ozaki, senior managing director; Mr. Kenji Suzuki, director; Mr. Shigeyasu Kosaki, department manager; and Dr. Takanori Ide, senior researcher. Their kindness and encouragement allowed me to attempt challenging research in an important academic field, and ultimately complete my doctoral course at Kyoto University.

Part of this research was carried out during my visit to the TopOpt research group at the Technical University of Denmark, and I am very grateful to Prof. Ole Sigmund for his supervision, support, and stimulating discussions. I am also extremely grateful to Dr. Jacob Andjkaer for always taking time to give me helpful advice and encouragement while he was a visiting researcher at Kyoto University, and for his great hospitality and assistance during my time in Denmark. Discussions with all members of the Danish TopOpt group were very rewarding, and their advice contributed greatly to my research.

I am also very grateful to Professor Nozomu Kogiso, Mr. Keiichi Ueda, and Mr. Hitoshi Horio at Osaka Prefecture University for their invaluable discussions and support during collaborative research on robust topology optimization and topology optimization for the design of shell structures.

I would also like to thank Professor Hisashi Morishita and Ph.D. candidate Mr. Nguyen Tuan Hung at National Defense Academy of Japan for their helpful discussion and support during collaborative research on topology optimization for the design of an antenna device.

In addition, I would like to thank my colleagues in the Manufacturing Systems Engineering Laboratory at Kyoto University for their tireless support and good cheer, and for creating an inspiring working environment. I would also like to thank Mr. John E. Goodman for his great help in editing my papers in English over the years.

Finally, I am most grateful to my parents and friends for their encouragement and support, and offer special thanks to my wife, Midori Otomori, and my son, Mukuto Otomori, for their support and patience during my doctoral studies.

Kyoto, March, 2013
Masaki Otomori

To my parents and my brother
To Midori, Mukuto and our coming baby

Contents

Abstract	iv
1 Introduction	1
1.1 Motivation	1
1.2 Structure of thesis	1
2 Topology optimization	5
2.1 Structural optimization	5
2.2 Topology optimization	5
2.3 Level set-based structural optimization	8
2.4 Formulation of topology optimization	10
2.4.1 Density-based method	11
2.4.2 Level set-based method	11
3 Multiple phase projection method	15
3.1 Introduction	15
3.2 Formulation	15
3.2.1 Heaviside projection method	15
3.2.2 Multiple phase projection method (MPPM)	18
3.2.3 Proposed MPPM	18
3.2.4 Optimization problem	19
3.3 Numerical implementation	20
3.3.1 Approximation of absolute values	20
3.3.2 Optimization algorithm	21
3.3.3 Updating scheme applied to optimization parameters.	21
3.4 Numerical examples	22
3.4.1 Minimum mean compliance problems	22
3.4.2 Compliant mechanism design problem	27
3.5 Conclusions	27
4 Level set-based method using mathematical programming	29
4.1 Introduction	29
4.2 Formulation	30
4.2.1 Level set function updating scheme	30
4.2.2 Minimum mean compliance problem	30

4.2.3	Minimum mean compliance problem with a mean compliance constraint	31
4.2.4	Compliant mechanism design problem with a mutual mean compliance constraint	32
4.2.5	Minimum mean compliance problem with a stress constraint	34
4.2.6	Compliant mechanism design problem with a stress constraint	35
4.3	Numerical implementation	36
4.3.1	Optimization algorithm	36
4.3.2	Computation of sensitivities	36
4.4	Numerical examples	38
4.4.1	Minimum mean compliance problem	38
4.4.2	Minimum mean compliance problem with a mean compliance constraint	41
4.4.3	Compliant mechanism design problem with a mutual mean compliance constraint	42
4.4.4	Minimum mean compliance problem with a stress constraint	43
4.4.5	Compliant mechanism design problem with a stress constraint	46
4.5	Conclusions	50
5	Negative permeability dielectric metamaterial design	51
5.1	Introduction	51
5.2	Formulation	53
5.2.1	Governing equation	53
5.2.2	Effective permeability	55
5.2.3	Optimization problem	57
5.2.4	Sensitivity analysis	60
5.3	Numerical implementation	62
5.3.1	Design variables	62
5.3.2	Optimization algorithm	63
5.4	Numerical examples	65
5.4.1	Two-dimensional problems: effect of positive peak position in the initial configuration	65
5.4.2	Two-dimensional problem: effective permeability design problem	73
5.4.3	Two-dimensional problems: material with a high dielectric constant	73
5.4.4	Three-dimensional problems	78
5.5	Conclusions	83
6	Inverse design of dielectric materials	87
6.1	Introduction	87
6.2	Formulation	88
6.2.1	Effective permittivity	88
6.2.2	Design variables	90
6.2.3	Optimization problem	91
6.2.4	Sensitivity analysis	91

6.3	Theoretical bounds	92
6.3.1	Review of theoretical bounds of effective permittivity for two-phase composite material	92
6.3.2	Bounds of real value effective permittivity in principal direction	96
6.4	Numerical implementation	97
6.4.1	Optimization algorithm	97
6.5	Numerical examples	97
6.5.1	Comparison of methods to obtain effective permittivity values	98
6.5.2	Two-dimensional problems: isotropic material design	99
6.5.3	Two-dimensional problems: anisotropic material design	101
6.5.4	Two-dimensional problems: anisotropic material design with nonzero off-diagonal terms	103
6.5.5	Two-dimensional problems: material with loss targeting extreme values	104
6.5.6	Two-dimensional problems: anisotropic material design with loss: effect of initial configurations	107
6.5.7	Three-dimensional problems: isotropic material design	109
6.5.8	Three-dimensional problems: anisotropic material design	110
6.6	Conclusions	112
7	Design of electromagnetic devices using ferrite material	113
7.1	Introduction	113
7.2	Formulation	114
7.2.1	Relative permeability of a ferrite material	114
7.2.2	Governing equation for wave propagation problem using ferrite	115
7.2.3	Design variables	117
7.2.4	Optimization problem	117
7.2.5	Sensitivity analysis	118
7.3	Numerical examples	119
7.3.1	Cylindrical cloaking design	119
7.3.2	Carpet cloaking design	120
7.3.3	Waveguide filter design	121
7.3.4	T-junction design	124
7.4	Conclusions	125
8	Thesis Conclusions	129
	Appendix	132
A	Derivation of first order absorbing boundary condition	132
B	Derivation of weak formulation	134
B.1	Two-dimensional case	134
B.2	Three-dimensional case	134
C	Sensitivity analysis of a complex function using the Adjoint Variable Method	136

References	148
List of publications	165

Chapter 1

Introduction

1.1 Motivation

Recent studies on artificial materials such as metamaterials have demonstrated that such materials can exhibit extraordinary electromagnetic properties not available in nature. These unusual properties can dramatically improve the performance of electromagnetic devices such as electrostatic actuators, waveguides, antennas, and so on, if artificial materials that provide certain prescribed properties can be effectively designed and fabricated. The macroscopic structural design of electromagnetic devices, such as the distribution of electromagnetic material in an antenna or waveguide, also greatly affects the response of these devices. Because it is usually difficult or time-consuming to find appropriate micro- or macrostructure designs by trial and error methods, there is a need for systematic design methods that assist or simplify the design of artificial materials. Furthermore, manufacturability and a various design requirements, such as the maximum volume of the material used, prevention of mechanical interference, maximum allowable stress, and so on, must all be satisfied in practical designs of mechanical and electromagnetic devices.

This thesis focuses on topology optimization for the microstructure design of dielectric-based electromagnetic materials that are artificially designed to exhibit desirable electromagnetic properties, and for the macrostructure design of electromagnetic devices that are fabricated from a ferrite material. In addition, topology optimization methods that handle the above design requirements are also discussed.

1.2 Structure of thesis

This thesis is a summary of research done during my doctoral course. The outline of each chapter is as follows:

Chapter 2 briefly introduces the concepts of structural optimization methods. A brief history of topology optimization is provided, and the formulations of the density-based topology optimization method and the level set-based topology optimization method used in later chapters are explained.

In Chapter 3, a topology optimization method that can consider manufacturability

is considered. A new projection function that reduces the number of design variables in a multiple phase projection method that imposes a minimum length scale in the topology optimization is formulated and applied to a minimum mean compliance problem and a compliant mechanism design problem.

In Chapter 4, a level set-based topology optimization method using mathematical programming is formulated to facilitate the treatment of constraint functionals. Several constraint functions are discussed and implemented. These include a mean compliance constraint that ensures that sufficient stiffness is obtained even when a load is applied in a direction slightly different from the prescribed direction, a mutual mean compliance constraint so that the structure deforms in a designed direction, and a stress constraint. The presented method updates the level set function using the Method of Moving Asymptotes (MMA). Stress constraints and mean compliance constraints are serially applied in a number of minimum mean compliance problems and compliant mechanism design problems.

Chapter 5 discusses a topology optimization method applied to the design of negative permeability dielectric metamaterials. The constructed optimization algorithm uses a level set-based topology optimization and the S-parameter retrieval method to obtain the effective permeability value that is the objective of the design optimization. The effective permeability minimization problem and the effective permeability design problem are formulated, and numerical results for two- and three-dimensional problems are provided to demonstrate that the presented method successfully finds clear configurations that have the desired negative effective permeability.

Chapter 6 deals with the microstructure design of dielectric materials that demonstrate a desired permittivity value. An energy-based homogenization method is used to obtain the permittivity tensor. Isotropic and anisotropic materials are designed using a density-based topology optimization method. The optimization problem is formulated to minimize the difference between the obtained effective value and the prescribed value. We derive the theoretical bounds of the two- and three-dimensional anisotropic effective property in the principal direction when the effective property in the other principal direction(s) is/are set to a prescribed value, to evaluate the effective permittivity values obtained by the optimization. The results show that the obtained values using the presented method are in good agreement with theoretical bounds.

Chapter 7 addresses the design of an electromagnetic cloaking device and a metallic waveguide, both using a ferrite material. Ferrite materials exhibit a frequency-dependent degree of permeability due to a magnetic resonance phenomenon that can be influenced by applying an external DC magnetic field. Thus, the use of an appropriately designed ferrite material for the electromagnetic cloaking device and metallic waveguide is expected to result in novel functions, such as on-off operation in response to on-off application of an external magnetic field, or a tunable frequency range under which the cloak or waveguide operates. A level set-based topology optimization method is used to design the configurations of the ferrite material and the optimization problem is formulated to minimize the integral value of the norm between the electric field and the reference field prescribed in the scattering domain for the cloak design problem and to maximize the transmission power for the waveguide.

uide design problem. The results show that the presented method yields appropriate optimization results.

Finally, conclusions for the entire thesis are provided in Chapter 8.

Chapter 2

Topology optimization

2.1 Structural optimization

Structural optimization methods can be categorized into three types, according to the degree of design flexibility: size, shape, and topology optimization. Size optimization [1, 2], first proposed by Schmit [1] in the 1960's, focuses on the size attributes of structural designs, such as thickness, width, and length. Shape optimization, studied from the 1970's [3–5], deals with design aspects pertaining to the shape of structures, such as their outer boundaries and the shapes of inner holes. Topology optimization [6–9], widely applied now in a range of industries, is the most flexible type of structural optimization method because it allows topological changes that include increasing the number of holes in the design domain, in addition to changes in a structure's shape.

2.2 Topology optimization

The basic ideas of topology optimization are (1) the extension of the design domain to a fixed design domain and (2) the replacement of the optimization problem by a material distribution problem in the fixed design domain, using the characteristic function [10]. Since the characteristic function is a discontinuous function that represents the structure using values of 0 or 1, optimization problems are usually ill-posed. Various approaches to overcome this difficulty have been proposed, such as the Homogenization Design Method (HDM) [6], and density approaches such as the SIMP method [7], in which optimized configurations are represented as density distributions that assume continuous values from 0 to 1. The obtained optimized configurations therefore often include grayscale areas where the density is an intermediate value between 0 and 1, and there also exist the problems of checkerboards and mesh-dependency. Various schemes have been proposed to overcome such problems and provide grayscale-free optimized configurations, or configurations that do not include impractically complex structures. These schemes can be roughly divided into two categories: those that impose geometric constraints, and filtering schemes. Detailed reviews [11, 12] of these methods are in the literature.

Concerning constraint schemes, Ambrosio and Buttazzo [13] and Haber et al.

[14] imposed a constraint on the perimeter of structural boundaries. Petersson and Sigmund [15] constrained local density gradients and Zhou et al. [16] extended this scheme to achieve structures with a minimum member size. Borrvall and Petersson [17] introduced a regularized penalty function to constrain intermediate densities. Poulsen [18] proposed the monotonicity-based minimum length scale (MOLE) method that imposes the same minimum length scale on both material and void domains. In the MOLE method, an additional constraint restricts the number of phase changes within the radius of a set minimum length scale.

Concerning filtering schemes, Sigmund [19, 20] first proposed a sensitivity filter in which filtered sensitivities used to update the design variables are obtained as weighted averages of sensitivities in mesh-independent neighborhood domains. Bruns and Tortorelli [21] introduced a density filter based on a sensitivity filter formulation [19, 20] and Bourdin [22] proved the existence of a solution to a minimum mean compliance problem, using a density filter [21]. Subsequently, Wang and Wang [23] introduced a bilateral filtering scheme originally developed for use in image processing, in which material densities are obtained as a nonlinearly weighted average of neighborhood density according to their closeness and similarity, using a Gaussian distribution function. Recently, several filtering schemes using a projection method have been proposed.

Guest et al. [24] proposed a Heaviside density filter that imposes a minimum length scale, using the Heaviside projection function so that all elements within the radius set by this scale become solid when a design variable has a nonzero value. Sigmund [12] used min/max operators so that the element volume fraction is defined as the min/max value within the radius of a minimum length scale. In this method, min/max operators are redefined using the Kreisselmeier and Steinhauser (KS) functions [25], and named dilate/erode operators. Based on a Heaviside density filter [24], Almeida et al. [26] introduced an inverse projection scheme where direct or inverse projections are used, depending on the volume of void surrounding elements, and Guest [27] proposed a multiple phase projection method (MPPM) to restrict the minimum length scale in both solid and void phases. Subsequently, Guest and Genut [28] proposed the use of adaptive design variables for the MPPM, to reduce computation times. Furthermore, based on the Heaviside filter, Guest [29] proposed a projection scheme that can impose both minimum and maximum length scales.

However, since the Heaviside density filter is not a volume-preserving filter, that is, since the volume of the design variables is not the same as that of the material density, and since the parameter β that controls the curvature of the smoothed Heaviside function is updated every several iterations during optimization procedure, the applied volume constraint is temporarily violated, leading to relatively poor optimization stability, as pointed out by Xu et al. [30]. Xu et al. proposed a volume preserving filter that combines a Heaviside filter [24] with a modified Heaviside filter [12]. To preserve the volume, the appropriate threshold value for the Heaviside function is obtained by a line search. Guest et al. [31] researched the parameters used in Heaviside density filters in order to improve the convergence of optimization computations. Note that the open/close operators in some research [12] are volume preserving, while basic filters, dilate/erode operators, are not.

Sigmund [32] and Wang et al. [33] proposed a robust topology optimization method using dilate and erode operators. Three designs, obtained using original, dilated, and eroded density distributions implicitly represent the manufacturing error, and the worst objective function of three designs is maximized or minimized during the optimization. This procedure guarantees optimized designs with good performance even for thin or broad structures. In [33], three threshold values for the Heaviside function are used to obtain three different designs, and a volume constraint is applied to the eroded design. The threshold values for the dilate and erode operators can be independently set in this method.

Furthermore, partial differential equation (PDE)-based filtering schemes have recently been proposed [34–36]. In most previously proposed filtering schemes, the filtered density or sensitivity values are obtained by a convolution operator [9] that computes weighted averages over neighborhood domains. In PDE-based filtering schemes, however, a Helmholtz-type PDE is used instead of a convolution operator. The relatively low computational cost is one advantage of PDE-based filters, as discussed in [33]. Another advantage is their ease of implementation, because such filters can directly use the FEM framework for solving state or adjoint problems. Lazarov and Sigmund applied a PDE-based filter to sensitivities [34] and, later, to densities [36]. Kawamoto et al. [35] introduced a PDE-based filter combined with the Heaviside function.

Topology optimization methods have been applied to a variety of problems, such as stiffness maximization problems [37], eigen-frequency problems [38], compliant mechanism design problem [20, 39], elastic wave propagation problems [40], thermal problems [41], fluid problems [42–44], magnetic problems [45], acoustic problems [46–48], and so on.

Topology optimization has also been applied to a variety of electromagnetic problems. To address antenna design problems, Kiziltas et al. [49, 50] applied topology optimization for the design of dielectric substrates for patch antennas. Nomura et al. [51] proposed a topology optimization method to the design of dielectric resonator antennas, integrating topology optimization with the Finite-Difference Time-Domain (FDTD) method so that multi-frequency problems can be easily handled. Erentok and Sigmund [52] applied topology optimization to sub-wavelength antenna designs in which the conductivity distribution is designed. Aage et al. [53] proposed a topology optimization method that imposes a design-dependent element impedance boundary condition on each finite element, to handle the problem of skin depth in the design of metallic devices, and applied this method to magnetic and electric resonator design problems and a monopole antenna design problem. For photonic crystal design problems, Jensen and Sigmund designed a photonic crystal waveguide [54] and T-junction [55] using topology optimization. Frei et al. [56] designed a photonic crystal waveguide termination that maximizes directional emission. A comprehensive review of topology optimization for nanophotonics is available [57]. Hirayama et al. [58] designed dielectric material distributions for a metallic waveguide and Nishiwawki et al. [59] developed cross-section designs for metallic waveguides. Andkjær et al. [60] designed a plasmonic grating coupler, and Soh et al. [61] and Soh and Yoo [62] designed thin film solar cells.

For metamaterial design problems, Diaz and Sigmund [63] proposed a topology optimization method for the design of negative permeability metamaterials using an S-parameter retrieval method, where the imaginary part of the effective permeability was minimized at a specific frequency, and several designs for metallic structures attached to dielectric substrates that achieve negative permeability were provided. Sigmund [64] proposed a density-based topology optimization method for dielectric metamaterials to obtain dielectric material designs that minimize the effective permeability at a specific frequency, which also employed the S-parameter retrieval method to obtain the effective properties. Choi and Yoo [65] introduced an inverse homogenization method [66] for the design of magnetic materials that attain a desirable prescribed effective permeability value. Zhou et al. [67] proposed an inverse homogenization method for the design of metamaterials, where both permittivity and permeability are simultaneously maximized. El-Kahlout and Kiziltas [68] introduced inverse homogenization methods for the design of dielectric materials that realize a prescribed effective permittivity value, using an asymptotic expansion-based homogenization method and Genetic Algorithms (GAs) [68]. GAs have also been used to find optimized layouts of the metallic inclusion in metamaterial unit cells for a negative permeability design problem [69], and for different multi-objective problems [70, 71] in which the refractive index and impedance were simultaneously designed [70], and the bandwidth of the negative refractive index was maximized and the dissipation minimized [71].

2.3 Level set-based structural optimization

A type of structural optimization method using level set boundary expressions has been proposed in which the boundaries of the optimal configuration are implicitly represented using the level set function. A level set-based structural optimization method was first proposed by Sethian and Wiegmann [72] where the level set function is updated based on the von Mises stress. Wang et al. [73] and Allaire et al. [74] proposed a level set-based structural optimization method where the level set function is updated using the Hamilton-Jacobi equation, based on the shape sensitivities. Level set-based structural optimization methods have been applied to many problem such as a multi-material problem [75, 76], and a stress minimization problem [77]. This method also extended to integrate with the boundary element method (BEM) [78], where the mesh immersion method is used to integrate the boundary element mesh with the Eulerian mesh in which the level set function is defined. However, because these particular level set-based methods are based on the boundary advection concept, the introduction of holes during the optimization procedure is not allowed, although the number of holes can be decreased. As a result, the obtained optimized configurations are greatly affected by initial configuration setting, and several approach have been proposed to alleviate this problem. Allaire et al. [79] proposed a level set-based approach where holes are introduced according to a topological gradient method [80, 81]) applied after a certain number of iterations, while the structural boundaries are updated by the Hamilton-Jacob equation based on smoothed shape sensitivities. Burger

et al. [82] introduced a topological derivative into the Hamilton-Jacobi equation, and He et al. [83] extended this method to deal with general objective functionals.

In level set-based methods using the Hamilton-Jacobi equation, the level set function must be re-initialized to maintain numerical accuracy, which is computationally costly. Several approaches that are not based on the boundary advection concept have been proposed. Wang and Wang [84] proposed a method that represents the level set function by superposition of a radial basis function. Luo and Tong [85] proposed a level set-based topology optimization method incorporating a radial basis function for the design of compliant mechanisms, but the choice of appropriate values for the radial basis function parameters depends on experience. Wei and Wang [86] proposed a method that uses a piecewise constant level set function [87] and updated the level set function using the additive operator splitting (AOS) scheme [88,89]. This method imposes a constraint, named a piecewise constant constraint, to ensure that the level set function has piecewise values, and the optimization problem is solved using the augmented Lagrangian method. However, the parameters used for handling constraint functionals affect the stability of optimizations and also the obtained configurations, as discussed in [86]. Yamada et al. [90] proposed a level set-based topology optimization method where the optimization problem is regularized using the Tikhonov regularization method [91]. In this method, a regularization term is added to the primary objective functional and the level set function is updated based on a reaction-diffusion equation. This method enables the complexity of optimized configurations to be adjusted by using appropriate magnitudes of a regularization parameter, and has been applied to a variety of problems such as stiffness maximization problems, eigen-frequency problems, compliant mechanism design problems [90], and problems to maximize thermal diffusivity [92].

Level set-based methods have been applied to many electromagnetic design problems, such as metallic waveguides [93,94] and dipole antennas [95]. For metamaterial design problems, Zhou et al. [96] proposed a level set-based structural optimization method for the design of double negative metamaterials, that is, metamaterials with negative permittivity and negative permeability. The aim of the optimization problem in this case was to find an optimized layout of metallic inclusions, and the objective function was formulated using current flow, instead of using the effective permittivity or permeability directly. Subsequently, Zhou et al. [97] proposed a level set-based structural optimization method in which the effective permeability is directly used as an objective function. Concerning the design optimization of metamaterial applications, Yamasaki et al. [98] proposed a level set-based structural optimization method for the design of composite right- and left-handed transmission lines consisting of a metallic waveguide with dielectric inclusions. The aim of optimization problem was to find the optimized configuration of the dielectric inclusion within the unit cell of the particular transmission line that provides desired dispersion behavior for the composite right- and left-handed lines.

2.4 Formulation of topology optimization

As mentioned above, the basic ideas of topology optimization are (1) the extension of the design domain to a fixed design domain D so that the fixed design domain D encompasses the entire original design domain Ω (Fig.2.1), and (2) the replacement of the optimization problem by a material distribution problem in the fixed design domain, using the characteristic function [10]. The characteristic function χ is defined as follows:

$$\chi(\mathbf{x}) = \begin{cases} 1 & \text{if } \mathbf{x} \in \Omega \\ 0 & \text{if } \mathbf{x} \in D \setminus \Omega, \end{cases} \quad (2.1)$$

where \mathbf{x} represents the coordinate in the fixed design domain.

Since this characteristic function lies in L^∞ and is allowed to be discontinuous everywhere, the optimization problem is usually ill-posed. As Cheng and Olhoff [99] and Haber et al. [14] described, an obtained optimized configuration may contain an infinite number of infinitely thin members. To overcome this obstacle, the Homogenization Design Method (HDM) [6], and density approaches such as the SIMP method [7, 100–102] were proposed, in which optimized configurations are represented as density distributions, with the density assuming continuous values from 0 to 1. Bendsøe and Kikuchi [6] proposed the HDM to relax the design domain, using the homogenization method [8, 103, 104]. In the HDM, a discontinuous material distribution is represented using a periodic microstructure and the problem of discontinuity is then solved by homogenizing the material property tensor. The HDM design variables are parameters that determine the geometrical configuration of a unit cell, such as the size or angle of an inner hole. Several unit cell geometries have been proposed, such as layered structures, square rectangular [7], and hexagonal [105] unit cells, according to the requirements of the material used and details of the design problem.

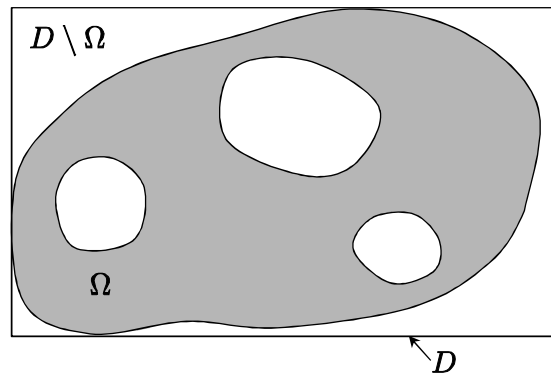


Figure 2.1: Fixed design domain D .

2.4.1 Density-based method

Here, a formulation of density-based topology optimization [7, 102] is briefly introduced. In this thesis, density-based topology optimizations are described and applied in Chapters 3 and 6. In a density-based approach, a material property tensor \mathbf{a} such as an elasticity tensor, permeability tensor, permittivity tensor, or the like, is represented using a density function $f(\rho)$, as follows.

$$\mathbf{a} = \mathbf{a}_1 f(\rho), \quad (2.2)$$

where ρ is the normalized density and \mathbf{a}_1 is the material property tensor in the material domain Ω .

The density function is often expressed as a power function, and the material property tensor is then defined as

$$\mathbf{a} = (\mathbf{a}_1 - \mathbf{a}_0) \rho^p + \mathbf{a}_0, \quad (2.3)$$

where p is a penalization parameter and \mathbf{a}_0 is the material property tensor in the void domain $D \setminus \Omega$. The design domain relaxation method employing Eq.2.3 is called the solid isotropic material with penalization (SIMP) method [7, 100–102]. Because this interpolation scheme, unlike the homogenization method, is not based on a mathematical or physical viewpoint, the material property tensor of obtained grayscale areas is hard to interpret. Bendsøe and Sigmund [102] rigorously compare the interpolation of the SIMP method with various theoretical bounds of composite materials, (e.g. the Hashin-Strikman bound [106, 107] and the Voigt-Reuss bound [108]), and demonstrate the use of several different microstructures that realize the material property tensor of grayscale areas obtained by the SIMP interpolation, based on the magnitude of normalized density.

The design variable in density-based topology optimization is the normalized density that is typically located at the nodes of a finite element mesh, or the center of finite elements, and it is usually updated using a mathematical programming method such as an Optimality Criteria (OC) method, Sequential Linear Programming (SLP), Sequential Quadratic Programming (SQP), a Convex Linearization (CONLIN) [109] method, or the Method of Moving Asymptotes (MMA) [110, 111]. Ma and Kikuchi [112] reviewed these methods and developed an extension, the Generalization of Sequential Approximation Optimization (GSAO) method.

2.4.2 Level set-based method

Here, a level set-based topology optimization method that incorporates a fictitious interface energy [90] is briefly introduced that will be used for the design of negative permeability dielectric metamaterials in Chapter 5, and the design of ferrite cloaking devices and waveguides in Chapter 7 in this thesis. This method is dealt with in Chapter 4 as well. The topology optimization problems in these examples are formulated using a fixed design domain D that consists of a domain Ω filled with solid material, a domain filled with void, and structural boundaries $\partial\Omega$. As shown in

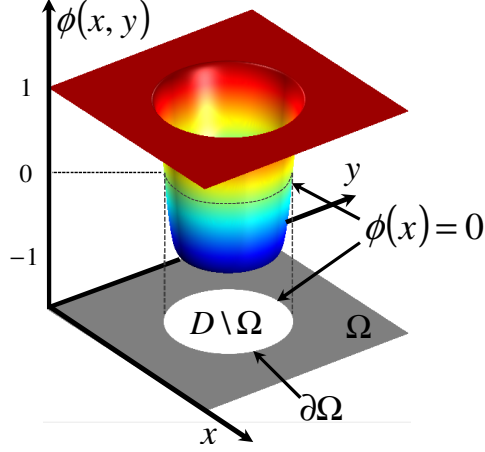


Figure 2.2: Fixed design domain D and level set function ϕ .

Fig.2.2, the structural boundaries in a level set-based topology optimization method are implicitly represented using the iso-surface of the level set function, as follows.

$$\begin{cases} 1 \geq \phi(\mathbf{x}) > 0 & \text{for } \forall \mathbf{x} \in \Omega \setminus \partial\Omega \\ \phi(\mathbf{x}) = 0 & \text{for } \forall \mathbf{x} \in \partial\Omega \\ 0 > \phi(\mathbf{x}) \geq -1 & \text{for } \forall \mathbf{x} \in D \setminus \Omega \end{cases} \quad (2.4)$$

The level set function ϕ is used to represent the boundaries of the target structure, where positive values represent the solid domain, negative values represent the void domain, and zero represents the structural boundaries. The optimization problem that minimizes objective functional F under a constraint functional G is then formulated as follows, using the above defined level set function ϕ .

$$\inf_{\chi_\phi} F(\chi_\phi) = \int_D f_1(\mathbf{x}, \chi_\phi) d\Omega + \int_\Gamma f_2(\mathbf{x}, \chi_\phi) d\Gamma \quad (2.5)$$

$$\text{subject to } G(\chi_\phi) = \int_D g(\mathbf{x}, \chi_\phi) d\Omega - G_{\max} \leq 0, \quad (2.6)$$

where f_1 and f_2 are density functions of the objective functional, g is the density function of the constraint functional, and G_{\max} is the upper limit value of G . The characteristic function $\chi_\phi(\phi)$ is defined as follows.

$$\chi_\phi(\phi) = \begin{cases} 1 & \text{if } \phi \geq 0 \\ 0 & \text{if } \phi < 0 \end{cases} \quad (2.7)$$

The above optimization problem is an ill-posed problem because the level set function is allowed to be discontinuous at every point, so the optimization problem must be regularized. Here, the Tikhonov regularization method is applied and the above

formulation is replaced with the following optimization problem:

$$\inf_{\phi} F_R(\chi_{\phi}, \phi) = F + R \quad (2.8)$$

$$\text{subject to } G(\chi_{\phi}) \leq 0, \quad (2.9)$$

where R in the above equation is defined so that with

$$R = \int_D \frac{1}{2} \tau |\nabla \phi|^2 d\Omega. \quad (2.10)$$

The τ parameter is a regularization parameter that can be used to adjust the degree of regularization. This formulation is then replaced with an optimization problem without constraints, using Lagrange's method of undetermined multipliers, as follows.

$$\inf_{\phi} \hat{F}_R(\chi_{\phi}, \phi) = \hat{F} + R, \quad (2.11)$$

where $\hat{F} = F + \lambda G$, \hat{F}_R is the Lagrangian, and λ is the Lagrange multiplier. Based on the above formulation, the KKT (Karush-Kuhn-Tucker) conditions of this optimization problem are described as

$$\left\langle \frac{d\hat{F}_R}{d\phi}, \tilde{\phi} \right\rangle = 0, \quad \lambda G = 0, \quad \lambda \geq 0, \quad G \leq 0, \quad (2.12)$$

where the notation $\left\langle \frac{d\hat{F}_R}{d\phi}, \tilde{\phi} \right\rangle$ represents the Fréchet derivative of the regularized Lagrangian \hat{F}_R with respect to ϕ .

Level set functions that satisfy the above KKT conditions are candidate solutions of the level set function that represent optimized configurations. However, optimized solutions are difficult to find directly, so the optimization problem is replaced by a time evolution equation, by introducing a fictitious time t . The level set function is updated by solving this equation, and an optimized configuration is ultimately obtained, as explained below.

Level set function updating scheme

For the following formulation, which introduces a fictitious time t , it is assumed that the variation of the level set function is proportional to the gradient of Lagrangian \hat{F}_R , as follows.

$$\frac{\partial \phi}{\partial t} = -K(\phi) \frac{d\hat{F}_R}{d\phi}, \quad (2.13)$$

where $K(\phi) > 0$ is a coefficient of proportionality. Substituting Eq.(2.11) into Eq.(2.13) and setting appropriate boundary conditions, the following equations are obtained.

$$\left\{ \begin{array}{l} \frac{\partial \phi}{\partial t} = -K(\phi) \left(\frac{d\hat{F}}{d\phi} - \tau \nabla^2 \phi \right) \\ \frac{\partial \phi}{\partial n} = 0 \\ \phi = 1 \end{array} \right. \quad \begin{array}{l} \text{on } \partial D \setminus \partial D_{ND} \\ \text{on } \partial D_{ND} \end{array} \quad (2.14)$$

where ∂D_{ND} is non-design boundaries where the Dirichlet boundary condition is applied. The optimized configuration can be then obtained by solving the above time evolution problem, and in this research, candidate optimum solutions are found by solving the above equation. Here, since the objective functional $\hat{F}(\chi_\phi)$ is represented as a functional of χ_ϕ , the derivative of $\hat{F}(\chi_\phi)$ is equivalent to the magnitude of the topological derivative (e.g., [80, 81, 113–115]). The derivative of $\hat{F}(\chi_\phi)$ can then be obtained as a derivative with respect to χ_ϕ , namely, $-\text{d}\hat{F}(\chi_\phi)/\text{d}\chi_\phi$ [83, 90].

Chapter 3

Multiple phase projection method

3.1 Introduction

This chapter discusses a new methodology for reducing the number of design variables in a multiple phase projection method (MPPM), which advantageously reduces the computation time. The MPPM is a density filtering method that imposes a minimum length scale on solid as well as void phases, and two design variables associated with these phases are typically required at each node, but the design variables themselves are physically meaningless. The design variables are first passed through the projection function to yield weighted average design variables. The projection function is a mesh-independent weighted average function based on the minimum length scale. The weighted average design variables are then passed through a Heaviside function to yield the element volume fractions. The approximated Heaviside function is an exponential function that approaches the Heaviside step function as the value of a parameter approaches infinity. Black and white solutions are obtained by the property of the approximated Heaviside function. The primary drawback of the MPPM is an increased number of design variables. Although two variables are required at each node in the previously proposed MPPMs, only one of the design variables has a nonzero value. The new methodology proposed here requires only a single design variable at each node, which can assume any value in a range from -1 through $+1$. Positive values of this design variable are associated with the solid phase and negative values are associated with the void phase. Optimum design examples for two minimum compliance problems and a compliant mechanisms design problem are provided to verify that the new methodology provides appropriate solutions that incorporate a given minimum length scale when a reduced number of design variables is used.

3.2 Formulation

3.2.1 Heaviside projection method

In this section, the Heaviside projection method (HPM) is briefly reviewed. In topology optimization methods, a structural optimization problem is replaced by a material

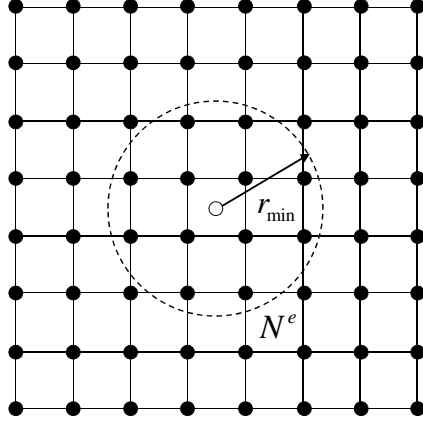


Figure 3.1: Domain showing constraint according to a minimum length scale.

distribution problem within a fixed design domain, and the material distribution is typically represented by normalized density values in finite elements or nodes. That is, a domain where the normalized density has a value of 1 represents a solid domain, and that with a value of 0 represents a void domain. In the HPM, the design variables ϕ_j are independent of the finite element mesh and can be located at any point in the design domain. In this study, the design variables are located at the nodes of the finite element mesh, and the normalized densities obtained after mapping through a projection function are located at the center of the finite elements, as in [24, 26, 27]. Figure 3.1 shows a domain neighborhood where the design variables that are mapped to the normalized density of the e -th finite element are defined. As shown in the figure, the design variables at the nodes in the area defined according to the radius of the prescribed minimum length scale r_{min} are defined as follows:

$$\phi_j \in N^e \text{ if } r \equiv |\mathbf{x}_j - \bar{\mathbf{x}}^e| \leq r_{min}, \quad (3.1)$$

where N^e is the domain neighborhood corresponding to the e -th finite element, \mathbf{x}_j is the location of design variable j , and $\bar{\mathbf{x}}^e$ is the location of the center of element e . The weighted average design variables μ^e are then computed using the following projection function,

$$\mu^e = \frac{\sum_{j \in N^e} \phi_j w(|\mathbf{x}_j - \bar{\mathbf{x}}^e|)}{\sum_{j \in N^e} w(|\mathbf{x}_j - \bar{\mathbf{x}}^e|)}, \quad (3.2)$$

where w is the distance weighting function that imposes increasing weights for closer design variables, defined as follows:

$$w(|\mathbf{x}_j - \bar{\mathbf{x}}^e|) = \begin{cases} \frac{r_{min} - r}{r_{min}} & \phi_j \in N^e \\ 0 & \text{otherwise.} \end{cases} \quad (3.3)$$

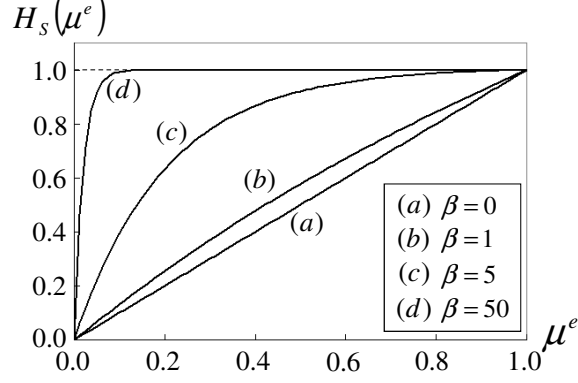


Figure 3.2: Smoothed Heaviside functions for μ^e .

The weighted average design variables μ^e are then passed through a Heaviside function to yield the element volume fractions ρ^e .

When a minimum length constraint is applied to solid domains, the normalized density for the e -th finite element is obtained by the Heaviside step function expressed as follows:

$$\rho_1^e = H(\mu^e) = \begin{cases} 1 & \text{if } \mu^e > 0 \\ 0 & \text{if } \mu^e = 0. \end{cases} \quad (3.4)$$

The basic idea of the Heaviside projection method is that the elements become solid when any design variable in the area defined by the radius of the minimum length scale has a nonzero value, and the elements become void only when all the design variables within this defined area have a value of zero. This condition prevents the creation of any feature smaller than the minimum length scale. Since the minimum length scale is not influenced by the mesh size, the Heaviside projection method is mesh-independent.

In the numerical computation, the above Heaviside step function is modified to the following continuous function so that the gradient with respect to μ^e , used in the optimization algorithm, can be obtained.

$$\rho_1^e = H_s(\mu^e) = 1 - e^{-\beta\mu^e} + \mu^e e^{-\beta}, \quad (3.5)$$

where β is a parameter that can be used to control the curvature of the approximated Heaviside function. Figure 3.2 shows the approximated Heaviside function for various magnitudes of β . The approximated Heaviside function approaches the Heaviside step function as the value of parameter β approaches infinity.

On the other hand, when the minimum length constraint is applied to void domains, the normalized density for the e -th finite element is obtained using the Heaviside step function as follows:

$$\rho_0^e = 1 - H(\mu^e) = \begin{cases} 0 & \text{if } \mu^e > 0 \\ 1 & \text{if } \mu^e = 0. \end{cases} \quad (3.6)$$

Again, the above Heaviside step function is modified in the numerical computation as follows.

$$\rho_0^e = 1 - H_s(\mu^e) = e^{-\beta\mu^e} - \mu^e e^{-\beta}. \quad (3.7)$$

As discussed above, the minimum length constraint can only be applied to either solid or void domains. Therefore, undesirably complex configurations may appear in domains that do not have a minimum length constraint applied.

3.2.2 Multiple phase projection method (MPPM)

To overcome the above problem, minimum length constraints are applied to both solid and void domains in the MPPM [27]. The MPPM uses two design variables in each node, ϕ_{1j} and ϕ_{0j} , associated with solid and void domains, respectively. Following the same procedure as that of the HPM, the weighted average design variables μ_1^e and μ_0^e are obtained using the projection function on domain neighborhoods N_1^e and N_0^e , defined using minimum length scales $r_{min,1}$ and $r_{min,0}$ applied to the solid and void domains, respectively. The normalized densities ρ_1^e and ρ_0^e that respectively correspond to the solid and void domains are then obtained using the Heaviside function, through Eqs.(3.4) and (3.6). Finally, the normalized density ρ^e for each finite element is computed as the average of the normalized densities ρ_1^e and ρ_0^e , as follows.

$$\rho^e = \frac{1}{2} (\rho_1^e + \rho_0^e) = \frac{1}{2} (H(\mu_1^e) + 1 - H(\mu_0^e)). \quad (3.8)$$

Again, in the numerical computation, the above Heaviside step function is modified as below.

$$\rho^e = \frac{1}{2} [(1 - e^{-\beta\mu_1^e} + \mu_1^e e^{-\beta}) + (e^{-\beta\mu_0^e} - \mu_0^e e^{-\beta})]. \quad (3.9)$$

In the above formulation, domains where $\rho_1^e = \rho_0^e = 1$, so that $\rho^e = 1$, represent solid domains, and domains where $\rho_1^e = \rho_0^e = 0$, so that $\rho^e = 0$, represent void domains. However, domains where $\rho_1^e = 1$ and $\rho_0^e = 0$, and domains where $\rho_1^e = 0$ and $\rho_0^e = 1$, represent grayscale areas. Such grayscale areas can be avoided by penalizing the element stiffness matrix using the SIMP method, as follows.

$$\mathbf{k}^e = [(\rho^e)^p + \rho_{min}] \mathbf{k}_0^e, \quad (3.10)$$

where p is the penalization parameter, \mathbf{k}_0^e represents the element stiffness matrix in solid domains, and ρ_{min} is a sufficiently small positive value applied to maintain a positive definite global stiffness matrix.

3.2.3 Proposed MPPM

The main drawback of the above MPPM is the increased number of design variables. Although this MPPM requires two variables at each node, only one of the design

variables has a nonzero value. Here, a new methodology is discussed, one that requires only a single design variable at each node, with values ranging from -1 through $+1$. Positive and negative values of this design variable are associated with the solid and void phase, respectively.

Solid phase projection

The projection function is modified as shown in Eq.(3.11) so that positive values of the design variable are associated with the solid phase. When any design variable ϕ_j within the radius of the minimum length scale N_1^e is positive, μ_1^e becomes positive, and when all design variables ϕ_j within this radius are non-positive, μ_1^e becomes zero.

$$\mu_1^e = \frac{\sum_{j \in N_1^e} (|\phi_j| + \phi_j)w(|\mathbf{x}_j - \bar{\mathbf{x}}^e|)}{2 \sum_{j \in N_1^e} w(|\mathbf{x}_j - \bar{\mathbf{x}}^e|)}. \quad (3.11)$$

Void phase projection

The projection function for the void phase is modified as follows so that negative values of the design variable are associated with the void phase. When any design variable ϕ_j within the radius of the minimum length scale is negative, μ_0^e becomes positive, and when all design variables ϕ_j within this radius are non-negative, μ_0^e becomes zero.

$$\mu_0^e = \frac{\sum_{j \in N^0} (|\phi_j| - \phi_j)w(|\mathbf{x}_j - \bar{\mathbf{x}}^e|)}{2 \sum_{j \in N^0} w(|\mathbf{x}_j - \bar{\mathbf{x}}^e|)}. \quad (3.12)$$

Normalized density

The normalized density ρ^e for each finite element is then defined as the mean value of μ_1^e and μ_0^e , the same as in Eq.(3.8). The rest of the procedure is the same as that used in the conventional MPPM.

3.2.4 Optimization problem

Consider a fixed design domain D and a material domain Ω . The displacement is fixed at boundary Γ_u and a traction \mathbf{f} is applied at boundary Γ_f . The objective is to find the optimum layout of the design space that minimizes the mean compliance under the given volume constraint.

The optimization problem is defined as follows:

$$\text{minimize } c = \mathbf{f}^T \mathbf{u} \quad (3.13)$$

$$\text{subject to } \sum_{e=1}^N \rho^e v^e \leq V_{max} \quad (3.14)$$

$$\mathbf{K} \mathbf{u} = \mathbf{f} \quad (3.15)$$

$$-1 \leq \rho_j \leq 1, \quad (3.16)$$

where c is the mean compliance, v is the volume of each finite element and \mathbf{u} is obtained displacement. \mathbf{K} is the global stiffness matrix, V_{max} is the given volume constraint, and N is the number of elements. Note that the optimization problem here is described using the discretized form, since the formulation used in the MPPM has been discussed in the previous subsections using this form.

The sensitivity of the minimum mean compliance problem can be derived as follows:

$$\frac{\partial c}{\partial \phi_j} = \sum_{e \in D} \frac{\partial c}{\partial \rho^e} \frac{\partial \rho^e}{\partial \phi_j}. \quad (3.17)$$

In the above equation, the sensitivity with respect to the normalized density of the e -th finite element $\frac{\partial c}{\partial \rho^e}$ can be obtained as follows, since the optimization problem is self-adjoint:

$$\frac{\partial c}{\partial \rho^e} = -\mathbf{u}^T \frac{\partial \mathbf{K}}{\partial \rho^e} \mathbf{u} = -p(\rho^e)^{p-1} \mathbf{u}^{eT} \mathbf{k}_0^e \mathbf{u}^e, \quad (3.18)$$

where \mathbf{u}^e represents the displacement of the e -th finite element. The sensitivities are finally obtained as follows by substituting Eq.(3.18) into Eq.(3.17).

$$\frac{\partial c}{\partial \phi_j} = - \sum_{e \in D} p(\rho^e)^{p-1} \mathbf{u}^{eT} \mathbf{k}_0^e \mathbf{u}^e \frac{\partial \rho^e}{\partial \phi_j}, \quad (3.19)$$

where

$$\frac{\partial \rho^e}{\partial \phi_j} = \sum_{i=1,0} \frac{\partial \rho^e}{\partial \mu_i^e} \frac{\partial \mu_i^e}{\partial \phi_j}, \quad (3.20)$$

$$\frac{\partial \rho^e}{\partial \mu_i^e} = \frac{1}{2}(-1)^{i+1} (\beta e^{-\beta \mu_i^e} + e^{-\beta}), \text{ and} \quad (3.21)$$

$$\frac{\partial \mu_i^e}{\partial \phi_j} = \left[\frac{\phi_j}{\sqrt{\phi_j^2 + \epsilon^2}} + (-1)^{i+1} \right] \frac{w(|\mathbf{x}_j - \bar{\mathbf{x}}^e|)}{(\sqrt{1 + \epsilon^2} + 1) \sum_{k \in N_i^e} w(|\mathbf{x}_k - \bar{\mathbf{x}}^e|)}. \quad (3.22)$$

3.3 Numerical implementation

3.3.1 Approximation of absolute values

The gradient of the absolute value is not continuous at $\phi_j = 0$. In order to use sensitivity analysis in the topology optimization, the absolute value $|\phi|$ is approximated

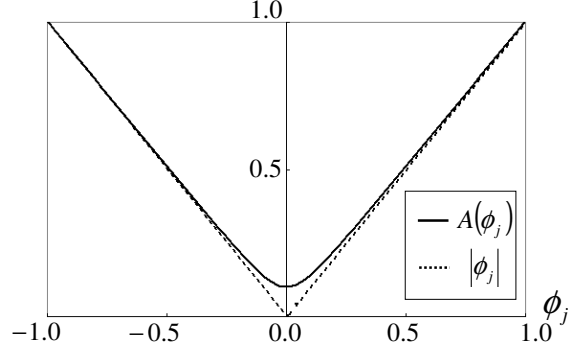


Figure 3.3: Approximated absolute value.

by the smoothed function $A(\phi_j) = \sqrt{\phi_j^2 + \varepsilon^2}$. Figure 3.3 shows the approximated absolute value. The parameter ε is given a small positive value. Several values were evaluated and $\varepsilon = 0.1$ is applied here, as in [18]. The weighted average design variables μ_1 and μ_0 are then modified to regularize their values so that they fall between 0 and 1, as follows:

$$\mu_1^e = \frac{\sum_{j \in N^1} \left(\sqrt{\phi_j^2 + \varepsilon^2} + \phi_j \right) w(|\mathbf{x}_j - \bar{\mathbf{x}}^e|)}{(\sqrt{1 + \varepsilon^2} + 1) \sum_{j \in N^1} w(|\mathbf{x}_j - \bar{\mathbf{x}}^e|)}, \quad (3.23)$$

$$\mu_0^e = \frac{\sum_{j \in N^0} \left(\sqrt{\phi_j^2 + \varepsilon^2} - \phi_j \right) w(|\mathbf{x}_j - \bar{\mathbf{x}}^e|)}{(\sqrt{1 + \varepsilon^2} + 1) \sum_{j \in N^0} w(|\mathbf{x}_j - \bar{\mathbf{x}}^e|)}. \quad (3.24)$$

3.3.2 Optimization algorithm

Figure 3.4 shows the optimization flowchart. First, the design variables are initialized. The weighted average design variable μ_1^e , μ_0^e and the element density ρ^e are then computed using the projection function and Heaviside function, respectively. The objective functional is computed using the FEM. If it is converged, the optimization procedure terminates, otherwise the sensitivities are computed using the adjoint variable method (AVM). The design variables are then updated using the method of moving asymptotes (MMA), and the process returns to the second step.

3.3.3 Updating scheme applied to optimization parameters.

Although larger values of the SIMP penalization parameter may reduce the number of grayscale areas in an obtained configuration, it is well known that such adjustment

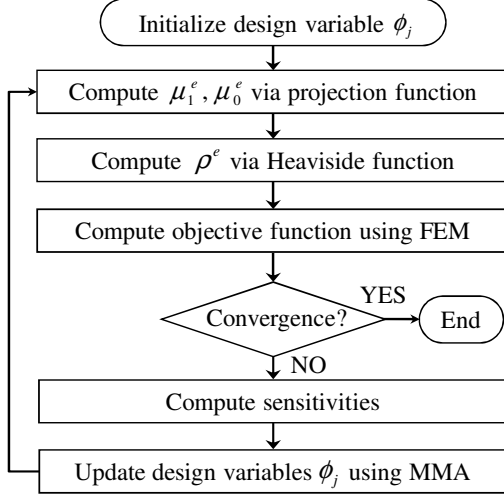


Figure 3.4: Flowchart of the optimization procedure.

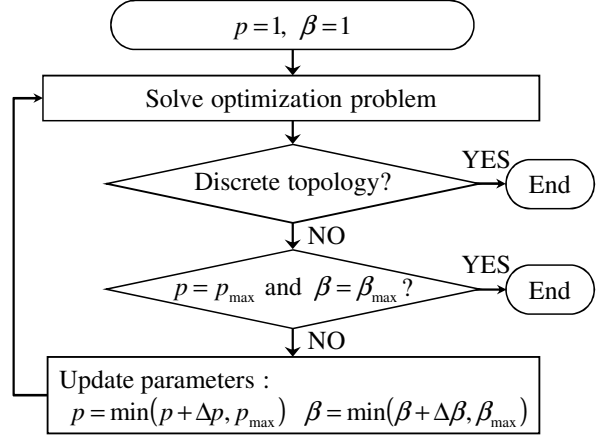


Figure 3.5: Flowchart of the parameter updating scheme.

is detrimental to the convergence of optimization computations. Therefore, the values of the penalization parameter p and the parameter β used in the Heaviside projection function are gradually increased from initially set low values during optimization, as implemented in [24, 26, 27]. Figure 3.5 shows the flowchart of the scheme used to update these parameters. In this research, p and β are gradually increased from initial values of 1, and the parameters used in the updating scheme are set to the following values: $\Delta p = 0.5$, $\Delta \beta = 1.1^k$, $p_{max} = 5.0$, and $\beta_{max} = 50.0$, where k is the iteration number.

3.4 Numerical examples

3.4.1 Minimum mean compliance problems

The design domain and boundary conditions for the first example are shown in Fig.3.6. The design domain has a length of 120, height of 20, and unit width. A force is applied at the center of the top of the domain. The volume constraint is set to 50.0% of the volume of the design domain. The domain is axially symmetric, so only the right half of the design domain is considered in the optimization problem.

Post processing

Figure 3.7 shows the obtained configuration obtained by the proposed MPPM, and significant grayscale areas around the boundaries of the structure are present. The small bars at the top right of the figure indicate the magnitude of the applied minimum length scale. Although the minimum length is defined according to a radius in the

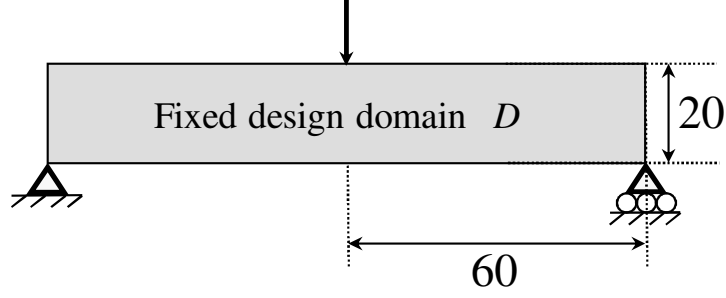


Figure 3.6: Design domain and boundary conditions for minimum mean compliance problem.

formulation, the bars in the figure represents the diameter $d_{min}(= 2r_{min})$. Here, the minimum length scale is set with $d_{min} = 2.0$.

Figure 3.8 shows the design variable distribution of the obtained configuration. As shown in the Fig.3.8, the neighboring domain around the structural boundaries, e.g, a domain A highlighted by circle in the figure, contains design variables that have both positive and negative values, so both solid and void domains are mapped by the projection function in domains near the structural boundaries. Therefore, the obtained configuration contains grayscale areas along the structural boundaries with the width of the applied minimum length. These grayscale areas are now removed, using the following procedure.

First, for elements with normalized density values of $0.25 < \rho^e < 0.75$, the average value of the normalized density $\hat{\rho}^e$ in the neighboring elements is computed as follows.

$$\hat{\rho}^e = \begin{cases} \frac{\sum_{j=N_e} \rho^j}{\sum_{j=N_e} 1} & \text{if } 0.25 < \rho^e < 0.75 \\ \rho^e & \text{if otherwise.} \end{cases} \quad (3.25)$$

The grayscale areas can then be removed by using an appropriate threshold value, ρ_{thres} , for the density value that maintains the volume constraint. This threshold value is obtained using the bi-section method, starting with an initial value of 0.5 and maintaining the value within a range from 0 to 1. The post processed normalized density $\bar{\rho}^e$ is then obtained as follows.

$$\bar{\rho}^e = \begin{cases} 1 & \text{if } \hat{\rho}^e \geq \rho_{thres} \\ 0 & \text{if } \hat{\rho}^e < \rho_{thres}. \end{cases} \quad (3.26)$$

Comparison of the HPM and the MPPM

Figures 3.9(a), (b), (c), and (d) respectively show the obtained configurations obtained using solid phase projection in the HPM [24], void phase projection in the HPM [12], a previous MPPM [27], and the proposed MPPM. The minimum length



Figure 3.7: Configuration using the proposed MPPM before removing grayscales.



Figure 3.8: Distribution of design variable ϕ using the proposed MPPM.

scale r_{min} is set to 2.0. The threshold value ρ_{thres} used to remove grayscale areas is 0.533. The small bar(s) at the top right in these figures indicate the applied minimum length, with NA indicating that the minimum length constraint was not applied.

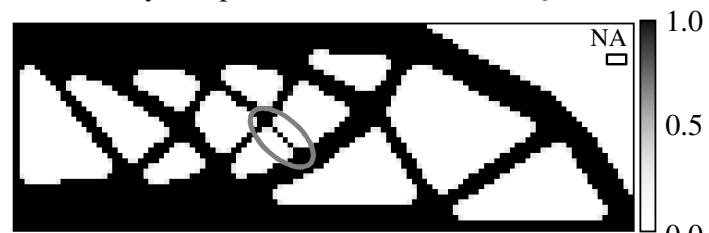
The gray circle and ellipse in the (a) and (b) figures, respectively, highlight the fact that the optimal configuration has very sharp corners and tiny holes when the minimum length scale is applied only to the solid phase (Fig.3.9 (a)), and that the fin-like structural members may become extremely thin when the minimum length scale is applied only to void phase (Fig.3.9 (b)). In contrast, the configuration obtained using either MPPM does not contain such complex structures.

The average computation times are now compared to demonstrate the utility of the proposed method. The computation time in seconds for the sensitivity analysis per iteration is shown at the bottom of each of the four figures in Fig.3.9. These values represent the average time per iteration for the first 100 iterations for each method, using the same computational environment and the same computer (a Intel[®] Core2[™] Quad CPU,Q6700 2.66GHz, 4.0GB RAM, and MATLAB version 7.5). The computation time consumed on tasks other than the sensitivity analysis was almost the same for all methods and is ignored in this comparison. The results show that the computation time was significantly reduced with the proposed MPPM, compared to that of the previous MPPM.

The numbers to the right of “Obj” in these figures indicate the obtained minimum mean compliance value for the optimal configuration. Although the value obtained by the proposed MPPM is about 3% higher than that obtained by the previous MPPM, an appropriate configuration was obtained by the proposed MPPM using roughly half the computation time.



(a) Solid phase projection in HPM
Sensitivity computation time: 19.37 Obj: 75.55



(b) Void phase projection in HPM
Sensitivity computation time: 19.36 Obj: 74.25



(c) Conventional MPPM
Sensitivity computation time: 37.64 Obj: 75.53



(d) Proposed MPPM
Sensitivity computation time: 19.25 Obj: 77.93

Figure 3.9: Optimal configurations obtained under various conditions.

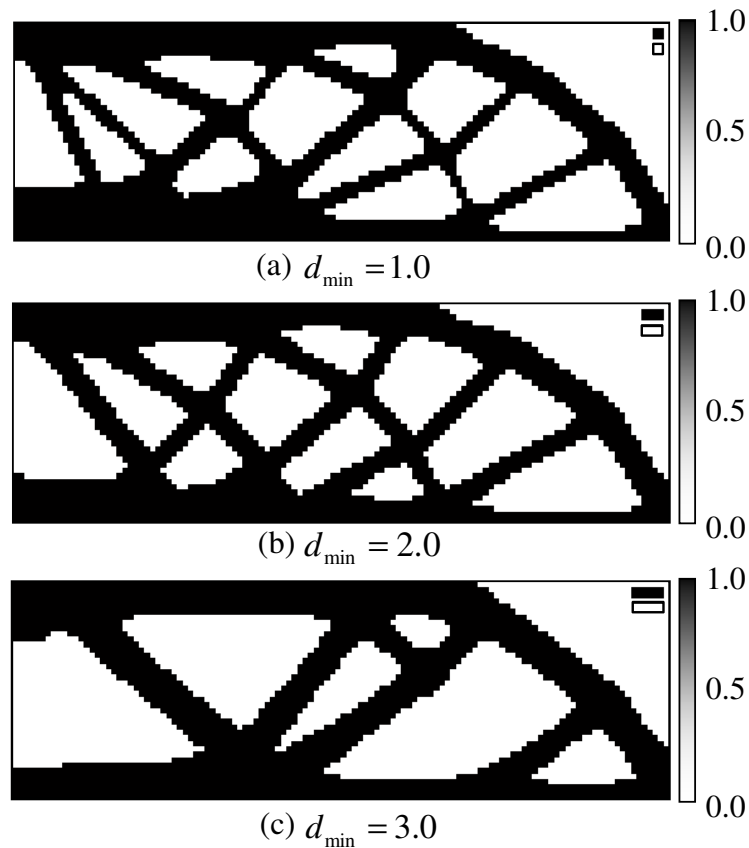


Figure 3.10: Optimal configurations via the proposed MPPM with various d_{\min} values.

Comparison of results when using different minimum lengths

Figure 3.10 shows configurations obtained with the proposed MPPM when different magnitudes of the minimum length, r_{\min} , are used. The results show that adjusting the minimum length scale successfully controls the complexity of the obtained configurations. When a small minimum length scale value is applied, a relatively complex configuration is obtained (Fig. 3.10(a)), and when a larger value is applied, a simpler configuration is obtained (Fig.3.10(c)).

To further investigate the utility of the proposed MPPM, a minimum mean compliance problem is considered with a different numerical model. Figure 3.11 shows the design domain and boundary conditions. A force is applied at the center of the bottom boundary. The displacement at the left bottom corner is fixed and the vertical displacement at the right bottom corner is constrained to zero.

Figure 3.12 shows obtained configurations using the proposed method with various magnitudes of r_{\min} . Again, the results show that the adjusting the value of the minimum length scale successfully controls the complexity of the obtained configurations.

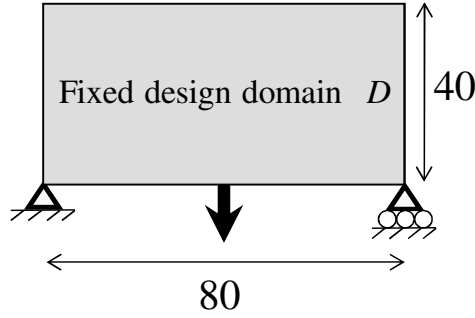


Figure 3.11: Design domain and boundary conditions for second minimum mean compliance problem.

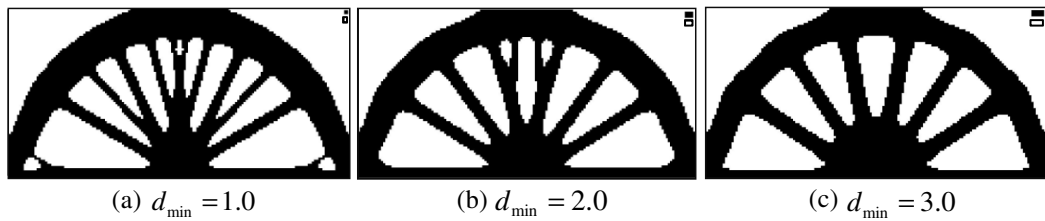


Figure 3.12: Optimal configurations for second minimum mean compliance problem via the proposed MPPM with various magnitudes of d_{\min} .

3.4.2 Compliant mechanism design problem

Here, a compliant mechanism design problem is considered. Figure 3.13 shows the design domain and boundary conditions. A force is applied at the center of the left boundary and the optimization objective is to maximize the displacement at the center of the right boundary in the direction opposite that of the applied force. The displacement at the upper and lower corners of the left boundary is fixed. A detailed formulation of this optimization problem is provided in the next chapter.

Figure 3.14 shows two configurations obtained via the proposed method when using two different magnitudes of r_{\min} . Again, the results show that adjusting the minimum length scale successfully controls the complexity of the obtained configurations.

3.5 Conclusions

This chapter discussed a new methodology that reduces the number of design variables needed in a multiple phase projection method (MPPM). This new MPPM formulation requires only a single design variable at each node, rather than the usual two, which advantageously reduces computation time. The proposed method was applied to two minimum mean compliance problems and a compliant mechanism design problem. Although the optimal configurations contained some grayscale areas, these can be

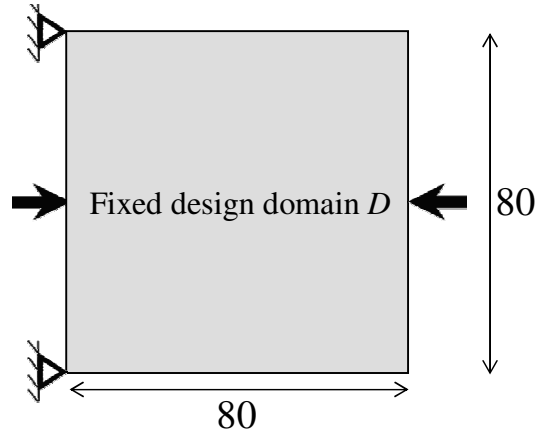


Figure 3.13: Design domain and boundary conditions for compliant mechanism design problem.

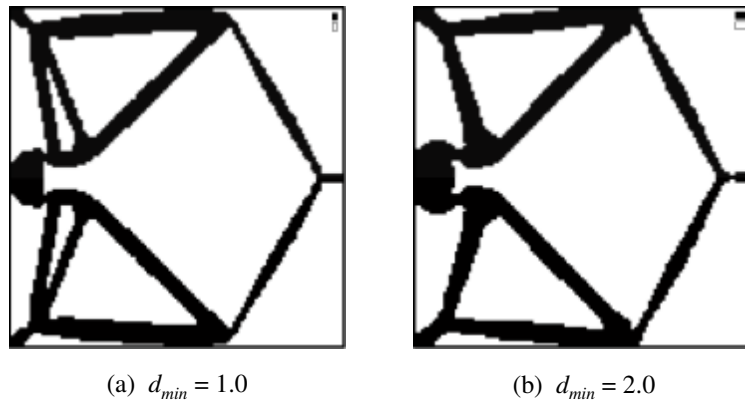


Figure 3.14: Optimal configurations for compliant mechanism design problem via the proposed MPPM with various magnitudes of d_{min} .

removed by using a threshold value obtained by the bi-section method, which allows appropriate configurations to be effectively obtained. Furthermore, the proposed method can successfully control the complexity of optimized configurations by varying the value of the minimum length scale applied in the optimization.

Chapter 4

Level set-based method using mathematical programming

4.1 Introduction

This chapter discusses a structural optimization method that is based on the level set method and uses mathematical programming, the method of moving asymptotes (MMA) [110]. The developed level set-based topology optimization method is applied to minimum mean compliance problems and two compliant mechanism design problems.

Several design requirements must be satisfied when developing practical designs for mechanical and electromagnetic devices. These requirements include the maximum volume of the material used, the prevention of mechanical interference, the maximum allowable stress, and so on, and are especially important for the design of devices that include a movable function, such as compliant mechanisms. A compliant mechanism is a monolithic joint-free mechanism designed to be flexible to obtain a specified motion. To successfully obtain a specified mechanical function, a compliant mechanism design must meet several requirements, such as deforming in a designed direction, and must also incorporate a consideration of stress concentrations.

Compliant mechanisms are gaining increasing attention as their application in myriad mechanical devices such as MEMS broadens. The major advantages of compliant mechanisms are their simplified manufacturing and assembly requirements, reduced cost, lack of mechanical play, silent operation, and freedom from lubrication requirements [116]. The first approach to compliant mechanism design was a kinematic synthesis approach in which rigid-body mechanisms were synthesized into compliant mechanisms (e.g., [117]). This approach, however, was limited to lumped compliant mechanism designs. For the design of fully compliant mechanisms, topology optimization methods using the continuum synthesis approach have been used. In such methods, Sigmund [20] formulated the objective function as the ratio between input and output forces, called the mechanical advantage. Nishiwaki et al. [39] presented a structural topology optimization method for compliant mechanisms in which the concept of mutual energy was used in the formulation of flexibility.

The aim of the research described in this chapter is to extend the previously proposed level set-based topology optimization method [90] so that the design requirements, such as the constraints on displacement and stress, can easily be considered. In this presented method, the level set function is updated using the MMA [110], to facilitate the treatment of constraint functionals. In Section 4.2, the formulation of the level set-based topology optimization procedure and the optimization problems are discussed. The numerical implementation is discussed in Section 4.3, and numerical examples are provided in Section 4.4. These examples include the design problem with a mean compliance constraint so that sufficient stiffness is obtained even when a load is applied in a direction slightly different from its prescribed direction, the problem with a mutual mean compliance constraint so that the structure deforms in a designed direction, and the problem with a stress constraint.

4.2 Formulation

4.2.1 Level set function updating scheme

As shown in Section 2.4.2, in level set-based topology optimization, the optimization problem is expressed as follows [90]:

$$\inf_{\phi} F_R(\chi_{\phi}, \phi) = F + R \quad (4.1)$$

$$\text{subject to } G(\chi_{\phi}) \leq 0. \quad (4.2)$$

The presented method updates the level set function ϕ using mathematical programming, the method of moving asymptotes (MMA) based on the sensitivities of the objective and constraint functionals.

4.2.2 Minimum mean compliance problem

Consider the design domain D where the displacement is fixed at boundary Γ_u , a force \mathbf{t} is imposed at boundary Γ_t , and a body force \mathbf{b} is applied on material domain Ω . The minimum mean compliance problem under the volume constraint is then formulated as

$$\inf_{\phi} F = l_1(\mathbf{u}) \quad (4.3)$$

$$\text{subject to } a(\mathbf{u}, \mathbf{v}) = l_1(\mathbf{v}) \text{ for } \forall \mathbf{v} \in U, \mathbf{u} \in U \quad (4.4)$$

$$G_1(\chi_{\phi}) = \int_D \chi_{\phi} d\Omega - V_{\max} \leq 0, \quad (4.5)$$

where,

$$a(\mathbf{u}, \mathbf{v}) = \int_D \boldsymbol{\epsilon}(\mathbf{u}) : \mathbf{E} : \boldsymbol{\epsilon}(\mathbf{v}) \chi_{\phi} d\Omega \quad (4.6)$$

$$l_1(\mathbf{v}) = \int_{\Gamma_1} \mathbf{t} \cdot \mathbf{v} d\Gamma + \int_D \mathbf{b} \cdot \mathbf{v} \chi_{\phi} d\Omega, \quad (4.7)$$

where u , ϵ , and \mathbf{E} are respectively the displacement, strain, and Young's modulus. V_{\max} is the upper limit of the volume constraint. U is the functional space defined with

$$U = \{\mathbf{v} = v_i \mathbf{e}_i : v_i \in H^1(D) \text{ with } \mathbf{v} = 0 \text{ on } \Gamma_u\}. \quad (4.8)$$

The sensitivities are obtained using the adjoint variable method (AVM). The Lagrangian of the optimization problem is given by the following.

$$\bar{F} = F - (a(\mathbf{u}, \mathbf{v}) - l_1(\mathbf{v})). \quad (4.9)$$

The sensitivity of F is obtained as follows.

$$\begin{aligned} \left\langle \frac{d\bar{F}}{d\chi_\phi}, \delta\chi_\phi \right\rangle &= \left\langle \frac{\partial l_1(\mathbf{u})}{\partial \mathbf{u}}, \delta \mathbf{u} \right\rangle \left\langle \frac{\partial \mathbf{u}}{\partial \chi_\phi}, \delta\chi_\phi \right\rangle - \left\langle \frac{\partial a(\mathbf{u}, \mathbf{v})}{\partial \mathbf{u}}, \delta \mathbf{u} \right\rangle \left\langle \frac{\partial \mathbf{u}}{\partial \chi_\phi}, \delta\chi_\phi \right\rangle \\ &\quad - \left\langle \frac{\partial a(\mathbf{u}, \mathbf{v})}{\partial \chi_\phi}, \delta\chi_\phi \right\rangle, \end{aligned} \quad (4.10)$$

$$= \left(\left\langle \frac{\partial l_1(\mathbf{u})}{\partial \mathbf{u}}, \delta \mathbf{u} \right\rangle - \left\langle \frac{\partial a(\mathbf{u}, \mathbf{v})}{\partial \mathbf{u}}, \delta \mathbf{u} \right\rangle \right) \left\langle \frac{\partial \mathbf{u}}{\partial \chi_\phi}, \delta\chi_\phi \right\rangle - \left\langle \frac{\partial a(\mathbf{u}, \mathbf{v})}{\partial \chi_\phi}, \delta\chi_\phi \right\rangle, \quad (4.11)$$

where $\left\langle \frac{\partial l_1(\mathbf{v})}{\partial \chi_\phi}, \delta\chi_\phi \right\rangle = 0$, and the adjoint field is defined so that the $\left\langle \frac{\partial \mathbf{u}}{\partial \chi_\phi}, \delta\chi_\phi \right\rangle$ term is canceled out. The following adjoint field is then obtained.

$$a(\mathbf{v}, \delta \mathbf{u}) = l_1(\delta \mathbf{u}) \quad \text{for } \forall \delta \mathbf{u} \in U, \mathbf{v} \in U. \quad (4.12)$$

Note that the a is bilinear, the minimum mean compliance problem is self-adjoint problem. The sensitivities are finally obtained using the following equation.

$$\left\langle \frac{d\bar{F}}{d\chi_\phi}, \delta\chi_\phi \right\rangle = - \left\langle \frac{\partial a(\mathbf{u}, \mathbf{v})}{\partial \chi_\phi}, \delta\chi_\phi \right\rangle.$$

4.2.3 Minimum mean compliance problem with a mean compliance constraint

Here, a mean compliance constraint is considered, so that sufficient stiffness is obtained even when a load is applied in a direction slightly different from its prescribed direction. Let l^+ and l^- be respective mean compliances when load \mathbf{t}_p^+ or load \mathbf{t}_p^- is applied orthogonally to the prescribed load \mathbf{t} , respectively, for two-dimensional design problem. The optimization problem with a mean compliance constraint is then defined as follows:

$$\inf_{\phi} \quad F = l_1(\mathbf{u}_1) \quad (4.13)$$

$$\text{subject to} \quad a(\mathbf{u}_1, \mathbf{v}) = l_1(\mathbf{v}) \quad \text{for } \forall \mathbf{v} \in U, \mathbf{u}_1 \in U \quad (4.14)$$

$$a(\mathbf{u}_2, \mathbf{v}) = l^+(\mathbf{v}) \quad \text{for } \forall \mathbf{v} \in U, \mathbf{u}_2 \in U \quad (4.15)$$

$$a(\mathbf{u}_3, \mathbf{v}) = l^-(\mathbf{v}) \quad \text{for } \forall \mathbf{v} \in U, \mathbf{u}_3 \in U \quad (4.16)$$

$$G_1 \leq 0 \quad (4.17)$$

$$G_2 = l^+(\mathbf{u}_2) - \alpha l_1(\mathbf{u}_1) \leq 0 \quad (4.18)$$

$$G_3 = l^-(\mathbf{u}_3) - \alpha l_1(\mathbf{u}_1) \leq 0, \quad (4.19)$$

where

$$l^+(\mathbf{v}) = \int_{\Gamma_1} \mathbf{t}_p^+ \cdot \mathbf{v} d\Gamma \quad (4.20)$$

$$l^-(\mathbf{v}) = \int_{\Gamma_1} \mathbf{t}_p^- \cdot \mathbf{v} d\Gamma. \quad (4.21)$$

where \mathbf{u}_2 and \mathbf{u}_3 are the displacement when \mathbf{t}_p^+ or \mathbf{t}_p^- is applied at boundary Γ_1 , respectively. α represents the ratio between mean compliance l and l^+ , and between l and l^- . As the magnitude of α is reduced, the orthogonal mean compliance constraint is increased so that the obtained configuration will have sufficient stiffness even when a load is applied in a direction slightly different from the prescribed direction.

4.2.4 Compliant mechanism design problem with a mutual mean compliance constraint

The optimum design problem of a compliant mechanism is briefly discussed now. The main goal of the present optimum design process is to maximize the output displacement in a desired direction. Consider a design domain D where the displacement is fixed at boundary Γ_u , an input force \mathbf{t}_{in} is applied at boundary Γ_{in} , and a dummy vector \mathbf{t}_{out} is introduced at the output port, boundary Γ_{out} , along the desired output direction.

The design of a compliant mechanism has three requirements. The first is to provide sufficient flexibility for deformation along a desired direction specified by a dummy vector \mathbf{t}_{out} when an input force is applied. The mutual mean compliance between Γ_{in} and Γ_{out} is used here to formulate the flexibility of the target structure. By maximizing the mutual mean compliance, the output displacement is maximized along the direction of the dummy vector \mathbf{t}_{out} . The second requirement is for sufficient stiffness to maintain the integrity of mechanism's structural shape when an input force is applied. Here, a dummy spring is imposed at the input port to represent the input force. And the third requirement is for sufficient stiffness to maintain the integrity of mechanism's structural shape when a workpiece reaction force is applied. Here, a dummy spring is imposed at the output port to represent this reaction force. The formulation of the optimum design problem for a compliant mechanism is now extended to a problem that includes a mutual mean compliance constraint, so that the displacement in the direction orthogonal to the desired output direction will be constrained.

$$\inf_{\phi} F = -l_2(\mathbf{u}_1) \quad (4.22)$$

$$\text{subject to} \quad a(\mathbf{u}_1, \mathbf{v}) + s_2(\mathbf{u}_1, \mathbf{v}) = l_1(\mathbf{v}) \quad \text{for } \forall \mathbf{v} \in U, \mathbf{u}_1 \in U \quad (4.23)$$

$$a(\mathbf{u}_2, \mathbf{v}) = l_1(\mathbf{v}) \quad \text{for } \forall \mathbf{v} \in U, \mathbf{u}_2 \in U \quad (4.24)$$

$$G_1 \leq 0 \quad (4.25)$$

$$G_2 = [l_3(\mathbf{u}_2)]^2 - \epsilon_0^2 \leq 0, \quad (4.26)$$

where

$$s_2(\mathbf{u}, \mathbf{v}) = \int_{\Gamma_{\text{out}}} (\mathbf{k}_{\text{out}} \mathbf{u}) \cdot \mathbf{v} d\Gamma \quad (4.27)$$

$$l_2(\mathbf{v}) = \int_{\Gamma_{\text{out}}} \mathbf{t}_{\text{out}} \cdot \mathbf{v} d\Gamma \quad (4.28)$$

$$l_3(\mathbf{v}) = \int_{\Gamma'_{\text{out}}} \mathbf{t}'_{\text{out}} \cdot \mathbf{v} d\Gamma. \quad (4.29)$$

where l_2 is the mutual mean compliance corresponding to dummy vector \mathbf{t}_{out} , \mathbf{u}_1 is the displacement when load \mathbf{t}_{in} is applied at boundary Γ_{in} , and a spring with spring constant \mathbf{k}_{out} is attached at boundary Γ_{out} to satisfy the third requirement mentioned above. \mathbf{u}_2 is the displacement when \mathbf{t}_{in} is applied at boundary Γ_{in} and spring is not attached at boundary Γ_{out} . l_3 represents the flexibility in the direction of \mathbf{t}'_{out} and G_2 is the constraint functional imposed on the displacement in the \mathbf{t}'_{out} direction along which the displacement is to be suppressed. The parameter ϵ_0 is a constant given a sufficiently small value, introduced to improve the convergence of the optimization computation.

The sensitivity of the objective functional is obtained as follows, using the adjoint variable method.

$$\begin{aligned} \left\langle \frac{dF}{d\chi_\phi}, \delta\chi_\phi \right\rangle &= - \left\langle \frac{\partial l_2(\mathbf{u}_1)}{\partial \mathbf{u}_1}, \delta \mathbf{u}_1 \right\rangle \left\langle \frac{\partial \mathbf{u}_1}{\partial \chi_\phi}, \delta\chi_\phi \right\rangle + \left\langle \frac{\partial a(\mathbf{u}_1, \mathbf{v})}{\partial \mathbf{u}_1}, \delta \mathbf{u}_1 \right\rangle \left\langle \frac{\partial \mathbf{u}_1}{\partial \chi_\phi}, \delta\chi_\phi \right\rangle \\ &\quad + \left\langle \frac{\partial a(\mathbf{u}_1, \mathbf{v})}{\partial \chi_\phi}, \delta\chi_\phi \right\rangle + \left\langle \frac{\partial s_2}{\partial \mathbf{u}_1}, \delta \mathbf{u}_1 \right\rangle \left\langle \frac{\partial \mathbf{u}_1}{\partial \chi_\phi}, \delta\chi_\phi \right\rangle \quad (4.30) \\ &= \left(- \left\langle \frac{\partial l_2(\mathbf{u}_1)}{\partial \mathbf{u}_1}, \delta \mathbf{u}_1 \right\rangle + \left\langle \frac{\partial a(\mathbf{u}_1, \mathbf{v})}{\partial \mathbf{u}_1}, \delta \mathbf{u}_1 \right\rangle + \left\langle \frac{\partial s_1}{\partial \mathbf{u}_1}, \delta \mathbf{u}_1 \right\rangle \right) \left\langle \frac{\partial \mathbf{u}_1}{\partial \chi_\phi}, \delta\chi_\phi \right\rangle \\ &\quad + \left\langle \frac{\partial a(\mathbf{u}_1, \mathbf{v})}{\partial \chi_\phi}, \delta\chi_\phi \right\rangle + \left\langle \frac{\partial s_2}{\partial \mathbf{u}_1}, \delta \mathbf{u}_1 \right\rangle \left\langle \frac{\partial \mathbf{u}_1}{\partial \chi_\phi}, \delta\chi_\phi \right\rangle - \left\langle \frac{\partial s_1}{\partial \mathbf{u}_1}, \delta \mathbf{u}_1 \right\rangle \left\langle \frac{\partial \mathbf{u}_1}{\partial \chi_\phi}, \delta\chi_\phi \right\rangle, \quad (4.31) \end{aligned}$$

where the adjoint field is defined as

$$a(\mathbf{v}, \delta \mathbf{u}_1) + s_1(\mathbf{v}, \delta \mathbf{u}_1) = l_2(\delta \mathbf{u}_1) \quad \text{for } \forall \delta \mathbf{u}_1 \in U, \mathbf{v} \in U, \quad (4.32)$$

and s_1 is defined as follows, using a spring with spring constant \mathbf{k}_{in} that is attached at boundary Γ_1 to satisfy the second requirement mentioned above:

$$s_1(\mathbf{u}, \mathbf{v}) = \int_{\Gamma_1} (\mathbf{k}_{\text{in}} \mathbf{u}) \cdot \mathbf{v} d\Gamma. \quad (4.33)$$

The sensitivities are finally obtained using the following equation.

$$\begin{aligned} \left\langle \frac{dF}{d\chi_\phi}, \delta\chi_\phi \right\rangle &= \left\langle \frac{\partial a(\mathbf{u}_1, \mathbf{v})}{\partial \chi_\phi}, \delta\chi_\phi \right\rangle \\ &\quad + \left\langle \frac{\partial s_2}{\partial \mathbf{u}_1}, \delta \mathbf{u}_1 \right\rangle \left\langle \frac{\partial \mathbf{u}_1}{\partial \chi_\phi}, \delta\chi_\phi \right\rangle - \left\langle \frac{\partial s_1}{\partial \mathbf{u}_1}, \delta \mathbf{u}_1 \right\rangle \left\langle \frac{\partial \mathbf{u}_1}{\partial \chi_\phi}, \delta\chi_\phi \right\rangle. \quad (4.34) \end{aligned}$$

The sensitivity of constraint functional G_2 is simply obtained as follows, using the AVM.

$$\left\langle \frac{dG_2}{d\chi_\phi}, \delta\chi_\phi \right\rangle = 2l_3(\mathbf{u}_2) \left\langle \frac{\partial a(\mathbf{u}_2, \mathbf{v})}{\partial \chi_\phi}, \delta\chi_\phi \right\rangle, \quad (4.35)$$

where the adjoint field is defined as follows:

$$a(\mathbf{v}, \delta\mathbf{u}_2) = l_3(\delta\mathbf{u}_2) \quad \text{for } \forall \delta\mathbf{u}_2 \in U, \mathbf{v} \in U. \quad (4.36)$$

4.2.5 Minimum mean compliance problem with a stress constraint

Several different stress constraint formulations have been studied, which can be broadly categorized into three types: local stress constraints [118], global stress constraints [119, 120], and a hybrid approach that combines local and global stress constraints [121]. These formulations are compared in the literature [120, 122, 123]. The implementation of local stress constraints is based on a straightforward approach, with stress constraints imposed at predefined points such as the center of finite elements, but this often increases computational demands to the point of intractability. On the other hand, global stress constraints impose a single global constraint that aggregates the effect of all local stress constraints. Although local stress constraints may not be strictly satisfied, the use of a global stress constraint greatly reduces computational demands. Martins and Poon [119], and París et al. [120–122] proposed a global stress constraint that aggregates the local stress constraints using an Kreisselmeier-Steinhauser function [25] to penalize any stress values that exceed that of a local stress constraint. Furthermore, Martins and Poon [119] improved the accuracy of the global stress constraint by adaptively adjusting a parameter that controls the magnitude of the penalization applied to stress values that violate the local stress constraint. Guo et al. [124] imposed a stress constraint only on the node where the stress is maximal, and Xia et al. [125] imposed stress constraints only on nodes where the stress exceeds a local stress constraint value. These methods [124, 125], therefore, encounter convergence problems during the optimization computation. On the other hand, París et al. [122] proposed a hybrid approach where the fixed design domain is divided into several blocks, and a global stress constraint is imposed on each divided block so that the number of stress constraints is the same as the number of blocks.

In this study, a global stress constraint [120] is used to reduce computation time, and for its ease of implementation. The minimum mean compliance problem with a stress constraint is formulated as follows.

$$\inf_{\phi} F = l_1(\mathbf{u}) \quad (4.37)$$

$$\text{subject to } a(\mathbf{u}, \mathbf{v}) = l_1(\mathbf{v}) \quad \text{for } \forall \mathbf{v} \in U, \mathbf{u} \in U \quad (4.38)$$

$$G_1 \leq 0 \quad (4.39)$$

$$G_{\text{global}}(\sigma_{\text{vm}}, \phi) \leq 0, \quad (4.40)$$

where

$$G_{\text{global}}(\sigma_{\text{vm}}, \phi) = \frac{1}{\mu} \ln \left[\int_{\Omega} e^{\mu(\sigma^* - 1)} d\Omega \right] - \frac{1}{\mu} \ln \left(\int_{\Omega} d\Omega \right). \quad (4.41)$$

μ in Eq.(4.41) is a parameter called the ‘‘aggregation parameter.’’ Increasing the magnitude of μ increases the penalty for violated local constraints. σ^* in Eq.(4.41) is defined as

$$\sigma^* = \frac{\sigma_{\text{vm}}}{\sigma_{\text{max}} \psi_e}, \quad (4.42)$$

where σ_{vm} represents the von Mises stress and σ_{max} is the applied stress constraint. ψ_e is a parameter called the ‘‘stress relaxation coefficient,’’ introduced to avoid singularity phenomena and formulated as

$$\psi_e = 1 - \hat{\epsilon} + \frac{\hat{\epsilon}}{H(\phi)}, \quad (4.43)$$

where $\hat{\epsilon}$ is a parameter called the ‘‘relaxation factor,’’ which adjusts the magnitude of the relaxation and $H(\phi)$ is a Heaviside function. Note that although two types of relaxation approach are commonly applied, ϵ -relaxation and the qp -approach, Bruggi and Venini [126] showed that the qp -approach is a type of adaptive ϵ -relaxation. ϵ -relaxation was applied in this study.

The sensitivity of the global stress constraint is formulated as follows:

$$\begin{aligned} \left\langle \frac{dG_{\text{global}}}{d\chi_{\phi}}, \delta\chi_{\phi} \right\rangle &= \left\langle \frac{\partial G_{\text{global}}}{\partial \sigma_{\text{vm}}}, \delta\sigma_{\text{vm}} \right\rangle \left\langle \frac{\partial \sigma_{\text{vm}}}{\partial \mathbf{u}}, \delta\mathbf{u} \right\rangle \left\langle \frac{\partial \mathbf{u}}{\partial \chi_{\phi}}, \delta\chi_{\phi} \right\rangle + \left\langle \frac{\partial G_{\text{global}}}{\partial \chi_{\phi}}, \delta\chi_{\phi} \right\rangle \\ &\quad - \left\langle \frac{\partial a(\mathbf{u}, \mathbf{v})}{\partial \mathbf{u}}, \delta\mathbf{u} \right\rangle \left\langle \frac{\partial \mathbf{u}}{\partial \chi_{\phi}}, \delta\chi_{\phi} \right\rangle - \left\langle \frac{\partial a(\mathbf{u}, \mathbf{v})}{\partial \chi_{\phi}}, \delta\chi_{\phi} \right\rangle \end{aligned} \quad (4.44)$$

$$= \left\langle \frac{\partial G_{\text{global}}}{\partial \chi_{\phi}}, \delta\chi_{\phi} \right\rangle - \left\langle \frac{\partial a(\mathbf{u}, \mathbf{v})}{\partial \chi_{\phi}}, \delta\chi_{\phi} \right\rangle, \quad (4.45)$$

where the adjoint field is defined as

$$\left\langle \frac{\partial G_{\text{global}}}{\partial \sigma_{\text{vm}}}, \delta\sigma_{\text{vm}} \right\rangle \left\langle \frac{\partial \sigma_{\text{vm}}}{\partial \mathbf{u}}, \delta\mathbf{u} \right\rangle - \left\langle \frac{\partial a(\mathbf{u}, \mathbf{v})}{\partial \mathbf{u}}, \delta\mathbf{u} \right\rangle = 0. \quad (4.46)$$

The sensitivities are then obtained using the following equation.

$$\left\langle \frac{dG_{\text{global}}}{d\chi_{\phi}}, \delta\chi_{\phi} \right\rangle = \left\langle \frac{\partial G_{\text{global}}}{\partial \chi_{\phi}}, \delta\chi_{\phi} \right\rangle - \left\langle \frac{\partial a(\mathbf{u}, \mathbf{v})}{\partial \chi_{\phi}}, \delta\chi_{\phi} \right\rangle,$$

4.2.6 Compliant mechanism design problem with a stress constraint

The formulation of the optimum design problem for a compliant mechanism is now extended to a problem that includes a stress constraint. Since the utility of compliant mechanisms depends on their structural flexibility, stress concentrations easily occur

at thin locations that are subject to repeated flexing. Therefore, the implementation of a stress constraint in the optimization method can facilitate the design of reliable compliant mechanisms that are robust against structural failures during their lifetime.

The optimization problem that includes a stress constraint is formulated as follows:

$$\inf_{\phi} F = -l_2(\mathbf{u}) \quad (4.47)$$

$$\text{subject to } a(\mathbf{u}, \mathbf{v}) + s_2(\mathbf{u}, \mathbf{v}) = l_1(\mathbf{v}) \quad \text{for } \forall \mathbf{v} \in U, \mathbf{u} \in U \quad (4.48)$$

$$G_1 \leq 0 \quad (4.49)$$

$$G_{\text{global}}(\sigma_{\text{vm}}, \phi) \leq 0, \quad (4.50)$$

4.3 Numerical implementation

4.3.1 Optimization algorithm

The optimization flowchart is shown in Fig.4.1. First, the level set function is initialized. Second, the equilibrium equation is solved using the Finite Element Method (FEM) and the objective functional and constraint functionals are then calculated, also using the FEM. If the objective functional is converged, the optimization procedure is terminated. If not, the sensitivities of the objective and constraint functionals, derived as a continuous expression in the previous section, are computed. The level set function is then updated using the MMA, and the process returns to the second step.

Note that in the method cited earlier [90], the level set function is updated using a reaction-diffusion equation that is derived based on the Lagrange multiplier method. The derivation of the Lagrange multiplier used in reaction-diffusion equations becomes complicated in multi-constraint problems, so the proposed method uses the MMA to update the level set function, since this facilitates the treatment of constraints. The objective and constraint functionals are approximated using a convex function, and the approximated subproblem is solved at each iteration.

4.3.2 Computation of sensitivities

In a level set-based structural optimization method, if the level set function is updated using non-smoothed sensitivities during the optimization, the updated level set function usually becomes non-smooth and the obtained structural boundaries also become non-smooth. In the method presented here, $\nabla^2\phi$ is used in the sensitivities of regularization term, so it must be accurately calculated in order to compute the sensitivity. A time evolutionary equation is introduced to compute this term, as shown below. Note that the variation of the regularization term is formulated as in [127]. Here, a Dirichlet boundary condition is applied on the non-design boundaries and a Neumann boundary condition is applied on the other boundaries so that the level set function is kept free from influences originating outside of the fixed design

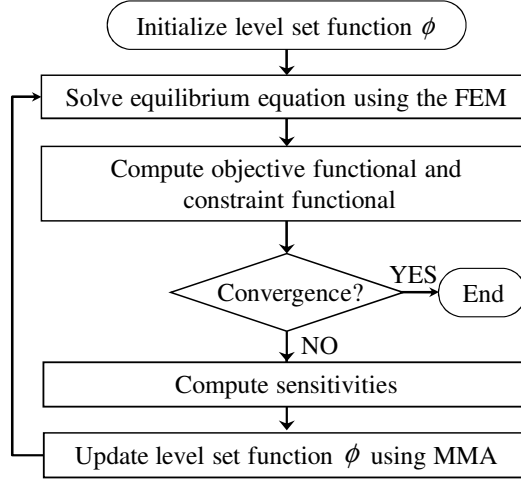


Figure 4.1: Optimization flowchart.

domain [90].

$$\begin{cases} \frac{\partial \phi}{\partial t} = - \left(C \frac{dF}{d\phi} - \tau \nabla^2 \phi \right) \\ \frac{\partial \phi}{\partial n} = 0 \quad \text{on } \partial D \setminus \partial D_{\text{ND}} \\ \phi = 1 \quad \text{on } \partial D_{\text{ND}}, \end{cases} \quad (4.51)$$

where C represents a normalization parameter, defined so that $C = c \int_D d\Omega / \int_D |\frac{dF}{d\phi}| d\Omega$. ∂D_{ND} is non-design boundaries where the Dirichlet boundary condition is applied.

Next, the above equation is discretized in the time domain using the finite difference method, which leads to the following equation.

$$\begin{cases} \frac{\phi(t + \Delta t) - \phi(t)}{\Delta t} = - \left(C \frac{dF}{d\phi} - \tau \nabla^2 \phi(t + \Delta t) \right) \\ \frac{\partial \phi}{\partial n} = 0 \quad \text{on } \partial D \setminus \partial D_{\text{ND}} \\ \phi = 1 \quad \text{on } \partial D_{\text{ND}}, \end{cases} \quad (4.52)$$

where Δt is the time increment. The above equation is then expressed in weak form as follows.

$$\begin{cases} \int_D \frac{\phi(t + \Delta t) - \phi(t)}{\Delta t} \tilde{\phi} dD + \int_D \nabla^T \phi(t + \Delta t) (\tau \nabla \tilde{\phi}) dD = \int_D \left(-C \frac{dF}{d\phi} + \frac{\phi(t)}{\Delta t} \right) \tilde{\phi} dD \\ \phi = 1 \quad \text{on } \partial D_{\text{ND}}, \end{cases} \quad \text{for } \forall \tilde{\phi} \in \tilde{\Phi} \quad (4.53)$$

where $\tilde{\Phi}$ is the following functional space,

$$\tilde{\Phi} = \{ \phi \in H^1(D) \quad \text{with } \phi = 1 \quad \text{on } \partial D_{\text{ND}} \}. \quad (4.54)$$

Using the obtained $\phi(t + \Delta t)$ solving the above equation, the sensitivity of the objective functional can be obtained by the following equation.

$$\frac{dF_R}{d\phi} \approx - \frac{\phi(t + \Delta t) - \phi(t)}{\Delta t} \quad (4.55)$$

Note that, using the above computation method, values of sensitivities can be computed using a first-order element, which is advantageous for computational time, while second-order or higher-order elements are usually required.

4.4 Numerical examples

4.4.1 Minimum mean compliance problem

First, a minimum mean compliance problem is considered to demonstrate the validity and utility of the proposed method. Figure 4.2 shows the design domain and boundary conditions. Displacement is fixed at the left boundary and a downward force is applied at the center of the right boundary. The upper limit of the volume fraction V_{\max} is set to 40% of the volume of the fixed design domain. The width w of the Heaviside function is set to 1.0×10^{-3} .

Figure 4.3 shows configurations obtained using different magnitudes of the regularization parameter τ , which was set to 7.0×10^{-4} , 3.0×10^{-4} , and 7.0×10^{-5} for Case 1, Case 2, and Case 3, respectively. The regularization parameter τ is a parameter to adjust the degree of regularization as explained in Eq.(2.10), Subsection 2.4.2. The results show that the complexity of the obtained configuration can be controlled by adjusting the magnitude of τ .

To further confirm the validity of the presented method, we consider a minimum mean compliance minimization problem using a different numerical model. Figure

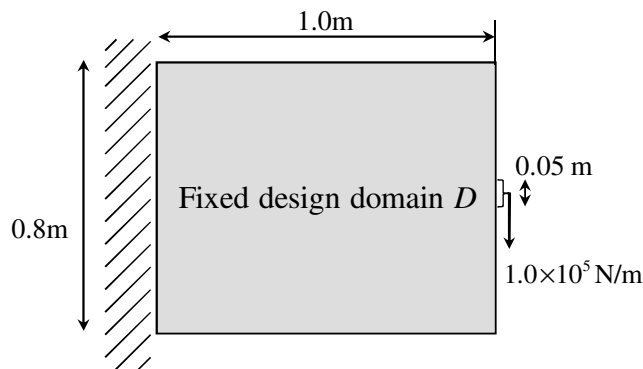


Figure 4.2: Design domain and boundary conditions of for minimum mean compliance problem.

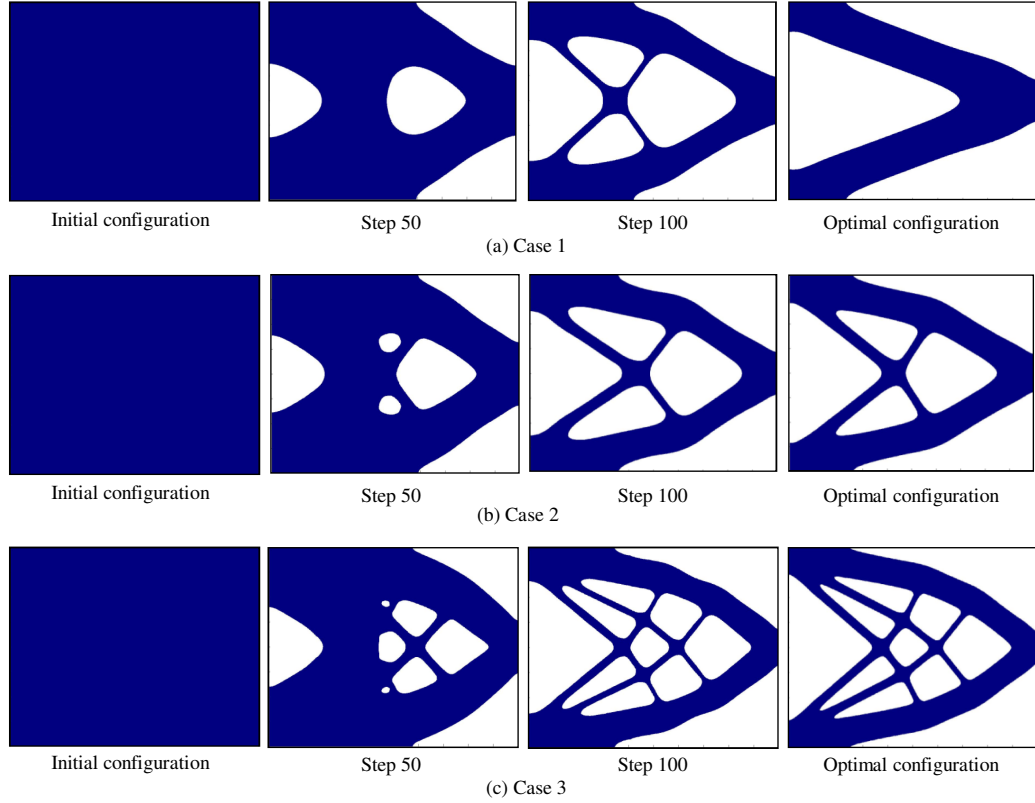


Figure 4.3: Optimal configurations and shape evolution for different τ values: (a) $\tau = 7.0 \times 10^{-4}$; (b) $\tau = 3.0 \times 10^{-4}$; (c) $\tau = 7.0 \times 10^{-5}$.

4.4 shows the design domain and boundary conditions. Displacement is fixed at the left bottom and right bottom corners and a downward force is applied at the center of the bottom boundary. The volume fraction V_{\max} is set to 40% of the volume of the fixed design domain. The width w of the Heaviside function is set to 1.0×10^{-3} .

Figure 4.3 shows the obtained configurations, using three different initial configurations. The initial configuration for Case 1 has the material domain filled with material; for Case 2, the initial configuration has 18 holes in the filled material domain; and for Case 3, the initial configuration has the material domain asymmetrically filled in the lower half of the fixed design domain. In all cases, clear and nearly the same configurations were obtained. Thus, the dependency of the obtained configurations upon the initial configurations is shown to be extremely low in this problem.

Figure 4.4 shows configurations obtained using different magnitudes of the regularization parameter τ , which was set to 1.0×10^{-5} , 7.0×10^{-6} , and 4.0×10^{-6} for Case 1, Case 2, and Case 3, respectively. The results show that the complexity of the configuration obtained using the presented method can be controlled by adjusting the magnitude of τ .

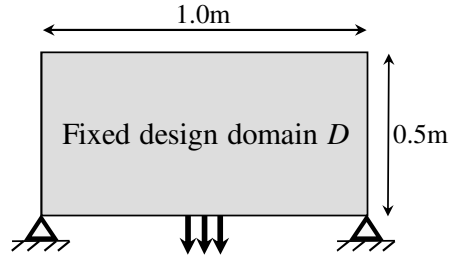


Figure 4.4: Fixed design domain and boundary conditions for second minimum mean compliance problem.

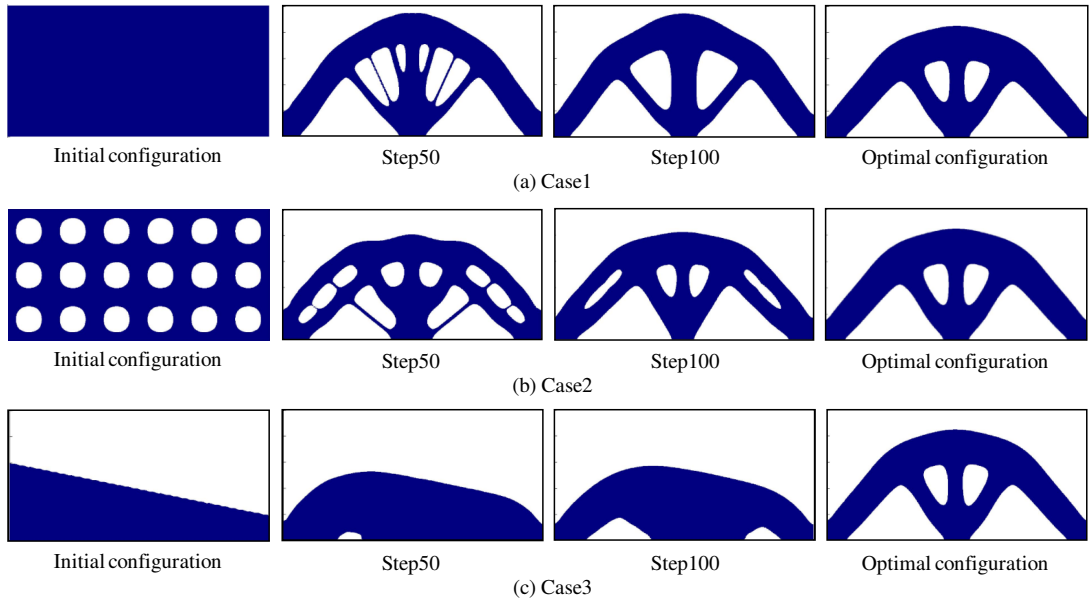


Figure 4.3: Initial configurations, intermediate results, and optimal configurations using three different initial configurations: (a) the configuration filled with material; (b) the configuration with 18 holes; (c) the configuration asymmetrically filled in the lower half of the fixed design domain.

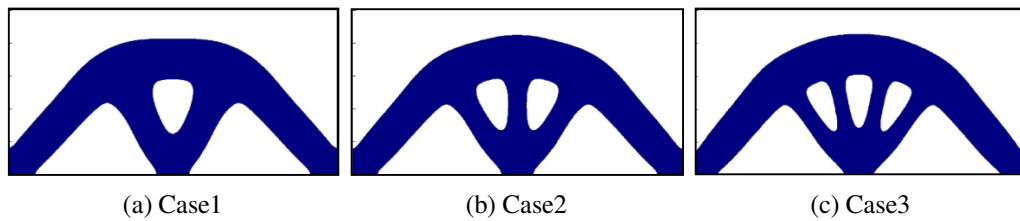


Figure 4.4: Optimal configurations for different magnitudes of τ : (a) $\tau = 1.0 \times 10^{-5}$; (b) $\tau = 7.0 \times 10^{-6}$; (c) $\tau = 4.0 \times 10^{-6}$.

4.4.2 Minimum mean compliance problem with a mean compliance constraint

A minimum mean compliance problem that has a mean compliance constraint imposed is considered now, using the numerical model shown in Fig.4.4. The volume fraction V_{\max} is set to 40% of the volume of the fixed design domain and the width w of the Heaviside function is set to 1.0×10^{-3} . The regularization parameter τ is set to 7.0×10^{-6} . A configuration filled with material is used as initial configuration for all cases.

Figure 4.5 compares configurations obtained using different magnitudes of the parameter α (explained at the end of Section 4.2.3), which was set to 2.0 and 1.0 for Case 2 and Case 3, respectively. A mean compliance constraint was not applied for Case 1. The optimization results show that physically reasonable configurations were obtained in all cases, and the configuration in Case 3 has a horizontal member at the bottom of the design domain, which provides high stiffness along horizontal directions. The mean compliance values for the obtained configurations are compared in Table 4.1. The values in parentheses to the right of each mean compliance value represent the ratio between l and l_1 , and l and l_2 . Even though the mean compliance l achieved with the constraint is larger than that without constraint, the mean compliance values l_1 and l_2 are smaller than those without constraint. That is, the configuration obtained when a mean compliance constraint is imposed has increased stiffness in the horizontal direction.

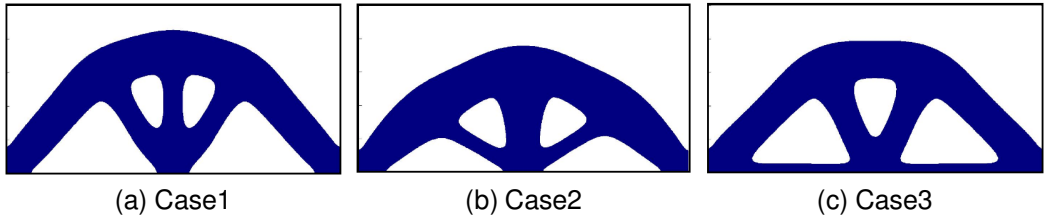


Figure 4.5: Obtained configurations that include a mean compliance constraint under horizontal loads for different magnitude of α : (a) constraint is not applied; (b) $\alpha=2.0$; (c) $\alpha=1.0$.

Table 4.1: Comparison of mean compliance of obtained optimal configurations.

	Case1 ($l_1/l_{+,-}$)	Case2 ($l_1/l_{+,-}$)	Case3 ($l_1/l_{+,-}$)
α	N/A	2.0	1.0
l_1	1.308×10^{-2}	1.399×10^{-2}	1.441×10^{-2}
l_+	9.098×10^{-2} (7.0)	2.798×10^{-2} (2.0)	1.441×10^{-2} (1.0)
l_-	9.098×10^{-2} (7.0)	2.798×10^{-2} (2.0)	1.441×10^{-2} (1.0)

4.4.3 Compliant mechanism design problem with a mutual mean compliance constraint

A compliant mechanism design problem that has a mutual mean compliance constraint imposed is considered next. Figure 4.6 shows the fixed design domain and boundary conditions for this model. A load is applied at the center of the left boundary and segments at the top of the left edge and extreme left of the bottom edge are fixed. A dummy vector \mathbf{t}_{out} is applied at the top right edge of the domain in the horizontal direction. The fixed design domain is discretized using an 80×80 mesh of quadrilateral finite elements. The regularization parameter τ is set to 7.0×10^{-5} . The transition width of the Heaviside function w is set to 0.2, to stabilize the optimization procedure.

Figure 4.7(a) shows the optimal configuration without an applied constraint, and Fig.4.7(c) showing its deformed shape. Figure 4.7(b) shows the optimal configuration with a constraint set so that the structure only deforms in the desired horizontal direction, and Fig.4.7(d) shows its deformed shape. As Fig.4.7(d) shows, the constraint effectively prevents deformation at the output port in a direction orthogonal to that of the applied load. The mutual mean compliance represented by dummy vector \mathbf{t}'_{out} is -2.43×10^{-9} without the constraint and -1.42×10^{-10} with the constraint, indicating that displacement in the vertical direction is significantly reduced. The value of the mutual mean compliance represented by dummy vector \mathbf{t}_{out} , however, is almost the same without and with the constraint, 3.65×10^{-9} and 3.60×10^{-9} , respectively.

Since the transition width of the Heaviside function w is set to 0.2, the optimal configuration contains some grayscale areas, which are removed by setting $w = 1.0 \times$

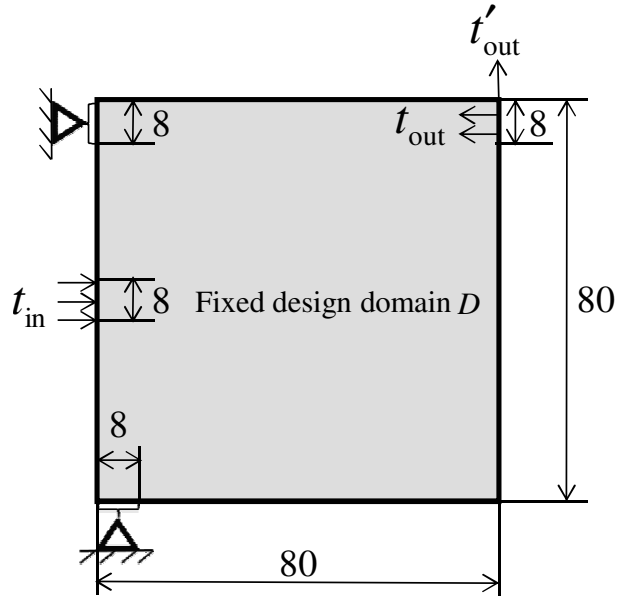


Figure 4.6: Fixed design domain and boundary conditions for compliant mechanism design problem with a mutual mean compliance constraint.

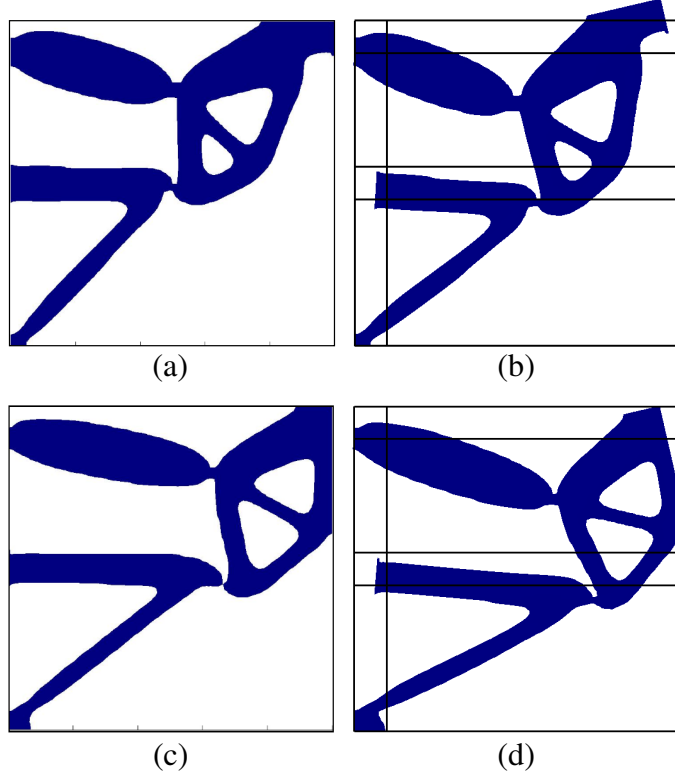


Figure 4.7: Optimal configurations and its deformed shape of a compliant mechanism design problem: (a) without mutual mean compliance constraint; (c) deformed shape of (a); (b) with mutual mean compliance constraint; (d) deformed shape of (b).

10^{-3} . The mutual mean compliance values represented by dummy vectors \mathbf{t}'_{out} and \mathbf{t}_{out} are then -1.42×10^{-10} and 3.60×10^{-9} , respectively, which are essentially the same as the values before the grayscale areas were removed. The numerical results show that the proposed method successfully imposed a displacement constraint for the design of a compliant mechanism, using a mutual mean compliance constraint.

4.4.4 Minimum mean compliance problem with a stress constraint

Figure 4.8 shows the design domain and boundary conditions of a minimum mean compliance problem with a stress constraint. The design domain is discretized using quadratic elements that are 1.25×10^{-2} m in size. Here, the small domain illustrated in black near the location of the imposed force is set as the non-design domain. The stress becomes very high at the location where the force is imposed, but reducing the stress in this domain is not the purpose of the optimization. Displacement is fixed at the left boundary and a downward force is applied at the center of the right boundary. The volume fraction V_{max} is set to 40% of the volume of the fixed design domain. The maximum stress value for the stress constraint is set to 100MPa. The parameters μ

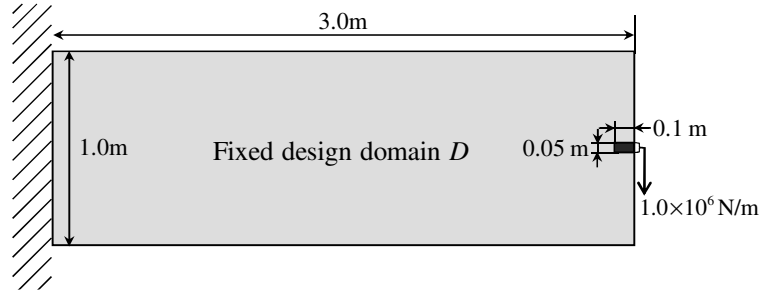


Figure 4.8: Design domain and boundary conditions for minimum mean compliance problem with a stress constraint.

and ϵ used for the stress constraint are respectively set to 20 and 0.1. The width w of the Heaviside function is set to 0.8. Figure 4.9(a) shows the obtained configuration and the corresponding von Mises stress distribution when only the volume fraction is applied. Figure 4.9(b) shows the obtained configuration when the stress constraint is applied in addition to the volume fraction, and the corresponding von Mises stress distribution. The maximum value of the von Mises stress is 203.05MPa without the stress constraint and 137.65MPa with the stress constraint. The magnitude of the local stress did not reach the stress constraint value because a global stress constraint was applied, but the maximum value of the von Mises stress was reduced. The obtained mean compliance values are roughly the same: 115.63J without the stress constraint vs. 118.42J with the stress constraint.

Since the transition width of the Heaviside function w was set to 0.8, the optimal configuration contains grayscale areas to some extent. The grayscale areas in the optimal configuration can be removed by setting $w = 1.0 \times 10^{-3}$. Figure 4.10 shows a comparison of density and stress distributions between an configuration obtained with a stress constraint, and the same configuration after grayscale areas were removed. The maximum stress values of the configuration after removing grayscale areas was 171.49MPa, indicating that, although removing the grayscale increased the maximum stress, the value of the maximum stress of the configuration after removing grayscale was reduced compared to that without the stress constraint.

To further demonstrate the validity of the presented method, a minimum mean compliance minimization problem with a stress constraint is considered using a different numerical model. Figure 4.11 shows the design domain and boundary conditions. The displacement is fixed at the upper boundary and a downward force is applied at the center of the right boundary. The volume fraction V_{\max} is set to 40% of the volume of the fixed design domain. The maximum value for the stress constraint is set to 250MPa. The parameters μ and ϵ used for the stress constraint are set to 20 and 0.1, respectively. The width w of the Heaviside function is set to 0.8.

Figure 4.12(a) shows the obtained configuration and its corresponding von Mises stress distribution when only the volume fraction is applied. Figure 4.12(b) shows the obtained configuration when the stress constraint is applied in addition to the volume

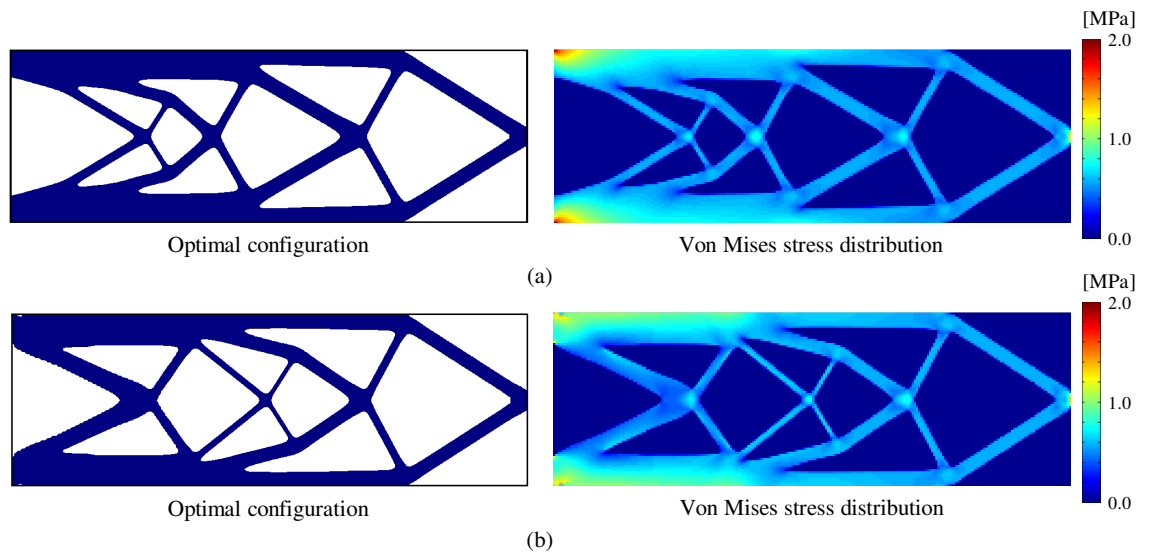


Figure 4.9: Comparison of optimal configurations and stress distributions: (a) without stress constraint; (b) with stress constraint.

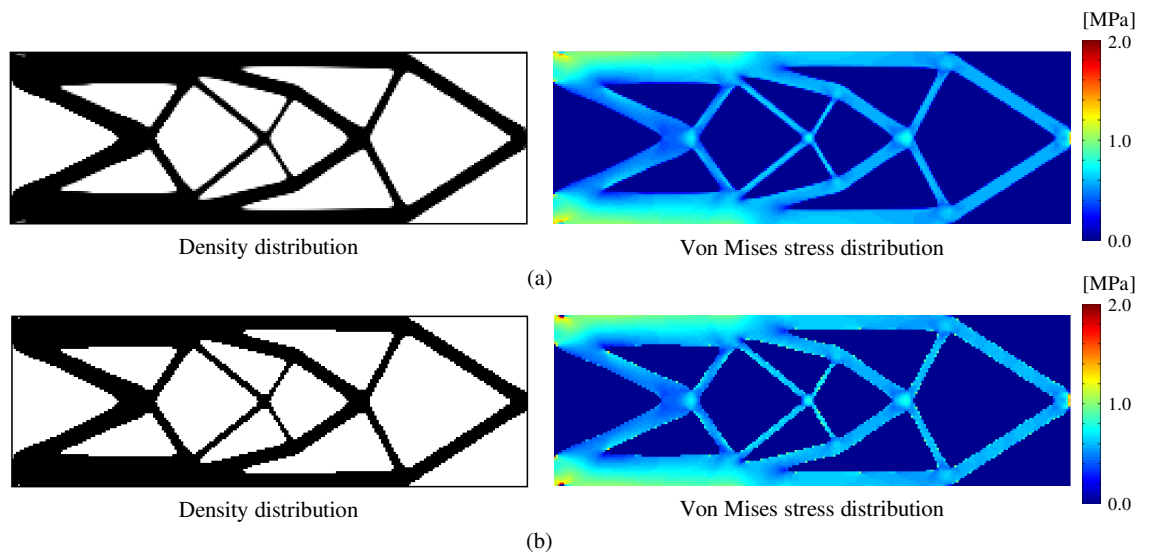


Figure 4.10: Comparison of density and stress distributions: (a) optimization results with stress constraint; (b) distributions after removing grayscale areas.

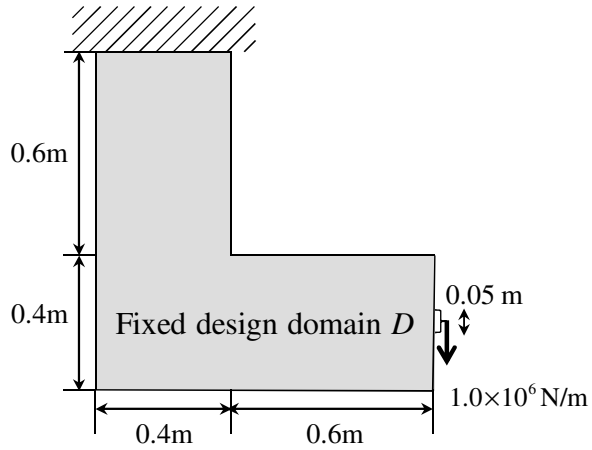


Figure 4.11: Design domain and boundary conditions for second minimum mean compliance problem with a stress constraint.

fraction, and its corresponding von Mises stress distribution. The maximum value of the von Mises stress was 431.85MPa without the stress constraint and 279.90MPa with the stress constraint. Again, the local stress did not reach the stress constraint value because a global stress constraint was applied, but the maximum value of the von Mises stress was reduced. The obtained mean compliance values show little difference: 115.56J without the stress constraint and 122.77J with the stress constraint.

Again, since the transition width of the Heaviside function w was set to 0.8, the optimal configuration contains some grayscale areas, but these can be removed by setting $w = 1.0 \times 10^{-3}$. Figure 4.13 shows a comparison of the density and stress distributions for the configuration obtained with a stress constraint, and the same configuration after grayscale areas were removed. The maximum stress values was 366.13MPa, indicating that the maximum stress in the configuration after removing grayscale was reduced compared to that without the stress constraint, although grayscale removal deleteriously affected the value.

4.4.5 Compliant mechanism design problem with a stress constraint

A compliant mechanism design problem with a stress constraint is considered using the model shown in Fig. 4.14. Small segments at the top and bottom of the left boundary are fixed, and a load is applied at the center of the left boundary. Since the design domain is symmetric, only the top half is analyzed in the optimization process. The applied stress constraint σ_{\max} is 5.0×10^3 . The design domain is discretized using an 80×80 mesh of quadrilateral finite elements and regularization parameter τ is set to 1.0×10^{-4} . The transition width of the Heaviside function w is set to 0.8 and the global stress constraint relaxation factor $\hat{\epsilon}$ is set to 0.1.

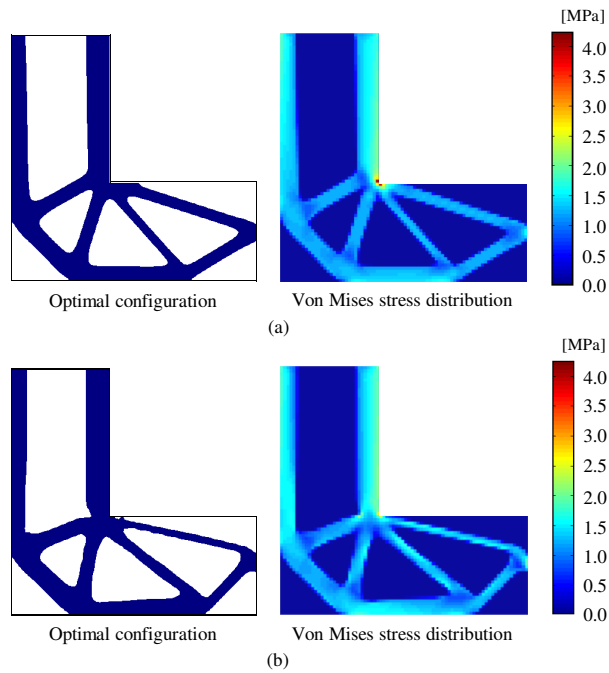


Figure 4.12: Comparison of optimal configurations and stress distributions: (a) without stress constraint; (b) with stress constraint.

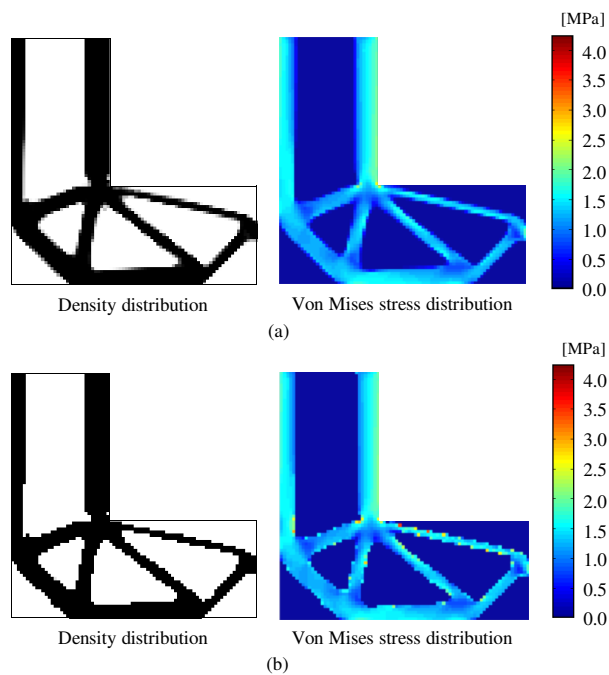


Figure 4.13: Comparison of density and stress distributions: (a) optimization results with stress constraint; (b) distributions after removing grayscale areas.

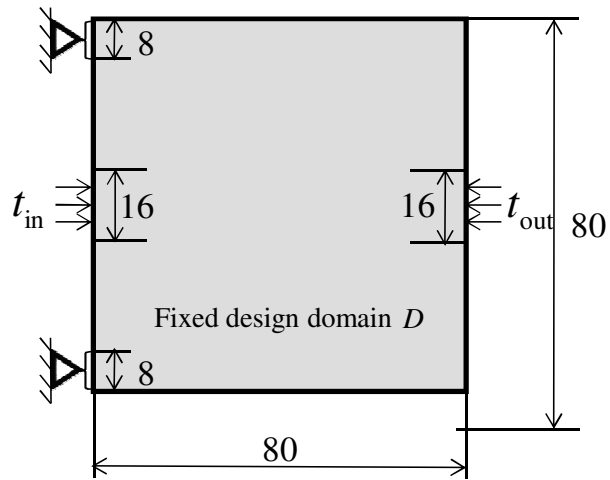


Figure 4.14: Fixed design domain and boundary conditions for compliant mechanism design problem with a stress constraint.

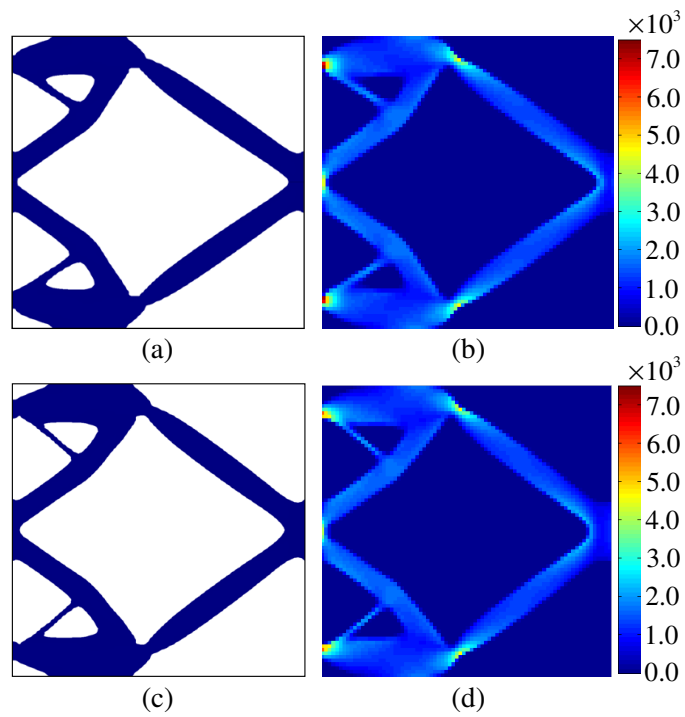


Figure 4.15: Optimal configurations: (a) without stress constraint; (c) von Mises stress distribution of (a); (b) with stress constraint; (d) von Mises stress distribution of (b).

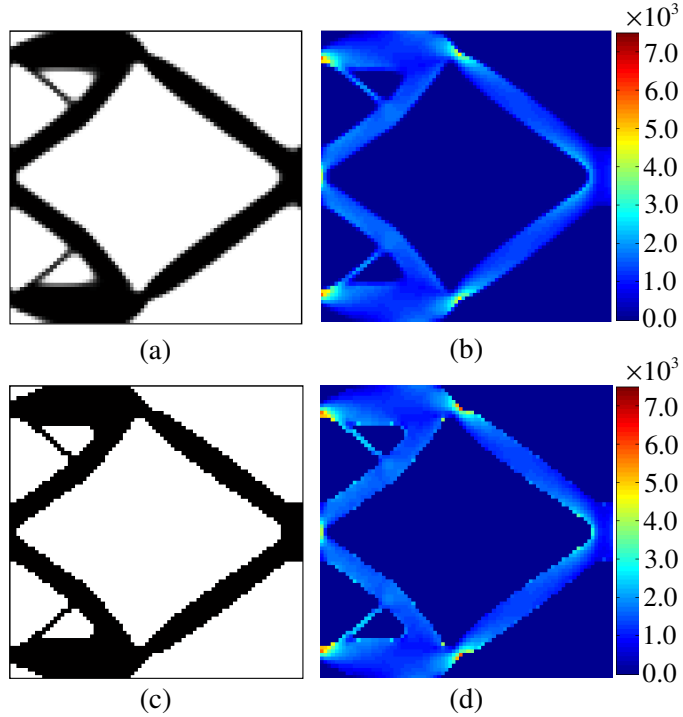


Figure 4.16: (a) Optimal configuration density distribution; (b) von Mises stress distribution of (a); (c) Configuration after removing grayscale areas; (d) von Mises stress distribution of (c).

Figure 4.15(a) shows the optimal configuration without an applied stress constraint and Fig.4.15(c) shows the von Mises stress distribution of this configuration. Figure 4.15(b) shows the optimal configuration with the stress constraint applied, and Fig.4.15(d) shows the corresponding von Mises stress distribution. The von Mises stresses at the center of the finite elements are considered. When the stress constraint is not applied, the maximum value of the von Mises stress is 7.18×10^3 , and with the constraint, it is 5.83×10^3 . Although the local stress constraints are not strictly satisfied, the maximum value of the von Mises stress is reduced and the obtained mutual mean compliance values show little difference: 7.62×10^{-10} without the stress constraint and 7.14×10^{-10} with the stress constraint.

Figure 4.16 shows the density distribution before and after removing grayscale areas that were present in the optimal configuration, by setting $w = 1.0 \times 10^{-3}$. The maximum value of the von Mises stress after removing grayscale areas was 5.86×10^3 , while the obtained mutual mean compliance was 7.25×10^{-10} . Although the maximum value of the von Mises stress is slightly increased after removing grayscale areas, the value is sufficiently reduced compared with that obtained without an applied stress constraint. Thus, useful optimal configurations can be qualitatively obtained using the proposed method.

4.5 Conclusions

In this chapter, a level set-based topology optimization method using mathematical programming was presented. The level set function is updated using the method of moving asymptotes to facilitate the treatment of constraint functionals. Such treatment is more difficult in a previous method that updates the level set function using a reaction-diffusion equation, because the derivation of the Lagrange multiplier becomes complicated in problems with multiple constraints. A new topology optimization method was presented and minimum mean compliance problems and compliant mechanisms design problems were formulated, using multiple constraint functionals. These include a mean compliance constraint, so that sufficient stiffness is obtained even when a load is applied in a direction slightly different from its prescribed direction, a mutual mean compliance constraints, so that the structure deforms in a designed direction, and a stress constraint.

The optimization results with a mean compliance constraint show that physically reasonable configurations were obtained, and the reduced mean compliance values when the load is applied in the horizontal indicate that the optimal configuration has increased stiffness in the horizontal direction.

The deformed shape obtained when a mutual mean compliance constraint was applied shows that the presented method can successfully impose a displacement constraint for the design of a compliant mechanism using a mutual mean compliance constraint.

Although the presented approach can not explicitly prevent the creation of lumped compliant mechanisms for compliant mechanisms problems, applying the stress constraint strongly inhibits this, since small areas subject to flexure, and notch hinges, tend to be locations where stress is high. A global stress constraint was applied, but because it does not require satisfaction of the stress constraint at every point in design domain, the optimal configurations do not strictly satisfy all local stress constraints, even though the global stress constraint is satisfied. The maximum stress was effectively reduced in the obtained optimal configurations. And, although the optimal configurations contained some grayscale areas, it was demonstrated that useful configurations can be qualitatively obtained using the proposed method.

Chapter 5

Negative permeability dielectric metamaterial design

5.1 Introduction

Electromagnetic metamaterials are artificial materials that exhibit extraordinary electromagnetic properties not available in nature, such as a negative refractive index, that is, negative permittivity and permeability. The existence of such materials was first proposed by Veselago [128] in 1968. After Pendry et al. [129] [130] and Smith et al. [131] showed that arrangements of split-ring resonators that have negative permeability and metallic wires that have negative permittivity can exhibit negative refraction at a certain frequency, considerable research was carried out to investigate the unusual properties of such materials, and develop certain applications, such as cloaking devices [132], waveguides [133], super lenses [134], leaky wave antennas [135], energy harvesting devices [136, 137], and the like. The comprehensive review of negative refractive index materials is provided in [138–143].

Furthermore, recently, new types of metamaterials that utilize the magnetic and electric resonance phenomena of dielectric materials rather than effects primarily derived from metallic inclusions have been proposed [144–148]. These new dielectric metamaterials are expected to offer advantages due to improved manufacturability and the possibility of achieving isotropic metamaterials that provide advanced functions under no metallic loss.

Holloway et al. [145] showed theoretically that negative effective permittivity and negative effective permeability can be simultaneously achieved with appropriately designed dielectric spheres embedded in a host material. Subsequently, more practical structures based on this approach were suggested, such as structures using dielectric particles of two different radii [146], structures using identically sized spheres but with different values of dielectric constant [147], and arrays of cylindrical dielectric materials [148]. Experimental verifications are provided for three-dimensionally isotropic dielectric metamaterials consisting of an array of dielectric cubes that exhibit negative permeability [149], and an array of dielectric rods [150], and cubic dielectric particles [151] that exhibit negative permittivity and negative permeability simultaneously.

Furthermore, applications such as all-dielectric cloaking devices [152] [153], as well as waveguides [154] and leaky wave antennas [155] composed of dielectric materials and metallic plates, have been discussed.

In addition, several other types of metamaterial components have been studied, including ferromagnetic materials, piezoelectric materials, and others. Because the permeability of ferromagnetic materials is frequency-dependent, due to a magnetic resonance phenomenon, and this dependency can be influenced by the magnitude of an externally applied DC magnetic field, such ferromagnetic materials allow the creation of metamaterials whose characteristics can be tuned within range of frequencies. Wu [156] demonstrated a negative refraction index at a microwave frequency in a periodic metal-ferrite film composite. Ueda and Tsutsumi [157] numerically developed a metallic waveguide with periodic dielectric and ferrite inclusions that provided left-handed behavior such as backward wave propagation. Wu and Ji [158] theoretically studied the existence of left-handed behavior in metallic magnetic composites. Zou et al. [159] later described a periodic ferrite-semiconductor layer with a tunable negative index, where the effect of the thickness ratio between ferrite and semiconductor was investigated numerically. Zhao et al. developed a composite consisting of a ferrite slab and metallic wires [160], and also an array of ferrite rods and metallic wires [144], which exhibited a negative refraction index and tunability, experimentally and through simulations. García-Miquel et al. [161] and Carbonell et al. [162] showed that glass coated amorphous microwires in a rectangular waveguide can behave as a double negative material with frequency tunability. Zharov and Kurin [163] demonstrated that composite nanostructure metamaterials enhance the Kerr effect. Engelbrecht et al. [164] experimentally showed a ferromagnetic metal, such as Co and Fe/Co, with a negative refractive index. A comprehensive review of ferromagnetic nanowire metamaterials is available [165]. Moreover, Acher et al. [166] developed piezoelectric materials that exhibit negative permeability.

Although the term “metamaterial” was originally applied in electromagnetic wave problems, research on microstructural designs that exhibit unusual properties have also been demonstrated in other physical problems, such as a negative thermal expansion coefficient [167], a negative Poisson’s ratio [168], an artificially designed Young’s modulus [66], and others. Recently, due to shared characteristics between electromagnetic and acoustic problems, acoustic metamaterials have also been studied and developed, such as those with negative bulk modulus [169, 170], negative mass density [171, 172], and double negative acoustic metamaterials [173–176]. Several interesting acoustic applications have also been reported, such as acoustic cloaks [177–179], acoustic super-lenses [180, 181], and others.

Most electromagnetic metamaterials consist of periodic arrays of unit cells that are adequately small compared to the wavelength of the target frequency, with cells composed of a layer of dielectric material, with or without metallic inclusions. The overall structure of such periodic arrays can be considered as an effectively homogeneous electromagnetic structure, so the electromagnetic metamaterial behaves as a material having negative properties exhibited globally, whereas the individual cell materials do not exhibit these properties.

Several unit cell layouts have been proposed that achieve good performance at

certain desired frequencies [182, 183]. However, the unit cell layout crucially affects the performance of metamaterials, and it is usually difficult or time-consuming to find appropriate unit cell designs by trial and error methods, even for expert engineers. Thus, there is a need for systematic design methods that assist or simplify the design of effective metamaterials. This chapter presents the level set-based topology optimization for the design of unit cell of dielectric metamaterials that demonstrate negative permeability value at desired frequencies.

5.2 Formulation

5.2.1 Governing equation

Two-dimensional electromagnetic wave propagation problem

The design domain for the two-dimensional dielectric metamaterial design problem is illustrated in Fig. 5.1. Transverse magnetic (TM) waves propagate in x - y direction where the magnetic field vector is polarized orthogonal to the wave direction, and the direction of wave amplitude is in the z -direction. Incident waves enter the domain from the left boundary Γ_1 and output waves are observed at the right boundary Γ_2 . The upper and lower boundaries Γ_{PEC} are set as Perfect Electric Conductors (PEC) under periodic conditions. In the two-dimensional case, the governing equation is the following Helmholtz equation, derived from Maxwell's equation, and the state variable of the governing equation is the magnetic field H_z in the z direction. Here, the relative permeability of both the background material and the dielectric material is set to 1, with air used as the background material.

$$\nabla \cdot (\epsilon_r^{-1} \nabla H_z) + k_0^2 H_z = 0, \quad (5.1)$$

where ϵ_r is the relative permittivity and k_0 is the wave number in a vacuum such that $k_0 = \omega \sqrt{\epsilon_0 \mu_0}$, where ω is the angular frequency and ϵ_0 and μ_0 are the permittivity and permeability in a vacuum, respectively. The boundary conditions are described as follows.

$$\mathbf{n} \cdot (\epsilon_r^{-1} \nabla H_z) + j k_0 H_z = 2 j k_0 H_z^i \quad \text{on } \Gamma_1 \quad (5.2)$$

$$\mathbf{n} \cdot (\epsilon_r^{-1} \nabla H_z) + j k_0 H_z = 0 \quad \text{on } \Gamma_2 \quad (5.3)$$

$$\mathbf{n} \cdot (\epsilon_r^{-1} \nabla H_z) = 0 \quad \text{on } \Gamma_{\text{PEC}} \quad (5.4)$$

where \mathbf{n} is the normal vector, j is the imaginary unit and H_z^i is an incident wave. Note that the boundary condition in 5.3 is a first-order absorbing boundary condition [184, 185]. The derivation of the first-order absorbing boundary condition is provided in Appendix A.

The weak formulation of Eqs.(5.1)-(5.4) is then derived as follows.

$$a_1(H_z, \tilde{H}_z) + a_2(H_z, \tilde{H}_z) = l(\tilde{H}_z) \quad \text{for } H_z \in U, \tilde{H}_z \in U \quad (5.5)$$

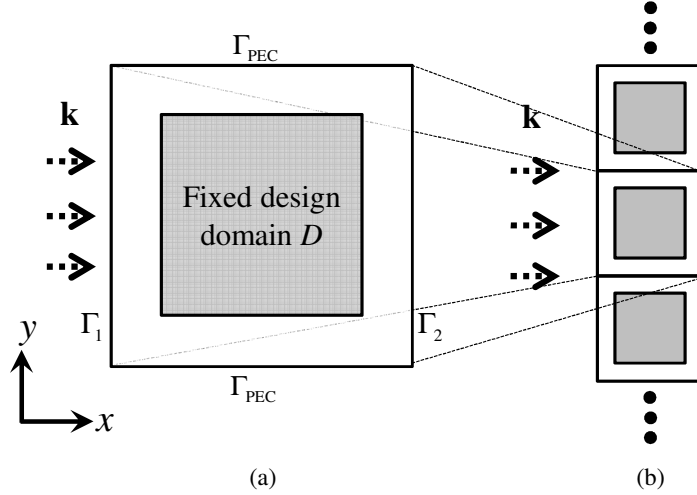


Figure 5.1: (a) Design domain and boundary conditions; (b) periodic structure for two-dimensional problem.

where

$$a_1(H_z, \tilde{H}_z) = \int_D \nabla \tilde{H}_z \cdot (\epsilon_r^{-1} \nabla H_z) d\Omega - k_0^2 \int_D \tilde{H}_z H_z d\Omega \quad (5.6)$$

$$a_2(H_z, \tilde{H}_z) = jk_0 \int_{\Gamma_1 \cup \Gamma_2} \tilde{H}_z H_z d\Gamma \quad (5.7)$$

$$l(\tilde{H}_z) = 2jk_0 \int_{\Gamma_1} H_z \tilde{H}_z d\Gamma \quad (5.8)$$

$$U = \{\tilde{H}_z \in H^1(\Omega)\}, \quad (5.9)$$

where \tilde{H}_z is a test function and H^1 is Sobolev space. Note that during the derivation of the weak formulation, the boundary integral for Γ_{PEC} becomes 0 due to the applied PEC condition. Additional details concerning the derivation of the weak formulation for the two-dimensional case are provided in Appendix B.1.

Three-dimensional electromagnetic wave propagation problem

The design domain for the three-dimensional problem is illustrated in Fig.5.2. Incident waves enter the domain from the left boundary Γ_1 . The upper and lower boundaries Γ_{PEC} are set as Perfectly Electric Conductors (PEC) and the front and rear boundaries Γ_{PMC} are set as Perfectly Magnetic Conductors (PMC) under periodic conditions. In the three-dimensional case, the following wave propagation equation is derived from Maxwell's equation and the state variable is the electric field \mathbf{E} . The relative permeability of both the background material and the dielectric material is again set to 1.

$$\nabla \times (\nabla \times \mathbf{E}) - k_0^2 \epsilon_r \mathbf{E} = 0 \quad (5.10)$$

The boundary conditions are described as follows.

$$\mathbf{n} \times (\nabla \times \mathbf{E}) - jk_0 \mathbf{n} \times (\mathbf{E} \times \mathbf{n}) = -2jk_0 \mathbf{E}^i \quad \text{on } \Gamma_1 \quad (5.11)$$

$$\mathbf{n} \times (\nabla \times \mathbf{E}) - jk_0 \mathbf{n} \times (\mathbf{E} \times \mathbf{n}) = 0 \quad \text{on } \Gamma_2 \quad (5.12)$$

$$\mathbf{n} \times \mathbf{E} = 0 \quad \text{on } \Gamma_{\text{PEC}} \quad (5.13)$$

$$\mathbf{n} \times \mathbf{H} = 0 \quad \text{on } \Gamma_{\text{PMC}}, \quad (5.14)$$

where \mathbf{E}^i is the incident field and \mathbf{H} is the magnetic field. The weak formulation of Eqs.(5.10)-(5.14) then derived as follows.

$$a_1(\mathbf{E}, \tilde{\mathbf{E}}) + a_2(\mathbf{E}, \tilde{\mathbf{E}}) = l(\tilde{\mathbf{E}}) \quad \text{for } \mathbf{E} \in U, \tilde{\mathbf{E}} \in U, \quad (5.15)$$

where

$$a_1(\mathbf{E}, \tilde{\mathbf{E}}) = \int_D (\nabla \times \tilde{\mathbf{E}}) \cdot (\nabla \times \mathbf{E}) d\Omega - k_0^2 \int_D \epsilon_r \tilde{\mathbf{E}} \cdot \mathbf{E} d\Omega \quad (5.16)$$

$$a_2(\mathbf{E}, \tilde{\mathbf{E}}) = jk_0 \int_{\Gamma_1 \cup \Gamma_2} (\mathbf{n} \times \tilde{\mathbf{E}}) \cdot (\mathbf{n} \times \mathbf{E}) d\Gamma \quad (5.17)$$

$$l(\tilde{\mathbf{E}}) = 2jk_0 \int_{\Gamma_1} \tilde{\mathbf{E}} \cdot \mathbf{E}^i d\Gamma \quad (5.18)$$

$$U = \{\tilde{\mathbf{E}} \in H^1(\Omega)\}, \quad (5.19)$$

where $\tilde{\mathbf{E}}$ is a test function. Note that during the derivation of the weak form, the boundary integral for Γ_{PMC} becomes 0, because $\mathbf{n} \times \mathbf{H} = 0$ and the relationship $\nabla \times \mathbf{E} = -j\omega\mu\mathbf{H}$ holds, which is derived from Faraday's law of Maxwell equations, replacing $\partial/\partial t$ with $j\omega$ for time-harmonic electromagnetic fields, and the same is true for Γ_{PEC} when the Galerkin finite element method is used [185]. Additional details for the derivation of the weak formulation for the three-dimensional case are provided in Appendix B.2.

5.2.2 Effective permeability

Several approaches can be used to compute an effective property, such as effective permeability and effective permittivity, and these are typically categorized into three types. One approach is to use a homogenization method, such as a method based on the asymptotic expansion [67, 103, 104, 186] and the energy-based method [187], another approach is to average the electric and magnetic fields in a unit cell [188], and the third approach is to compute the effective properties based on the S-parameter, namely, the complex transmission and reflection coefficients [189–192]. The first approach can only be applied when the periodic unit cell can be considered as infinitely small compared to the wavelength. Since the unit cell size is relatively large in this design problems, consisting of one unit cell in wave propagation direction, on the order of $1/10 \sim 1/4$ of the wavelength, this approach is not appropriate. The second approach obtains the effective properties based on the relation of electric field \mathbf{E} and

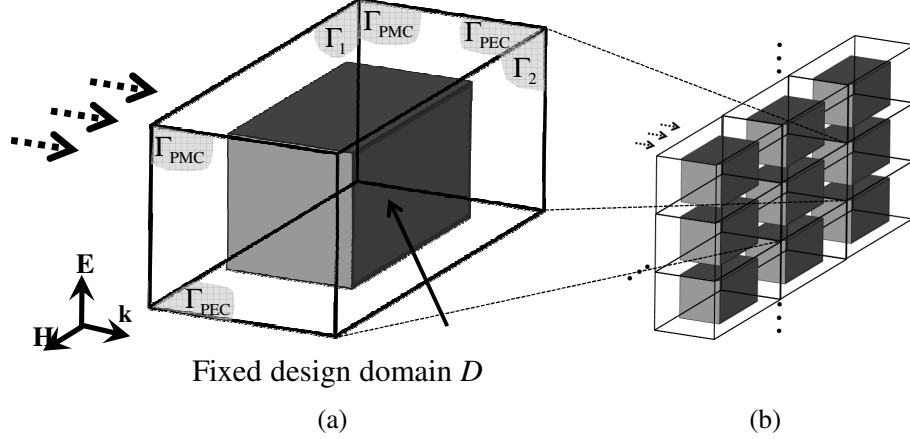


Figure 5.2: (a) Design domain and boundary conditions; (b) periodic structure for three-dimensional problem.

electric flux density \mathbf{D} , and also the magnetic field \mathbf{H} and magnetic field density \mathbf{B} , using the integral form of Maxwell's equations. However, it has been pointed out that this approach becomes less effective with increasing complexity of metamaterial cell structure [188].

The S-parameter-based approach was first proposed by Smith et al. [189]. Chen et al. [190] proposed an improvement to this method, which can determine the sign of the effective impedance and the correct branch of the real part of the refractive index, but it includes an iterative process, so it is not appropriate as an optimization process because the sensitivity may become exceedingly complicated. In the method of Lubkowski et al. [191], the effective properties are retrieved using parameterized Drude and Lorentz models, but the Drude model does not capture the effective permittivity appropriately for all-dielectric metamaterials. Smith et al. extended their original approach to deal with inhomogeneous cases [192]. Here, the extended approach [192] is applied, with the effective parameters computed based on S-parameters that can be obtained via the following equations:

$$S_{11} = \frac{\int_{\Gamma_1} (\mathbf{E}_1 - \mathbf{E}^i) \cdot \mathbf{E}^{i*} d\Gamma}{\int_{\Gamma_1} \mathbf{E}^i \cdot \mathbf{E}^{i*} d\Gamma} \quad (5.20)$$

$$S_{21} = \frac{\int_{\Gamma_2} \mathbf{E}_1 \cdot \mathbf{E}^{i*} d\Gamma}{\int_{\Gamma_2} \mathbf{E}^i \cdot \mathbf{E}^{i*} d\Gamma} \quad (5.21)$$

$$S_{22} = \frac{\int_{\Gamma_2} (\mathbf{E}_2 - \mathbf{E}^i) \cdot \mathbf{E}^{i*} d\Gamma}{\int_{\Gamma_2} \mathbf{E}^i \cdot \mathbf{E}^{i*} d\Gamma} \quad (5.22)$$

where \mathbf{E}^{i*} denotes the complex conjugate transpose of \mathbf{E}^i , \mathbf{E}_1 is electric field when

the incident field enter the domain from the left boundary Γ_1 and \mathbf{E}_2 is electric field when the incident field enter the domain from the right boundary Γ_2 . The effective permeability μ_{eff} is then obtained by following equation.

$$\mu_{\text{eff}} = Zn, \quad (5.23)$$

where

$$Z = \sqrt{\frac{(1 + S_{11})(1 + S_{22}) - S_{21}^2}{(1 - S_{11})(1 - S_{22}) - S_{21}^2}}, \quad (5.24)$$

$$n = \cos^{-1} \left(\frac{\beta}{2S_{21}} \right) \frac{\lambda}{2\pi d}, \quad (5.25)$$

where λ is the wavelength and d is the unit cell length, and

$$\beta = 1 - S_{11}S_{22} + S_{21}^2. \quad (5.26)$$

Note that in two-dimensional transverse magnetic (TM) wave propagation problems, $E_z = 0, H_x = 0, H_y = 0$. In addition, E_x and E_y can be obtained using the following relationship between \mathbf{E} and \mathbf{H} , derived from Ampere's law of Maxwell equations, $\nabla \times \mathbf{H} = \partial(\epsilon\mathbf{E})/\partial t$, and replacing $\partial/\partial t$ with $j\omega$ for time-harmonic electromagnetic fields.

$$E_x = \frac{1}{j\omega\epsilon} \frac{\partial H_z}{\partial y} \quad (5.27)$$

$$E_y = \frac{-1}{j\omega\epsilon} \frac{\partial H_z}{\partial x} \quad (5.28)$$

Therefore, S_{ij} can be computed using H_z in two-dimensional problems, and $S_{ij}(H_z)$ is then a functional of H_z . Note that the above formulation [64, 192] is an extended formulation of the one provided in an earlier paper [189], where S_{22} is used in addition to S_{11} and S_{21} , for inhomogeneous inclusions. By using the extended formulation, symmetric configurations can be obtained because it is symmetric with respect to S_{11} and S_{22} .

5.2.3 Optimization problem

One particularly interesting optimization problem aims to obtain metamaterial designs that exhibit highly negative permeability values. In this case, the objective of the optimization problem is to find a distribution of dielectric material within the fixed design domain that minimizes the effective permeability, and it can be formulated as a problem to minimize the effective permeability at a prescribed frequency. On the other hand, to obtain an effective cloaking device, the metamaterial design must exhibit a certain desirable value for the effective permeability, so the objective of the optimization problem then is to find a distribution of dielectric material that provides the desired value of effective permeability, and the optimization problem can be formulated to minimize the square of the difference between the effective permeability and a prescribed value at a prescribed frequency.

Effective permeability minimization problem

The purpose of the optimization here is to minimize the real part of the effective permeability at a desired frequency. A typical effective permeability curve is shown in Fig.5.3(a), where μ' and μ'' show the real and imaginary part of the effective permeability, respectively. The real part of the effective permeability has a positive peak as well as an anti-resonance point, where the effective permeability has a desirable negative value. However, if the positive peak lies between the initial anti-resonance point in the optimization and the target frequency, that is, if the target frequency is located in the hatched area for the case shown in Fig.5.3(a), configurations that demonstrate negative effective permeability cannot be obtained directly because the level set function must always return a lower value of the objective function after updating.

For example, considering a case where the target value is set to 3.0THz as shown in Fig.5.3(b), and the real part of the effective permeability is minimized directly, an increase in the frequency of the resonance frequency results in a decrease of the objectives. When the level set function is updated, the anti-resonance point moves toward higher frequencies, which prevents obtaining a configuration that demonstrate negative effective permeability. Thus, a two-stage optimization procedure [64] is applied, where the imaginary part of permeability μ'' is minimized during the first stage, taking advantage of the fact that the imaginary part of the permeability does not have positive peak (Fig.5.3(c)). The optimization problem for this first stage is described as follows.

$$\inf_{\phi} \quad F = \mu'' \quad (5.29)$$

$$\text{subject to } G \leq 0 \quad (5.30)$$

$$\text{Governing equation} \quad (5.31)$$

$$\text{Boundary conditions} \quad (5.32)$$

where F is the objective functional and G is the constraint functional of the optimization problem. For the second stage of the optimization, the real part of the effective permeability is minimized, using the configuration obtained in the first stage as the initial configuration (Fig.5.3(d)). The optimization problem for the second stage is described as follows.

$$\inf_{\phi} \quad F = \mu' \quad (5.33)$$

$$\text{subject to } G \leq 0 \quad (5.34)$$

$$\text{Governing equation} \quad (5.35)$$

$$\text{Boundary conditions} \quad (5.36)$$

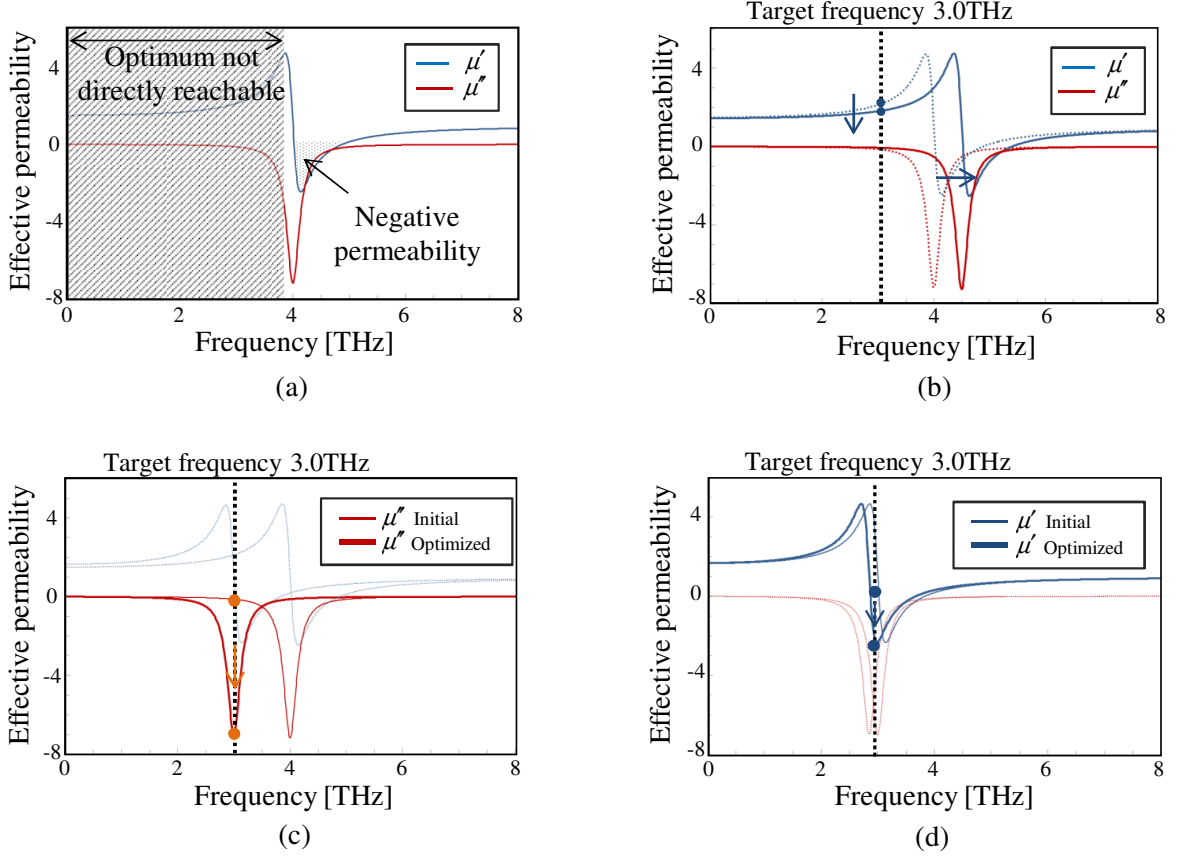


Figure 5.3: (a) A typical effective permeability curve; (b) effective permeability curve when real part of effective permeability is minimized directly; (c) 1st stage; (d) 2nd stage of two-stage optimization procedure.

Effective permeability design problem

The purpose of the optimization here is to obtain a distribution of dielectric material which achieves the target value of the effective permeability μ'_{tar} at a desired frequency. The optimization problem can be formulated as a problem to minimize the square of the difference between the effective permeability and a prescribed value. Again, if the positive peak lies between the initial anti-resonance point in the optimization and the target frequency, obtaining a configuration that demonstrate negative effective permeability directly is problematic, so the two-stage optimization procedure is again used. That is, the imaginary part of the permeability μ'' is minimized during the first stage, as described in the previous subsection, and the square of the difference between the effective permeability and a prescribed value is then minimized during the second stage. The optimization problem for the second stage is described as

follows.

$$\inf_{\phi} \quad F = (\mu' - \mu'_{\text{tar}})^2 \quad (5.37)$$

$$\text{subject to } G \leq 0 \quad (5.38)$$

$$\text{Governing Equation} \quad (5.39)$$

$$\text{Boundary conditions} \quad (5.40)$$

5.2.4 Sensitivity analysis

Two-dimensional case

Now, the sensitivity analysis is considered for a two-dimensional case, using the Adjoint Variable Method (AVM). The Lagrangian of the optimization problem is formulated as follows.

$$\hat{F} = F - \sum_{ij=11,21,22} \left(a_1(H_z, \tilde{H}_{z,ij}) + a_2(H_z, \tilde{H}_{z,ij}) - l(\tilde{H}_{z,ij}) \right) + \lambda G, \quad (5.41)$$

where $\tilde{H}_{z,ij}$ denotes the adjoint variables with respect to S_{ij} . The level set function is updated based on the gradient of the Lagrangian using a reaction diffusion equation. The sensitivity of the Lagrangian is obtained using the AVM, as follows.

$$\begin{aligned} \left\langle \frac{d\hat{F}}{d\chi_{\phi}}, \tilde{\chi}_{\phi} \right\rangle &= \sum_{ij=11,21,22} \left\langle \frac{\partial F}{\partial S_{ij}}, \tilde{S}_{ij} \right\rangle \left\langle \frac{\partial S_{ij}}{\partial H_z}, \tilde{H}_z \right\rangle \left\langle \frac{\partial H_z}{\partial \chi_{\phi}}, \tilde{\chi}_{\phi} \right\rangle \\ &\quad - \sum_{ij=11,21,22} \left(\left\langle \frac{\partial a_1}{\partial H_z}, \tilde{H}_z \right\rangle \left\langle \frac{\partial H_z}{\partial \chi_{\phi}}, \tilde{\chi}_{\phi} \right\rangle + \left\langle \frac{\partial a_2}{\partial H_z}, \tilde{H}_z \right\rangle \left\langle \frac{\partial H_z}{\partial \chi_{\phi}}, \tilde{\chi}_{\phi} \right\rangle \right. \\ &\quad \left. + \left\langle \frac{\partial a_1}{\partial \chi_{\phi}}, \tilde{\chi}_{\phi} \right\rangle + \left\langle \frac{\partial a_2}{\partial \chi_{\phi}}, \tilde{\chi}_{\phi} \right\rangle - \left\langle \frac{\partial l}{\partial \chi_{\phi}}, \tilde{\chi}_{\phi} \right\rangle \right) + \lambda \left\langle \frac{\partial G}{\partial \chi_{\phi}}, \tilde{\chi}_{\phi} \right\rangle, \end{aligned} \quad (5.42)$$

where $\left\langle \frac{\partial a_2}{\partial \chi_{\phi}}, \tilde{\chi}_{\phi} \right\rangle = 0$ and $\left\langle \frac{\partial l}{\partial \chi_{\phi}}, \tilde{\chi}_{\phi} \right\rangle = 0$, since a_2 and the incident field are independent of the design variables. Arranging the above equation in order to cancel out the $\left\langle \frac{\partial H_z}{\partial \chi_{\phi}}, \tilde{\chi}_{\phi} \right\rangle$ term, the above equation is transformed as follows.

$$\begin{aligned} \left\langle \frac{d\hat{F}}{d\chi_{\phi}}, \tilde{\chi}_{\phi} \right\rangle &= \sum_{ij=11,21,22} \left(\left\langle \frac{\partial F}{\partial S_{ij}}, \tilde{S}_{ij} \right\rangle \left\langle \frac{\partial S_{ij}}{\partial H_z}, \tilde{H}_z \right\rangle - \left\langle \frac{\partial a_1}{\partial H_z}, \tilde{H}_z \right\rangle - \left\langle \frac{\partial a_2}{\partial H_z}, \tilde{H}_z \right\rangle \right) \left\langle \frac{\partial H_z}{\partial \chi_{\phi}}, \tilde{\chi}_{\phi} \right\rangle \\ &\quad - \sum_{ij=11,21,22} \left\langle \frac{\partial a_1}{\partial \chi_{\phi}}, \tilde{\chi}_{\phi} \right\rangle + \lambda \left\langle \frac{\partial G}{\partial \chi_{\phi}}, \tilde{\chi}_{\phi} \right\rangle, \end{aligned} \quad (5.43)$$

where the adjoint variable $\tilde{H}_{z,ij}$ is obtained by solving the following equation.

$$a_1(\tilde{H}_{z,ij}, \delta H_z) + a_2(\tilde{H}_{z,ij}, \delta H_z) = \left\langle \frac{\partial F}{\partial S_{ij}}, \tilde{S}_{ij} \right\rangle (S_{ij}(\delta H_z) + \delta_{ij})$$

$$\text{for } \tilde{H}_{z,ij} \in U, \quad \forall \delta H_z \in U, \quad (5.44)$$

where δH_z is the variation of H_z , and δ_{ij} is the Kronecker delta such that $\delta_{11} = \delta_{22} = 1$, $\delta_{21} = 0$. The sensitivities are finally obtained using the following equation.

$$\left\langle \frac{d\hat{F}}{d\chi_\phi}, \tilde{\chi}_\phi \right\rangle = - \sum_{ij=11,21,22} \left\langle \frac{\partial a_1(H_z, \tilde{H}_{z,ij})}{\partial \chi_\phi}, \tilde{\chi}_\phi \right\rangle + \lambda \left\langle \frac{\partial G}{\partial \chi_\phi}, \tilde{\chi}_\phi \right\rangle \quad (5.45)$$

Note that, although the objective function is separately formulated for the two stages of the optimization, the sensitivities of the real and imaginary parts of the effective permeability are obtained by sensitivity analysis of the complex function. Therefore, the obtained sensitivity $\left\langle \frac{d\hat{F}}{d\chi_\phi}, \tilde{\chi}_\phi \right\rangle$ is a complex function where the sensitivities of the real and imaginary parts of the objective function are respectively obtained by the real and imaginary parts of the derived sensitivity, namely, $\text{Re} \left(\left\langle \frac{d\hat{F}}{d\chi_\phi}, \tilde{\chi}_\phi \right\rangle \right)$ and $\text{Im} \left(\left\langle \frac{d\hat{F}}{d\chi_\phi}, \tilde{\chi}_\phi \right\rangle \right)$. Additional details are provided in Appendix C.

Three-dimensional case

The Lagrangian of the optimization problem for a three-dimension case is formulated as follows.

$$\hat{F} = F - \sum_{ij=11,21,22} \left(a_1(\mathbf{E}, \tilde{\mathbf{E}}_{ij}) + a_2(\mathbf{E}, \tilde{\mathbf{E}}_{ij}) - l(\tilde{\mathbf{E}}_{ij}) \right) + \lambda G, \quad (5.46)$$

where $\tilde{\mathbf{E}}_{ij}$ denotes the adjoint variables with respect to S_{ij} . The sensitivity of the Lagrangian is obtained as follows.

$$\begin{aligned} \left\langle \frac{d\hat{F}}{d\chi_\phi}, \tilde{\chi}_\phi \right\rangle &= \sum_{ij=11,21,22} \left\langle \frac{\partial F}{\partial S_{ij}}, \tilde{S}_{ij} \right\rangle \left\langle \frac{\partial S_{ij}}{\partial \mathbf{E}}, \tilde{\mathbf{E}} \right\rangle \left\langle \frac{\partial \mathbf{E}}{\partial \chi_\phi}, \tilde{\chi}_\phi \right\rangle \\ &- \sum_{ij=11,21,22} \left(\left\langle \frac{\partial a_1}{\partial \mathbf{E}}, \tilde{\mathbf{E}} \right\rangle \left\langle \frac{\partial \mathbf{E}}{\partial \chi_\phi}, \tilde{\chi}_\phi \right\rangle + \left\langle \frac{\partial a_2}{\partial \mathbf{E}}, \tilde{\mathbf{E}} \right\rangle \left\langle \frac{\partial \mathbf{E}}{\partial \chi_\phi}, \tilde{\chi}_\phi \right\rangle + \left\langle \frac{\partial a_1}{\partial \chi_\phi}, \tilde{\chi}_\phi \right\rangle \right) + \lambda \left\langle \frac{\partial G}{\partial \chi_\phi}, \tilde{\chi}_\phi \right\rangle \\ &= \sum_{ij=11,21,22} \left(\left\langle \frac{\partial F}{\partial S_{ij}}, \tilde{S}_{ij} \right\rangle \left\langle \frac{\partial S_{ij}}{\partial \mathbf{E}}, \tilde{\mathbf{E}} \right\rangle - \left\langle \frac{\partial a_1}{\partial \mathbf{E}}, \tilde{\mathbf{E}} \right\rangle - \left\langle \frac{\partial a_2}{\partial \mathbf{E}}, \tilde{\mathbf{E}} \right\rangle \right) \left\langle \frac{\partial \mathbf{E}}{\partial \chi_\phi}, \tilde{\chi}_\phi \right\rangle \\ &- \sum_{ij=11,21,22} \left\langle \frac{\partial a_1}{\partial \chi_\phi}, \tilde{\chi}_\phi \right\rangle + \lambda \left\langle \frac{\partial G}{\partial \chi_\phi}, \tilde{\chi}_\phi \right\rangle, \end{aligned} \quad (5.47)$$

where the adjoint variable $\tilde{\mathbf{E}}_{ij}$ is obtained by solving the following equation.

$$a_1(\tilde{\mathbf{E}}_{ij}, \delta \mathbf{E}) + a_2(\tilde{\mathbf{E}}_{ij}, \delta \mathbf{E}) = \left\langle \frac{\partial F}{\partial S_{ij}}, \tilde{S}_{ij} \right\rangle (S_{ij}(\delta \mathbf{E}) + \delta_{ij})$$

$$\text{for } \tilde{\mathbf{E}}_{ij} \in U, \quad \forall \delta \mathbf{E} \in U, \quad (5.48)$$

where $\delta \mathbf{E}$ is the variation of \mathbf{E} . The sensitivities are then obtained by the following equation.

$$\left\langle \frac{d\hat{F}}{d\chi_\phi}, \tilde{\chi}_\phi \right\rangle = - \sum_{ij=11,21,22} \left\langle \frac{\partial a_1(\tilde{\mathbf{E}}_{ij}, \mathbf{E})}{\partial \chi_\phi}, \tilde{\chi}_\phi \right\rangle + \lambda \left\langle \frac{\partial G}{\partial \chi_\phi}, \tilde{\chi}_\phi \right\rangle \quad (5.49)$$

Note that in the three-dimensional case, the adjoint equation, Eq.(5.48), can be solved efficiently, as described below. The left-hand side is the same as that of the governing equation, Eq.(5.15). Considering the right-hand side, the right-hand side of the adjoint equation is linearly proportional to that of the governing equation for $ij = 11$. Therefore, the adjoint field is self-adjoint and its solution is linearly proportional to that of the governing equation. For $ij = 21$ and $ij = 22$, the solutions of the adjoint equation, Eq.(5.48), are obtained by switching the location of the input and output boundaries. Further details concerning this approach are given in [97].

5.3 Numerical implementation

5.3.1 Design variables

Two-dimensional case

The distribution of dielectric material inside the fixed design domain is expressed using the level set function. In this method, a reciprocal formulation is used of the relative electric permittivity to stabilize the optimization calculations, so ϵ_r in the fixed design domain is defined using the characteristic function χ_ϕ as follows.

$$\epsilon_r^{-1} = (\epsilon_1^{-1} - \epsilon_0^{-1}) \chi_\phi(\phi) + \epsilon_0^{-1}, \quad (5.50)$$

where ϵ_1 is the relative permittivity of the dielectric material and ϵ_0 is the relative permittivity of the background material. For the numerical implementation, the above characteristic function is approximated by the following smoothed Heaviside function $H(\phi)$.

$$H(\phi) = \begin{cases} 0 & (\phi < -w) \\ \frac{1}{2} + \frac{\phi}{w} \left(\frac{15}{16} - \frac{\phi^2}{w^2} \left(\frac{5}{8} - \frac{3}{16} \frac{\phi^2}{w^2} \right) \right) & (-w \leq \phi < w) \\ 1 & (w \leq \phi), \end{cases} \quad (5.51)$$

where w is the transition width of the Heaviside function, which is set to a sufficiently small value.

In cases where the relative permittivity is represented using a linear formulation, it is defined as follows.

$$\epsilon_r = (\epsilon_1 - \epsilon_0) \chi_\phi(\phi) + \epsilon_0. \quad (5.52)$$

The $\left\langle \frac{\partial a}{\partial \chi_\phi}, \tilde{\chi}_\phi \right\rangle$ term used in the sensitivity analysis is given by the following equation.

$$\left\langle \frac{\partial a}{\partial \chi_\phi}, \tilde{\chi}_\phi \right\rangle = \int_D \frac{-1}{\epsilon_r^2} (\epsilon_1 - \epsilon_0) \nabla H_z \cdot \nabla \tilde{H}_z \tilde{\chi}_\phi d\Omega \quad (5.53)$$

In the above formulation, the $-1/\epsilon_r^2$ term is included in the equation. In level set-based topology optimization methods, structural boundaries are clearly represented by the level set function, so values of the relative permittivity ϵ_r change drastically near these boundaries, assuming values between ϵ_0 and ϵ_1 . Thus, the sensitivity also changes drastically near the structural boundaries, and the sensitivity distribution becomes discontinuous. On the other hand, by using the reciprocal formulation, the $\left\langle \frac{\partial a}{\partial \chi_\phi}, \tilde{\chi}_\phi \right\rangle$ term used in sensitivity analysis is given by following equation.

$$\left\langle \frac{\partial a}{\partial \chi_\phi}, \tilde{\chi}_\phi \right\rangle = \int_D (\epsilon_1^{-1} - \epsilon_0^{-1}) \nabla H_z \cdot \nabla \tilde{H}_z \tilde{\chi}_\phi d\Omega \quad (5.54)$$

In this formulation, ϵ_r is not included in the equation, so the sensitivity distribution remains continuous and optimization calculations are stable. Note that the reciprocal formulation and the linear formulation respectively represent lower and upper theoretical bounds of the effective properties of the composite materials investigated here [193], so the reciprocal formulation is physically reasonable.

Three-dimensional case

In the three-dimensional case, the relative electric permittivity ϵ_r is simply defined using the linear formulation in Eq.(5.52). In this case, the $\left\langle \frac{\partial a}{\partial \chi_\phi}, \tilde{\chi}_\phi \right\rangle$ term used in the sensitivity analysis is given by the following equation.

$$\left\langle \frac{\partial a}{\partial \chi_\phi}, \tilde{\chi}_\phi \right\rangle = -k_0^2 \int_D (\epsilon_1 - \epsilon_0) \tilde{\mathbf{E}} \cdot \mathbf{E} \tilde{\chi}_\phi d\Omega \quad (5.55)$$

In the above formulation, ϵ_r does not appear as a term in the sensitivity analysis, so the sensitivity distribution remains continuous and optimization calculations are stable.

5.3.2 Optimization algorithm

Effective permeability minimization problem

As described in the previous section, for the problem to minimize the effective permeability, a two-stage optimization procedure is used in which the imaginary part of the effective permeability is first minimized and the real part of the effective permeability is minimized during the second stage.

- 1st stage: Minimize imaginary part of effective permeability.
- 2nd stage: Minimize real part of effective permeability, using configuration obtained in first stage as initial configuration.

Effective permeability design problem

A two-stage optimization procedure is also used in the effective permeability design problem. Assuming that the target permeability is set to a negative value, such as occurs at the anti-resonance point, a configuration that achieves the target value cannot be obtained directly if the positive peak lies between the initial antiresonance point and the target frequency. This behavior is the same as that encountered in the permeability minimization problem. Moreover, in the same manner as in the case when the target value is set to a negative value, when the target permeability is set to a value much larger than 1, such as occurs near the resonance point, a configuration that achieves the target value cannot be obtained directly if the anti-resonance point lies between the initial resonance point and the target frequency. Therefore, a two-stage optimization are also used. The imaginary part of the effective permeability is minimized in the first stage of the optimization, and the square of the difference between the real part of the effective permeability and the effective permeability target value is minimized during the second stage.

- 1st stage: Minimize imaginary part of effective permeability.
- 2nd stage: Minimize square of difference between real part of effective permeability and target value, using configuration obtained in first stage as initial configuration.

Flowchart for each stage

The optimization flowchart for the 1st and 2nd stages described above, are summarized as follows.

- 1: Initialize level set function.
- 2: Solve equilibrium equation using the Finite Element Method (FEM) and calculate the objective functional and constraint functional.
- 3: If objective functional has converged, terminate the optimization procedure and if not, compute the sensitivities of the objective and constraint functionals using the AVM.
- 4: Update the level set function using the reaction diffusion equation and return to step 2 of the optimization procedure.

The volume constraint is handled using the augmented Lagrangian method [194,195] by estimating the Lagrange multiplier λ at every iteration to satisfy $G(\phi(t+\Delta t)) = 0$. Further details are given in [90]. In the following numerical examples, the optimization terminates if the objective function does not improve during 20 consecutive iterations. The FEM is used for solving the equilibrium and adjoint equations for its ease of implementation in the level set-based method, but other computational methods such as the FDTD method could be applied. Note that the FEM is also stable and fast, especially when applied to single frequency analysis such as in the metamaterial design problems considered here.

5.4 Numerical examples

In this section, several numerical examples are provided to confirm the utility and validity of the presented method for two- and three-dimensional negative permeability dielectric metamaterial design problems.

5.4.1 Two-dimensional problems: effect of positive peak position in the initial configuration

In the two-dimensional design problems, effective permeability minimization problems are first addressed where the target frequencies are set either higher or lower than that of the positive peak of the initial configuration, to examine whether the optimization can successfully find configurations that demonstrates negative effective permeability, independent of the location of the positive peak of the initial configuration. Figure 5.4 shows the design domain and boundary conditions. The size of the analysis domain is set to $120\mu\text{m} \times 120\mu\text{m}$ and the size of the fixed design domain is set to $80\mu\text{m} \times 80\mu\text{m}$. The analysis domain is discretized using 120×120 square elements. The relative permittivity ϵ_1 of the dielectric material is set to $100 - 1i$ and the relative permittivity ϵ_0 of the background material is set to 1. The transition width w of the Heaviside function is set to 0.001.

Effective permeability minimization problem targeting 0.30THz

For the effective permeability minimization problem, the target frequency is set to 0.30THz to examine a case where the target frequency is lower than where the anti-

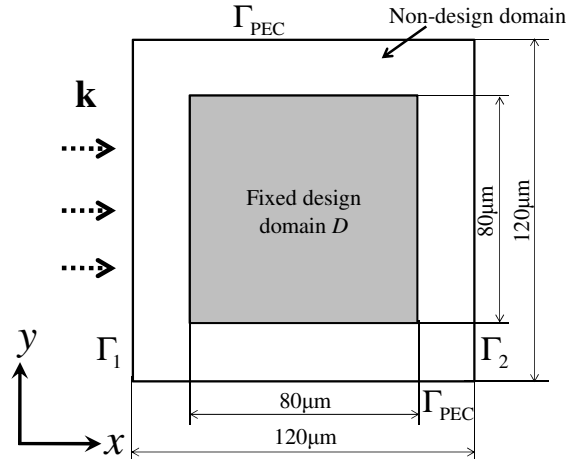


Figure 5.4: Design domain and boundary conditions for two-dimensional problem.

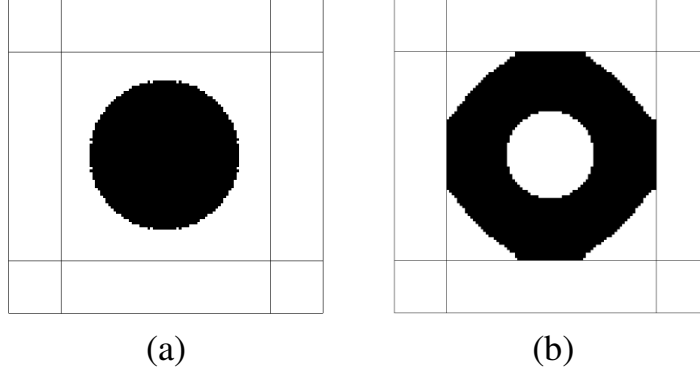


Figure 5.5: Comparison of configurations from 1st optimization stage for two-dimensional effective permeability minimization problem targeting 0.30THz: (a) initial; (b) obtained configuration

resonance point of the initial configuration occurs. A circular rod shape with a volume fraction of 40% of the volume of the fixed design domain is used as the initial configuration and the upper limit of the volume fraction is set to 70% of the volume of the fixed design domain.

The initial configuration and the distribution obtained in the first stage, i.e., the distribution after minimizing the imaginary part of the effective permeability, are shown in Fig. 5.5. The effective permeability curves for the initial configuration and the distribution obtained in the first stage are shown in Fig. 5.6. The frequency of the negative peak of the imaginary part of the effective permeability gradually decreases during the optimization procedure and finally reaches the prescribed frequency. The value of the imaginary part of the effective permeability of the initial configuration at 0.30THz is -0.01 , and the frequency of the negative peak of the imaginary part of the effective permeability is approximately 0.41THz. The value of the imaginary part of the effective permeability of the obtained configuration at 0.30THz is -13.23 . Figure 5.7 shows the convergence history of the objective function. The objective function sharply decreased after iteration 170 because the negative peak of the imaginary part of the effective permeability approached the target frequency, and the objective function sharply decreases near this peak.

During the second stage of the optimization, the real part of the effective permeability is minimized using the configuration obtained in the first stage as the initial configuration. Figure 5.8 shows the initial configuration and the configuration obtained in the second stage. The effective permeability curves of the initial and optimized configurations obtained are shown in Fig. 5.9. The anti-resonance point of the real part of the effective permeability gradually decreases during the optimization procedure and finally reaches the prescribed frequency at the end of the optimization procedure. The values of the real part of the effective permeability of the initial configuration of the first stage and the optimized configuration obtained in the second stage at 0.30THz are respectively 1.33 and -5.06 , which shows that the optimization

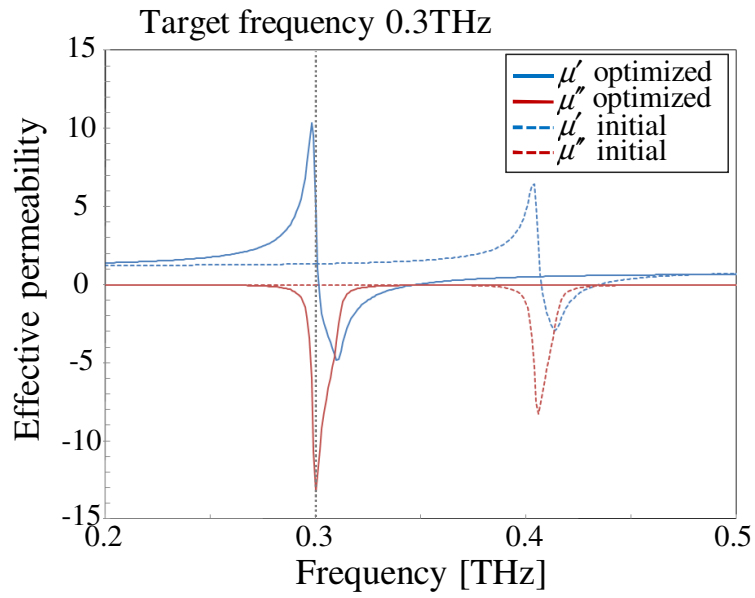


Figure 5.6: Effective permeability curves of 1st optimization stage for two-dimensional effective permeability minimization problem targeting 0.30THz.

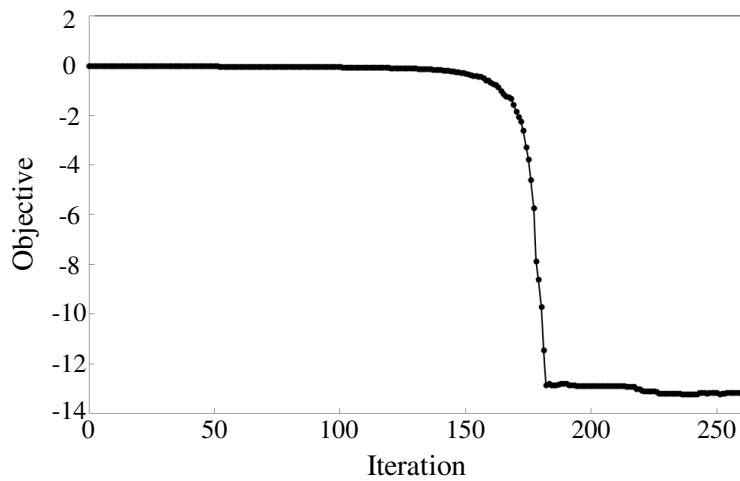


Figure 5.7: Convergence history of objective function of 1st optimization stage for two-dimensional effective permeability minimization problem targeting 0.30THz.

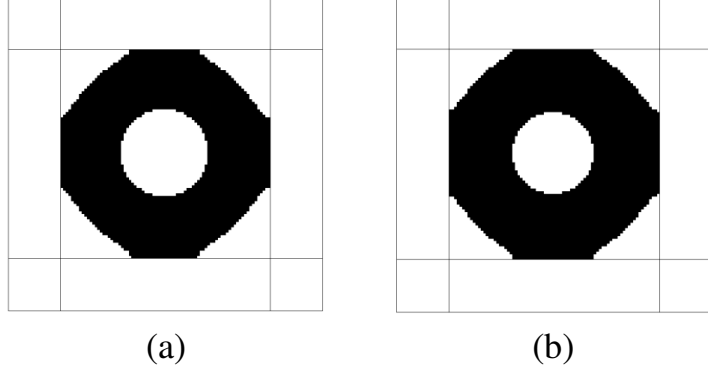


Figure 5.8: Comparison of configurations from 2nd optimization stage for two-dimensional effective permeability minimization problem targeting 0.30THz: (a) initial; (b) obtained configuration.

successfully found an optimized solution that has negative effective permeability. The values of the imaginary part of the effective permeability of the initial configuration used in the first stage of the optimization and the optimized configuration obtained in the second stage of the optimization at 0.30THz are respectively -0.01 and -3.22 . The volume fraction of the optimized configuration is 69.8% of the volume of the fixed design domain. Figure 5.10 shows the convergence history of the objective function during the second stage of the optimization.

Figure 5.11 shows the magnetic field of the initial configuration for the first stage of the optimization, and that of the optimized configuration obtained after the second stage of the optimization. Note that the ranges in the color bars of the two figures are different. The black arrows in these illustrations indicate the electric field. It can be seen that a circular electric field is generated in the center of the design domain of the optimized configuration, which induces a significant opposing magnetic field along the z -axis, whereas the electric field of the initial configuration lacks this feature. Although a comparison of methods for obtaining effective permeabilities is beyond the scope of this study, Note that the effective permeability can be also obtained as follows, using the method described in [130,188].

$$\mu_{\text{eff}} = \frac{1}{d} \frac{\int_D H_z(x, y) d\Omega}{H_z(0, 0)}. \quad (5.56)$$

Here, $H_z(0, 0)$ is positive, so when $\int_D H_z(x, y) d\Omega$ is negative, the effective permeability becomes negative. Thus, it is apparent that the strong opposing magnetic field described above is responsible for the obtained negative permeability in the metamaterial.

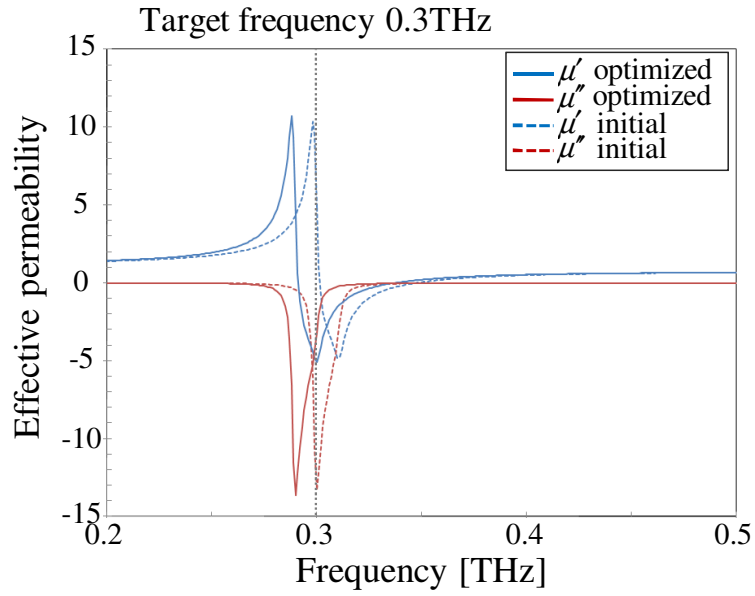


Figure 5.9: Effective permeability curves for 2nd optimization stage for two-dimensional effective permeability minimization problem targeting 0.30THz.

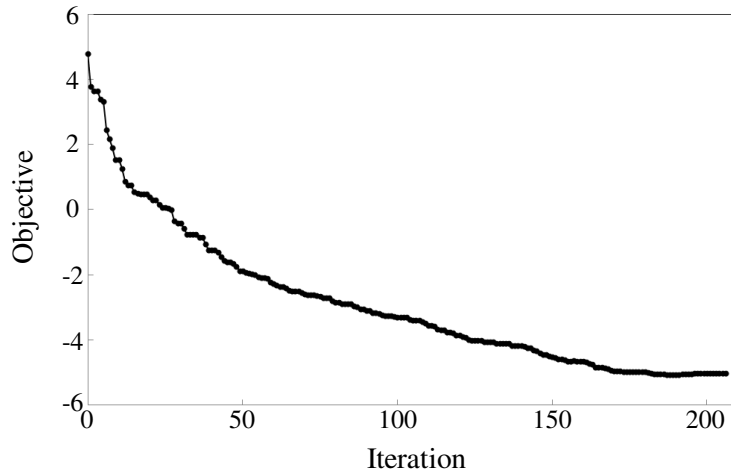


Figure 5.10: Convergence history of objective function of 2nd stage for two-dimensional effective permeability minimization problem targeting 0.30THz.

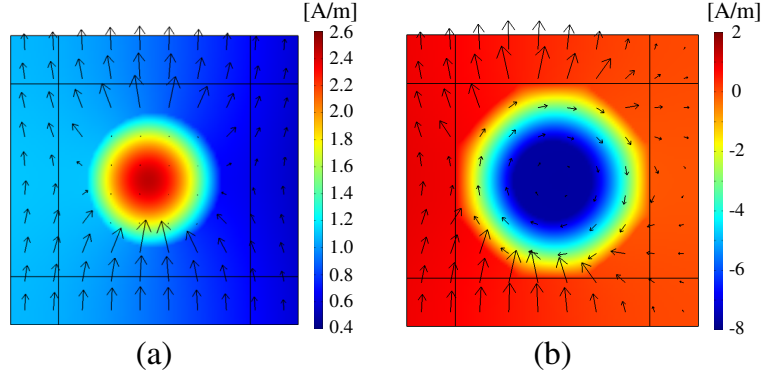


Figure 5.11: Magnetic and electric field distributions for two-dimensional effective permeability minimization problem targeting 0.30THz: (a) initial; (b) optimized.

Effective permeability minimization problem targeting 0.45THz

For the second two-dimensional problem, the target frequency is set to 0.45THz to examine a case where the target frequency is higher than that of the anti-resonance point of the initial configuration. A circular rod shape with a volume fraction of 50% of the volume of the fixed design domain is used as the initial configuration, but a volume constraint is not applied.

The initial configuration used in the first stage of the optimization and the optimized configuration after the second stage of the optimization are shown in Fig. 5.12, and the corresponding effective permeability curves for the initial and optimized configurations are shown in Fig. 5.13. The anti-resonance point of the real part of the effective permeability gradually increases during the optimization procedure and finally reaches the prescribed frequency. The real part of the effective permeability of the initial configuration at 0.45THz is 0.64, and the frequency at the anti-resonance point of the real part of the effective permeability is approximately 0.37THz. The real part of the effective permeability of the optimized configuration at 0.45THz is -2.45 , which shows that the optimization successfully found an optimized solution that exhibits negative effective permeability. The values of the imaginary part of the effective permeability of the initial configuration used in the first stage of the optimization and the optimized configuration obtained in the second stage of the optimization at 0.45THz are respectively -0.01 and -2.26 . Figure 5.14 shows the convergence histories of the objective function during the first and second stages of the optimization, respectively. Figure 5.15 shows the magnetic field of the initial configuration used in the first stage of the optimization, and that of the optimized configuration obtained after the second stage of the optimization. The black arrows in Fig.5.15 show the electric field, and the figure shows again that a circular electric field is generated in the center of the design domain of the optimized configuration. A strong opposing magnetic field is also induced in the optimized configuration, which generates the negative permeability.

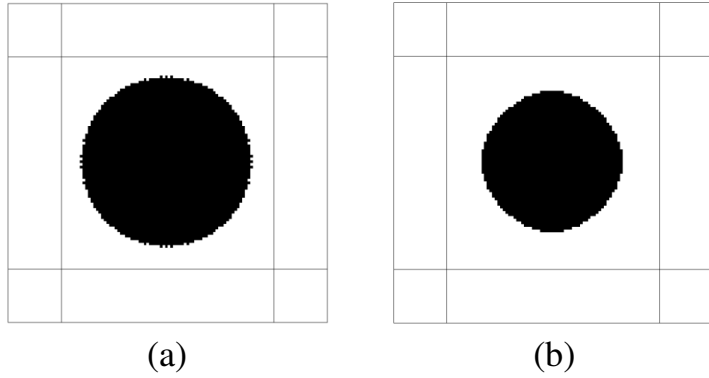


Figure 5.12: Comparison of configurations for two-dimensional effective permeability minimization problem targeting 0.45THz: (a) initial; (b) optimized.

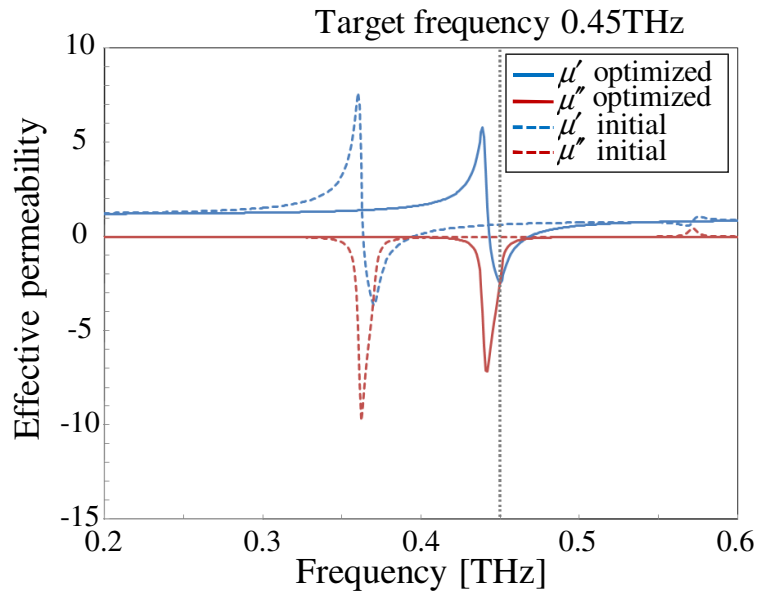


Figure 5.13: Effective permeability curves for two-dimensional effective permeability minimization problem targeting 0.45THz.

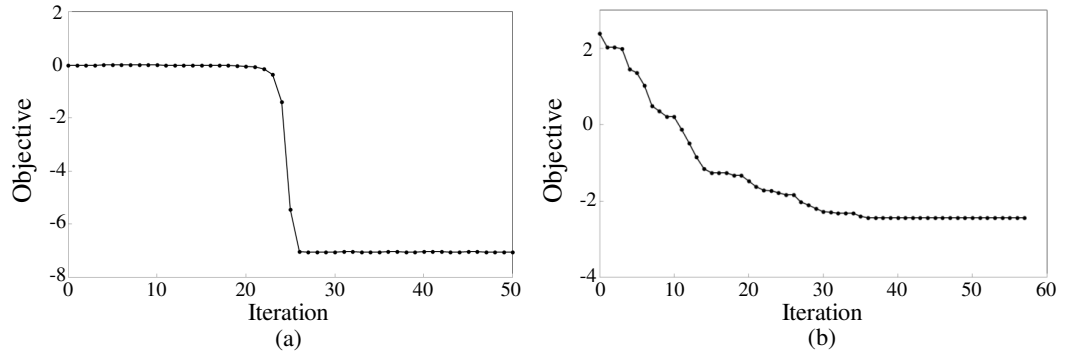


Figure 5.14: Convergence histories of objective function for two-dimensional effective permeability minimization problem targeting 0.45THz: (a) 1st optimization stage; (b) 2nd optimization stage.

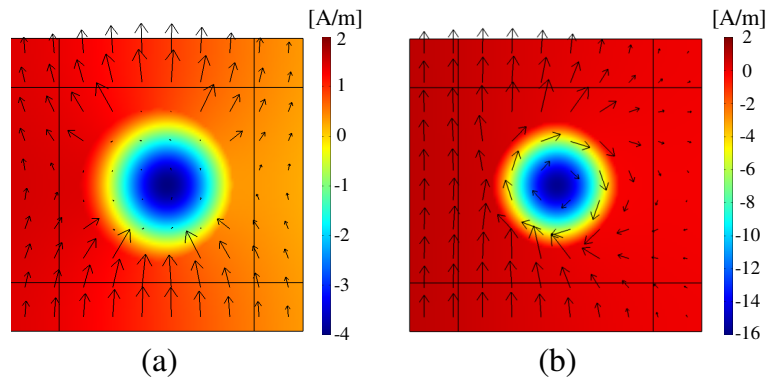


Figure 5.15: Magnetic and electric field distributions for two-dimensional effective permeability minimization problem targeting 0.45THz: (a) initial; (b) optimized.

5.4.2 Two-dimensional problem: effective permeability design problem

Next, an effective permeability design problem is considered to find an optimized dielectric distribution that exhibits a prescribed value of the effective permeability. The numerical settings of the optimization problem are the same as those used in the previous subsection. The target frequency is set to 0.30THz and the target value for the effective permeability is set to -3.0 . A circular rod shape with a volume fraction of 40% of the volume of the fixed design domain is used as the initial configuration. The upper limit of the volume fraction is set to 70% of the volume of the fixed design domain. During the first stage of the optimization, the imaginary part of the effective permeability is minimized, as described in subsection 5.4.1. The square of the difference between the effective permeability and a prescribed value is then minimized during the second stage of the optimization.

The initial configuration used in the first stage of the optimization and the optimized configuration after the second stage of the optimization are shown in Fig. 5.16, and the corresponding effective permeability curves for the initial and optimized configurations are shown in Fig. 5.17. The real part of the effective permeability of the optimized configuration at 0.30THz is -3.00 , which indicates that the optimization successfully found an optimized configuration that has a desirable value for the effective permeability at the target frequency. The values of the imaginary part of the effective permeability of the initial configuration used in the first stage of the optimization and the optimized configuration obtained in the second stage of the optimization at 0.30THz are respectively -0.01 and -7.44 . Figure 5.18 shows the convergence history of the objective function during the second stage of the optimization. Figure 5.19 shows the magnetic field of the initial configuration used in the first stage of the optimization, and that of the optimized configuration obtained after the second stage of the optimization. The black arrows in Fig. 5.19 show the electric field, and the figure shows that a strong opposing magnetic field is induced in the center of the design domain of the optimized configuration, which generates the negative permeability.

5.4.3 Two-dimensional problems: material with a high dielectric constant

To further verify the usefulness of the present method, a effective permeability minimization problems is provided for materials with a high dielectric constant. The numerical settings of the optimization problems are the same as those used in subsection 5.4.1. The relative permittivity ϵ_1 of the dielectric material is set to $200 - 5i$ and the relative permittivity ϵ_0 of the background material is set to 1. A configuration filled with dielectric material is used as the initial configuration, since the effect of the positive peak position is not considered, here. A volume constraint is not applied in the following examples.

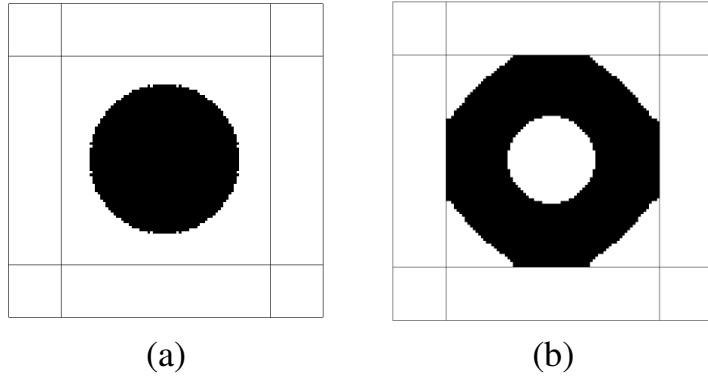


Figure 5.16: Comparison of configurations for two-dimensional effective permeability design problem: (a) initial; (b) optimized.

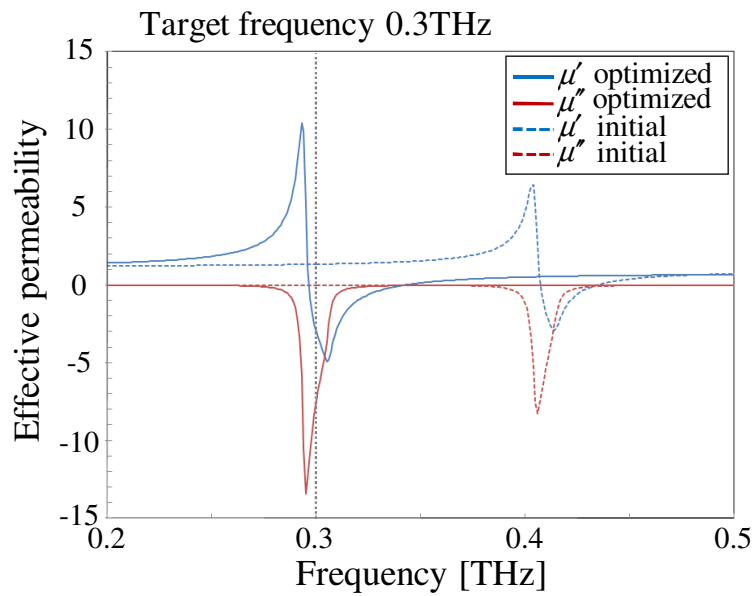


Figure 5.17: Effective permeability curves for two-dimensional effective permeability design problem.

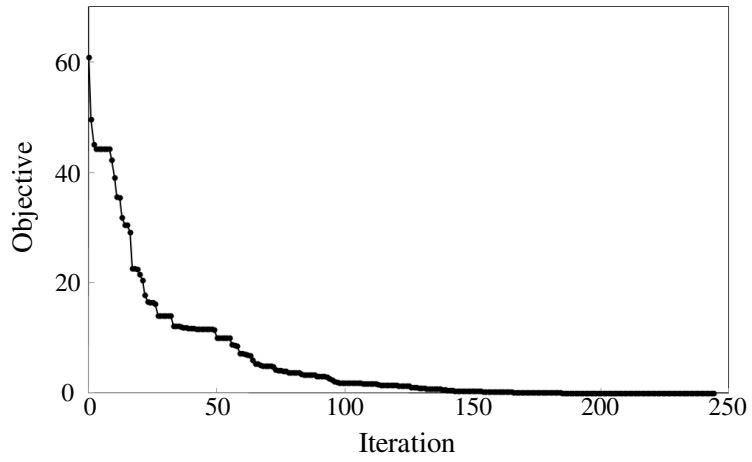


Figure 5.18: Convergence history of objective function of 2nd optimization stage for two-dimensional effective permeability design problem.

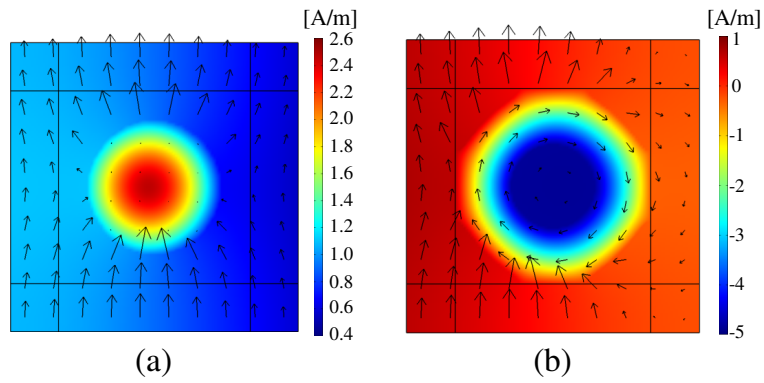


Figure 5.19: Magnetic and electric field distributions for two-dimensional effective permeability minimization problem targeting 0.30THz: (a) initial; (b) optimized.

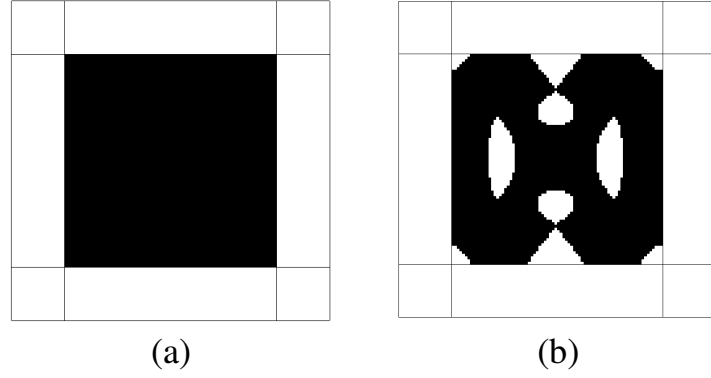


Figure 5.20: Comparison of configurations for two-dimensional effective permeability minimization problem targeting 0.30THz: (a) initial; (b) optimized.

Effective permeability minimization problem targeting 0.30THz

Here, the target frequency is set to 0.30THz. The initial configuration used in the first stage of the optimization and the optimized configuration after the second stage of the optimization are shown in Fig. 5.20, and the corresponding effective permeability curves for the initial and optimized configurations are shown in Fig. 5.21. The anti-resonance point of the real part of the effective permeability gradually increases during the optimization procedure and finally reaches the prescribed frequency. The real part of the effective permeability of the initial configuration at 0.30THz is 0.70, and the frequency at the anti-resonance point of the real part of the effective permeability is approximately 0.19THz. The real part of the effective permeability of the optimized configuration at 0.30THz is -2.89 , which shows that the optimization successfully found an optimized solution that exhibits negative effective permeability. The values of the imaginary part of the effective permeability of the initial configuration used in the first stage of the optimization and the optimized configuration obtained in the second stage of the optimization at 0.30THz are respectively 0.00 and -2.26 . Figure 5.22 shows the convergence histories of the objective function during the first and second stages of the optimization. Figure 5.23 shows the magnetic field of the initial configuration used in the first stage of the optimization, and that of the optimized configuration obtained after the second stage of the optimization. Once more, a strong opposing magnetic field is induced in the left and right-center areas of the optimized configuration, which generates the negative permeability.

Effective permeability minimization problem targeting 0.45THz

Next, the target frequency is set to 0.45THz. The initial configuration used in the first stage of the optimization and the optimized configuration after the second stage of the optimization are shown in Fig. 5.24, and the corresponding effective permeability curves for the initial and optimized configurations are shown in Fig. 5.25. Again, the anti-resonance point of the real part of the effective permeability gradually increases

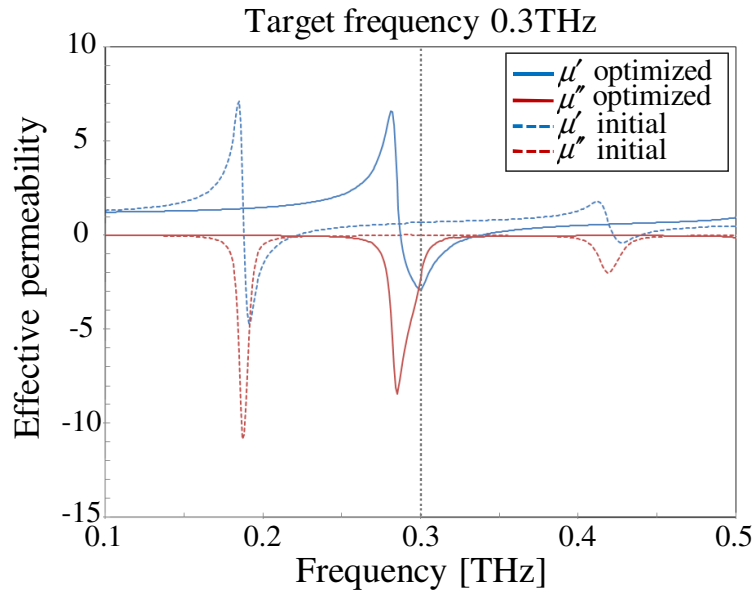


Figure 5.21: Effective permeability curves for two-dimensional effective permeability minimization problem targeting 0.30THz.

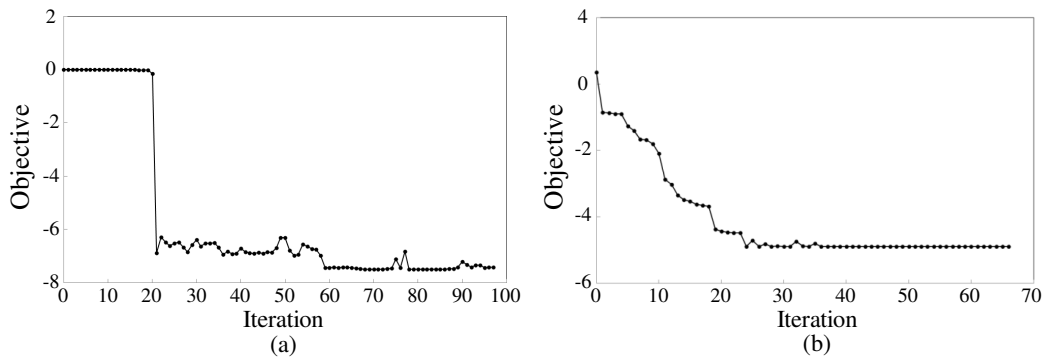


Figure 5.22: Convergence histories of objective function for two-dimensional effective permeability minimization problem targeting 0.30THz: (a) 1st optimization stage; (b) 2nd optimization stage.

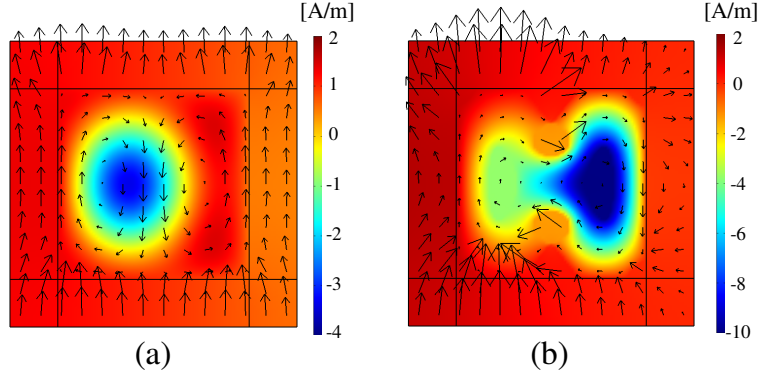


Figure 5.23: Magnetic and electric field distributions for two-dimensional effective permeability minimization problem targeting 0.30THz: (a) initial; (b) optimized.

during the optimization procedure and finally reaches the prescribed frequency. The real part of the effective permeability of the initial configuration at 0.45THz is 0.22, and the frequency at the anti-resonance point of the real part of the effective permeability is approximately 0.43THz. The real part of the effective permeability of the optimized configuration at 0.45THz is -0.58 , which shows that the optimization successfully found an optimized solution that exhibits negative effective permeability. The values of the imaginary part of the effective permeability of the initial configuration used in the first stage of the optimization and the optimized configuration obtained in the second stage of the optimization at 0.45THz are respectively -0.08 and -1.18 . Figure 5.26 shows the convergence histories of the objective function during the first and second stages of the optimization. Figure 5.27 shows the magnetic field of the initial configuration used in the first stage of the optimization, and the optimized configuration obtained after the second stage of the optimization. Although a strong magnetic field is induced in the center of the optimized configuration, a strong opposing magnetic field is induced in areas around the center, generating a negative permeability overall.

5.4.4 Three-dimensional problems

Now two three-dimensional effective permeability minimization problems are considered where the target frequencies are either higher or lower than that of the positive peak of the initial configuration, to show that the optimization can successfully find optimized configurations that demonstrates negative effective permeability, regardless of the location of the positive peak of the initial configuration. Figure 5.28 shows the design domain and boundary conditions. The size of the analysis domain is set to $120\mu\text{m} \times 120\mu\text{m} \times 150\mu\text{m}$ and the size of the fixed design domain is set to $80\mu\text{m} \times 80\mu\text{m} \times 110\mu\text{m}$. The analysis domain is discretized using $48 \times 48 \times 60$ square elements. The relative permittivity ϵ_1 of the dielectric material is set to $100 - 1i$ and the relative permittivity ϵ_0 of the background material is set to 1. The transition width w of the Heaviside function is set to 0.001.

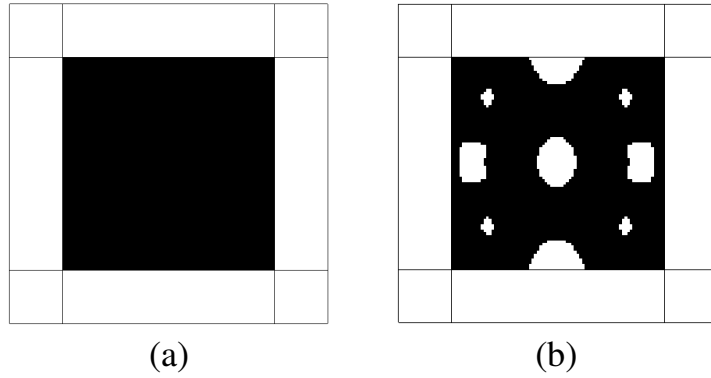


Figure 5.24: Comparison of configurations for two-dimensional effective permeability minimization problem targeting 0.45THz: (a) initial; (b) optimized.

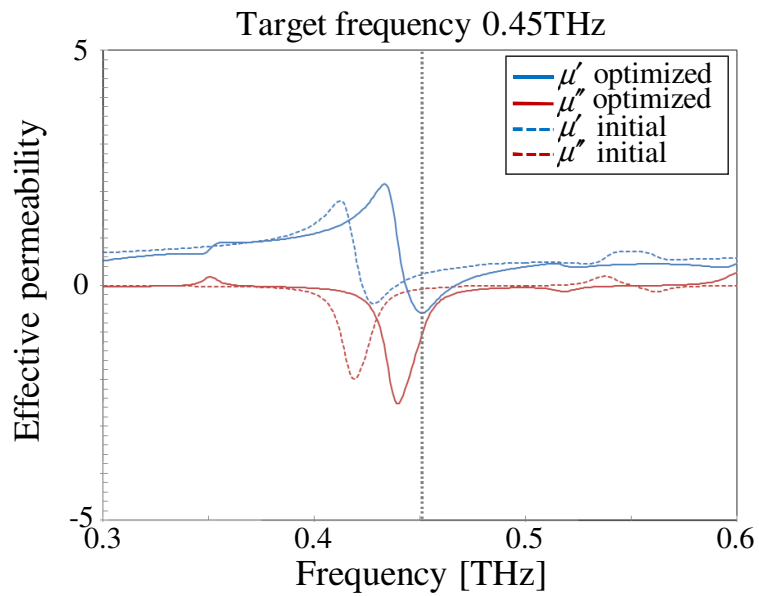


Figure 5.25: Effective permeability curves for two-dimensional effective permeability minimization problem targeting 0.45THz.

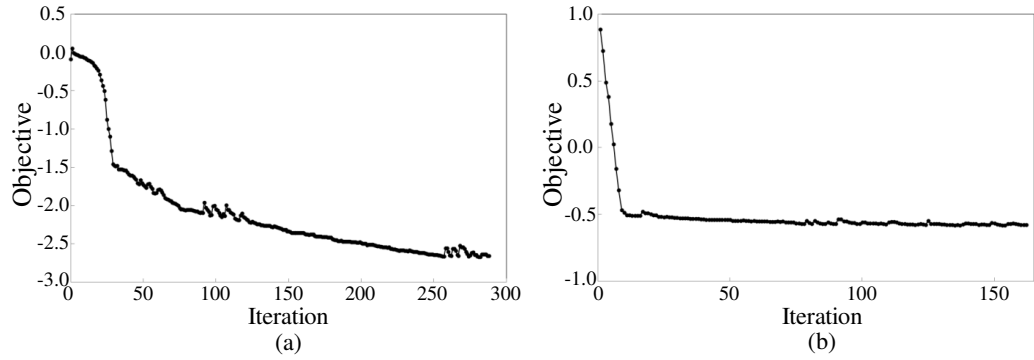


Figure 5.26: Convergence histories of objective function for two-dimensional effective permeability minimization problem targeting 0.45THz: (a) 1st optimization stage; (b) 2nd optimization stage.

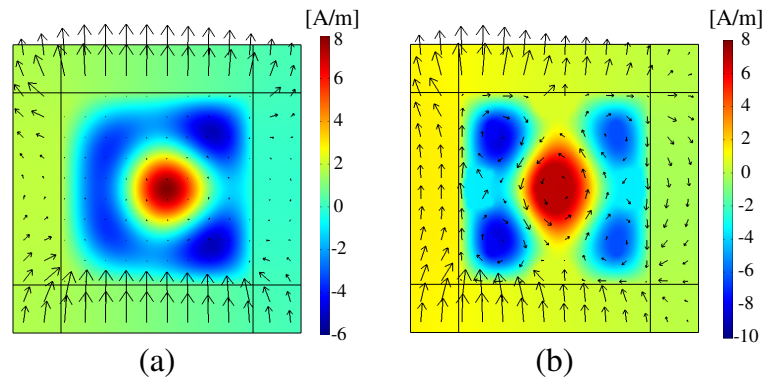


Figure 5.27: Magnetic and electric field distributions for two-dimensional effective permeability minimization problem targeting 0.45THz: (a) initial; (b) optimized.

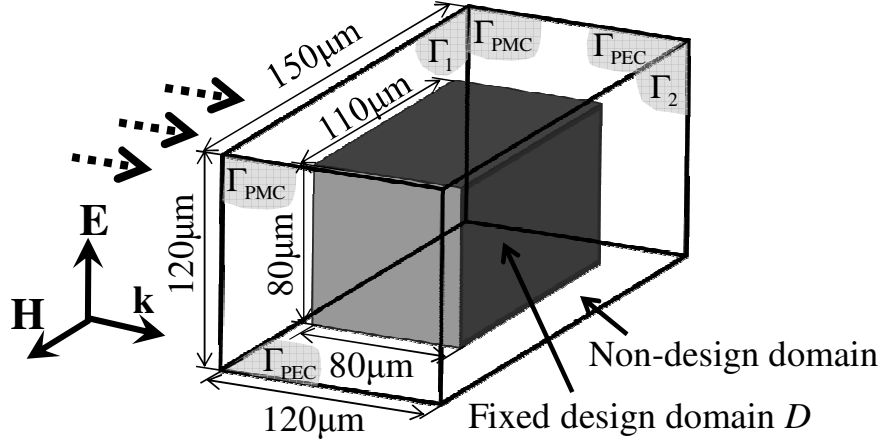


Figure 5.28: Design domain and boundary conditions for three-dimensional design problem.

Effective permeability minimization problem targeting 0.30THz

The effective permeability minimization problem where the target frequency is set to 0.30THz examines a case where the target frequency is lower than that of the anti-resonance point of the initial configuration. A spherical shape with a volume fraction of 25% of the volume of the fixed design domain is used as the initial configuration. The upper limit of the volume fraction is set to 90% of the volume of the fixed design domain. The initial configuration used in the first stage of the optimization and the optimized configuration after the second stage of the optimization are shown in Fig. 5.29, and the corresponding effective permeability curves are shown in Fig. 5.30. The anti-resonance point of the real part of the effective permeability gradually decreases during the optimization procedure and finally reaches the prescribed frequency. The real part of the effective permeability of the initial and optimized configurations at 0.30THz are respectively 1.06 and -3.48 , which shows that the optimization can successfully find an optimized solution that demonstrates negative effective permeability. The values of the imaginary part of the effective permeability used in the initial configuration of the first stage and the optimized configuration obtained in the second stage at 0.30THz are respectively 0.00 and -2.68 . The volume fraction of the optimized configuration is 90.0% of the volume of the fixed design domain. Figure 5.31 shows the convergence histories of the objective function during the first and second stages of the optimization.

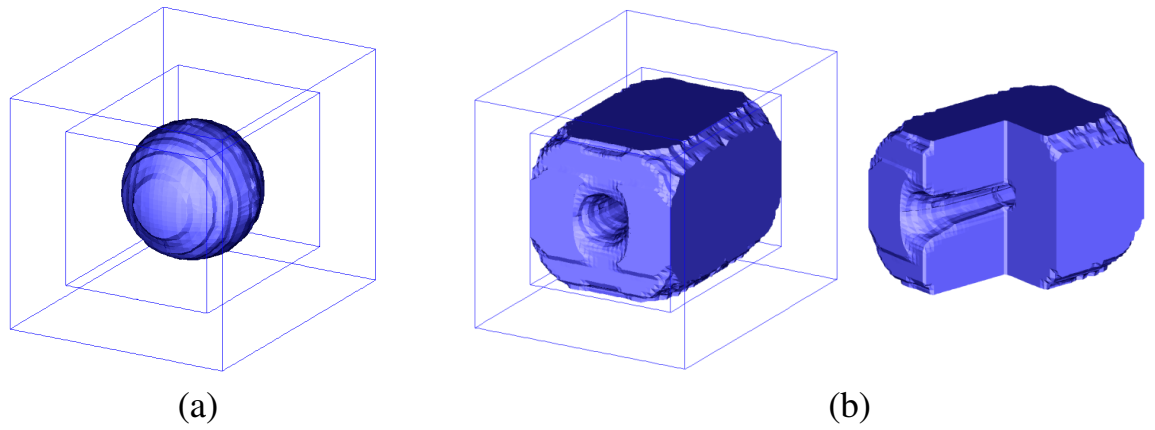


Figure 5.29: Comparison of configurations for three-dimensional effective permeability minimization problem targeting 0.30THz: (a) initial; (b) optimized.

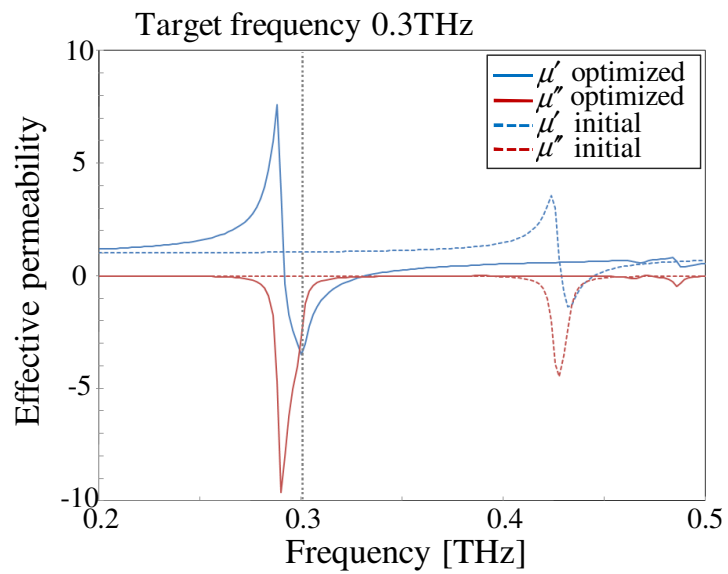


Figure 5.30: Effective permeability curves for three-dimensional effective permeability minimization problem targeting 0.30THz.

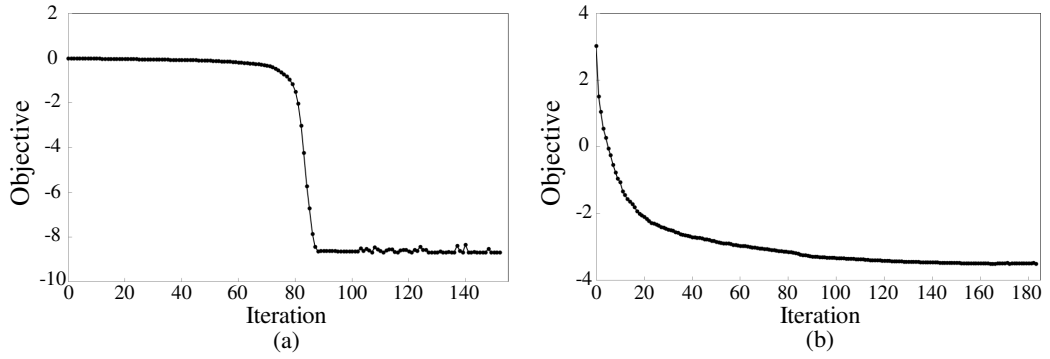


Figure 5.31: Convergence histories of objective function for three-dimensional effective permeability minimization problem targeting 0.30THz: (a) 1st optimization stage; (b) 2nd optimization stage of the optimization.

Effective permeability minimization problem targeting 0.45THz

The effective permeability minimization problem where the target frequency is set to 0.45THz now examines a case where the target frequency is higher than that of the anti-resonance point of the initial configuration. A spherical shape with a volume fraction of 40% of the volume of the fixed design domain is used as the initial configuration, and a volume constraint is not applied. The initial configuration used in the first stage of the optimization and the optimized configuration after the second stage of the optimization are shown in Fig. 5.32, and the corresponding effective permeability curves are shown in Fig. 5.33. The anti-resonance point of the real part of the effective permeability gradually increases during the optimization procedure and finally reaches the prescribed frequency. The real part of the effective permeability of the initial and optimized configuration at 0.45THz are respectively 0.64 and -1.61 , which shows that the optimization can successfully find an optimized solution that has negative effective permeability. The values of the imaginary part of the effective permeability of the initial configuration used in the first stage of the optimization and the optimized configuration obtained in the second stage of the optimization at 0.45THz are respectively -0.01 and -1.99 . Figure 5.34 shows the convergence histories of the objective function during the first and second stages.

5.5 Conclusions

This chapter presented a level set-based topology optimization method for the design of negative permeability dielectric metamaterials. The following is a achievement through this study:

(1) The optimization problems for both two- and three-dimensional problems were formulated to minimize the effective permeability, and to obtain a prescribed effective permeability at a target frequency. A level set-based boundary expression was

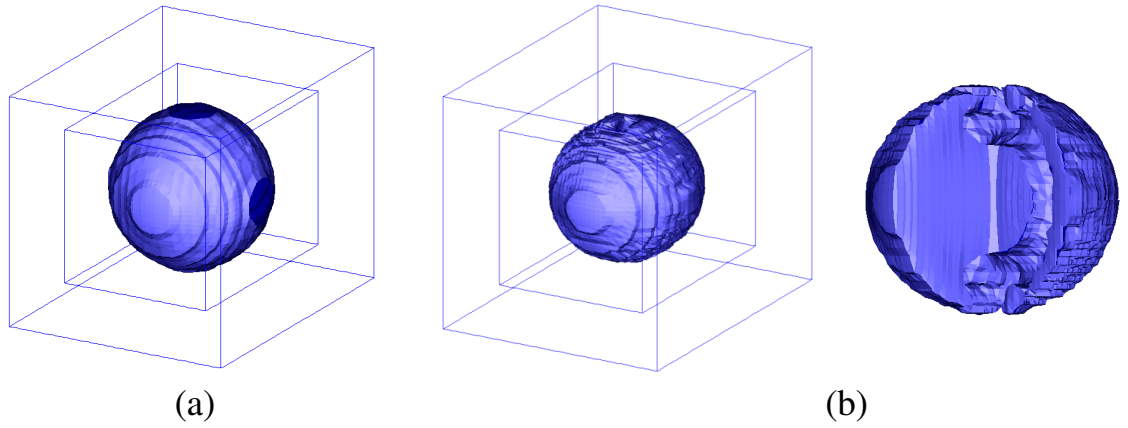


Figure 5.32: Comparison of configurations for three-dimensional effective permeability minimization problem targeting 0.45THz: (a) initial; (b) optimized.

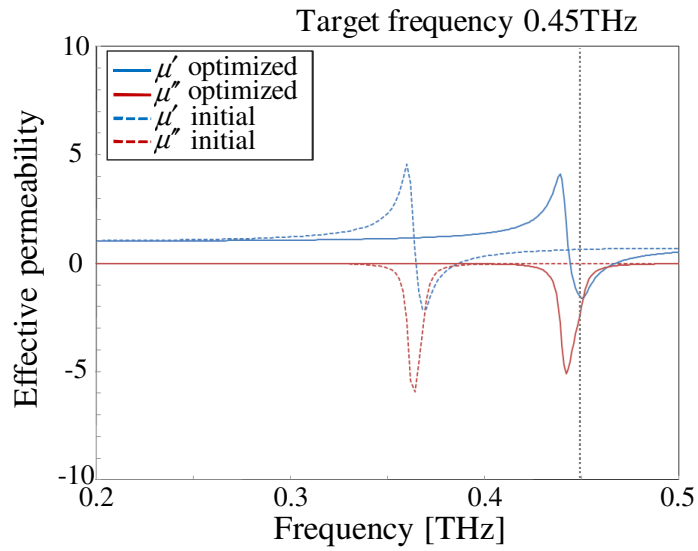


Figure 5.33: Effective permeability curves for three-dimensional effective permeability minimization problem targeting 0.45THz.

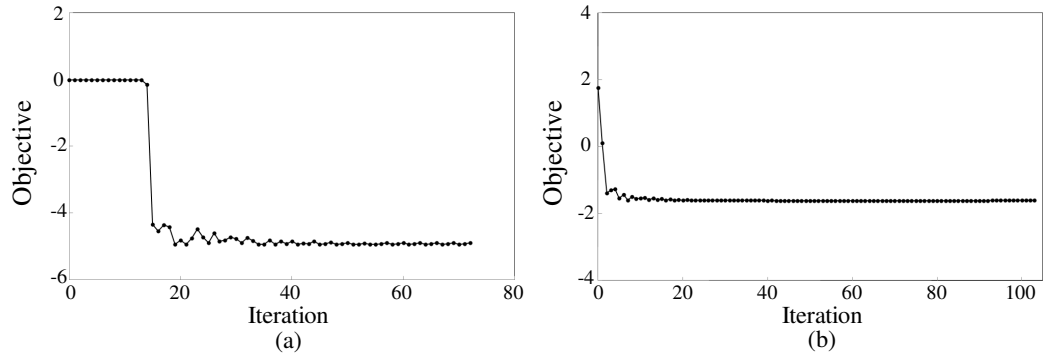


Figure 5.34: Convergence histories of objective function for three-dimensional effective permeability minimization problem targeting 0.45THz: (a) 1st optimization stage; (b) 2nd optimization stage.

applied to obtain clear boundaries, and an S-parameter-based approach was applied to compute the effective permeability of the metamaterials.

(2) Based on the formulation of the optimization problem, an optimization algorithm was constructed. The FEM was used to solve the electromagnetic wave problems and update the level set function, and the Adjoint Variable Method was used when computing sensitivity analyses.

(3) Several numerical examples for both two- and three-dimensional problems were provided to examine the validity of the presented method. It was confirmed that the presented method successfully finds optimized configurations that minimize the effective permeability, and also finds optimized configurations that achieve a prescribed degree of effective permeability. Finally, it was also confirmed that the presented method obtains smooth and clear optimized configurations for all the presented cases.

Chapter 6

Inverse design of dielectric materials

6.1 Introduction

Artificial dielectric materials that are engineered to have an extreme dielectric constant are of great interest for improving electromagnetic devices such as electrostatic actuators, waveguides, antennas and so on. In this chapter, a systematic design methodology for the microstructure design of composites made from two dielectric materials with different dielectric constants, or a single dielectric material and air. Topology optimization is applied to find the shape and distribution of dielectric elements that exhibits a prescribed desirable dielectric constant.

Topology optimization has been successfully applied to various microstructure design problems aiming to develop materials that have extreme properties such as a negative thermal expansion coefficient [167], a negative Poisson's ratio [168], and materials with a prescribed value of a constitutive tensor such as Young's modulus [66], magnetic permeability [65], a dielectric constant [68], and so on. These problems are called inverse homogenization problems [66].

There are various methods for obtaining an effective permittivity value for dielectric composites. Analytic methods such as the Clausius-Mossotti, Maxwell-Garnett, and Bruggman formulas, which are also called mixing formulas, compute the effective permittivity of composites based on the volume of the inclusions [196], however the accuracy is valid only for certain inclusion shapes such as spheres, cylinders, and ellipsoids. A homogenization method such as a method based on asymptotic expansion [103, 104], and also an energy-based method [187], can be used when dealing with more complicated shapes where the effective properties are obtained based on the results of finite element analysis. In this study, an energy-based method is used to obtain the effective permittivity of the dielectric materials.

There is considerable literature on the investigation of the theoretical bounds for the effective properties of composites (e.g., [197]). The primal bounds for two-phase dielectric materials are given by arithmetic and harmonic means of each dielectric constant. Tighter bounds can be obtained based on certain available information

about the composites, such as their volume fractions and/or isotropy. In this work, to evaluate the permittivity values obtained in optimization, the theoretical bounds of the two- three-dimensional anisotropic effective property in the principal direction when that of the other principal direction is set to a prescribed value are derived. Permittivity values obtained in optimizations are compared with these derived theoretical bounds.

In a previous study on the microstructure design of dielectric materials [68], a genetic algorithm (GA) was used in the optimization method. However, meta-heuristic approaches such as GAs, Particle Swarm Optimization (PSO), and Simulated Annealing (SA) are generally not suitable for topology optimization since the number of design variables is usually so large that the optimization becomes too computationally costly [198]. Hence in [68] design resolution was limited to extremely coarse discretizations. In this work, a gradient-based topology optimization method is used to find the distribution of dielectric material for the unit cell of a periodic microstructure, where densities are updated based on the sensitivities. The computation of sensitivities is significantly streamlined by using the adjoint variable method (AVM). In this way, it is available to solve problems with very fine discretizations and hence obtain accurate results and detailed boundary descriptions. The objective of the optimization is to design dielectric materials that exhibit a prescribed effective permittivity. Therefore, the optimization problem is formulated as a problem to minimize the square of the difference between the effective permittivity and a prescribed value. The optimization algorithm uses the finite element method (FEM) for solving the equilibrium and adjoint equations, respectively. A Heaviside projection filter [24] is used to obtain clear optimized configurations. In this study, several design problems are considered including the design of an isotropic material, an anisotropic material, an anisotropic material with nonzero off-diagonal terms, and an anisotropic material with loss. Moreover, the obtained results are compared with derived theoretical bounds to confirm the validity of the results.

6.2 Formulation

6.2.1 Effective permittivity

In this study, the electrostatic effective permittivity is obtained on the basis of the energy-based approach that employ conductivity average theorems [187] (see also [66]), where the effective permittivities are expressed in terms of mutual energies as follows. This method assume that the mutual energies accumulated in the original unit cell and in the homogenized cell are equivalent. The mutual energy accumulated in the original unit cell is given as

$$Q_{ij} = \frac{1}{2} \int_{\Omega} \epsilon_r \nabla \bar{\phi}_i \cdot \nabla \phi_j d\Omega, \quad (6.1)$$

where ϵ_r represents the element of electric permittivity tensor and ϕ_i and ϕ_j are the electric potentials obtained when an electric voltage is applied in the x_i and x_j

directions, respectively (Fig.6.1), where $ij=11, 12, 21, 22$, and $\bar{\phi}_i$ denotes the conjugate complex number of ϕ_i . On the other hand, the mutual energy accumulated in the homogenized cell is given as

$$Q_{ij}^H = \frac{1}{2} \epsilon_{\text{eff},ij} V_i^0 V_j^0 V, \quad (6.2)$$

where V is the volume and V_i^0 is the applied voltage defined in a boundary condition that produce homogeneous fields. By assuming $Q_{ij} = Q_{ij}^H$, the elements of the effective permittivity tensor, $\epsilon_{\text{eff},ij}$ in Eq.(6.2), are determined as follows.

$$\epsilon_{\text{eff}} = \begin{bmatrix} \epsilon_{\text{eff},11} & \epsilon_{\text{eff},12} \\ \epsilon_{\text{eff},21} & \epsilon_{\text{eff},22} \end{bmatrix}, \quad (6.3)$$

where

$$\epsilon_{\text{eff},11} = \frac{1}{V_1^0{}^2 V} \int_{\Omega} \epsilon_r(\mathbf{x}) \nabla \bar{\phi}_1(\mathbf{x}) \cdot \nabla \phi_1(\mathbf{x}) d\Omega \quad (6.4)$$

$$\epsilon_{\text{eff},22} = \frac{1}{V_2^0{}^2 V} \int_{\Omega} \epsilon_r(\mathbf{x}) \nabla \bar{\phi}_2(\mathbf{x}) \cdot \nabla \phi_2(\mathbf{x}) d\Omega \quad (6.5)$$

$$\epsilon_{\text{eff},12} = \frac{1}{V_1^0 V_2^0 V} \int_{\Omega} \epsilon_r(\mathbf{x}) \nabla \bar{\phi}_2(\mathbf{x}) \cdot \nabla \phi_1(\mathbf{x}) d\Omega \quad (6.6)$$

$$\epsilon_{\text{eff},21} = \frac{1}{V_1^0 V_2^0 V} \int_{\Omega} \epsilon_r(\mathbf{x}) \nabla \bar{\phi}_1(\mathbf{x}) \cdot \nabla \phi_2(\mathbf{x}) d\Omega, \quad (6.7)$$

The electric potential ϕ_i are obtained by solving the following governing equation using the FEM.

$$\nabla \cdot [\epsilon_r(\mathbf{x}) \nabla \phi_i(\mathbf{x})] = 0, \quad (6.8)$$

The left and right boundaries, and the upper and lower boundaries are, respectively, set to a periodic boundary condition as follows, in the case when an electric voltage is applied in the horizontal direction (Fig.6.1(a)).

$$\phi_1(x_1, x_2) = \phi_1(x_1 - L_1, x_2) + V_1^0 \quad \text{on } \Gamma_3 \quad (6.9)$$

$$\phi_1(x_1, x_2) = \phi_1(x_1, x_2 - L_2) \quad \text{on } \Gamma_4, \quad (6.10)$$

where V_1^0 is an applied voltage in the horizontal direction and, L_1 and L_2 are the unit cell lengths in the x_1 and x_2 directions, respectively.

The left and right boundaries, and the upper and lower boundaries are, respectively, set to a periodic boundary condition as follows, in the case when an electric voltage is applied in the vertical direction (Fig.6.1(b)).

$$\phi_2(x_1, x_2) = \phi_2(x_1 - L_1, x_2) \quad \text{on } \Gamma_3 \quad (6.11)$$

$$\phi_2(x_1, x_2) = \phi_2(x_1, x_2 - L_2) + V_2^0 \quad \text{on } \Gamma_4, \quad (6.12)$$

where V_2^0 is an applied voltage in the vertical direction. The effective permittivities are obtained by substituting obtained electric potentials into Eq.(6.4)-(6.7).

6.2.2 Design variables

In this work, the distribution of dielectric material inside the fixed design domain is expressed using relative element densities $\tilde{\rho}_e \in [0, 1]$. That is, the relative electric permittivity ϵ_r inside the fixed design domain is defined using $\tilde{\rho}_e$ following the concept of the SIMP method.

$$\epsilon_r = (\epsilon_1 - \epsilon_0) \tilde{\rho}_e^p + \epsilon_0, \quad (6.13)$$

where ϵ_1 is the relative permittivity of the dielectric material, ϵ_0 is the relative permittivity of the background material, and p is a penalization parameter. For problems that have an active volume constraint, a large value of $p > 1$ penalizes intermediate element densities, since the volume is proportional to $\tilde{\rho}_e$ but the permittivity values fall below the line of proportionality. The parameter $p \geq 3$ is typically used in structural optimization problems, since the bulk modulus and shear modulus of interpolated stiffness tensor are required to satisfy the Hashin-Shtrikman bounds, which isotropic materials should satisfy [102]. Here, $p = 3$ is used in the following numerical examples. It is because the profile of interpolated permittivity by $p = 3$ respect to the element density is similar to, even though it is not the same as, that of the Hashin-Shtrikman bounds when the loss of dielectric materials is small.

To ensure that the optimal design is independent of the mesh, and to obtain a clear optimal configuration, the Heaviside projection filter is used in this work [24]. Using this filter, the relative element densities $\tilde{\rho}_e$ can be computed as shown in the following procedures. First, intermediate variables μ_e are computed using design variables ρ_e that are typically located in nodes or the center of the finite elements, as follows.

$$\mu_e = \sum_{j \in N^e} \rho_e w / \sum_{j \in N^e} w, \quad (6.14)$$

where N^e is the neighborhood of elements specified by a circle with the given filter radius, and w is a weighting function that imposes higher weights for closer design

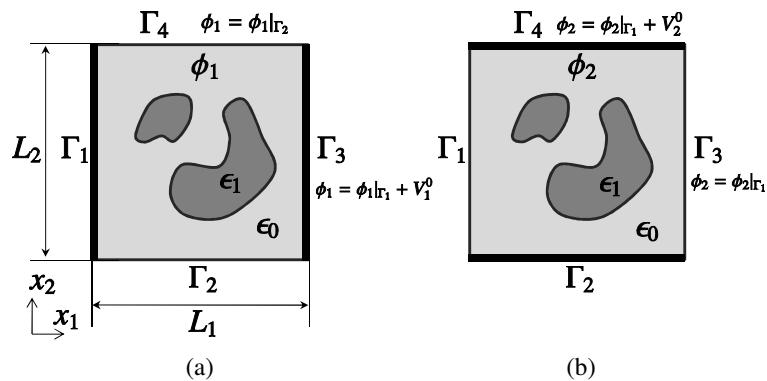


Figure 6.1: Analysis model and boundary conditions for the case of an electric voltage applied in (a) the horizontal direction, and (b) the vertical direction.

variables. The relative element densities are then obtained using the Heaviside function as follows.

$$\tilde{\rho}_e = H_s(\mu_e) = 1 - e^{-\beta\mu_e} + \mu_e e^{-\beta}, \quad (6.15)$$

where β is a parameter that adjusts the curvature of the Heaviside function. To ensure stable convergence of the optimization, the magnitude of parameter β is gradually increased from 1 to sufficiently large value (e.g. 500) during the optimization procedure. Published references provide more details concerning the use of density filters [12, 24].

6.2.3 Optimization problem

Here, the formulation of the optimization problem is discussed that will be applied to the dielectric material design problems. The purpose of the optimization is to obtain layouts of dielectric material that achieve the desired dielectric permittivity. Thus, the objective of the optimization problem can be formulated as to minimize the square of the difference between the target permittivity and obtained effective permittivity. The optimization problem is described as follows.

$$\inf_{\rho_e} \quad F(\rho_e) = \log \sum_{ij} |\epsilon_{\text{eff},ij}^* / \epsilon_{\text{tar},ij}^* - 1|^2 \quad (6.16)$$

$$\text{subject to} \quad G = \frac{1}{V_D} \int_D \tilde{\rho}_e d\Omega - V_{\text{max}} \leq 0 \quad (6.17)$$

$$\text{Poisson equation: Eq.(6.8)} \quad (6.18)$$

$$\text{Boundary conditions: Eqs.(6.9)–(6.12)} \quad (6.19)$$

where ϵ_{eff} and ϵ_{tar} respectively represent the effective permittivity and the target permittivity. The * denotes the use of either ' or '' that apply to the real or imaginary part of the effective permittivity, respectively. The subscript $ij = 11, 12, 21, 22$ denotes the elements of the dielectric tensor. V_D is the volume of the fixed design domain and V_{max} is the upper limit of volume fraction. Note that the logarithm of the sum of the differences is used as an objective functional to obtain better numerical scaling. When the differences become smaller during optimization, the magnitude of the sensitivities also diminish, which slows convergence.

6.2.4 Sensitivity analysis

The sensitivities of the objective functional for the gradient-based topology optimization are obtained using the adjoint variable method (AVM). The governing equation is discretized and solved using the FEM. The discretized governing equation can be described as follows.

$$\mathbf{S}\phi_i = \mathbf{f}, \quad (6.20)$$

where \mathbf{S} is the stiffness matrix and \mathbf{f} is the load vector. The sensitivity of the objective functional F is then given as

$$\frac{dF}{d\rho} = \frac{\partial F}{\partial \rho} + 2Re \left(\lambda^T \left(\frac{\partial \mathbf{S}}{\partial \rho} \phi_i - \frac{\partial \mathbf{f}}{\partial \rho} \right) \right), \quad (6.21)$$

where λ is an adjoint variable. The adjoint variable λ is obtained by solving following adjoint problem.

$$\mathbf{S}^T \lambda = -\frac{\partial F}{\partial \phi_i}. \quad (6.22)$$

With A as the integrand of the objective functional, the derivative of the objective functional with respect to the state variable $\frac{\partial F}{\partial \phi_i}$ can be computed directly as follows.

$$\frac{\partial F}{\partial \phi_i} = \frac{1}{V^2} \int_D \left(\frac{\partial A}{\partial \phi_i} + \frac{\partial A}{\partial \nabla \phi_i} \cdot \nabla \right) dD, \quad (6.23)$$

where,

$$\frac{\partial A}{\partial \phi_i} = 0 \quad (6.24)$$

$$\frac{\partial A}{\partial \nabla \phi_i} = \epsilon_r \nabla \bar{\phi}_i. \quad (6.25)$$

In Eq.(6.21), $\frac{\partial \mathbf{f}}{\partial \rho} = 0$ since the applied voltage is independent with respect to the design variables. Computation of the derivative using Eq.(6.21) can be simplified by following Olesen et al.'s implementation technique [43].

6.3 Theoretical bounds

In this section, the theoretical bounds of the effective permittivity for two-phase dielectric composites are discussed.

6.3.1 Review of theoretical bounds of effective permittivity for two-phase composite material

Bounds of complex value effective permittivity

Let ϵ_{eff} be the effective permittivity of a two-phase composite with complex dielectric constants ϵ_1 and ϵ_2 . The analytical bounds of ϵ_{eff} can be illustrated as shown in Fig.6.2. Here, as an example, the dielectric constants for phases 1 and 2 are set to $\epsilon_1 = -2 + 3i$ and $\epsilon_2 = 1 + 1i$, respectively, and the volume fraction for phase 1 is set to 0.6 for bounds Ω' , Ω'' , (the same example as chap.27 in [197]). These bounds are obtained as follows. Note that for composites made from a single dielectric material and air, the bounds are obtained by setting $\epsilon_2 = 1$.

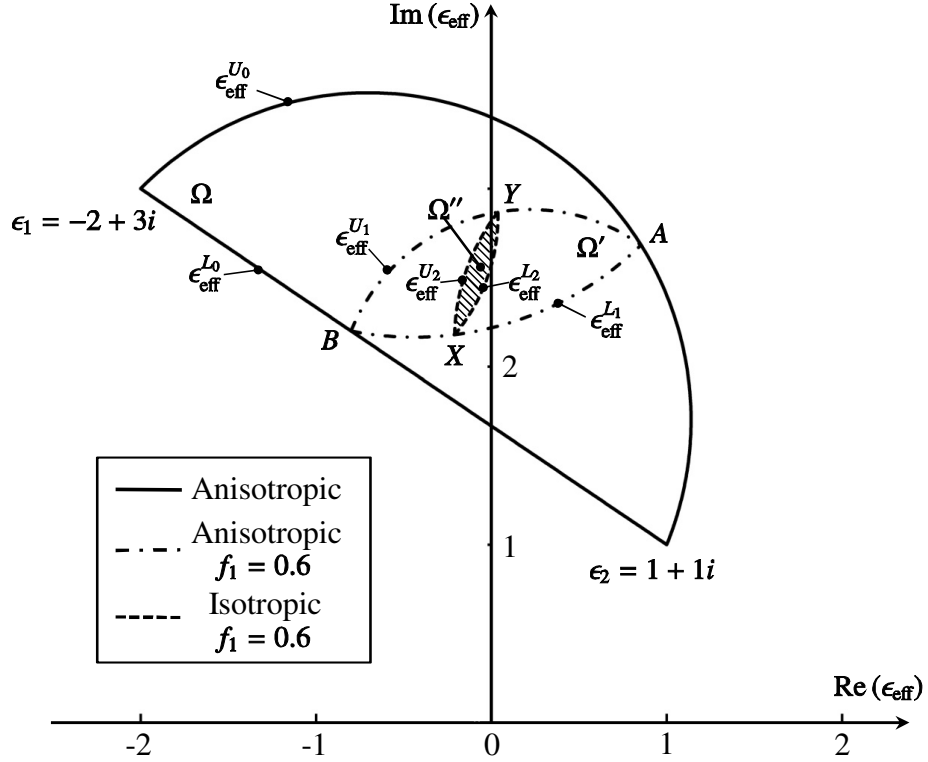


Figure 6.2: Bounds of effective permittivity for two constituent materials with properties $\epsilon_1 = -2 + 3i$ and $\epsilon_2 = 1 + i$. In the absence of specific information concerning the dielectric materials, the effective permittivity is confined to the region Ω . If the volume fraction of phase 1 is $f_1 = 0.6$, the effective permittivity is confined to the region Ω' . Furthermore, if the composite is a two-dimensional isotropic material, the effective permittivity is confined to the region Ω'' .

In the absence of specific information concerning the topological distribution of the constituent, the corresponding bounds are the Wiener harmonic and arithmetic mean bounds expressed by following equations.

$$\epsilon_{\text{eff}}^{U_0}(v) = \left(\frac{v}{\epsilon_1} + \frac{1-v}{\epsilon_2} \right)^{-1} \quad (6.26)$$

$$\epsilon_{\text{eff}}^{L_0}(w) = w\epsilon_1 + (1-w)\epsilon_2, \quad (6.27)$$

as parameters v and w are varied from 0 to 1.

The boundary $\epsilon_{\text{eff}}^{U_0}(v)$ represents the composite as a laminate material oriented so that the applied field V^0 is parallel to the direction of lamination (see Fig.6.3(a)). On the other hand, boundary $\epsilon_{\text{eff}}^{L_0}(w)$ represents the composite as a laminate material oriented so that the applied field V^0 is orthogonal to the direction of lamination (see Fig.6.3(b)).

In addition, if the volume fraction of phase 1, f_1 , is known, the effective permittivities at points A and B on the above boundaries $\epsilon_{\text{eff}}^{U_0}$ and $\epsilon_{\text{eff}}^{L_0}$ in Fig.6.2 are determined

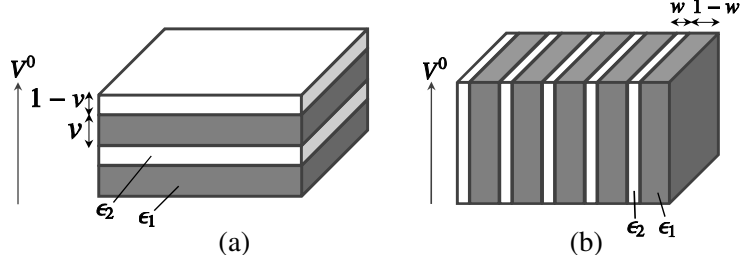


Figure 6.3: Laminate model.

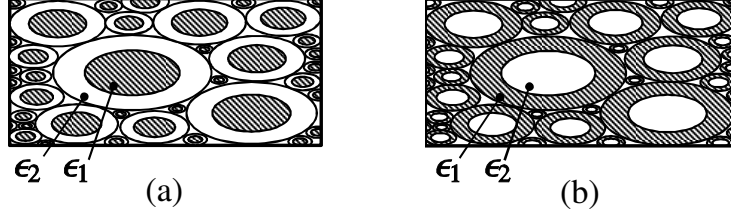


Figure 6.4: Cross section of the coated elliptic assemblage.

as follows.

$$\epsilon_{\text{eff}}^A = \left(\frac{f_1}{\epsilon_1} + \frac{f_2}{\epsilon_2} \right)^{-1} \quad (6.28)$$

$$\epsilon_{\text{eff}}^B = f_1 \epsilon_1 + f_2 \epsilon_2, \quad (6.29)$$

where $f_2 = 1 - f_1$ is the volume fraction of phase 2. Tighter boundaries are expressed by an arc joining the point A and B that when extended passes through ϵ_2 and an arc that passes through ϵ_1 , that can be expressed by the following equations as the parameters v and w are varied from 0 to 1.

$$\epsilon_{\text{eff}}^{U_1} = \epsilon_2 + \frac{f_1 \epsilon_2 (\epsilon_1 - \epsilon_2)}{\epsilon_2 + v f_2 (\epsilon_1 - \epsilon_2)} \quad (6.30)$$

$$\epsilon_{\text{eff}}^{L_1} = \epsilon_1 + \frac{f_2 \epsilon_1 (\epsilon_2 - \epsilon_1)}{\epsilon_1 + w f_1 (\epsilon_2 - \epsilon_1)}. \quad (6.31)$$

The boundary $\epsilon_{\text{eff}}^{U_1}(v)$ represents an elliptic assemblage with a core of component 1 surrounded by component 2 (see Fig.6.4(a)). On the other hand, the boundary $\epsilon_{\text{eff}}^{L_1}(w)$ represents an elliptic assemblage with a core of component 2 surrounded by component 1 (see Fig.6.4(b)). The major and minor diameters of the phase 1 structure, D_{1a} , D_{1b} , and of the phase 2 structure, D_{2a} , D_{2b} , have following relationship since the inner and outer ellipses are confocal [199].

$$D_{2a}^2 - D_{2b}^2 = D_{1a}^2 - D_{1b}^2. \quad (6.32)$$

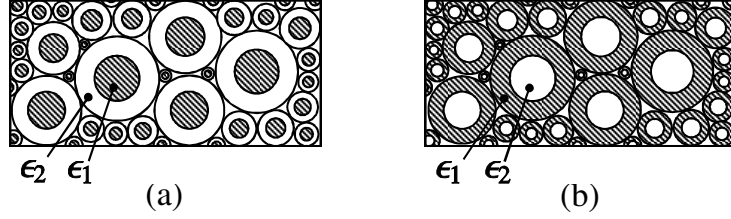


Figure 6.5: Cross section of the coated cylindrical assemblage.

Therefore, volume fraction f_1 and parameter v are described as follows.

$$f_1 = \frac{D_{1a}D_{1b}}{D_{2a}D_{2b}} \quad (6.33)$$

$$v = \frac{D_{1a}D_{2a}}{D_{1a}D_{2a} + D_{1b}D_{2b}}. \quad (6.34)$$

Moreover, if it is known that the composite is a two-dimensional isotropic material, then the effective permittivities at points X and Y on the above boundaries, ϵ_{eff}^U and ϵ_{eff}^L , respectively, can be defined using the following equation.

$$\epsilon_{\text{eff}}^X = \epsilon_1 + \frac{2f_2\epsilon_1(\epsilon_2 - \epsilon_1)}{2\epsilon_1 + f_1(\epsilon_2 - \epsilon_1)} \quad (6.35)$$

$$\epsilon_{\text{eff}}^Y = \epsilon_2 + \frac{2f_1\epsilon_2(\epsilon_1 - \epsilon_2)}{2\epsilon_2 + f_2(\epsilon_1 - \epsilon_2)}. \quad (6.36)$$

The tighter boundaries are expressed by an arc joining the point X and Y that when extended passes through ϵ_2 and an arc that passes through ϵ_1 . These bounds are expressed by following equations as the parameters v and w are varied from 0 to 1.

$$\epsilon_{\text{eff}}^{U_2} = \epsilon_{\text{eff}}^X + \frac{1 - v}{1/(\epsilon_{\text{eff}}^Y - \epsilon_{\text{eff}}^X) + v/(\epsilon_{\text{eff}}^X - \epsilon_2)} \quad (6.37)$$

$$\epsilon_{\text{eff}}^{L_2} = \epsilon_{\text{eff}}^X + \frac{1 - w}{1/(\epsilon_{\text{eff}}^Y - \epsilon_{\text{eff}}^X) + w/(\epsilon_{\text{eff}}^X - \epsilon_1)}. \quad (6.38)$$

The boundary $\epsilon_{\text{eff}}^{U_2}(v)$ represents the composite as a cylindrical assemblage with phase 1 as core material and phase 2 as the material surrounding the core (see Fig.6.5(a)). Similarly, the boundary $\epsilon_{\text{eff}}^{L_2}(w)$ represents the composite as a cylindrical assemblage with phase 2 as core material and phase 1 as the material surrounding the core (see Fig.6.5(b)).

Apart from the elliptic and cylindrical assemblages [106] there exist a number of other microgeometries that can be shown to realize any material properties on (and within) the bounds. These include so-called rank- n laminates [200–203] and hybrid structures [204]. Excluding multiple microstructural length-scales, so-called Vigdergauz structures have also been shown to attain the bounds in certain cases [205–207]. Here this work is limited to one length-scale and easily manufacturable microstructures and show that Vigdergauz-like structures are solutions to a variety of different inverse design problems with real and complex effective properties.

Bounds of real value effective permittivity

The bounds of real value effective permittivity versus the volume fraction f_1 is obtained as follows. In the absence of specific information, $\epsilon_{\text{eff}}^A(f_1)$ in Eq.(6.28) is the lower bound and $\epsilon_{\text{eff}}^B(f_1)$ in Eq.(6.29) is the upper bound of the effective permittivity of the composite materials versus volume fraction f_1 . In addition, if it is known that the composite is isotropic material, the point $\epsilon_{\text{eff}}^X(f_1)$ in Eq.(6.35) and $\epsilon_{\text{eff}}^Y(f_1)$ in Eq.(6.36) are the upper and lower bounds of the effective permittivity of the composite materials versus volume fraction f_1 .

6.3.2 Bounds of real value effective permittivity in principal direction

Based on the description in previous subsection, the bounds of the real value anisotropic effective permittivity in principal direction when that of the other(s) principal direction is/are known can be derived as follows.

Two-dimensional case

From Eqs.(6.34),

$$1 - v = \frac{D_{1b}D_{2b}}{D_{1a}D_{2a} + D_{1b}D_{2b}} \quad (6.39)$$

Eq.(6.34) and Eq.(6.39) are symmetric with respect to the principal directions, a and b, so $\epsilon(v)$ and $\epsilon(1-v)$ show the effective permittivities of the two principal directions. If it is known that the permittivity value of one of the principal directions and let it be ϵ^* , the parameter v and w in Eqs.(6.30) and (6.31) is obtained as,

$$v^* = \frac{f_1\epsilon_2(\epsilon_1 - \epsilon_2) - \epsilon_2(\epsilon^* - \epsilon_2)}{f_2(\epsilon_1 - \epsilon_2)(\epsilon^* - \epsilon_2)} \quad (6.40)$$

$$w^* = \frac{f_2\epsilon_1(\epsilon_2 - \epsilon_1) - \epsilon_1(\epsilon^* - \epsilon_1)}{f_1(\epsilon_2 - \epsilon_1)(\epsilon^* - \epsilon_1)}. \quad (6.41)$$

The following bounds are then derived, substituting $1 - v^*$ and $1 - w^*$ into Eqs.(6.30) and (6.31).

$$\epsilon_{\text{eff}}^L = \epsilon_2 + \frac{f_1\epsilon_2(\epsilon_1 - \epsilon_2)}{\epsilon_2 + (1 - v^*)f_2(\epsilon_1 - \epsilon_2)} \quad (6.42)$$

$$\epsilon_{\text{eff}}^U = \epsilon_1 + \frac{f_2\epsilon_1(\epsilon_2 - \epsilon_1)}{\epsilon_1 + (1 - w^*)f_1(\epsilon_2 - \epsilon_1)}. \quad (6.43)$$

Three-dimensional case

By similar argument, the bounds of the anisotropic effective permittivity in the principal direction for three-dimensional case can be derived, when those of the other

principal directions are known. for the ellipsoid with a core of component 1 and surrounded by component 2, three principal permittivities are $\epsilon_{\text{eff}}^X(u)$, $\epsilon_{\text{eff}}^X(v)$ and $\epsilon_{\text{eff}}^X(w)$, where $u + v + w = 1$ [199]. If the permittivity values of the other principal directions, ϵ_{22}^* , ϵ_{33}^* , are known, the parameter v and w can be obtained as,

$$v^* = \frac{f_1 \epsilon_2 (\epsilon_1 - \epsilon_2) - \epsilon_2 (\epsilon_{22}^* - \epsilon_2)}{f_2 (\epsilon_1 - \epsilon_2) (\epsilon_{22}^* - \epsilon_2)} \quad (6.44)$$

$$w^* = \frac{f_1 \epsilon_2 (\epsilon_1 - \epsilon_2) - \epsilon_2 (\epsilon_{33}^* - \epsilon_2)}{f_2 (\epsilon_1 - \epsilon_2) (\epsilon_{33}^* - \epsilon_2)} \quad (6.45)$$

Then the following bounds are derived, substituting $1 - v^* - w^*$ into Eqs.(6.30) and (6.31).

$$\epsilon_{\text{eff}}^L = \epsilon_2 + \frac{f_1 \epsilon_2 (\epsilon_1 - \epsilon_2)}{\epsilon_2 + (1 - v^* - w^*) f_2 (\epsilon_1 - \epsilon_2)}$$

$$\epsilon_{\text{eff}}^U = \epsilon_1 + \frac{f_2 \epsilon_1 (\epsilon_2 - \epsilon_1)}{\epsilon_1 + (1 - v^* - w^*) f_1 (\epsilon_2 - \epsilon_1)}.$$

6.4 Numerical implementation

6.4.1 Optimization algorithm

The optimization flowchart is shown in Fig.6.6. First, the design variables are initialized. Next, the filtered design variable $\tilde{\rho}_e$ is computed using the projection function and the Heaviside function. Objective and constraint functionals are then computed using the FEM. If the objective functional has converged, the optimization procedure is terminated. If not, the sensitivities of the objective and constraint functionals are computed using the AVM. The design variables are then updated using the method of moving asymptotes (MMA) [111] and the process returns to the second step.

6.5 Numerical examples

Numerical examples are now presented to demonstrate the validity and capability of our method for the design of microstructures based on dielectric materials. First, the asymptotic expansion-based approach and energy-based approach used to obtain effective permittivity values for the dielectric composites considered here, are compared. The following design examples include the design of an isotropic material, an anisotropic material, an anisotropic material with a nonzero off-diagonal terms, and an anisotropic material with loss. The optimization target in all examples is to minimize the square of the difference between the effective permittivity and a target value. The design domain is discretized using 200×200 square elements. A circular rod shape with a volume fraction of 50% is used as the initial configuration unless otherwise specified in the following examples.

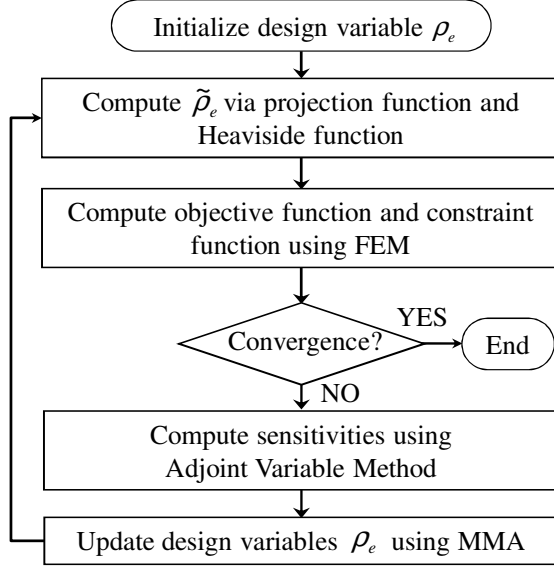


Figure 6.6: Flowchart of optimization algorithm.

6.5.1 Comparison of methods to obtain effective permittivity values

Here, the asymptotic expansion-based approach and the energy-based approach are compared to show the validity of the energy-based approach used in this paper to obtain effective permittivity values for the dielectric materials. Figure 6.7 shows a comparison of the effective permittivity values obtained using both approaches for composites made from a single dielectric material with $\epsilon_1=100$ and air, ($\epsilon_0=1$). Four inclusion shapes with volume fractions of 50% are considered for the comparison. That is, inclusions with a cylindrical hole (Fig.6.7(a)), cylindrical inclusions (Fig.6.7(b)), vertically oriented laminates (Fig.6.7(c)), and vertically oriented laminates rotated 26.57 degrees in the counterclockwise direction (Fig.6.7(d)) are considered. The effective permeability values obtained using analytic methods are also compared for reference. For a square lattice with cylindrical holes and a lattice with cylindrical inclusions, the Rayleigh formula, defined as follows [208, 209], provides sufficient accuracy.

$$\epsilon_{\text{eff}} = \epsilon_e + \frac{2p\epsilon_e}{\frac{\epsilon_i + \epsilon_e}{\epsilon_i - \epsilon_e} - p - \frac{\epsilon_i - \epsilon_e}{\epsilon_i + \epsilon_e}(0.3058p^4 + 0.0134p^8)}, \quad (6.46)$$

where ϵ_i is the permittivity of the cylindrical component, p is its volume fraction, and ϵ_e is the permittivity of the background material. For laminate inclusions, the effective permittivity can be obtained using the Wiener harmonic and arithmetic means (Eqs.(6.26)(6.27)).

$$\epsilon_{\text{eff}} = \begin{bmatrix} 50.5 & 0.0 \\ 0.0 & 1.980 \end{bmatrix}. \quad (6.47)$$

The effective permittivity values for vertically oriented laminates rotated 26.57 degrees in the counterclockwise direction are obtained by rotating the effective permittivity tensor of the vertically oriented laminates as follows.

$$\epsilon_{\text{eff}} = \begin{bmatrix} \cos\theta & \sin\theta \\ -\sin\theta & \cos\theta \end{bmatrix}^T \begin{bmatrix} 50.5 & 0.0 \\ 0.0 & 1.980 \end{bmatrix} \begin{bmatrix} \cos\theta & \sin\theta \\ -\sin\theta & \cos\theta \end{bmatrix} = \begin{bmatrix} 40.796 & 19.408 \\ 19.408 & 11.684 \end{bmatrix}, \quad (6.48)$$

where θ is set to 26.57 degrees. Note that analytic methods are valid only for certain inclusion shapes.

For both the asymptotic expansion-based and energy-based approaches, the effective permittivity values are obtained using the FEM. Here, the analysis domain is discretized using 200×200 square elements. The effective permittivity values using the asymptotic expansion-based approach are obtained via following equation.

$$\epsilon_{\text{eff},ij}^{AS} = \frac{1}{Y} \int_{\Omega} \epsilon_r(\mathbf{x}) \left(\delta_{ij} + \frac{\partial \chi_j}{\partial x_i} \right) d\Omega, \quad (6.49)$$

where Y is the unit cell length and χ_j is obtained by solving following equation with periodic boundary conditions imposed.

$$-\nabla \cdot (\epsilon_r \nabla \chi_j) = \frac{\partial \epsilon_r}{\partial x_j}. \quad (6.50)$$

As shown in Fig.6.7, the effective permittivity values obtained using the analytic methods and the asymptotic expansion-based and energy-based approaches are very close for the above four inclusion shapes, demonstrating the validity of the energy-based approach used in this paper.

6.5.2 Two-dimensional problems: isotropic material design

Here, the design of an isotropic material are discussed. The target value is set to $\epsilon_{\text{tar},11} = \epsilon_{\text{tar},22} = 70$. The relative permittivity of the dielectric material is set to 100 and the relative permittivity of the background material is set to 1. The maximum volume fraction is set to 82.5%, a value chosen from theoretical bounds that will be discussed below.

The optimization results are shown in Fig.6.8. The obtained effective permittivity is

$$\epsilon_{\text{eff}} = \begin{bmatrix} 70.00 & 0.00 \\ 0.00 & 70.00 \end{bmatrix}. \quad (6.51)$$

The permittivity values and optimal configuration show that the optimization successfully obtained a clear structure that provides the target permittivity.

Figure 6.10 shows the theoretical bounds for the effective permittivity of composite materials composed of the above-mentioned dielectric and background materials, where the horizontal axis shows the volume fraction of the dielectric material and the vertical axis shows the effective permittivity of the composite material. The theoretical bounds for anisotropic and isotropic materials are shown by solid and dashed


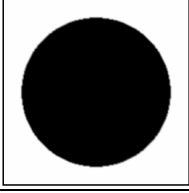
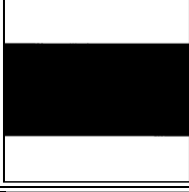

	Analytical method	Asymptotic expansion-based approach $\epsilon_{\text{eff}}^{\text{AS}} = \begin{bmatrix} \epsilon_{\text{eff},11}^{\text{AS}} & \epsilon_{\text{eff},12}^{\text{AS}} \\ \epsilon_{\text{eff},21}^{\text{AS}} & \epsilon_{\text{eff},22}^{\text{AS}} \end{bmatrix}$	Energy-based approach $\epsilon_{\text{eff}} = \begin{bmatrix} \epsilon_{\text{eff},11} & \epsilon_{\text{eff},12} \\ \epsilon_{\text{eff},21} & \epsilon_{\text{eff},22} \end{bmatrix}$
(a) 	Rayleigh formula $\begin{bmatrix} 33.396 & - \\ - & 33.396 \end{bmatrix}$	$\begin{bmatrix} 32.968 & 0.000 \\ 0.001 & 32.980 \end{bmatrix}$	$\begin{bmatrix} 33.032 & 0.000 \\ 0.000 & 33.032 \end{bmatrix}$
(b) 	Rayleigh formula $\begin{bmatrix} 2.994 & - \\ - & 2.994 \end{bmatrix}$	$\begin{bmatrix} 3.028 & 0.000 \\ 0.000 & 3.034 \end{bmatrix}$	$\begin{bmatrix} 3.298 & 0.000 \\ 0.000 & 3.298 \end{bmatrix}$
(c) 	Wiener harmonic and arithmetic means $\begin{bmatrix} 50.5 & 0.0 \\ 0.0 & 1.980 \end{bmatrix}$	$\begin{bmatrix} 50.348 & 0.000 \\ 0.000 & 1.990 \end{bmatrix}$	$\begin{bmatrix} 50.5 & 0.000 \\ 0.000 & 1.980 \end{bmatrix}$
(d) 	Wiener harmonic and arithmetic means $\begin{bmatrix} 40.796 & 19.408 \\ 19.408 & 11.684 \end{bmatrix}$	$\begin{bmatrix} 40.329 & 19.070 \\ 19.159 & 11.771 \end{bmatrix}$	$\begin{bmatrix} 40.517 & 19.256 \\ 19.256 & 11.623 \end{bmatrix}$

Figure 6.7: Comparison of effective permittivity values obtained using asymptotic expansion-based and energy-based approaches for composites made from a single dielectric material (black: $\epsilon_1=100$) and air (white: $\epsilon_0=1$): (a) inclusions with a cylindrical hole, (b) cylindrical inclusions, (c) vertically oriented laminates and (d) vertically oriented laminates rotated 26.57 degrees in the counterclockwise direction.

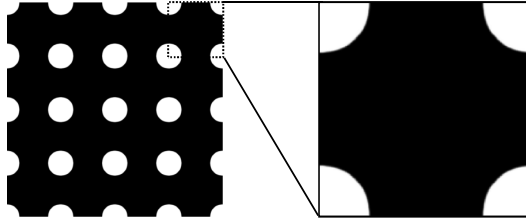


Figure 6.8: Optimized configuration of isotropic material design problem for volume fraction $V_{\text{max}} = 0.825$ of $\epsilon_1 = 100$ (black), and $\epsilon_0 = 1$ (white). The targets are $\epsilon_{\text{tar},11} = \epsilon_{\text{tar},22} = 70$ and the achieved properties are $\epsilon_{\text{eff},11} = \epsilon_{\text{eff},22} = 70$.

lines, respectively. The effective permittivity of the optimized configuration is shown as the black square in Fig.6.10 for comparison with the theoretical bound curve, and demonstrates that the obtained result is in good agreement with theoretical bounds.

6.5.3 Two-dimensional problems: anisotropic material design

Next, the design of an anisotropic material is considered. The target value is set to $\epsilon_{\text{tar},11} = 45$, and $\epsilon_{\text{tar},22} = 70$. The relative permittivity of the dielectric material is set to 100 and the relative permittivity of the background material is set to 1. The maximum volume fraction is set to 76%, a value chosen from theoretical bounds.

The optimization results are shown in Fig.6.9. The obtained effective permittivity is

$$\epsilon_{\text{eff}} = \begin{bmatrix} 45.00 & 0.00 \\ 0.00 & 70.00 \end{bmatrix}. \quad (6.52)$$

The permittivity values and optimal configuration show that the optimization obtained the target permittivity for the anisotropic material to a highly practical extent. Figure 6.10 shows the theoretical bounds for the effective permittivity. The effective permittivity of the optimized configuration is shown as the black dot in Fig.6.10 for comparison with the theoretical bound curve. The highly sloped dot-dashed line plots the upper limit of the permittivity of the anisotropic material versus the volume fraction when ϵ_{22} is 70. Similarly, the dot-dashed line that is partially obscured by solid line in the lower right corner of the graph shows the lower limit of the permittivity of the anisotropic material versus the volume fraction when ϵ_{22} is 70. The black dot indicates the effective permittivity value of obtained dielectric materials as optimization results and that the obtained result is in good agreement with theoretical bounds.

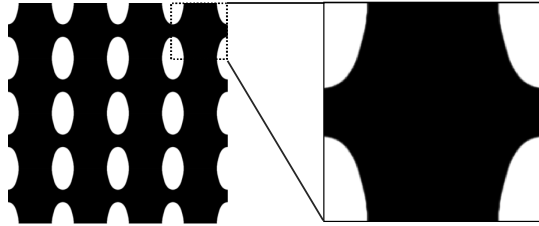


Figure 6.9: Optimized configuration of the anisotropic material design problem for volume fraction $V_{\text{max}} = 0.76$ of $\epsilon_1 = 100$ (black), and $\epsilon_0 = 1$ (white). The targets are $\epsilon_{\text{tar},11} = 45$ and $\epsilon_{\text{tar},22} = 70$ and the achieved properties are $\epsilon_{\text{eff},11} = 45.00$ and $\epsilon_{\text{eff},22} = 70.00$.

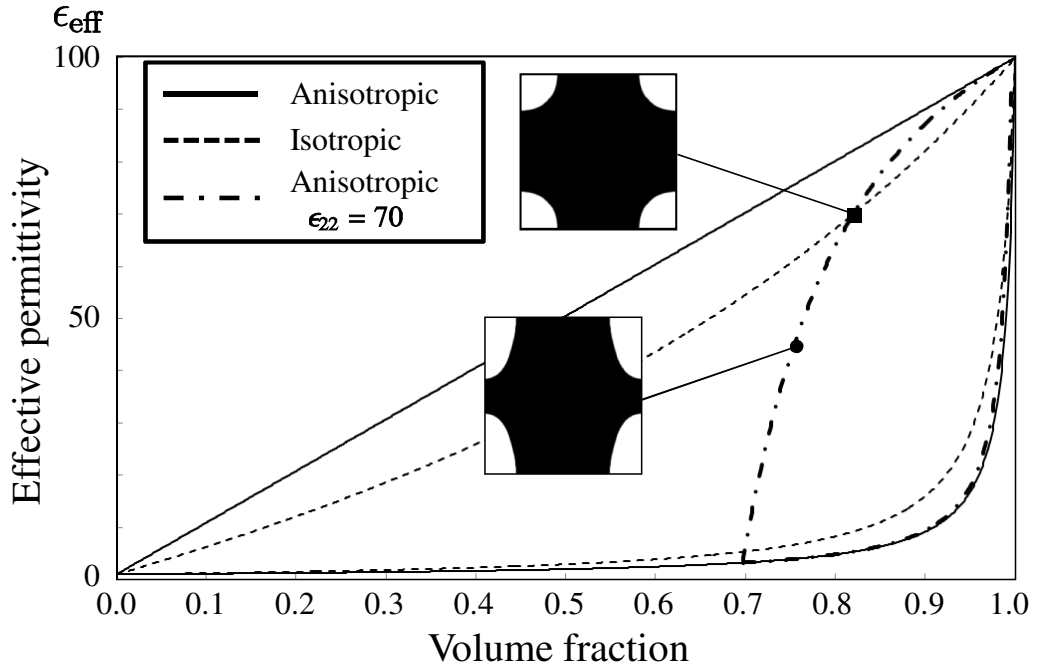


Figure 6.10: Theoretical bounds for isotropic and anisotropic material design problems with properties $\epsilon_1 = 100$ and $\epsilon_0 = 1$. The solid and dashed lines show the theoretical bounds for isotropic and anisotropic material, respectively. The dot-dashed line plots the upper and lower limit of the permittivity of the anisotropic material versus the volume fraction when $\epsilon_{22} = 70$. The effective permittivity of the optimized configuration, $\epsilon_{\text{eff},11} = \epsilon_{\text{eff},22} = 70.00$, of Subsection 6.5.2 is shown as the black square, and the effective permittivity of the optimized configuration, $\epsilon_{\text{eff},11} = 45.00$ and $\epsilon_{\text{eff},22} = 70.00$, of Subsection 6.5.3 is shown as the black dot, for comparison with the theoretical bound curve.

6.5.4 Two-dimensional problems: anisotropic material design with nonzero off-diagonal terms

Here, the design of an anisotropic material with nonzero off-diagonal terms is considered. The target dielectric permittivity is set to

$$\epsilon_{\text{tar}} = \begin{bmatrix} \epsilon_a + \delta \cos 2\phi & \delta \sin 2\phi \\ \delta \sin 2\phi & \epsilon_a - \delta \cos 2\phi \end{bmatrix}, \quad (6.53)$$

where ϕ is set to 15 degrees and ϵ_a and δ are respectively set to 125 and 40. That is,

$$\epsilon_{\text{tar}} = \begin{bmatrix} 159.64 & -20 \\ -20 & 90.36 \end{bmatrix}. \quad (6.54)$$

The relative permittivity of the dielectric material is set to 240 and the relative permittivity of the background material is set to 20. The maximum volume fraction is set to 69%, a value chosen from theoretical bounds.

The optimization results are shown in Fig.6.11. The obtained effective permittivity is

$$\epsilon_{\text{eff}} = \begin{bmatrix} 159.63 & -20 \\ -20 & 90.36 \end{bmatrix}. \quad (6.55)$$

The results show the optimization successfully obtained an optimal configuration that provides the desired permittivity for an anisotropic material that has nonzero off-diagonal terms.

Figure 6.12 shows the theoretical bounds for the effective permittivity. Here, the obtained effective permittivities in the principal direction are considered, namely,

$$\epsilon_{\text{eff}} = \begin{bmatrix} 164.99 & 0.00 \\ 0.00 & 85.00 \end{bmatrix}. \quad (6.56)$$

The effective permittivity of the optimized configuration is shown as the black dot for comparison with the theoretical bound curve. The dot-dashed lines plot the

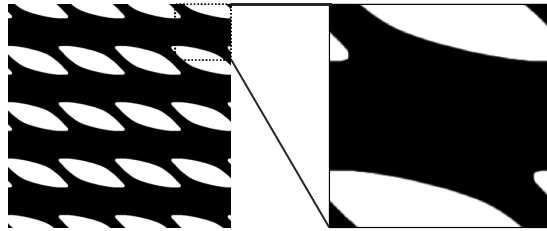


Figure 6.11: The optimized configuration of the anisotropic material design problem with nonzero off-diagonal terms for volume fraction $V_{\text{max}} = 0.69$ of $\epsilon_1 = 240$ (black), and $\epsilon_0 = 20$ (white). The targets are $\epsilon_{\text{tar},11} = 159.64$, $\epsilon_{\text{tar},22} = 90.36$ and $\epsilon_{\text{tar},12} = \epsilon_{\text{tar},21} = -20.00$ and the achieved properties are $\epsilon_{\text{eff},11} = 159.63$, $\epsilon_{\text{eff},22} = 90.36$ and $\epsilon_{\text{eff},12} = \epsilon_{\text{eff},21} = -20.00$.

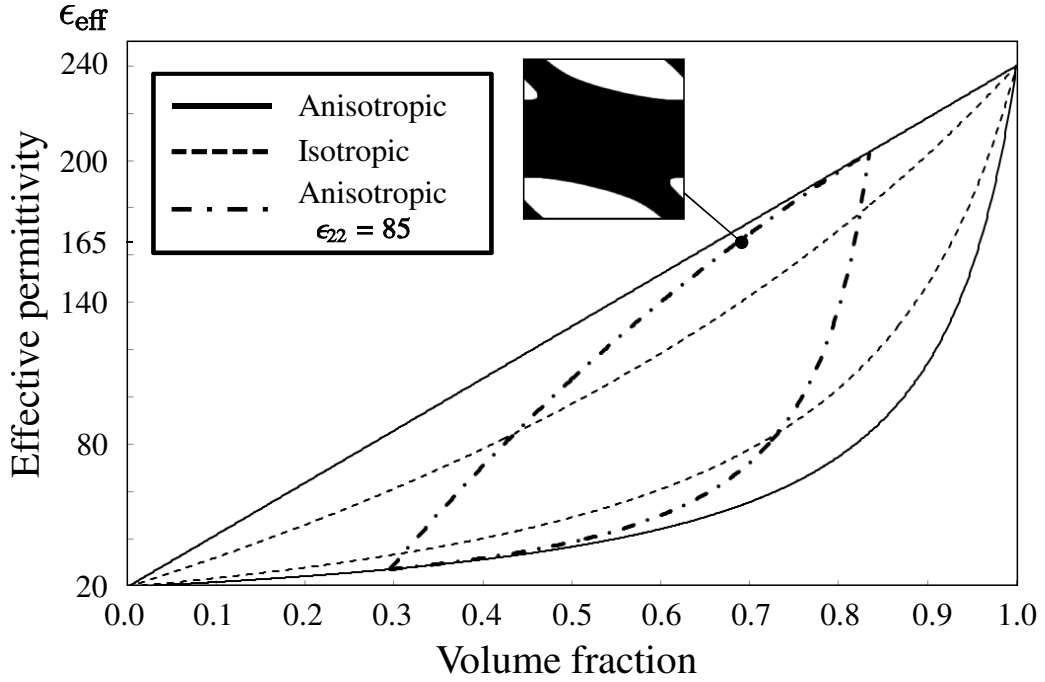


Figure 6.12: Theoretical bounds for anisotropic material designs with properties $\epsilon_1 = 240$ and $\epsilon_0 = 20$. The solid and dashed lines show the theoretical bounds for isotropic and anisotropic material, respectively. The dot-dashed line plots the upper limit of the permittivity of the anisotropic material versus the volume fraction when $\epsilon_{22} = 85$. The effective permittivity of the optimized configuration, $\epsilon_{\text{eff},11} = 164.99$ and $\epsilon_{\text{eff},22} = 85.00$, in the principal direction is shown as the black dot for comparison with the theoretical bound curve.

upper and lower limit of the permittivity of the anisotropic material versus the volume fraction when ϵ_{22} is 85.

6.5.5 Two-dimensional problems: material with loss targeting extreme values

Finally, this design example considers materials with loss. To consider the design of a lossy material, design problems where target values are known from a theoretical point of view are considered. In these examples, the relative permittivity of the dielectric material is set to $2 + 1i$ and the relative permittivity of the background material is set to 1. The maximum volume fraction is set to 50%. Figure 6.13 shows the upper and lower bounds for the effective permittivity of composite materials composed of dielectric and background materials. The theoretical bounds for an anisotropic material, an anisotropic material with a volume fraction of 50%, and an isotropic material with a volume fraction of 50% are respectively shown by the solid

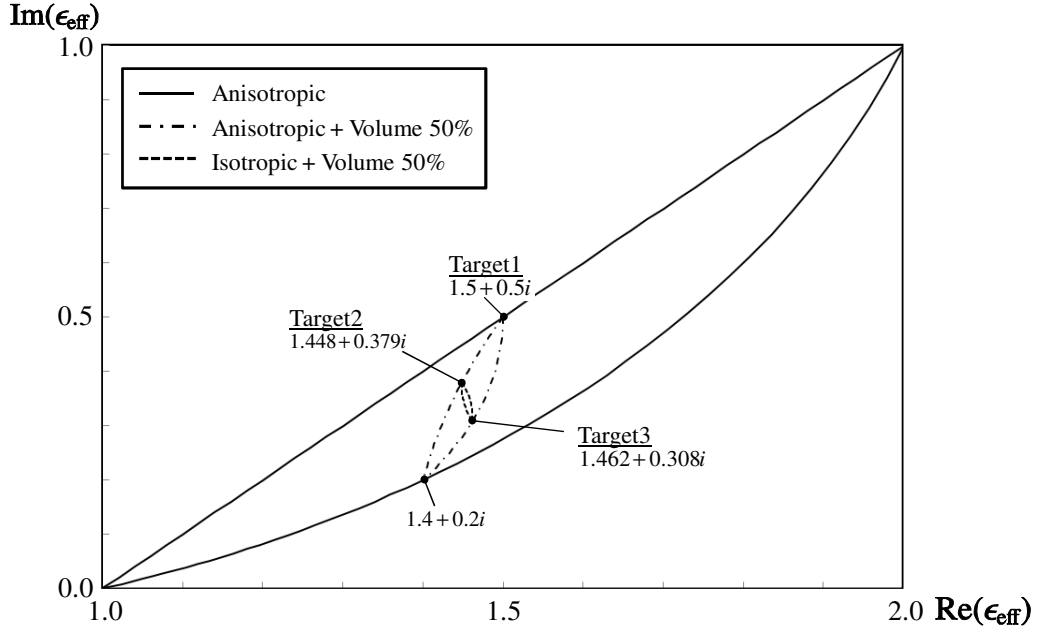


Figure 6.13: Theoretical bounds for lossy materials with properties $\epsilon_1 = 2 + 1i$ and $\epsilon_0 = 1$. The solid line shows the theoretical bounds for two constituent materials, and the dashed-dot line and dashed line show the theoretical bounds for anisotropic and isotropic material with a volume fraction of 50%, respectively. The black dots indicate the target values used in the optimization in Section 6.5.5.

line, the dot-dashed line, and the dashed line.

Based on these theoretical bounds, three target values were used to validate the present method. As shown in Fig.6.13, the target values for the three examples were as follows:

For Example1, the anisotropic material design problem, $\epsilon_{\text{tar},11} = 1.5 + 0.5i$. For Example2, the isotropic material design problem with maximum loss, $\epsilon_{\text{tar},11} = \epsilon_{\text{tar},22} = 1.4483 + 0.3793i$. And, for Example3, the isotropic material design problem with minimum loss, $\epsilon_{\text{tar},11} = \epsilon_{\text{tar},22} = 1.4615 + 0.3077i$.

Figure 6.14, 6.15 and 6.16 show the respective optimization results for each example. The obtained effective permittivity in Example1 is

$$\epsilon_{\text{eff}} = \begin{bmatrix} 1.500 + 0.500i & 0.0 \\ 0.0 & 1.400 + 0.200i \end{bmatrix}. \quad (6.57)$$

Although only ϵ_{11} was considered as the target value in the optimization, the obtained value of ϵ_{22} is in good agreement with the theoretical value of ϵ_{22} , that is, $\epsilon_{22} = 1.4 + 0.2i$.

The obtained effective permittivity for Example2 is

$$\epsilon_{\text{eff}} = \begin{bmatrix} 1.446 + 0.377i & 0.0 \\ 0.0 & 1.446 + 0.377i \end{bmatrix}, \quad (6.58)$$

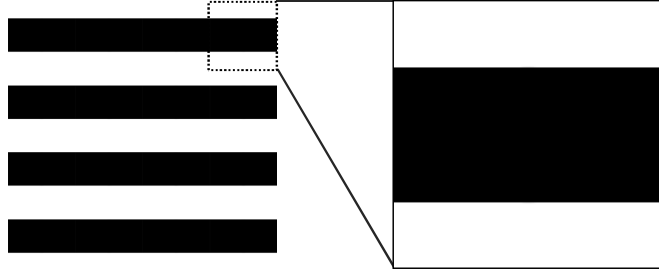


Figure 6.14: The optimized configuration of a lossy material design problem: target1, for volume fraction $V_{\max} = 0.5$ of $\epsilon_1 = 2 + 1i$ (black - lossy material) and $\epsilon_0 = 1$ (white). The target is $\epsilon_{\text{tar},11} = 1.5 + 0.5i$ and the obtained properties are $\epsilon_{\text{eff},11} = 1.500 + 0.500i$, $\epsilon_{\text{eff},22} = 1.400 + 0.200i$, and $\epsilon_{\text{eff},12} = \epsilon_{\text{eff},21} = 0.0$.

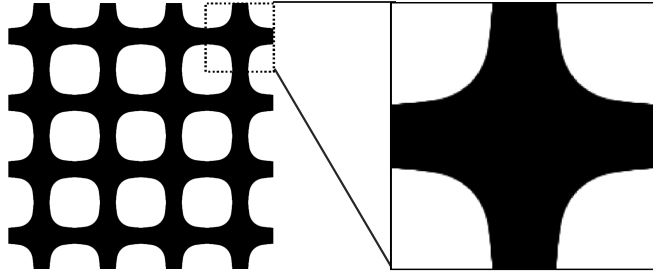


Figure 6.15: The optimized configuration of a maximum loss material design problem: target2, for volume fraction $V_{\max} = 0.5$ of $\epsilon_1 = 2 + 1i$ (black - lossy material) and $\epsilon_0 = 1$ (white). The target is $\epsilon_{\text{tar},11} = \epsilon_{\text{tar},22} = 1.448 + 0.379i$ and the obtained properties are $\epsilon_{\text{eff},11} = \epsilon_{\text{eff},22} = 1.446 + 0.377i$ and $\epsilon_{\text{eff},12} = \epsilon_{\text{eff},21} = 0.0$.

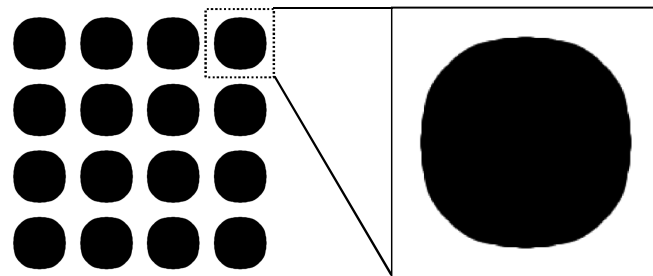


Figure 6.16: The optimized configuration of a minimum loss material design problem: target3, for volume fraction $V_{\max} = 0.5$ of $\epsilon_1 = 2 + 1i$ (black - lossy material) and $\epsilon_0 = 1$ (white). The target is $\epsilon_{\text{tar},11} = \epsilon_{\text{tar},22} = 1.462 + 0.308i$ and the obtained properties are $\epsilon_{\text{eff},11} = \epsilon_{\text{eff},22} = 1.459 + 0.308i$ and $\epsilon_{\text{eff},12} = \epsilon_{\text{eff},21} = 0.0$.

and the obtained effective permittivity for Example3 is

$$\epsilon_{\text{eff}} = \begin{bmatrix} 1.459 + 0.308i & 0.0 \\ 0.0 & 1.459 + 0.308i \end{bmatrix}. \quad (6.59)$$

These results show that the optimization can successfully find an optimal configuration that has a desired permittivity even for the design of a lossy material.

Observing the optimized structures for maximum damping (Example2) and minimum damping (Example3) it is worth to mention that the results match intuition. For the lossy design, the lossy constituent provides the matrix and the non-lossy is an isolated inclusion – and vice versa.

6.5.6 Two-dimensional problems: anisotropic material design with loss: effect of initial configurations

Here, the design of anisotropic materials with loss is considered. The relative permittivity of the dielectric materials is set to $140 - 0.196i$ and the relative permittivity of the background material is set to $20 - 0.012i$. Three different initial configurations are used in this design problem. The target values are set to $\epsilon_{\text{tar},11} = 60 - 0.06i$ and $\epsilon_{\text{tar},22} = 70 - 0.08i$.

Figures 6.17, 6.18 and 6.19 show the optimization results based on different initial configurations. Figure 6.17(a) shows the rod-shaped initial configuration and Fig.6.17(b) shows its optimized configuration. The volume fraction of the optimized configuration is 60.13%. The obtained effective permittivity is

$$\epsilon_{\text{eff}} = \begin{bmatrix} 59.80 - 0.060i & 0.0 \\ 0.0 & 69.64 - 0.080i \end{bmatrix}. \quad (6.60)$$

Figure 6.18(a) shows the cross-shaped initial configuration and Fig.6.18(b) shows its optimized configuration. The volume fraction of the optimized configuration is 61.50%. The obtained effective permittivity is

$$\epsilon_{\text{eff}} = \begin{bmatrix} 59.97 - 0.060i & 0.0 \\ 0.0 & 70.00 - 0.080i \end{bmatrix}. \quad (6.61)$$

Fig.6.19(a) shows the initial configuration in which the density gradually changes over the design domain, from a maximum value at the center ($\rho = 1$) to zero density at the boundaries ($\rho = 0$). Fig.6.19(b) show the optimized configuration based on this initial configuration. The volume fraction of the optimized configuration is 61.56%. The obtained effective permittivity is

$$\epsilon_{\text{eff}} = \begin{bmatrix} 60.00 - 0.060i & 0.0 \\ 0.0 & 69.82 - 0.080i \end{bmatrix}. \quad (6.62)$$

The different optimized structures obtained from the three different initial configurations indicate that this problem has several local optima. Although the obtained

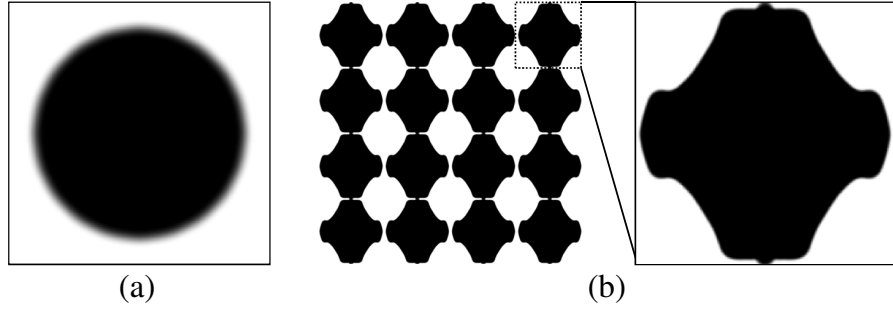


Figure 6.17: (a) The rod-shaped initial configuration, and (b) the optimized configuration of an anisotropic lossy material design problem, for $\epsilon_1 = 140 - 0.196i$ (black) and $\epsilon_0 = 20 - 0.012i$ (white). The target is $\epsilon_{\text{tar},11} = 60.00 - 0.060i$ and $\epsilon_{\text{tar},22} = 70.00 - 0.080i$, and the obtained properties are $\epsilon_{\text{eff},11} = 59.80 - 0.060i$, $\epsilon_{\text{eff},22} = 69.64 - 0.080i$ and $\epsilon_{\text{eff},12} = \epsilon_{\text{eff},21} = 0.0$.

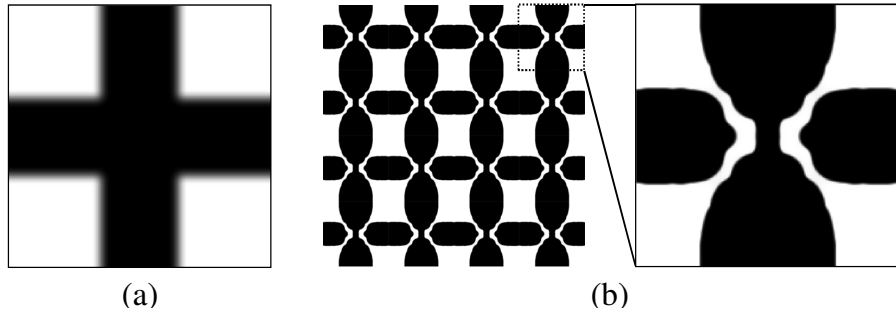


Figure 6.18: (a) The cross-shaped initial configuration, and (b) the optimized configuration of an anisotropic lossy material design problem for $\epsilon_1 = 140 - 0.196i$ (black) and $\epsilon_0 = 20 - 0.012i$ (white). The target is $\epsilon_{\text{tar},11} = 60.00 - 0.060i$ and $\epsilon_{\text{tar},22} = 70.00 - 0.080i$, and the obtained properties are $\epsilon_{\text{eff},11} = 59.97 - 0.060i$, $\epsilon_{\text{eff},22} = 70.00 - 0.080i$ and $\epsilon_{\text{eff},12} = \epsilon_{\text{eff},21} = 0.0$.

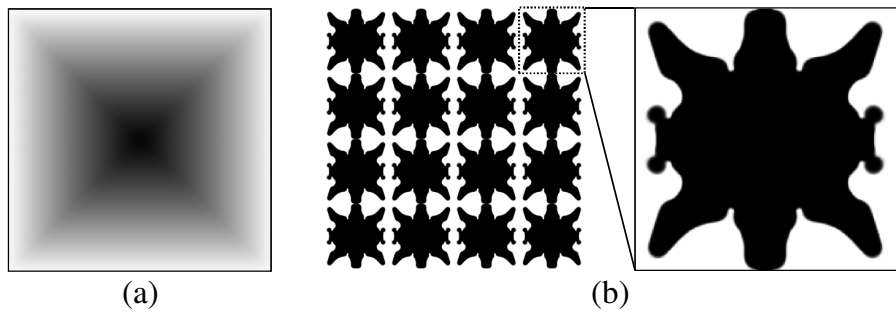


Figure 6.19: (a) The initial configuration in which the density gradually changes over the design domain, and (b) the optimized configuration of an anisotropic lossy material design problem, for $\epsilon_1 = 140 - 0.196i$ (black) and $\epsilon_0 = 20 - 0.012i$ (white). The target is $\epsilon_{\text{eff},11} = 60.00 - 0.060i$ and $\epsilon_{\text{eff},22} = 70.00 - 0.080i$, and the obtained properties are $\epsilon_{\text{eff},11} = 60.00 - 0.060i$, $\epsilon_{\text{eff},22} = 69.82 - 0.080i$ and $\epsilon_{\text{eff},12} = \epsilon_{\text{eff},21} = 0.0$.

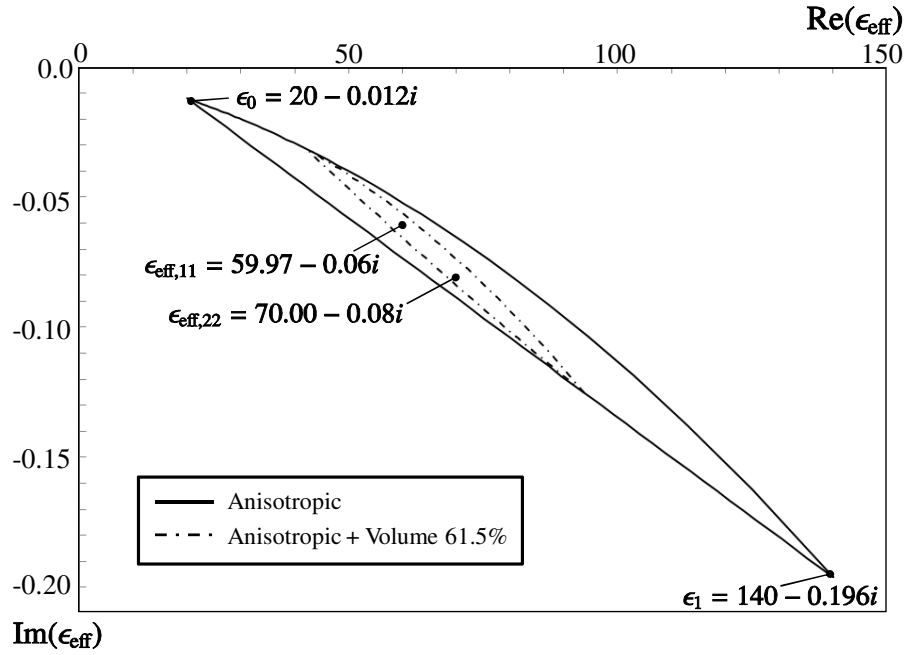


Figure 6.20: Theoretical bounds of anisotropic lossy material with properties $\epsilon_1 = 140 - 0.196i$ and $\epsilon_0 = 20 - 0.012i$. The solid line shows the theoretical bounds for two constituent materials, and the dashed-dot line shows the theoretical bounds for an anisotropic material with a volume fraction of 61.5%. Two black dots show the effective permittivity of the optimized configuration when using the cross-shaped initial configuration.

optimal values differ slightly from the target value, clear optimized configurations that achieve the prescribed permittivity value are obtained.

Figure 6.20 shows the upper and lower bounds of the effective permittivity of composite materials composed of the two different lossy dielectric materials. The solid line shows the theoretical bounds for two constituent materials, and the dashed-dot line shows the theoretical bounds for the anisotropic material with loss that has a volume fraction of 61.5%. The two black dots represent the effective permittivity values of the optimized configuration based on the cross-shaped initial configuration. Here, only the effective permittivity values obtained in the optimization using the cross-shaped initial configuration are evaluated, but the evaluations are very similar to those for the other two cases.

6.5.7 Three-dimensional problems: isotropic material design

Here, the design of an isotropic material is considered for the first three-dimensional problem. The objective of the optimization is to maximize the effective permittivity, $F = -(\epsilon_{\text{eff},11} + \epsilon_{\text{eff},22} + \epsilon_{\text{eff},33})$, under a volume fraction setting of 75%. The optimized configuration is shown in Fig.6.21(a) and the effective permittivities of the optimized

configuration are

$$\epsilon_{\text{eff}} = \begin{bmatrix} 66.5 & 0.00 & 0.00 \\ 0.00 & 66.5 & 0.00 \\ 0.00 & 0.00 & 66.5 \end{bmatrix}. \quad (6.63)$$

Figure 6.22 shows the theoretical bounds for the effective permittivity of composite materials composed of the above-mentioned dielectric and background materials, where the horizontal axis shows the volume fraction of the dielectric material and the vertical axis shows the effective permittivity of the composite material. The theoretical bounds for anisotropic and isotropic materials are shown by the solid and dashed lines, respectively. The effective permittivity of the optimized configuration is represented by the black square in Fig.6.22 for comparison with the theoretical bound curve, and demonstrates that the obtained result is in good agreement with theoretical bounds.

6.5.8 Three-dimensional problems: anisotropic material design

Here, the design of an anisotropic material is considered for the second three-dimensional problem. The objective of the optimization is to maximize the effective permittivity, $F = \epsilon_{\text{eff},11}$, under the constraint $G_1 = (1 - 3\epsilon_{\text{eff},22}/2\epsilon_{\text{eff},11})^2 - \epsilon^2 < 0$, $G_2 = (1 - 3\epsilon_{\text{eff},11}/2\epsilon_{\text{eff},22})^2 - \epsilon^2 < 0$, which constrain the ratio of the three permittivities in the principal directions so that $\epsilon_{\text{eff},22}/\epsilon_{\text{eff},11} = \epsilon_{\text{eff},33}/\epsilon_{\text{eff},11} = 2/3$, with a volume fraction of 75%. The relative permittivity of the dielectric material is set to 100 and the relative permittivity of the background material is set to 1. The optimized configuration is shown in Fig.6.21(b) and the effective permittivities of the optimized configuration are

$$\epsilon_{\text{eff}} = \begin{bmatrix} 75.15 & 0.00 & 0.00 \\ 0.00 & 50.15 & 0.00 \\ 0.00 & 0.00 & 50.15 \end{bmatrix}. \quad (6.64)$$

Figure 6.22 shows the theoretical bounds for the effective permittivity. The effective permittivity of the optimized configuration is represented by the black dot in Fig.6.22 for comparison with the theoretical bound curve. The highly sloped dot-dashed line plots the upper limit of the permittivity of the anisotropic material versus the volume fraction when ϵ_{22} and ϵ_{33} are set to 50.15. Similarly, the dot-dashed line that is partially obscured by the solid line in the lower right corner of the graph shows the lower limit of the permittivity of the anisotropic material versus the volume fraction when ϵ_{22} and ϵ_{33} are set to 50.15. The black dot represents the effective permittivity value of the dielectric material obtained by the optimization, which is in good agreement with theoretical bounds.

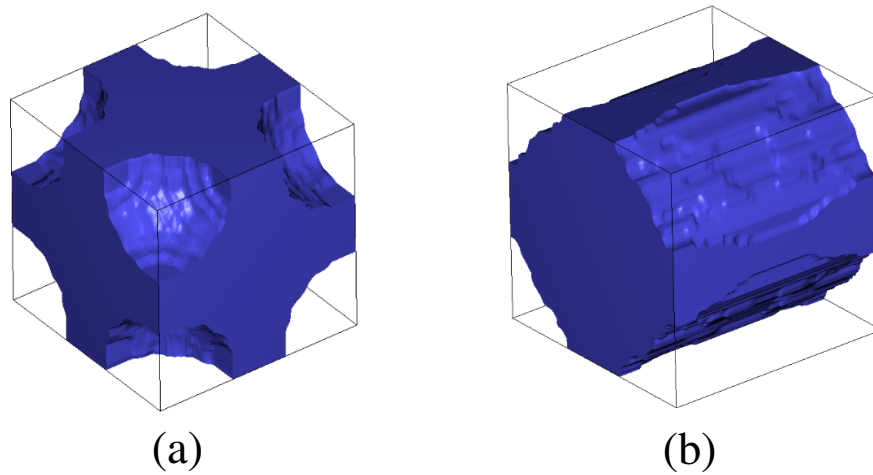


Figure 6.21: Optimized configuration of the three-dimensional permeability maximization problem: (a) isotropic case, (b) anisotropic case.

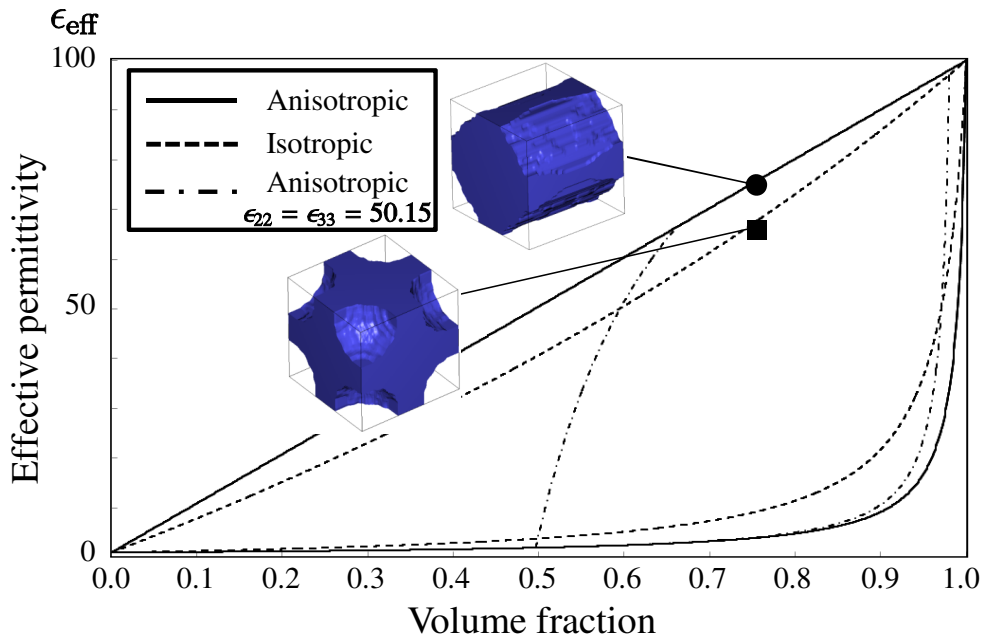


Figure 6.22: Theoretical bounds for isotropic and anisotropic material design problems with properties $\epsilon_1 = 100$ and $\epsilon_0 = 1$. The solid and dashed lines show the theoretical bounds for isotropic and anisotropic material, respectively. The dot-dashed line plots the upper and lower limit of the permittivity of the anisotropic material versus the volume fraction.

6.6 Conclusions

In this chapter, a gradient-based topology optimization method that can be applied to the design of microstructures based on a periodic array of dielectric materials to achieve desired electric permittivities were presented. A simple homogenization method was used to obtain the effective permittivity and the validity of the proposed method was demonstrated through several design problems, namely, those dealing with an isotropic material, an anisotropic material, an anisotropic material with a nonzero off-diagonal term, and an anisotropic material with loss. Clear optimized configurations with prescribed electric permittivities were obtained for all the presented cases. Moreover, the theoretical bounds of the two- and three-dimensional anisotropic effective property in the principal direction when the effective property in the other principal direction was set to a prescribed value were derived, to evaluate the effective permittivity values obtained by the optimization. Our results showed that the optimized values are in good agreement with theoretical bounds, confirming that our method yields appropriate and useful solutions. The Vigdergauz-like optimized structures obtained in this paper provide a directly manufacturable alternative to the multi-length scale microstructures from the literature.

Chapter 7

Design of electromagnetic devices using ferrite material

7.1 Introduction

This chapter discusses the macrostructure design of electromagnetic devices, electromagnetic cloaking, and metallic waveguide devices using a ferrite material. A level set-based topology optimization method is used to design the ferrite material configurations.

Electromagnetic cloaks are devices that render an object, illuminated by electromagnetic waves of certain wavelengths, undetectable by an observer. Andkjær et al. [210] presented a gradient-based topology optimization method for the design of optical cloaks made of dielectric materials. In this work, a level set-based topology optimization method is applied for the design of an electromagnetic cloak using a ferrite material. Ferrite materials exhibit a frequency-dependent degree of permeability, due to magnetic resonance phenomenon that can be influenced by changing the magnitude of an externally applied DC magnetic field. Thus, such ferrite cloaks have the potential to provide novel functions, such as on-off operation in response to on-off application of an external magnetic field, or a tunable frequency range under which the cloak operates.

A waveguide is an electromagnetic device which guides the transmission of electromagnetic waves. They are widely used in electromagnetic devices such as antennas, cell phone base stations, and the like. Rectangular waveguides with periodic ferrite inserts have been recently proposed that demonstrate left-handed behavior such as backward wave propagation [157]. Waveguides with ferrite inclusions are expected to have advantages in that they can function under a tunable range of operating frequencies and be made compact, because electromagnetic waves can propagate at a frequency lower than the cut-off frequency that typically limits the minimum size of a waveguide.

For the structural optimization method applied to the design of a metallic waveguide, Hirayama et al. [58] proposed a density-based topology optimization method for the design of dielectric materials in a metallic waveguide. Nishiwawki et al. [59]

proposed a density-based method for the cross-section design of dielectric waveguides. Subsequently, Hirayama et al. [94] proposed a level set-based structural optimization method for the design of dielectric inclusions and Yamasaki et al. [93] proposed a level set-based structural optimization method for the design of metallic inclusions of a waveguide. For the structural optimization method applied to the design of a metallic waveguide, Hirayama et al. [58] proposed a density-based topology optimization method for the design of dielectric materials in a metallic waveguide. Nishiwawki et al. [59] proposed a density-based method for the cross-section design of dielectric waveguides. Subsequently, Hirayama et al. [94] proposed a level set-based structural optimization method for the design of dielectric inclusions and Yamasaki et al. [93] proposed a level set-based structural optimization method for the design of metallic inclusions of a waveguide.

In this chapter, a level set-based topology optimization [90] is applied to find the configuration of ferrite materials that minimizes the norm of the difference between the obtained electric field and a reference electric field, for the design of an electromagnetic cloaking device, and that maximizes the transmission power of electromagnetic waves at prescribed frequencies for the design of a metallic waveguide. The Landau-Lifshitz model is used to model the permeability of the ferrite material [211]. Numerical examples for a cylindrical cloak, a carpet cloak, a waveguide filter, and a T-junction design problem are provided to examine the validity and utility of the presented method.

7.2 Formulation

7.2.1 Relative permeability of a ferrite material

Ferrite materials exhibit a frequency-dependent permeability due to a magnetic resonance phenomenon, and the permeability can be altered by changing the magnitude of an externally applied DC magnetic field. The relative magnetic permeability of a ferrite material can be described using the Landau-Lifshitz model [211], as follows.

$$\bar{\mu}_f = \begin{bmatrix} \mu & \kappa j & 0 \\ -\kappa j & \mu & 0 \\ 0 & 0 & 1 \end{bmatrix}$$

where

$$\mu = \frac{\omega^2 - \omega_0^2}{\omega^2 - \omega_h^2}$$

$$\kappa = \frac{\omega\omega_m}{\omega^2 - \omega_h^2}$$

In the above equations, ω is the angular frequency and ω_0 is the precession frequency. ω_0 , ω_h and ω_m are defined as follows.

$$\begin{aligned}\omega_0 &= \sqrt{\omega_h(\omega_h + \omega_m)} \\ \omega_h &= \gamma\mu_0 \left(H_0 + j\frac{\Delta H}{2} \right) \\ \omega_m &= \gamma\mu_0 M_s\end{aligned}$$

where γ and μ_0 are the gyromagnetic ratio of ferrite and the magnetic permeability of a vacuum, respectively. H_0 , ΔH and M_s are the magnitude of an externally applied DC magnetic field, the resonance line width of the ferrite material, and the degree of magnetization saturation, respectively.

7.2.2 Governing equation for wave propagation problem using ferrite

Using permeability tensor discussed above, the governing equation for wave propagation problem can be described by following wave propagation equation that is derived from Maxwell's equations.

$$\nabla \times (\bar{\mu}_f^{-1} \nabla \times \mathbf{E}) - k_0^2 \epsilon_f \mathbf{E} = 0 \quad (7.1)$$

where ϵ_f is the relative permittivity of ferrite material, \mathbf{E} is electric field. k_0 is the wave number in a vacuum such that $k_0 = \omega\sqrt{\epsilon_0\mu_0}$, where ϵ_0 and μ_0 are the relative permittivity and permeability in a vacuum.

Here two-dimensional wave propagation problems are considered, where transverse electric waves propagate in x-y direction and where the electric field vector is polarized orthogonal to the direction of wave propagation. The governing equation can be derived as the following two-dimensional Helmholtz equation from the wave propagation equation assuming that the wave is time harmonic and $\frac{\partial}{\partial z} = 0$,

$$\nabla \cdot (\mu_f^{-1} \nabla E_z) + k_0^2 \epsilon_f E_z = 0, \quad (7.2)$$

where μ_f is the relative permeability of ferrite material for two dimensional problem, namely,

$$\mu_f = \begin{bmatrix} \mu & \kappa j \\ -\kappa j & \mu \end{bmatrix}. \quad (7.3)$$

Cloak design problem

For cloak design problem, the outer boundaries Γ_{out} are set to a first order absorbing boundary condition [185], the approximation of the Sommerfeld radiation condition [184], to truncate the infinite domain. The scattering object located inside the design domain is modeled using a perfect electrically conducting (PEC) boundary condition Γ_{PEC} .

Based on the discussion above, the governing equation for cloak design problem is provided as follows.

$$\nabla \cdot (\mu_r^{-1} \nabla E_z) + k_0^2 \epsilon_r E_z = 0, \quad (7.4)$$

where μ_r is the relative permeability that $\mu_r = \mu_f$ where the ferrite material is distributed, and $\mu_r = \mu_d \delta_{ij}$ in background material. δ_{ij} is the Kronecker's delta.

The boundary conditions are described as follows:

$$\mathbf{n} \cdot (\mu_r^{-1} \nabla E_z) + jk_0 \sqrt{\mu_r^{-1}} E_z = (1 - \mathbf{k} \cdot \mathbf{n}) j \sqrt{\mu_r} k_0 E^i \quad \text{on } \Gamma_{\text{out}} \quad (7.5)$$

$$E_z = 0 \quad \text{on } \Gamma_{\text{PEC}}, \quad (7.6)$$

where \mathbf{n} is the normal vector and E^i is an incident wave.

The weak formulation of Eqs.(7.4)-(7.6) is then derived as follows.

$$a_1(E_z, \tilde{E}_z) + a_2(E_z, \tilde{E}_z) = l(\tilde{E}_z) \quad \text{for } E_z \in U, \tilde{E}_z \in U \quad (7.7)$$

where

$$a_1(E_z, \tilde{E}_z) = \int_D \nabla \tilde{E}_z \cdot (\mu_r^{-1} \nabla E_z) d\Omega - k_0^2 \int_D \tilde{E}_z E_z d\Omega \quad (7.8)$$

$$a_2(E_z, \tilde{E}_z) = jk_0 \int_{\Gamma_{\text{out}}} \sqrt{\epsilon_r} \tilde{E}_z E_z d\Gamma \quad (7.9)$$

$$l(\tilde{E}_z) = 2jk_0 \int_{\Gamma_{\text{out}}} \sqrt{\epsilon_r} E_z^i \tilde{E}_z d\Gamma \quad (7.10)$$

$$U = \{\tilde{E}_z \in H^1(\Omega)\}, \quad (7.11)$$

where \tilde{E}_z is a test function and H^1 is Sobolev space.

Waveguide design problem

For waveguide design problem, incident waves enter the domain from the boundary Γ_1 and output waves are observed at the boundaries Γ_i . The boundaries Γ_{PEC} are set as perfect electric conductors (PEC) to describe the metallic waveguide walls. Similarly, the governing equation for metallic waveguide design problem is provided as follows.

$$\nabla \cdot (\mu_r^{-1} \nabla E_z) + k_0^2 \epsilon_r E_z = 0, \quad (7.12)$$

The boundary conditions are described as follows:

$$\mathbf{n} \cdot (\mu_r^{-1} \nabla E_z) + jk_0 \sqrt{\mu_r^{-1}} E_z = 2j \sqrt{\mu_r} k_0 E^i \quad \text{on } \Gamma_1 \quad (7.13)$$

$$\mathbf{n} \cdot (\mu_r^{-1} \nabla E_z) + jk_0 \sqrt{\mu_r^{-1}} E_z = 0 \quad \text{on } \Gamma_2 \cdots \Gamma_n \quad (7.14)$$

$$E_z = 0 \quad \text{on } \Gamma_{\text{PEC}}, \quad (7.15)$$

The weak formulation of Eqs.(7.12)-(7.15) is then derived as follows.

$$a_1(E_z, \tilde{E}_z) + a_2(E_z, \tilde{E}_z) = l(\tilde{E}_z) \quad \text{for } E_z \in U, \tilde{E}_z \in U \quad (7.16)$$

where

$$a_1(E_z, \tilde{E}_z) = \int_D \nabla \tilde{E}_z \cdot (\mu_r^{-1} \nabla E_z) d\Omega - k_0^2 \int_D \tilde{E}_z E_z d\Omega \quad (7.17)$$

$$a_2(E_z, \tilde{E}_z) = jk_0 \int_{\bigcup_{i=1}^n \Gamma_i} \sqrt{\epsilon_r} \tilde{E}_z E_z d\Gamma \quad (7.18)$$

$$l(\tilde{E}_z) = 2jk_0 \int_{\Gamma_1} \sqrt{\epsilon_r} E_z \tilde{E}_z d\Gamma \quad (7.19)$$

$$U = \{\tilde{E}_z \in H^1(\Omega)\}, \quad (7.20)$$

7.2.3 Design variables

The distribution of ferrite material inside the fixed design domain is expressed using the level set function. In the presented method, the relative magnetic permeability μ_r in the fixed design domain is defined using the reciprocal of the relative permeability and the relative electric permittivity ϵ_r is defined using linear form of the relative permittivity as follows.

$$\mu_r^{-1} = (\mu_f^{-1} - \hat{\mu}_d^{-1}) \chi_\phi(\phi) + \hat{\mu}_d^{-1}, \quad (7.21)$$

$$\epsilon_r = (\epsilon_f - \epsilon_d) \chi_\phi(\phi) + \epsilon_d, \quad (7.22)$$

where

$$\mu_f^{-1} = \frac{1}{\mu^2 - \kappa^2} \begin{bmatrix} \mu & -\kappa j \\ \kappa j & \mu \end{bmatrix}, \quad \hat{\mu}_d^{-1} = \mu_d^{-1} \begin{bmatrix} 1 & 0 \\ 0 & 1 \end{bmatrix}, \quad (7.23)$$

where μ_d is the relative permeability of the dielectric material, ϵ_f and ϵ_d are the relative permittivity of ferrite and dielectric. $H(\phi)$ is the Heaviside function.

7.2.4 Optimization problem

Electromagnetic cloaking design problem

Incident waves enter the scattering domain from the left, and the outer boundary of this domain is set to function under an absorbing boundary condition. The inner boundary is set as a perfect electric conductor (PEC). The optimization objective is to minimize the norm of the scattering field and is described as follows.

$$\inf_{\phi} \quad F = \int_{\Omega_{\text{out}}} (E_z - E_z^{\text{ref}})^* (E_z - E_z^{\text{ref}}) d\Omega, \quad (7.24)$$

$$\text{subject to} \quad G = \frac{1}{V_D} \int_D \chi_\phi d\Omega - V_{\text{max}} \leq 0 \quad (7.25)$$

$$\text{Helmholtz equation} \quad (7.26)$$

$$\text{Boundary conditions} \quad (7.27)$$

where E^{ref} is the reference field that is obtained when there is no scattering object located inside the domain, and $*$ denotes a complex conjugate. The optimization

algorithm uses the adjoint variable method for the sensitivity analysis and the finite element method for solving the electromagnetic propagation and adjoint problems. The level set function is updated by solving a reaction diffusion equation.

Waveguide filter design problem

Here, the purpose of the optimization problem is set as to design a waveguide filter. The objective function is formulated to maximize the transmission power at frequency ω_i as follows:

$$\inf_{\phi} \quad F = - \sum_i \alpha_i |S_{21}|_{\omega=\omega_i}^2, \quad (7.28)$$

$$\text{subject to} \quad G = \frac{1}{V_D} \int_D \chi_{\phi} d\Omega - V_{\max} \leq 0 \quad (7.29)$$

$$\text{Helmholtz equation} \quad (7.30)$$

$$\text{Boundary conditions} \quad (7.31)$$

where α_i is a weighting coefficient, and S_{21} is a transmission coefficient of scattering parameters that represents the electromagnetic power ratio between the transmission power through Γ_2 and the input power at Γ_1 . The transmission coefficient for Γ_i can be generally defined as the following equation.

$$S_{j1} = \frac{\int_{\Gamma_j} E_z E_z^* d\Gamma}{\int_{\Gamma_j} E_z^i E_z^{i*} d\Gamma} \quad (7.32)$$

T-junction design problem

For T-junction design problem, The optimization purpose is set to equally maximize the transmission power at all the output ports. The objective function is formulated to maximize the reciprocal value of the sum of the reciprocal value of all the S-parameters, so as to maximize the least transmission power at the output port. The similar formulation is used in eigen-frequency design problem [212], as follows:

$$\inf_{\phi} \quad F(\phi) = - \left(\sum_{j=2}^n \frac{1}{|S_{j1}|^2} \right)^{-1} \quad (7.33)$$

$$\text{subject to} \quad G = \frac{1}{V_D} \int_D \chi_{\phi} d\Omega - V_{\max} \leq 0 \quad (7.34)$$

$$\text{Helmholtz equation} \quad (7.35)$$

$$\text{Boundary conditions} \quad (7.36)$$

7.2.5 Sensitivity analysis

The sensitivity analysis is now considered. The Lagrangian of the optimization problem is formulated as follows:

$$\hat{F} = F - \left(a_1(E_z, \tilde{E}_z) + a_2(E_z, \tilde{E}_z) - l(\tilde{E}_z) \right) + \lambda G, \quad (7.37)$$

where \tilde{E}_z denotes the adjoint variables. The sensitivity of the Lagrangian is obtained using the AVM, as follows.

$$\begin{aligned} \left\langle \frac{d\hat{F}}{d\chi_\phi}, \tilde{\chi}_\phi \right\rangle &= \left(\left\langle \frac{\partial F}{\partial E_z}, \tilde{E}_z \right\rangle - \left\langle \frac{\partial a_1}{\partial E_z}, \tilde{E}_z \right\rangle - \left\langle \frac{\partial a_2}{\partial E_z}, \tilde{E}_z \right\rangle \right) \left\langle \frac{\partial E_z}{\partial \chi_\phi}, \tilde{\chi}_\phi \right\rangle \\ &\quad - \left\langle \frac{\partial a_1}{\partial \chi_\phi}, \tilde{\chi}_\phi \right\rangle + \lambda \left\langle \frac{\partial G}{\partial \chi_\phi}, \tilde{\chi}_\phi \right\rangle, \end{aligned} \quad (7.38)$$

where the adjoint variable \tilde{E}_z is obtained by solving the following equation.

$$a_1(\tilde{E}_z, \delta E_z) + a_2(\tilde{E}_z, \delta E_z) = \left\langle \frac{\partial F}{\partial E_z}, \tilde{E}_z \right\rangle \quad \text{for } \tilde{E}_z \in U, \quad \forall \delta E_z \in U, \quad (7.39)$$

where δE_z is the variation of E_z . The sensitivities are finally obtained using the following equation.

$$\left\langle \frac{d\hat{F}}{d\chi_\phi}, \tilde{\chi}_\phi \right\rangle = - \left\langle \frac{\partial a_1(E_z, \tilde{E}_z)}{\partial \chi_\phi}, \tilde{\chi}_\phi \right\rangle + \lambda \left\langle \frac{\partial G}{\partial \chi_\phi}, \tilde{\chi}_\phi \right\rangle \quad (7.40)$$

Note that the adjoint equation, Eq.(7.39), can be solved efficiently as described below. Considering the the fact that $a_1(\mu_r, E_z, \tilde{E}_z) = a_1(\mu_r^T, \tilde{E}_z, E_z)$, the solutions of the adjoint equation, Eq.(7.39), are obtained by solving the state problem using the permeability tensor μ_r^T instead of μ_r used in the state problem, and changing the location of the incident field.

7.3 Numerical examples

Here the presented method is applied to a cylindrical cloak, a carpet cloak [213–215], waveguide filter and T-junction design problems. The conceptual ferrite material used in the following numerical examples has the following parameter values: $\gamma = 1.759T^{-1}s^{-1}$, $\Delta H = 1\text{mT}$, and $\mu_0 M_0 = 173\text{mT}$, assuming that the ferrite material resembles a Yttrium-iron garnet (YIG). The relative permittivity of the ferrite is set as $\epsilon_f = 10$. A configuration filled with ferrite material is used as the initial configuration for both cases.

7.3.1 Cylindrical cloaking design

The design domain and boundary conditions are shown in Fig.7.1(a). The radii of the inner, middle, and outer domains are set to 0.2, 1.0, and 2.5m, respectively, and the operating frequency is set as 0.2GHz. The magnitude of externally applied magnetic field is set $\mu_0 H_0 = 300\text{mT}$, the relative permittivity in air is set to 1. The magnitude of the regularization parameter τ is set to 1.0×10^{-4} .

Fig. 7.1(b) shows the optimized configuration of ferrite material. Fig. 7.2(a) shows the electric field without the cloak and Fig. 7.2(b) shows the electric field of the optimized cloak during operation. As Fig. 7.2(a) shows, the electromagnetic

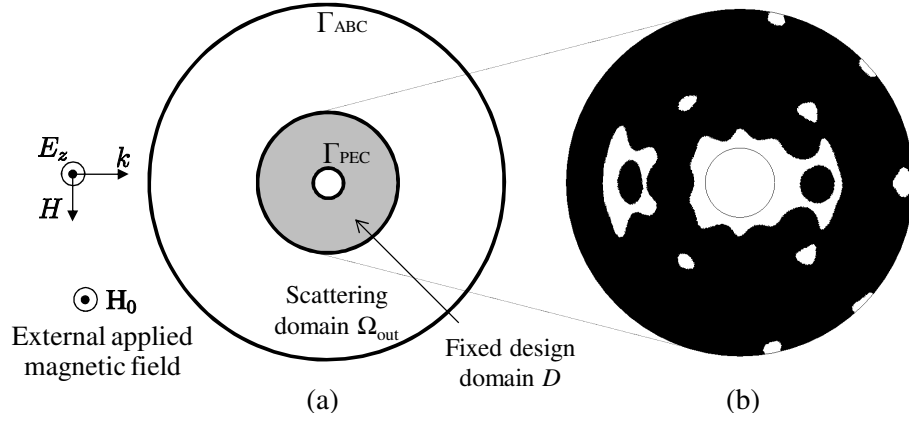


Figure 7.1: (a) Cylindrical cloak model and (b) optimized configuration of ferrite material.

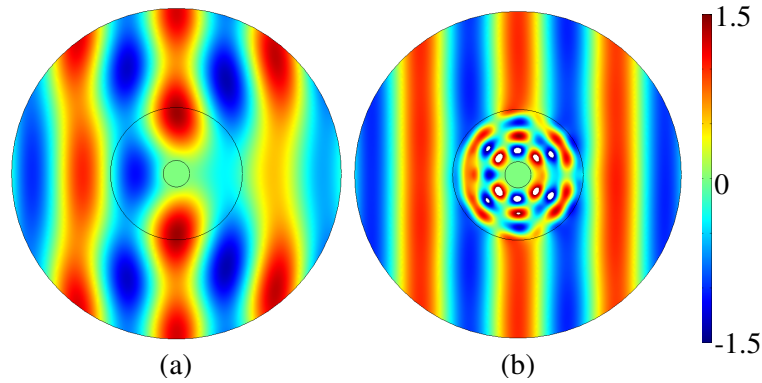


Figure 7.2: Total electric field of carpet cloak design problem: (a) no cloak, namely no external magnetic field; (b) optimized cloak.

waves are scattered by the cylindrical object without the cloak, but scattering is much reduced with the cloak operating, as shown in Fig. 7.2(b). The values of the objective function without and with the cloak are 1.18 and 0.04, respectively. Fig.7.3 shows the norm of the difference between electric field and reference electric field with no cloak, namely no external magnetic field, and optimized cloak. These results indicate that the optimization successfully found an appropriate ferrite configuration for a cylindrical electromagnetic cloak.

7.3.2 Carpet cloaking design

The design domain and boundary conditions of the carpet cloaking model are shown in Fig.7.4(a). Here, the inner semi-ellipse located at the bottom center represents the scattering object that is to be hidden by the cloak. The major axis radius of the inner semi-ellipse is set 0.3m and the minor axis radius is set to 0.2m. The major axis

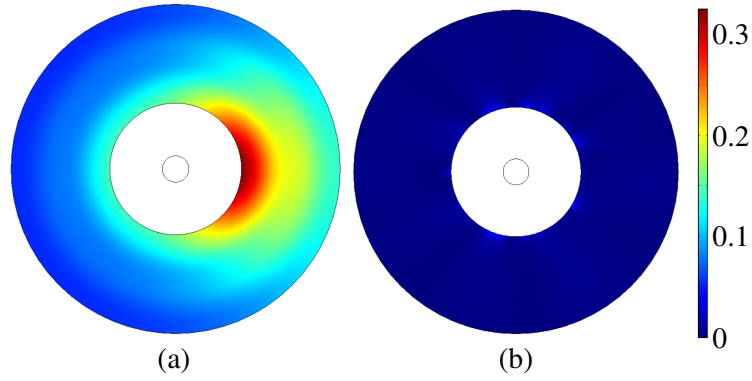


Figure 7.3: Norm of the difference between electric field and reference electric field of carpet cloak design problem: (a) no cloak, namely no external magnetic field; (b) optimized cloak.

radius of the outer semi-ellipse of the cloaking domain is set to 1.0m and the minor axis radius is set to 0.5m. The radius of the outer hemispheres is set to 5.0m, and the operating frequency is set as 0.5GHz. Here, incident waves enter the scattering domain from the left top, and the electromagnetic waves are reflected at the bottom boundary. The objective of the optimization is to make the electromagnetic waves reflect as if no scattering object is present at the bottom of the design domain. Here the objective function is set to minimize the norm of the difference between the electric field and the reference electric field that is obtained when there is no scattering object located inside the domain. Fig.7.5 shows the reference electric field. The same values for the optimization parameters are used as the one used in previous example.

Fig. 7.4(b) shows the optimized configuration of ferrite material. Fig. 7.6(a) shows the electric field when the cloak is not operating, namely, in the absence of an externally applied magnetic field. Fig 7.6(b) shows the electric field of the optimized cloak during operation. As Fig.7.6(a) shows, the electromagnetic waves are scattered by the semi-elliptical object without the cloak and they propagate in two directions. However, the scattering is much reduced when the cloak is operating, as shown in Fig.7.6(b), where the waves propagate in one direction only. The values of the objective function without and with cloak are 4.46 and 0.24, respectively. Fig.7.7 shows the norm of the difference between electric field and reference electric field with no cloak, namely no external magnetic field, and optimized cloak. These results demonstrate that the optimization successfully found an appropriate ferrite configuration for a carpet cloak.

7.3.3 Waveguide filter design

Fig.7.8 shows the design domain and boundary conditions for the waveguide design example. The height and width of the waveguide are set to 10 mm and 30 mm, respectively. Incident waves enter the domain from the left boundary, and the upper and lower boundaries are set as having the condition of a perfect electric conductor (PEC).

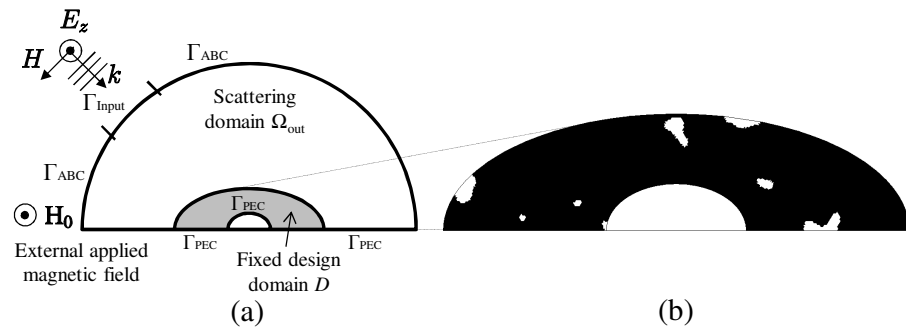


Figure 7.4: (a) Carpet cloak model and (b) optimized configuration of ferrite material.

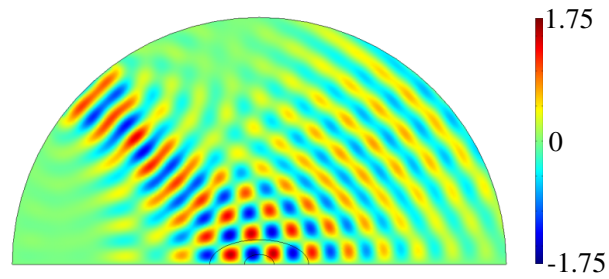


Figure 7.5: Reference electric field for carpet cloak design problem.

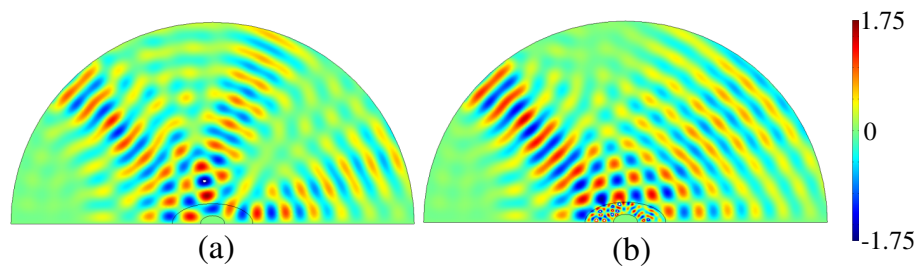


Figure 7.6: Total electric field of carpet cloak design problem: (a) no cloak, namely no external magnetic field; (b) optimized cloak.

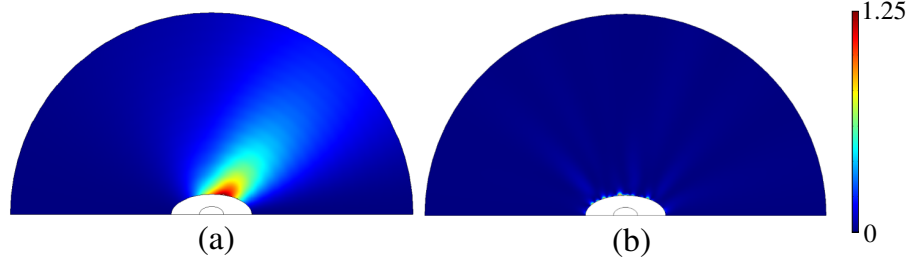


Figure 7.7: Norm of the difference between electric field and reference electric field of carpet cloak design problem: (a) no cloak, namely no external magnetic field; (b) optimized cloak.

The input and output port are located in the left and right side of the waveguide to numerically support the wave propagation, where the relative permittivity constant is set to $\epsilon_{\text{side}} = 25$. The entire domain is discretized using 14,400 rectangular elements. The relative permittivity constant of the dielectric material ϵ_r is set to 5. The target frequency of the optimization is set to 2.0GHz. The magnitude of externally applied magnetic field is set $\mu_0 H_0 = 30\text{mT}$. The magnitude of the regularization parameter τ is set to 1.0×10^{-3} .

Fig.7.9 shows the optimized configuration in the design domain. The asymmetry in the optimized configuration is caused by the anisotropy of the ferrite permeability. Fig.7.10 shows the frequency characteristics of the scattering parameters S_{11} and S_{21} , as the transmission coefficients S_{21} of initial and optimized configuration at 2.0GHz are -24.7dB and -3.3dB, respectively. Fig.7.11 shows the frequency characteristics of the scattering parameters S_{21} for the optimized configuration when different magnitudes of an external magnetic field are applied, with $\mu_0 H_0 = 30\text{mT}$, 60mT, and 90mT, respectively. These illustrate the tunability of the operating frequency by the application of externally magnetic fields. Fig.7.12(a)-(d) show the electric field at 2.0GHz at different phases of incident waves, namely, (a) 0° , (b) 60° , (c) 120° , and (d) 180° , that show forward wave propagations in the waveguide. As the optimization

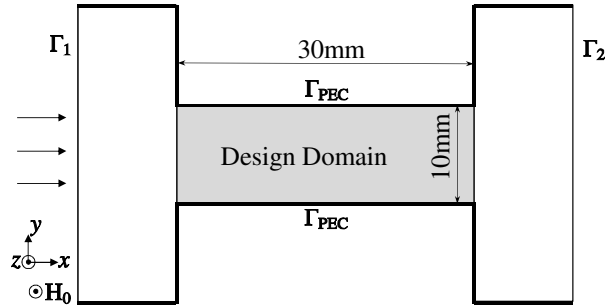


Figure 7.8: Design domain and boundary conditions for waveguide filter design problem.

results show, the optimized configuration consists of two bars located in the upper and lower areas of the design domain. Electromagnetic waves propagate in the dielectric material between the upper and lower ferrite bars that guide the transmission of electromagnetic waves.

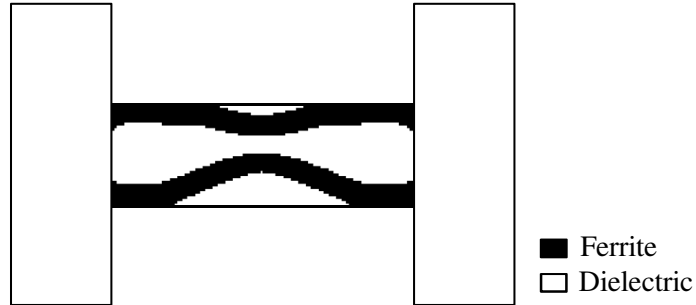


Figure 7.9: Obtained optimized configuration of waveguide filter design problem, maximizing S_{21} .

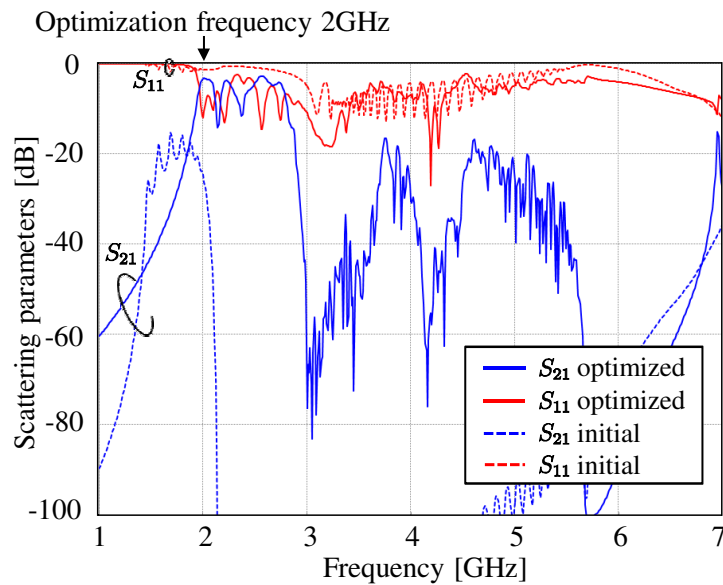


Figure 7.10: Frequency characteristic of S_{11} and S_{21} , obtained using the initial and optimized configurations.

7.3.4 T-junction design

Fig.7.13 shows the design domain and boundary conditions for the T-junction design problem. Incident waves enter the domain from the upper boundary. The optimization purpose is set to equally maximize the transmission power S_{21} and S_{31} . The

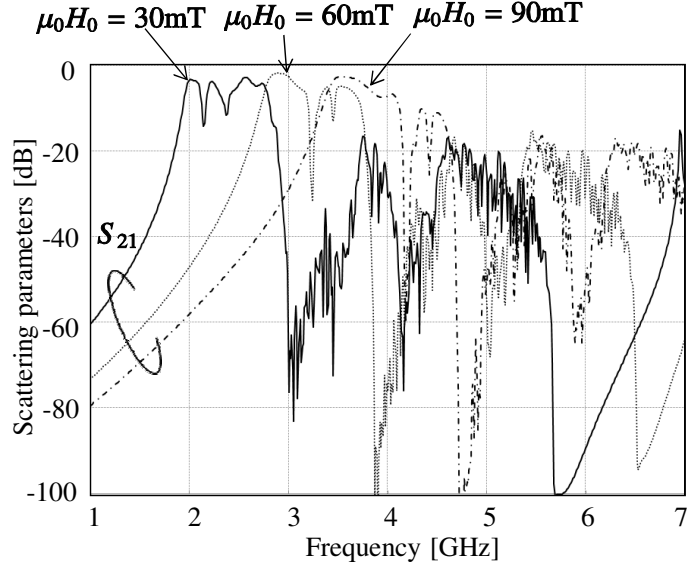


Figure 7.11: Frequency characteristic of S_{21} , obtained using the optimized configuration, with applied magnetic field $\mu_0 H_0 = 30, 60, 90\text{mT}$.

target frequency of the optimization is set to 2.0 GHz. The magnitude of externally applied magnetic field is set $\mu_0 H_0 = 30\text{mT}$. The magnitude of the regularization parameter τ is set to 1.0×10^{-3} .

Fig.7.14 shows the optimized configuration in the design domain. Fig.7.15 shows the frequency characteristics of the scattering parameters S_{11} , S_{21} and S_{31} , as the transmission coefficients S_{21} of initial and optimized configurations at 2.0GHz are -43.29dB and -7.48dB respectively, and S_{31} are -57.48dB and -7.49dB , respectively. Fig.7.16(a)-(d) show the electric field at 2.0GHz at different phases of incident waves, namely, (a) 0° , (b) 60° , (c) 120° , and (d) 180° .

7.4 Conclusions

In this chapter, a level set-based topology optimization [90] is applied for the design of electromagnetic devices, including electromagnetic cloaks and metallic waveguides. The governing equation of wave propagation problems using a ferrite material was derived and the optimization problems were formulated to minimize the norm of the difference between the obtained electric field and a reference electric field, for the design of an electromagnetic cloaking device, and to maximize the transmission power of electromagnetic waves at prescribed frequencies for the design of a metallic waveguide. The results in numerical examples of a cylindrical cloaking device, a carpet cloaking device, a waveguide filter, and a T-junction design problem showed that the optimization method successfully found appropriate ferrite configurations that provide the desired performance.

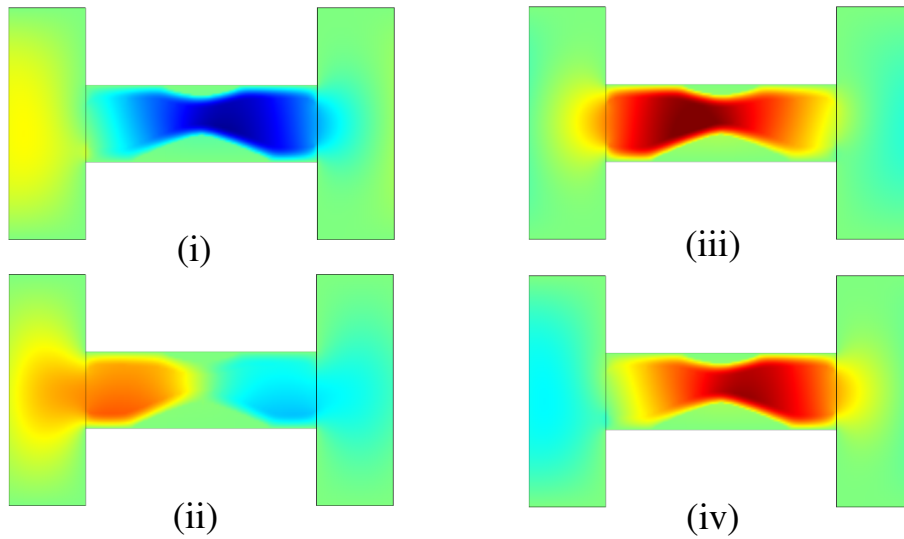


Figure 7.12: Electric field of optimized configuration at 2.0 GHz for various phases of incident waves: (a) 0° ; (b) 60° ; (c) 120° ; (d) 180° .

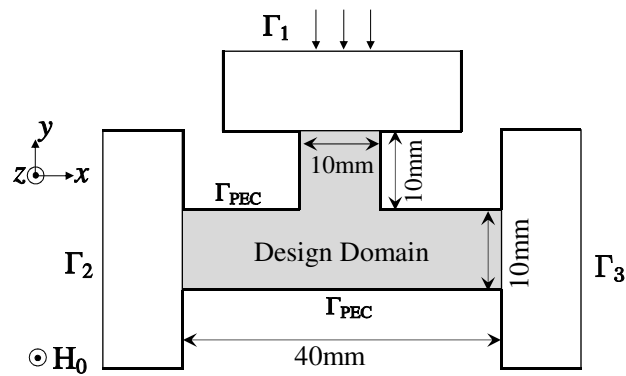


Figure 7.13: The model for T-junction design problem.



Figure 7.14: Optimized configuration of T-junction design problem.

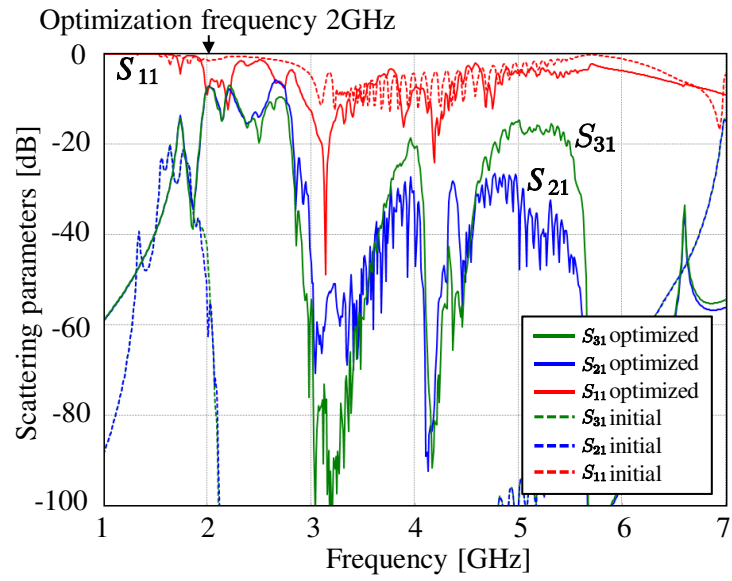


Figure 7.15: Frequency response of S-parameter for the T-junction design problem.

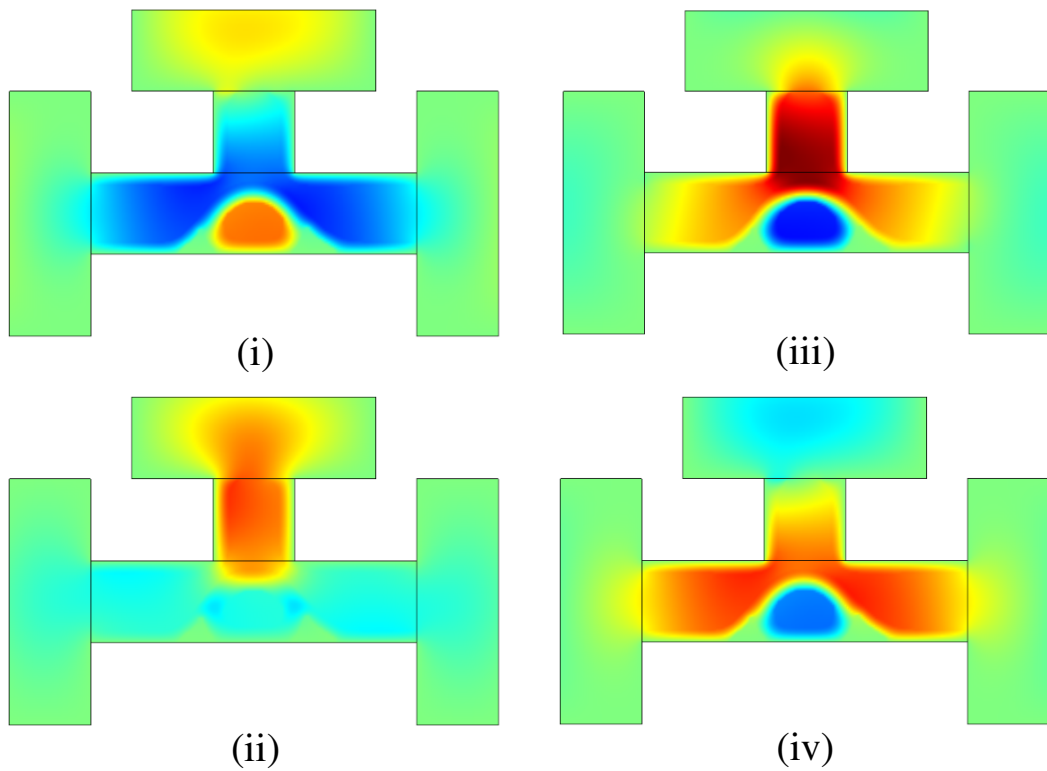


Figure 7.16: Electric field of obtained configuration with phase (i)0, (ii)60, (iii)120 and (iv)180 degree.

Chapter 8

Thesis Conclusions

This thesis focused on topology optimization for the microstructure design of dielectric-based electromagnetic materials that were artificially designed to exhibit desired electromagnetic properties, and for the macrostructure design of electromagnetic devices using a ferrite material. In addition, topology optimization methods that integrate the consideration of various design requirements were also presented. The following is a summary of my achievements.

In Chapter 3, a new formulation that reduces the number of design variables needed in a multiple phase projection method (MPPM) was discussed. This new MPPM formulation requires only a single design variable at each node, rather than the usual two, which advantageously reduces computation time. The proposed method was applied to two minimum mean compliance problems and a compliant mechanism design problem, and appropriate optimized configurations were effectively obtained. Furthermore, the proposed method can successfully control the complexity of optimized configurations by varying the value of the minimum length scale applied in the optimization.

In Chapter 4, a level set-based topology optimization using mathematical programming was offered. The proposed method updates the level set function using mathematical programming, the MMA, to facilitate the treatment of the constraint functionals and applied to minimum mean compliance problems and compliant mechanism design problems, using multiple constraint functionals. These include a mean compliance constraint, so that sufficient stiffness is obtained even when a load is applied in a direction slightly different from its prescribed direction, a mutual mean compliance constraints, so that the structure deforms in a designed direction, and a stress constraint. The optimization results with a mean compliance constraint showed that physically reasonable configurations were obtained, and the reduced mean compliance values when the load was applied in the horizontal direction indicated that the optimal configuration has increased stiffness in the horizontal direction. The deformed shape obtained when a mutual mean compliance constraint was applied showed that the presented method can successfully impose a displacement constraint for the design of a compliant mechanism using a mutual mean compliance constraint. A global stress constraint was applied but because this does not require the satisfaction of the stress constraint at every point in design domain, the optimal configuration does not

strictly satisfy all local stress constraints, even though the global stress constraint is satisfied. However, the maximum stress was effectively reduced in the obtained optimal configuration. Although the optimal configurations contained grayscale areas to some extent, useful optimal configurations can be qualitatively obtained using the proposed method.

In Chapter 5, optimization problems for negative permeability dielectric metamaterials for both two- and three-dimensional problems were formulated to minimize the effective permeability, and to obtain a prescribed effective permeability at a target frequency. A level set-based boundary expression was applied to obtain clear boundaries, and an S-parameter-based approach was applied to compute the effective permeability of the metamaterials. Based on the formulation of the optimization problem, an optimization algorithm was constructed. Several numerical examples for both two- and three-dimensional problems were provided to examine the validity of the presented method. This method successfully found optimized configurations that minimize the effective permeability, and also found optimized configurations that achieve a prescribed degree of effective permeability.

In Chapter 6, a gradient-based topology optimization method was presented and applied to the design of microstructures based on a periodic array of dielectric materials, to achieve desired electric permittivities. A energy-based homogenization method was used to obtain the effective permittivity and the validity of the proposed method was demonstrated through several design problems that dealt with an isotropic material, an anisotropic material, an anisotropic material with a non-zero off-diagonal term, and an anisotropic material with loss. Clear optimized configurations with prescribed electric permittivities were obtained for all the presented cases. Moreover, the theoretical bounds of the two- and three-dimensional anisotropic effective property in the principal direction when the effective property in the other principal direction was set to a prescribed value were derived, to evaluate the effective permittivity values obtained by the optimization. The results showed that the optimized values are in good agreement with theoretical bounds, confirming that this method yields appropriate and useful solutions. Moreover, the Vigdergauz-like optimized structures provide a directly manufacturable alternative to the multi-length scale microstructures described in the literature. This scheme should be directly extendible to designs with more than two constituents, and to metamaterial design.

In Chapter 7, a level set-based topology optimization method was constructed for the layout design of a ferrite material and applied to the design of a cloaking device and a waveguide. Optimization problems were formulated to minimize the norm of the difference between the electric field and a reference field for the cloaking design problem, and to maximize the transmission power for waveguide design problem. Numerical results showed that the presented method successfully found optimized ferrite configurations for the cloaking and waveguide designs.

It is my hope that the research I was able to carry out during my doctoral studies will be useful to other researchers in the field. I look forward to applying what I have learned to the development of more fully optimized devices that provide enhanced performance in a variety of practical applications.

Appendix

A Derivation of first order absorbing boundary condition

Here, the derivation of the first order absorbing boundary condition used in Chapter 5 and 7 is discussed. Although the wave propagate to infinity in most wave propagation problems, the infinite domain must be truncated in the framework of the finite element method. The boundary condition applied to outer boundaries to truncate the infinite domain are called as a radiation condition. Sommerfeld radiation condition are the radiation condition exactly valid at infinity and the first order absorbing boundary condition is the approximation of Sommerfeld radiation condition.

Let medium 1 be a domain inside the design domain, and medium 2 be outside the design domain that is truncated by the absorbing boundary condition. At a source free interface between two media, the following boundary condition for electric and magnetic field must be satisfied [216].

$$\mathbf{n} \times (\mathbf{E}^{(2)} - \mathbf{E}^{(1)}) = 0, \quad (\text{A.1})$$

$$\mathbf{n} \times (\mathbf{H}^{(2)} - \mathbf{H}^{(1)}) = 0. \quad (\text{A.2})$$

where \mathbf{n} is the unit vector normal to the interface. $\mathbf{E}^{(1)}$ and $\mathbf{E}^{(2)}$ are the electric field, and $\mathbf{H}^{(1)}$ and $\mathbf{H}^{(2)}$ are the magnetic field in medium 1 and 2, respectively.

From Faraday's law of Maxwell equations for time-harmonic field, the following relationship between electric and magnetic fields holds.

$$\mathbf{H}^{(i)} = j/(\omega\mu^{(i)}) (\nabla \times \mathbf{E}^{(i)}). \quad (\text{A.3})$$

Substituting Eq.(A.3) into Eq. (A.2),

$$\mathbf{n} \times (j/(\omega\mu^{(2)}) (\nabla \times \mathbf{E}^{(2)}) - j/(\omega\mu^{(1)}) (\nabla \times \mathbf{E}^{(1)})) = 0. \quad (\text{A.4})$$

Considering the waves vertical to the interface in medium 2, and describing it as $\mathbf{E}^{(2)} = \mathbf{E}_0 e^{j(\omega t - k\mathbf{n}\cdot\mathbf{r})}$. Taking the divergence of both sides,

$$\nabla \times \mathbf{E}^{(2)} = -jk\mathbf{n} \times \mathbf{E}_0 e^{j(\omega t - k\mathbf{n}\cdot\mathbf{r})} = -jk\mathbf{n} \times \mathbf{E}^{(2)} \quad (\text{A.5})$$

Substituting Eq.(A.5) into Eq.(A.4), and multiplying it by $j\omega$,

$$j\mathbf{n} \times (k\mu^{(2)^{-1}} (\mathbf{n} \times \mathbf{E}^{(2)})) + \mathbf{n} \times (\mu^{(1)^{-1}} (\nabla \times \mathbf{E}^{(1)})) = 0. \quad (\text{A.6})$$

From Eq.(A.1), $\mathbf{n} \times \mathbf{E}^{(2)} = \mathbf{n} \times \mathbf{E}^{(1)}$. Substituting this relationship into Eq.(A.6), and let $\mu^{(2)} = \mu^{(1)} = \mu$ since the truncated domain has the same material properties.

$$j\mathbf{n} \times (k\mu^{-1} (\mathbf{n} \times \mathbf{E}^{(1)})) + \mathbf{n} \times \mu^{-1} (\nabla \times \mathbf{E}^{(1)}) = 0. \quad (\text{A.7})$$

Let \mathbf{E}^i and \mathbf{E}^{sc} be the incident and scattered field. The total electric field \mathbf{E} is simply obtained as $\mathbf{E} = \mathbf{E}^i + \mathbf{E}^{sc}$. The scattered field \mathbf{E}^{sc} is the field that is to be let propagate to infinity as if there is no interface. Therefore, applying the derived condition Eq.(A.7) for the scattered field \mathbf{E}^{sc} ,

$$j\mathbf{n} \times (k\mu^{-1} (\mathbf{n} \times \mathbf{E}^{sc})) + \mathbf{n} \times \mu^{-1} (\nabla \times \mathbf{E}^{sc}) = 0. \quad (\text{A.8})$$

That is,

$$j\mathbf{n} \times (k\mu^{-1} (\mathbf{n} \times \mathbf{E})) + \mathbf{n} \times \mu^{-1} (\nabla \times \mathbf{E}) = j\mathbf{n} \times (k\mu^{-1} (\mathbf{n} \times \mathbf{E}^i)) + \mathbf{n} \times \mu^{-1} (\nabla \times \mathbf{E}^i) \quad (\text{A.9})$$

Let \mathbf{E}^i be the plane wave in the \mathbf{k} direction, then $\nabla \times \mathbf{E}^i = -jk\mathbf{k} \times \mathbf{E}^i$. Substituting this relationship to Eq.(A.9), the first order absorbing boundary is obtained as follows.

$$\mathbf{n} \times \mu^{-1} (\nabla \times \mathbf{E}) - jk_0 \mathbf{n} \times \left(\sqrt{\epsilon_r \mu_r^{-1}} (\mathbf{E} \times \mathbf{n}) \right) = -\mathbf{n} \times (\mathbf{E}^i \times jk_0 (\mathbf{n} - \mathbf{k})) \quad (\text{A.10})$$

B Derivation of weak formulation

B.1 Two-dimensional case

Here, the weak formulation of the governing equation is derived for the two-dimensional case. Multiplying Eq.(5.1) by a test function \tilde{H}_z , and integrating over domain D , we have,

$$\int_D \tilde{H}_z [\nabla \cdot (\epsilon_r^{-1} \nabla H_z)] d\Omega + \int_D \tilde{H}_z (k_0^2 H_z) d\Omega = 0. \quad (\text{B.1})$$

The first term on the left-hand side of above equation can be transformed as follows, applying the method of integration by parts.

$$\int_D \tilde{H}_z [\nabla \cdot (\epsilon_r^{-1} \nabla H_z)] d\Omega = \int_D \nabla \cdot (\tilde{H}_z \epsilon_r^{-1} \nabla H_z) d\Omega - \int_D \nabla \tilde{H}_z \cdot (\epsilon_r^{-1} \nabla H_z) d\Omega. \quad (\text{B.2})$$

Moreover, the first term on the right-hand side of the above equation can be expressed by a boundary integral, using Gauss's theorem, as follows.

$$\int_D \nabla \cdot (\tilde{H}_z \epsilon_r^{-1} \nabla H_z) d\Omega = \int_\Gamma \tilde{H}_z [\mathbf{n} \cdot (\epsilon_r^{-1} \nabla H_z)] d\Gamma. \quad (\text{B.3})$$

Substituting the above two equations into Eq.(B.1), we obtain,

$$\int_\Gamma \tilde{H}_z [\mathbf{n} \cdot (\epsilon_r^{-1} \nabla H_z)] d\Gamma - \int_D \nabla \tilde{H}_z \cdot (\epsilon_r^{-1} \nabla H_z) d\Omega + k_0^2 \int_D \tilde{H}_z H_z d\Omega = 0. \quad (\text{B.4})$$

Substituting the boundary conditions expressed in Eqs.(B.2)-(B.4) into the boundary integral of the above equation, we obtain the following weak formulation.

$$\int_D \nabla \tilde{H}_z \cdot (\epsilon_r^{-1} \nabla H_z) d\Omega - k_0^2 \int_D \tilde{H}_z H_z d\Omega + jk_0 \int_{\Gamma_1 \cup \Gamma_2} \tilde{H}_z H_z d\Gamma = 2jk_0 \int_{\Gamma_1} H_z^i \tilde{H}_z d\Gamma, \quad (\text{B.5})$$

where the boundary integral for Γ_{PEC} in Eq.(B.4) assumes a value of 0 due to the PEC condition, $\mathbf{n} \cdot (\epsilon_r^{-1} \nabla H_z) = 0$.

B.2 Three-dimensional case

Next, the weak formulation of the governing equation is derived for the three-dimensional case. Multiplying Eq.(5.10) by a test function $\tilde{\mathbf{E}}$, and integrating over domain D , we have,

$$\int_D \tilde{\mathbf{E}} \cdot [\nabla \times (\nabla \times \mathbf{E})] d\Omega - \int_D \tilde{\mathbf{E}} \cdot (k_0^2 \epsilon_r \mathbf{E}) d\Omega = 0. \quad (\text{B.6})$$

Invoking the following vector identity,

$$\tilde{\mathbf{E}} \cdot [\nabla \times (\nabla \times \mathbf{E})] = (\nabla \times \tilde{\mathbf{E}}) \cdot (\nabla \times \mathbf{E}) - \nabla \cdot [\tilde{\mathbf{E}} \times (\nabla \times \mathbf{E})], \quad (\text{B.7})$$

and using Gauss's theorem, we obtain,

$$\int_D \nabla \cdot [\tilde{\mathbf{E}} \times (\nabla \times \mathbf{E})] d\Omega = \int_{\Gamma} \mathbf{n} \cdot [\tilde{\mathbf{E}} \times (\nabla \times \mathbf{E})] d\Gamma \quad (\text{B.8})$$

$$= - \int_{\Gamma} \tilde{\mathbf{E}} \cdot [\mathbf{n} \times (\nabla \times \mathbf{E})] d\Gamma, \quad (\text{B.9})$$

where the vector identity $\mathbf{a} \cdot (\mathbf{b} \times \mathbf{c}) = \mathbf{b} \cdot (\mathbf{c} \times \mathbf{a})$ is applied in the second line of the above equation. Substituting the above two equations into Eq.(B.6), we obtain,

$$\int_D (\nabla \times \tilde{\mathbf{E}}) \cdot (\nabla \times \mathbf{E}) d\Omega + \int_{\Gamma} \tilde{\mathbf{E}} \cdot [\mathbf{n} \times (\nabla \times \mathbf{E})] d\Gamma - \int_D \tilde{\mathbf{E}} \cdot (k_0^2 \epsilon_r \mathbf{E}) d\Omega = 0. \quad (\text{B.10})$$

Substituting the boundary conditions described in Eqs.(5.11)-(5.14) into the boundary integral of the above equation,

$$\begin{aligned} \int_D (\nabla \times \tilde{\mathbf{E}}) \cdot (\nabla \times \mathbf{E}) d\Omega - k_0^2 \int_D \epsilon_r \tilde{\mathbf{E}} \cdot \mathbf{E} d\Omega + jk_0 \int_{\Gamma_1 \cup \Gamma_2} \tilde{\mathbf{E}} \cdot [\mathbf{n} \times (\mathbf{E} \times \mathbf{n})] d\Gamma \\ = 2jk_0 \int_{\Gamma_1} \tilde{\mathbf{E}} \cdot \mathbf{E}^i d\Gamma. \end{aligned} \quad (\text{B.11})$$

Applying the vector identities $\mathbf{a} \cdot (\mathbf{b} \times \mathbf{c}) = \mathbf{b} \cdot (\mathbf{c} \times \mathbf{a})$ and $(\mathbf{a} \times \mathbf{b}) = -(\mathbf{b} \times \mathbf{a})$ for the third term on the left-hand side of the above equation, we obtain the following weak formulation.

$$\begin{aligned} \int_D (\nabla \times \tilde{\mathbf{E}}) \cdot (\nabla \times \mathbf{E}) d\Omega - k_0^2 \int_D \epsilon_r \tilde{\mathbf{E}} \cdot \mathbf{E} d\Omega + jk_0 \int_{\Gamma_1 \cup \Gamma_2} (\mathbf{n} \times \tilde{\mathbf{E}}) \cdot (\mathbf{n} \times \mathbf{E}) d\Gamma \\ = 2jk_0 \int_{\Gamma_1} \tilde{\mathbf{E}} \cdot \mathbf{E}^i d\Gamma \end{aligned} \quad (\text{B.12})$$

We note that the boundary integral in Eq.(B.10) for Γ_{PMC} assumes a value of 0 because $\mathbf{n} \times \mathbf{H} = 0$. That is, $\mathbf{n} \times (\nabla \times \mathbf{E}) = 0$, based on the relationship $\nabla \times \mathbf{E} = -j\omega\mu\mathbf{H}$, which is derived from Faraday's law of Maxwell equations, $\nabla \times \mathbf{E} = -\partial(\mu\mathbf{H})/\partial t$, replacing $\partial/\partial t$ with $j\omega$ for time-harmonic electromagnetic fields. We also note that the same is true for Γ_{PEC} when the Galerkin finite element method is used, where $\mathbf{n} \times \tilde{\mathbf{E}} = 0$ holds on Γ_{PEC} . The integrand of the boundary integral in Eq.(A.10) can be transformed as $\tilde{\mathbf{E}} \cdot [\mathbf{n} \times (\nabla \times \mathbf{E})] = (\mathbf{n} \times \tilde{\mathbf{E}}) \cdot (\nabla \times \mathbf{E})$, applying the vector identity. Thus, the boundary integral for Γ_{PEC} assumes a value of 0 [185, 216].

C Sensitivity analysis of a complex function using the Adjoint Variable Method

In subsection 5.2.4, the sensitivities for the real and the imaginary parts of the objective function are derived simultaneously using the AVM. In this appendix, we show that these sensitivities are equivalent to the sensitivities of the real and imaginary parts obtained individually using the AVM. Although we use the strong form here to clarify the derivation, the equivalence of the sensitivities would be the same for a derivation using the weak form.

Let Ψ be the objective function that has complex values, namely, $\Psi = \Psi' + i\Psi''$. The sensitivities for the real and imaginary parts can be simultaneously obtained following the standard AVM in the following procedure. First, an additional term is added to the original objective function Ψ , as follows.

$$\hat{\Psi} = \Psi(\phi, \mathbf{u}) + \lambda^T (\mathbf{S}\mathbf{u} - \mathbf{f}), \quad (\text{C.1})$$

where ϕ is the design variables, λ is the adjoint variables, \mathbf{S} is the stiffness matrix, and \mathbf{f} is the load vector. The sensitivity of the objective function is then given as,

$$\begin{aligned} \frac{d\hat{\Psi}}{d\phi} &= \frac{\partial\Psi}{\partial\phi} + \frac{\partial\Psi}{\partial\mathbf{u}} \frac{\partial\mathbf{u}}{\partial\phi} + \lambda^T \left(\frac{\partial\mathbf{S}}{\partial\phi} \mathbf{u} + \mathbf{S} \frac{\partial\mathbf{u}}{\partial\phi} - \frac{\partial\mathbf{f}}{\partial\phi} \right) \\ &= \frac{\partial\Psi}{\partial\phi} + \lambda^T \left(\frac{\partial\mathbf{S}}{\partial\phi} \mathbf{u} - \frac{\partial\mathbf{f}}{\partial\phi} \right) + \left(\frac{\partial\Psi}{\partial\mathbf{u}} + \lambda^T \mathbf{S} \right) \frac{\partial\mathbf{u}}{\partial\phi}. \end{aligned} \quad (\text{C.2})$$

The sensitivity can then be written as,

$$\frac{d\hat{\Psi}}{d\phi} = \frac{\partial\Psi}{\partial\phi} + \lambda^T \left(\frac{\partial\mathbf{S}}{\partial\phi} \mathbf{u} - \frac{\partial\mathbf{f}}{\partial\phi} \right), \quad (\text{C.3})$$

where the adjoint variable λ satisfies the following adjoint equation.

$$\mathbf{S}\lambda = - \left(\frac{\partial\Psi}{\partial\mathbf{u}} \right)^T. \quad (\text{C.4})$$

The sensitivities of the real and imaginary parts of the objective function can be obtained by the real and imaginary parts of the obtained sensitivity, respectively.

Next, we consider the sensitivities for the real and imaginary parts of the objective function Ψ individually, and show that the obtained sensitivities are the same as the real and imaginary parts of the sensitivity obtained by Eq.(C.3). First, we derive the sensitivity for the real part of the objective function Ψ' . Following the AVM, two extra terms are added to the original objective function in order to cancel out the imaginary part, as follows [55, 60], in the case where the response of the governing equation u is a complex function, namely $u = u' + iu''$.

$$\hat{\Psi}' = \Psi'(\phi, \mathbf{u}', \mathbf{u}'') + \lambda_R^T (\mathbf{S}\mathbf{u} - \mathbf{f}) + \bar{\lambda}_R^T (\bar{\mathbf{S}}\bar{\mathbf{u}} - \bar{\mathbf{f}}), \quad (\text{C.5})$$

where λ_R is the adjoint variable and subscript R indicates the correspondence to the real part of objective function. $\bar{\lambda}_R$ denotes the complex conjugate of λ_R . The sensitivity of the objective function is then given as,

$$\begin{aligned} \frac{d\hat{\Psi}'}{d\phi} &= \frac{\partial\Psi'}{\partial\phi} + \frac{\partial\Psi'}{\partial\mathbf{u}'} \frac{\partial\mathbf{u}'}{\partial\phi} + \frac{\partial\Psi'}{\partial\mathbf{u}''} \frac{\partial\mathbf{u}''}{\partial\phi} \\ &+ \lambda_R^T \left(\frac{\partial\mathbf{S}}{\partial\phi} \mathbf{u}' + \mathbf{S} \frac{\partial\mathbf{u}'}{\partial\phi} + i \frac{\partial\mathbf{S}}{\partial\phi} \mathbf{u}'' + i\mathbf{S} \frac{\partial\mathbf{u}''}{\partial\phi} - \frac{\partial\mathbf{f}}{\partial\phi} \right) \\ &+ \bar{\lambda}_R^T \left(\frac{\partial\bar{\mathbf{S}}}{\partial\phi} \mathbf{u}' + \bar{\mathbf{S}} \frac{\partial\mathbf{u}'}{\partial\phi} - i \frac{\partial\bar{\mathbf{S}}}{\partial\phi} \mathbf{u}'' - i\bar{\mathbf{S}} \frac{\partial\mathbf{u}''}{\partial\phi} - \frac{\partial\bar{\mathbf{f}}}{\partial\phi} \right). \end{aligned} \quad (\text{C.6})$$

Rearranging the above equation, we obtain following.

$$\begin{aligned} \frac{d\hat{\Psi}'}{d\phi} &= \frac{\partial\Psi'}{\partial\phi} + \lambda_R^T \left(\frac{\partial\mathbf{S}}{\partial\phi} \mathbf{u}' + i \frac{\partial\mathbf{S}}{\partial\phi} \mathbf{u}'' - \frac{\partial\mathbf{f}}{\partial\phi} \right) + \bar{\lambda}_R^T \left(\frac{\partial\bar{\mathbf{S}}}{\partial\phi} \mathbf{u}' - i \frac{\partial\bar{\mathbf{S}}}{\partial\phi} \mathbf{u}'' - \frac{\partial\bar{\mathbf{f}}}{\partial\phi} \right) \\ &+ \left(\frac{\partial\Psi'}{\partial\mathbf{u}'} + \lambda_R^T \mathbf{S} + \bar{\lambda}_R^T \bar{\mathbf{S}} \right) \frac{\partial\mathbf{u}'}{\partial\phi} + \left(\frac{\partial\Psi'}{\partial\mathbf{u}''} + i\lambda_R^T \mathbf{S} - i\bar{\lambda}_R^T \bar{\mathbf{S}} \right) \frac{\partial\mathbf{u}''}{\partial\phi} \end{aligned} \quad (\text{C.7})$$

To delete the $\frac{\partial\mathbf{u}'}{\partial\phi}$ and $\frac{\partial\mathbf{u}''}{\partial\phi}$ terms, the following two equations must be satisfied.

$$\lambda_R^T \mathbf{S} + \bar{\lambda}_R^T \bar{\mathbf{S}} = -\frac{\partial\Psi'}{\partial\mathbf{u}'} \quad (\text{C.8})$$

$$i\lambda_R^T \mathbf{S} - i\bar{\lambda}_R^T \bar{\mathbf{S}} = -\frac{\partial\Psi'}{\partial\mathbf{u}''} \quad (\text{C.9})$$

From the above equations, the following two adjoint equations are obtained.

$$\mathbf{S}\lambda_R = -\frac{1}{2} \left(\frac{\partial\Psi'}{\partial\mathbf{u}'} - i \frac{\partial\Psi'}{\partial\mathbf{u}''} \right)^T \quad (\text{C.10})$$

$$\bar{\mathbf{S}}\bar{\lambda}_R = -\frac{1}{2} \left(\frac{\partial\Psi'}{\partial\mathbf{u}'} + i \frac{\partial\Psi'}{\partial\mathbf{u}''} \right)^T \quad (\text{C.11})$$

The above two adjoint equations are equivalent, so λ_R can be obtained by solving Eq.(C.10). Finally, the sensitivity for the real part is obtained as follows.

$$\frac{d\hat{\Psi}'}{d\phi} = \frac{\partial\Psi'}{\partial\phi} + \lambda_R^T \left(\frac{\partial\mathbf{S}}{\partial\phi} \mathbf{u} - \frac{\partial\mathbf{f}}{\partial\phi} \right) + \bar{\lambda}_R^T \left(\frac{\partial\bar{\mathbf{S}}}{\partial\phi} \bar{\mathbf{u}} - \frac{\partial\bar{\mathbf{f}}}{\partial\phi} \right), \quad (\text{C.12})$$

where

$$\mathbf{S}\lambda_R = -\frac{1}{2} \left(\frac{\partial\Psi'}{\partial\mathbf{u}'} - i \frac{\partial\Psi'}{\partial\mathbf{u}''} \right)^T. \quad (\text{C.13})$$

Following the same procedure, the sensitivity for the imaginary part of the objective function is obtained as follows.

$$\frac{d\hat{\Psi}''}{d\phi} = \frac{\partial\Psi''}{\partial\phi} + \lambda_I^T \left(\frac{\partial\mathbf{S}}{\partial\phi} \mathbf{u} - \frac{\partial\mathbf{f}}{\partial\phi} \right) + \bar{\lambda}_I^T \left(\frac{\partial\bar{\mathbf{S}}}{\partial\phi} \bar{\mathbf{u}} - \frac{\partial\bar{\mathbf{f}}}{\partial\phi} \right), \quad (\text{C.14})$$

where λ_I is the adjoint variable that corresponds to the imaginary part of the objective function, and

$$\mathbf{S}\lambda_I = -\frac{1}{2} \left(\frac{\partial \Psi''}{\partial \mathbf{u}'} - i \frac{\partial \Psi''}{\partial \mathbf{u}''} \right)^T. \quad (\text{C.15})$$

Multiplying Eq.(C.14) by i and adding the result to Eq.(C.12), we obtain

$$\begin{aligned} \frac{d\hat{\Psi}'}{d\phi} + i \frac{d\hat{\Psi}''}{d\phi} &= \frac{\partial \Psi'}{\partial \phi} + i \frac{\partial \Psi''}{\partial \phi} \\ &+ (\lambda_R + i\lambda_I)^T \left(\frac{\partial \mathbf{S}}{\partial \phi} \mathbf{u} - \frac{\partial \mathbf{f}}{\partial \phi} \right) + (\bar{\lambda}_R + i\bar{\lambda}_I)^T \left(\frac{\partial \bar{\mathbf{S}}}{\partial \phi} \bar{\mathbf{u}} - \frac{\partial \bar{\mathbf{f}}}{\partial \phi} \right). \end{aligned} \quad (\text{C.16})$$

Considering the conjugate form of Eq.(C.13) and Eq.(C.15),

$$\bar{\mathbf{S}}\bar{\lambda}_R = -\frac{1}{2} \left(\frac{\partial \Psi'}{\partial \mathbf{u}'} + i \frac{\partial \Psi'}{\partial \mathbf{u}''} \right)^T \quad (\text{C.17})$$

$$\bar{\mathbf{S}}\bar{\lambda}_I = -\frac{1}{2} \left(\frac{\partial \Psi''}{\partial \mathbf{u}'} + i \frac{\partial \Psi''}{\partial \mathbf{u}''} \right)^T. \quad (\text{C.18})$$

Multiplying Eq.(C.18) by i and adding the result to Eq.(C.17), we obtain the following.

$$\begin{aligned} \bar{\mathbf{S}}(\bar{\lambda}_R + i\bar{\lambda}_I) &= -\frac{1}{2} \left(\left(\frac{\partial \Psi'}{\partial \mathbf{u}'} + i \frac{\partial \Psi'}{\partial \mathbf{u}''} \right) + i \left(\frac{\partial \Psi''}{\partial \mathbf{u}'} + i \frac{\partial \Psi''}{\partial \mathbf{u}''} \right) \right)^T \\ &= -\frac{1}{2} \left(\left(\frac{\partial \Psi'}{\partial \mathbf{u}'} + i \frac{\partial \Psi''}{\partial \mathbf{u}'} \right) + i \left(\frac{\partial \Psi'}{\partial \mathbf{u}''} + i \frac{\partial \Psi''}{\partial \mathbf{u}''} \right) \right)^T \\ &= -\frac{1}{2} \left(\frac{\partial \Psi}{\partial \mathbf{u}'} + i \frac{\partial \Psi}{\partial \mathbf{u}''} \right)^T \end{aligned} \quad (\text{C.19})$$

When Ψ can be expressed explicitly using \mathbf{u} (without using \mathbf{u}' and/or \mathbf{u}''), the following relationships hold.

$$\frac{\partial \Psi}{\partial \mathbf{u}'} = \frac{\partial \Psi}{\partial \mathbf{u}} \frac{\partial \mathbf{u}}{\partial \mathbf{u}'} = \frac{\partial \Psi}{\partial \mathbf{u}} \quad (\text{C.20})$$

$$\frac{\partial \Psi}{\partial \mathbf{u}''} = \frac{\partial \Psi}{\partial \mathbf{u}} \frac{\partial \mathbf{u}}{\partial \mathbf{u}''} = i \frac{\partial \Psi}{\partial \mathbf{u}} \quad (\text{C.21})$$

Substituting the above equations into Eq.(C.19),

$$\bar{\mathbf{S}}(\bar{\lambda}_R + i\bar{\lambda}_I) = -\frac{1}{2} \left(\frac{\partial \Psi}{\partial \mathbf{u}} - \frac{\partial \Psi}{\partial \mathbf{u}} \right)^T = 0. \quad (\text{C.22})$$

Therefore, $\bar{\lambda}_R + i\bar{\lambda}_I = 0$, because the stiffness matrix \mathbf{S} is a full-rank matrix. Substituting this into Eq.(C.16), we obtain,

$$\frac{d\hat{\Psi}}{d\phi} = \frac{\partial \Psi}{\partial \phi} + \lambda^T \left(\frac{\partial \mathbf{S}}{\partial \phi} \mathbf{u} - \frac{\partial \mathbf{f}}{\partial \phi} \right), \quad (\text{C.23})$$

where $\lambda = \lambda_R + i\lambda_I$. Eq.(C.23) is equivalent to Eq.(C.3). In addition, the adjoint variable λ is obtained as follows. Multiplying Eq.(C.13) by i and adding the result to Eq.(C.15), we have,

$$\begin{aligned} \mathbf{S}(\lambda_R + i\lambda_I) &= -\frac{1}{2} \left(\left(\frac{\partial \Psi'}{\partial \mathbf{u}'} - i \frac{\partial \Psi'}{\partial \mathbf{u}''} \right) + i \left(\frac{\partial \Psi''}{\partial \mathbf{u}'} - i \frac{\partial \Psi''}{\partial \mathbf{u}''} \right) \right)^T \\ &= -\frac{1}{2} \left(\frac{\partial \Psi}{\partial \mathbf{u}'} - i \frac{\partial \Psi}{\partial \mathbf{u}''} \right)^T. \end{aligned} \quad (\text{C.24})$$

Using the same relationships for Eqs.(C.20) and (C.21),

$$\mathbf{S}\lambda = - \left(\frac{\partial \Psi}{\partial \mathbf{u}} \right)^T. \quad (\text{C.25})$$

Thus, Eq.(C.25) is equivalent to Eq.(C.4).

List of Figures

2.1	Fixed design domain D	10
2.2	Fixed design domain D and level set function ϕ	12
3.1	Domain showing constraint according to a minimum length scale. . .	16
3.2	Smoothed Heaviside functions for μ^e	17
3.3	Approximated absolute value.	21
3.4	Flowchart of the optimization procedure.	22
3.5	Flowchart of the parameter updating scheme.	22
3.6	Design domain and boundary conditions for minimum mean compliance problem.	23
3.7	Configuration using the proposed MPPM before removing grayscales.	24
3.8	Distribution of design variable ϕ using the proposed MPPM.	24
3.9	Optimal configurations obtained under various conditions.	25
3.10	Optimal configurations via the proposed MPPM with various d_{\min} values.	26
3.11	Design domain and boundary conditions for second minimum mean compliance problem.	27
3.12	Optimal configurations for second minimum mean compliance problem via the proposed MPPM with various magnitudes of d_{\min}	27
3.13	Design domain and boundary conditions for compliant mechanism design problem.	28
3.14	Optimal configurations for compliant mechanism design problem via the proposed MPPM with various magnitudes of d_{\min}	28
4.1	Optimization flowchart.	37
4.2	Design domain and boundary conditions of for minimum mean compliance problem.	38
4.3	Optimal configurations and shape evolution for different τ values: (a) $\tau = 7.0 \times 10^{-4}$; (b) $\tau = 3.0 \times 10^{-4}$; (c) $\tau = 7.0 \times 10^{-5}$	39
4.4	Fixed design domain and boundary conditions for second minimum mean compliance problem.	40
4.3	Initial configurations, intermediate results, and optimal configurations using three different initial configurations: (a) the configuration filled with material; (b) the configuration with 18 holes; (c) the configuration asymmetrically filled in the lower half of the fixed design domain.	40
4.4	Optimal configurations for different magnitudes of τ : (a) $\tau = 1.0 \times 10^{-5}$; (b) $\tau = 7.0 \times 10^{-6}$; (c) $\tau = 4.0 \times 10^{-6}$	40

4.5	Obtained configurations that include a mean compliance constraint under horizontal loads for different magnitude of α : (a) constraint is not applied; (b) $\alpha=2.0$; (c) $\alpha=1.0$	41
4.6	Fixed design domain and boundary conditions for compliant mechanism design problem with a mutual mean compliance constraint.	42
4.7	Optimal configurations and its deformed shape of a compliant mechanism design problem: (a) without mutual mean compliance constraint; (c) deformed shape of (a); (b) with mutual mean compliance constraint; (d) deformed shape of (b).	43
4.8	Design domain and boundary conditions for minimum mean compliance problem with a stress constraint.	44
4.9	Comparison of optimal configurations and stress distributions: (a) without stress constraint; (b) with stress constraint.	45
4.10	Comparison of density and stress distributions: (a) optimization results with stress constraint; (b) distributions after removing grayscale areas.	45
4.11	Design domain and boundary conditions for second minimum mean compliance problem with a stress constraint.	46
4.12	Comparison of optimal configurations and stress distributions: (a) without stress constraint; (b) with stress constraint.	47
4.13	Comparison of density and stress distributions: (a) optimization results with stress constraint; (b) distributions after removing grayscale areas.	47
4.14	Fixed design domain and boundary conditions for compliant mechanism design problem with a stress constraint.	48
4.15	Optimal configurations: (a) without stress constraint; (c) von Mises stress distribution of (a); (b) with stress constraint; (d) von Mises stress distribution of (b).	48
4.16	(a) Optimal configuration density distribution; (b) von Mises stress distribution of (a); (b) Configuration after removing grayscale areas; (d) von Mises stress distribution of (b).	49
5.1	(a) Design domain and boundary conditions; (b) periodic structure for two-dimensional problem.	54
5.2	(a) Design domain and boundary conditions; (b) periodic structure for three-dimensional problem.	56
5.3	(a) A typical effective permeability curve; (b) effective permeability curve when real part of effective permeability is minimized directly; (c) 1 st stage; (d) 2 nd stage of two-stage optimization procedure.	59
5.4	Design domain and boundary conditions for two-dimensional problem.	65
5.5	Comparison of configurations from 1 st optimization stage for two-dimensional effective permeability minimization problem targeting 0.30THz: (a) initial; (b) obtained configuration	66
5.6	Effective permeability curves of 1 st optimization stage for two-dimensional effective permeability minimization problem targeting 0.30THz.	67

5.7	Convergence history of objective function of 1 st optimization stage for two-dimensional effective permeability minimization problem targeting 0.30THz.	67
5.8	Comparison of configurations from 2 nd optimization stage for two-dimensional effective permeability minimization problem targeting 0.30THz: (a) initial; (b) obtained configuration.	68
5.9	Effective permeability curves for 2 nd optimization stage for two-dimensional effective permeability minimization problem targeting 0.30THz.	69
5.10	Convergence history of objective function of 2 nd stage for two-dimensional effective permeability minimization problem targeting 0.30THz.	69
5.11	Magnetic and electric field distributions for two-dimensional effective permeability minimization problem targeting 0.30THz: (a) initial; (b) optimized.	70
5.12	Comparison of configurations for two-dimensional effective permeability minimization problem targeting 0.45THz: (a) initial; (b) optimized.	71
5.13	Effective permeability curves for two-dimensional effective permeability minimization problem targeting 0.45THz.	71
5.14	Convergence histories of objective function for two-dimensional effective permeability minimization problem targeting 0.45THz: (a) 1 st optimization stage; (b) 2 nd optimization stage.	72
5.15	Magnetic and electric field distributions for two-dimensional effective permeability minimization problem targeting 0.45THz: (a) initial; (b) optimized.	72
5.16	Comparison of configurations for two-dimensional effective permeability design problem: (a) initial; (b) optimized.	74
5.17	Effective permeability curves for two-dimensional effective permeability design problem.	74
5.18	Convergence history of objective function of 2 nd optimization stage for two-dimensional effective permeability design problem.	75
5.19	Magnetic and electric field distributions for two-dimensional effective permeability minimization problem targeting 0.30THz: (a) initial; (b) optimized.	75
5.20	Comparison of configurations for two-dimensional effective permeability minimization problem targeting 0.30THz: (a) initial; (b) optimized.	76
5.21	Effective permeability curves for two-dimensional effective permeability minimization problem targeting 0.30THz.	77
5.22	Convergence histories of objective function for two-dimensional effective permeability minimization problem targeting 0.30THz: (a) 1 st optimization stage; (b) 2 nd optimization stage.	77
5.23	Magnetic and electric field distributions for two-dimensional effective permeability minimization problem targeting 0.30THz: (a) initial; (b) optimized.	78
5.24	Comparison of configurations for two-dimensional effective permeability minimization problem targeting 0.45THz: (a) initial; (b) optimized.	79

5.25	Effective permeability curves for two-dimensional effective permeability minimization problem targeting 0.45THz.	79
5.26	Convergence histories of objective function for two-dimensional effective permeability minimization problem targeting 0.45THz: (a) 1 st optimization stage; (b) 2 nd optimization stage.	80
5.27	Magnetic and electric field distributions for two-dimensional effective permeability minimization problem targeting 0.45THz: (a) initial; (b) optimized.	80
5.28	Design domain and boundary conditions for three-dimensional design problem.	81
5.29	Comparison of configurations for three-dimensional effective permeability minimization problem targeting 0.30THz: (a) initial; (b) optimized.	82
5.30	Effective permeability curves for three-dimensional effective permeability minimization problem targeting 0.30THz.	82
5.31	Convergence histories of objective function for three-dimensional effective permeability minimization problem targeting 0.30THz: (a) 1 st optimization stage; (b) 2 nd optimization stage of the optimization.	83
5.32	Comparison of configurations for three-dimensional effective permeability minimization problem targeting 0.45THz: (a) initial; (b) optimized.	84
5.33	Effective permeability curves for three-dimensional effective permeability minimization problem targeting 0.45THz.	84
5.34	Convergence histories of objective function for three-dimensional effective permeability minimization problem targeting 0.45THz: (a) 1 st optimization stage; (b) 2 nd optimization stage.	85
6.1	Analysis model and boundary conditions for the case of an electric voltage applied in (a) the horizontal direction, and (b) the vertical direction.	90
6.2	Bounds of effective permittivity for two constituent materials with properties $\epsilon_1 = -2 + 3i$ and $\epsilon_2 = 1 + 1i$. In the absence of specific information concerning the dielectric materials, the effective permittivity is confined to the region Ω . If the volume fraction of phase 1 is $f_1 = 0.6$, the effective permittivity is confined to the region Ω' . Furthermore, if the composite is a two-dimensional isotropic material, the effective permittivity is confined to the region Ω''	93
6.3	Laminate model.	94
6.4	Cross section of the coated elliptic assemblage.	94
6.5	Cross section of the coated cylindrical assemblage.	95
6.6	Flowchart of optimization algorithm.	98

6.7	Comparison of effective permittivity values obtained using asymptotic expansion-based and energy-based approaches for composites made from a single dielectric material (black: $\epsilon_1=100$) and air (white: $\epsilon_0=1$): (a) inclusions with a cylindrical hole, (b) cylindrical inclusions, (c) vertically oriented laminates and (d) vertically oriented laminates rotated 26.57 degrees in the counterclockwise direction.	100
6.8	Optimized configuration of isotropic material design problem for volume fraction $V_{\max} = 0.825$ of $\epsilon_1 = 100$ (black), and $\epsilon_0 = 1$ (white). The targets are $\epsilon_{\text{tar},11} = \epsilon_{\text{tar},22} = 70$ and the achieved properties are $\epsilon_{\text{eff},11} = \epsilon_{\text{eff},22} = 70$	100
6.9	Optimized configuration of the anisotropic material design problem for volume fraction $V_{\max} = 0.76$ of $\epsilon_1 = 100$ (black), and $\epsilon_0 = 1$ (white). The targets are $\epsilon_{\text{tar},11} = 45$ and $\epsilon_{\text{tar},22} = 70$ and the achieved properties are $\epsilon_{\text{eff},11} = 45.00$ and $\epsilon_{\text{eff},22} = 70.00$	101
6.10	Theoretical bounds for isotropic and anisotropic material design problems with properties $\epsilon_1 = 100$ and $\epsilon_0 = 1$. The solid and dashed lines show the theoretical bounds for isotropic and anisotropic material, respectively. The dot-dashed line plots the upper and lower limit of the permittivity of the anisotropic material versus the volume fraction when $\epsilon_{22} = 70$. The effective permittivity of the optimized configuration, $\epsilon_{\text{eff},11} = \epsilon_{\text{eff},22} = 70.00$, of Subsection 6.5.2is shown as the black square, and the effective permittivity of the optimized configuration, $\epsilon_{\text{eff},11} = 45.00$ and $\epsilon_{\text{eff},22} = 70.00$, of Subsection 6.5.3is shown as the black dot, for comparison with the theoretical bound curve.	102
6.11	The optimized configuration of the anisotropic material design problem with nonzero off-diagonal terms for volume fraction $V_{\max} = 0.69$ of $\epsilon_1 = 240$ (black), and $\epsilon_0 = 20$ (white). The targets are $\epsilon_{\text{tar},11} = 159.64$, $\epsilon_{\text{tar},22} = 90.36$ and $\epsilon_{\text{tar},12} = \epsilon_{\text{tar},21} = -20.00$ and the achieved properties are $\epsilon_{\text{eff},11} = 159.63$, $\epsilon_{\text{eff},22} = 90.36$ and $\epsilon_{\text{eff},12} = \epsilon_{\text{eff},21} = -20.00$	103
6.12	Theoretical bounds for anisotropic material designs with properties $\epsilon_1 = 240$ and $\epsilon_0 = 20$. The solid and dashed lines show the theoretical bounds for isotropic and anisotropic material, respectively. The dot-dashed line plots the upper limit of the permittivity of the anisotropic material versus the volume fraction when $\epsilon_{22} = 85$. The effective permittivity of the optimized configuration, $\epsilon_{\text{eff},11} = 164.99$ and $\epsilon_{\text{eff},22} = 85.00$, in the principal direction is shown as the black dot for comparison with the theoretical bound curve.	104
6.13	Theoretical bounds for lossy materials with properties $\epsilon_1 = 2 + 1i$ and $\epsilon_0 = 1$. The solid line shows the theoretical bounds for two constituent materials, and the dashed-dot line and dashed line show the theoretical bounds for anisotropic and isotropic material with a volume fraction of 50%, respectively. The black dots indicate the target values used in the optimization in Section 6.5.5.	105

6.14	The optimized configuration of a lossy material design problem: target1, for volume fraction $V_{\max} = 0.5$ of $\epsilon_1 = 2 + 1i$ (black - lossy material) and $\epsilon_0 = 1$ (white). The target is $\epsilon_{\text{tar},11} = 1.5 + 0.5i$ and the obtained properties are $\epsilon_{\text{eff},11} = 1.500 + 0.500i$, $\epsilon_{\text{eff},22} = 1.400 + 0.200i$, and $\epsilon_{\text{eff},12} = \epsilon_{\text{eff},21} = 0.0$	106
6.15	The optimized configuration of a maximum loss material design problem: target2, for volume fraction $V_{\max} = 0.5$ of $\epsilon_1 = 2 + 1i$ (black - lossy material) and $\epsilon_0 = 1$ (white). The target is $\epsilon_{\text{tar},11} = \epsilon_{\text{tar},22} = 1.448 + 0.379i$ and the obtained properties are $\epsilon_{\text{eff},11} = \epsilon_{\text{eff},22} = 1.446 + 0.377i$ and $\epsilon_{\text{eff},12} = \epsilon_{\text{eff},21} = 0.0$	106
6.16	The optimized configuration of a minimum loss material design problem: target3, for volume fraction $V_{\max} = 0.5$ of $\epsilon_1 = 2 + 1i$ (black - lossy material) and $\epsilon_0 = 1$ (white). The target is $\epsilon_{\text{tar},11} = \epsilon_{\text{tar},22} = 1.462 + 0.308i$ and the obtained properties are $\epsilon_{\text{eff},11} = \epsilon_{\text{eff},22} = 1.459 + 0.308i$ and $\epsilon_{\text{eff},12} = \epsilon_{\text{eff},21} = 0.0$	106
6.17	(a) The rod-shaped initial configuration, and (b) the optimized configuration of an anisotropic lossy material design problem, for $\epsilon_1 = 140 - 0.196i$ (black) and $\epsilon_0 = 20 - 0.012i$ (white). The target is $\epsilon_{\text{tar},11} = 60.00 - 0.060i$ and $\epsilon_{\text{tar},22} = 70.00 - 0.080i$, and the obtained properties are $\epsilon_{\text{eff},11} = 59.80 - 0.060i$, $\epsilon_{\text{eff},22} = 69.64 - 0.080i$ and $\epsilon_{\text{eff},12} = \epsilon_{\text{eff},21} = 0.0$	108
6.18	(a) The cross-shaped initial configuration, and (b) the optimized configuration of an anisotropic lossy material design problem for $\epsilon_1 = 140 - 0.196i$ (black) and $\epsilon_0 = 20 - 0.012i$ (white). The target is $\epsilon_{\text{tar},11} = 60.00 - 0.060i$ and $\epsilon_{\text{tar},22} = 70.00 - 0.080i$, and the obtained properties are $\epsilon_{\text{eff},11} = 59.97 - 0.060i$, $\epsilon_{\text{eff},22} = 70.00 - 0.080i$ and $\epsilon_{\text{eff},12} = \epsilon_{\text{eff},21} = 0.0$	108
6.19	(a) The initial configuration in which the density gradually changes over the design domain, and (b) the optimized configuration of an anisotropic lossy material design problem, for $\epsilon_1 = 140 - 0.196i$ (black) and $\epsilon_0 = 20 - 0.012i$ (white). The target is $\epsilon_{\text{eff},11} = 60.00 - 0.060i$ and $\epsilon_{\text{eff},22} = 70.00 - 0.080i$, and the obtained properties are $\epsilon_{\text{eff},11} = 60.00 - 0.060i$, $\epsilon_{\text{eff},22} = 69.82 - 0.080i$ and $\epsilon_{\text{eff},12} = \epsilon_{\text{eff},21} = 0.0$	108
6.20	Theoretical bounds of anisotropic lossy material with properties $\epsilon_1 = 140 - 0.196i$ and $\epsilon_0 = 20 - 0.012i$. The solid line shows the theoretical bounds for two constituent materials, and the dashed-dot line shows the theoretical bounds for an anisotropic material with a volume fraction of 61.5%. Two black dots show the effective permittivity of the optimized configuration when using the cross-shaped initial configuration.	109
6.21	Optimized configuration of the three-dimensional permeability maximization problem: (a) isotropic case, (b) anisotropic case.	111

6.22	Theoretical bounds for isotropic and anisotropic material design problems with properties $\epsilon_1 = 100$ and $\epsilon_0 = 1$. The solid and dashed lines show the theoretical bounds for isotropic and anisotropic material, respectively. The dot-dashed line plots the upper and lower limit of the permittivity of the anisotropic material versus the volume fraction.	111
7.1	(a) Cylindrical cloak model and (b) optimized configuration of ferrite material.	120
7.2	Total electric field of carpet cloak design problem: (a) no cloak, namely no external magnetic field; (b) optimized cloak.	120
7.3	Norm of the difference between electric field and reference electric field of carpet cloak design problem: (a) no cloak, namely no external magnetic field; (b) optimized cloak.	121
7.4	(a) Carpet cloak model and (b) optimized configuration of ferrite material.	122
7.5	Reference electric field for carpet cloak design problem.	122
7.6	Total electric field of carpet cloak design problem: (a) no cloak, namely no external magnetic field; (b) optimized cloak.	122
7.7	Norm of the difference between electric field and reference electric field of carpet cloak design problem: (a) no cloak, namely no external magnetic field; (b) optimized cloak.	123
7.8	Design domain and boundary conditions for waveguide filter design problem.	123
7.9	Obtained optimized configuration of waveguide filter design problem, maximizing S_{21}	124
7.10	Frequency characteristic of S_{11} and S_{21} , obtained using the initial and optimized configurations.	124
7.11	Frequency characteristic of S_{21} , obtained using the optimized configuration, with applied magnetic field $\mu_0 H_0 = 30, 60, 90\text{mT}$	125
7.12	Electric field of optimized configuration at 2.0 GHz for various phases of incident waves: (a) 0° ; (b) 60° ; (c) 120° ; (d) 180°	126
7.13	The model for T-junction design problem.	126
7.14	Optimized configuration of T-junction design problem.	126
7.15	Frequency response of S-parameter for the T-junction design problem.	127
7.16	Electric field of obtained configuration with phase (i)0, (ii)60, (iii)120 and (iv)180 degree.	127

References

- [1] L. A. Schmit, Structural design by systematic synthesis, Proceeding of 2nd Conference on Electronic Computation ASCE, New York (1960) 105–122.
- [2] W. Prager, A note on discretized michell structures, Computer Methods in Applied Mechanics and Engineering 3 (3) (1974) 349–355.
- [3] R. H. Gallagher, O. C. Zienkiewicz, Optimum Structural Design - Theory and Applications, John Wiley & Sons., 1977.
- [4] M. H. Imam, Three-dimensional shape optimization, International Journal for Numerical Methods in Engineering 18 (5) (1982) 661–673.
- [5] O. Pironneau, Optimal shape design for elliptic systems, Springer-Verlag, Berlin, 1984.
- [6] M. P. Bendsøe, N. Kikuchi, Generating optimal topologies in structural design using a homogenization method, Computer Methods in Applied Mechanics and Engineering 71 (2) (1988) 197–224.
- [7] M. P. Bendsøe, Optimal shape design as a material distribution problem, Structural and Multidisciplinary Optimization 1 (4) (1989) 193–202.
- [8] G. Allaire, Shape optimization by the homogenization method, Springer-Verlag, 2002.
- [9] M. P. Bendsøe, O. Sigmund, Topology Optimization: Theory, Methods, and Applications, Springer-Verlag, Berlin, 2004.
- [10] F. Murat, L. Tartar, Optimality conditions and homogenization, Proceedings of Nonlinear Variational Problems, A. Mario, L. Modica, S. Spagnolo and M. Degiovanni (Eds), Pitman Publishing Program, Boston, (1985) 1–8.
- [11] O. Sigmund, J. Petersson, Numerical instabilities in topology optimization: a survey on procedures dealing with checkerboards, mesh-dependencies and local minima, Structural and Multidisciplinary Optimization 16 (1) (1998) 68–75.
- [12] O. Sigmund, Morphology-based black and white filters for topology optimization, Structural and Multidisciplinary Optimization 33 (4–5) (2007) 401–424.

- [13] L. Ambrosio, G. Buttazzo, An optimal design problem with perimeter penalization, *Calculus of Variations and Partial Differential Equations* 1 (1) (1993) 55–69.
- [14] R. B. Haber, C. S. Jog, M. P. Bendsøe, A new approach to variable-topology shape design using a constraint on perimeter, *Structural and Multidisciplinary Optimization* 11 (1–2) (1996) 1–12.
- [15] J. Petersson, O. Sigmund, Slope constrained topology optimization, *International Journal for Numerical Methods in Engineering* 41 (8) (1998) 1417–1434.
- [16] M. Zhou, Y. K. Shyy, H. L. Thomas, Checkerboard and minimum member size control in topology optimization, *Structural and Multidisciplinary Optimization* 21 (2) (2001) 152–158.
- [17] T. Borrvall, J. Petersson, Topology optimization using regularized intermediate density control, *Computer Methods in Applied Mechanics and Engineering* 190 (37–38) (2001) 4911–4928.
- [18] T. A. Poulsen, A new scheme for imposing a minimum length scale in topology optimization, *International Journal for Numerical Methods in Engineering* 57 (6) (2003) 741–760.
- [19] O. Sigmund, Design of material structures using topology optimization, PhD thesis, Department of Solid Mechanics, The Danish Center for Applied Mathematics and Mechanics, DCAMM Special Report No. S69, 1994.
- [20] O. Sigmund, On the design of compliant mechanisms using topology optimization, *Mechanics of Structures and Machines* 25 (4) (1997) 493–524.
- [21] T. E. Bruns, D. A. Tortorelli, Topology optimization of non-linear elastic structures and compliant mechanisms, *Computer Methods in Applied Mechanics and Engineering* 190 (26–27) (2001) 3443–3459.
- [22] B. Bourdin, Filters in topology optimization, *International Journal for Numerical Methods in Engineering* 50 (9) (2001) 2143–2158.
- [23] M. Y. Wang, S. Wang, Bilateral filtering for structural topology optimization, *International Journal for Numerical Methods in Engineering* 63 (13) (2005) 1911–1938.
- [24] J. K. Guest, J. H. Prévost, T. Belytschko, Achieving minimum length scale in topology optimization using nodal design variables and projection functions, *International Journal for Numerical Methods in Engineering* 61 (2) (2004) 238–254.
- [25] G. Kreisselmeier, R. Steinhauser, Application of vector performance optimization to a robust-control loop design for a fighter aircraft, *International Journal of Control* 37 (2) (1983) 251–284.

- [26] S. R. M. Almeida, G. H. Paulino, E. C. N. Silva, A simple and effective inverse projection scheme for void distribution control in topology optimization, *Structural and Multidisciplinary Optimization* 39 (4) (2009) 359–371.
- [27] J. K. Guest, Topology optimization with multiple phase projection, *Computer Methods in Applied Mechanics and Engineering* 199 (1–4) (2009) 123–135.
- [28] J. K. Guest, L. C. S. Genut, Reducing dimensionality in topology optimization using adaptive design variable fields, *International Journal for Numerical Methods in Engineering* 81 (8) (2010) 1019–1045.
- [29] J. K. Guest, Imposing maximum length scale in topology optimization, *Structural and Multidisciplinary Optimization* 37 (5) (2009) 463–473.
- [30] S. Xu, Y. Cai, G. Cheng, Volume preserving nonlinear density filter based on heaviside functions, *Structural and Multidisciplinary Optimization* 41 (4) (2010) 495–505.
- [31] J. K. Guest, A. Asadpoure, S.-H. Ha, Eliminating beta-continuation from Heaviside projection and density filter algorithms, *Structural and Multidisciplinary Optimization* 44 (4) (2011) 443–453.
- [32] O. Sigmund, Manufacturing tolerant topology optimization, *Acta Mechanica Sinica* 25 (2) (2009) 227–239.
- [33] F. Wang, B. S. Lazarov, O. Sigmund, On projection methods, convergence and robust formulations in topology optimization, *Structural and Multidisciplinary Optimization* 43 (6) (2011) 767–784.
- [34] B. Lazarov, O. Sigmund, Sensitivity filters in topology optimisation as a solution to Helmholtz type differential equation, In: *Proceedings of the 8th World Congress on Structural and Multidisciplinary Optimization (WCSMO8)*, Lisbon, 2009.
- [35] A. Kawamoto, T. Matsumori, S. Yamasaki, T. Nomura, T. Kondoh, S. Nishiwaki, Heaviside projection based topology optimization by a PDE-filtered scalar function, *Structural and Multidisciplinary Optimization* 44 (1) (2011) 19–24.
- [36] B. S. Lazarov, O. Sigmund, Filters in topology optimization based on Helmholtz-type differential equations, *International Journal for Numerical Methods in Engineering* 86 (6) (2011) 765–781.
- [37] K. Suzuki, N. Kikuchi, A homogenization method for shape and topology optimization, *Computer Methods in Applied Mechanics and Engineering* 93 (3) (1991) 291–318.
- [38] A. R. Diaz, N. Kikuchi, Solutions to shape and topology eigenvalue optimization problems using a homogenization method, *International Journal for Numerical Methods in Engineering* 35 (7) (1992) 1487–1502.

- [39] S. Nishiwaki, M. I. Frecker, S. Min, N. Kikuchi, Topology optimization of compliant mechanisms using the homogenization method, *International Journal for Numerical Methods in Engineering* 42 (3) (1998) 535–559.
- [40] O. Sigmund, J. S. Jensen, Systematic design of phononic band-gap materials and structures by topology optimization, *Philosophical Transactions of the Royal Society of London Series A-Mathematical Physical and Engineering Sciences* 361 (1806) (2003) 1001–1019.
- [41] A. Iga, S. Nishiwaki, K. Izui, M. Yoshimura, Topology optimization for thermal conductors considering design-dependent effects, including heat conduction and convection, *International Journal of Heat and Mass Transfer* 52 (11–12) (2009) 2721–2732.
- [42] T. Borrvall, J. Petersson, Topology optimization of fluids in stokes flow, *International Journal for Numerical Methods in Fluids* 41 (1) (2003) 77–107.
- [43] L. H. Olesen, F. Okkels, H. Bruus, A high-level programming-language implementation of topology optimization applied to steady-state navier-stokes flow, *International Journal for Numerical Methods in Engineering* 65 (7) (2006) 975–1001.
- [44] T. Kondoh, T. Matsumori, A. Kawamoto, Drag minimization and lift maximization in laminar flows via topology optimization employing simple objective function expressions based on body force integration, *Structural and Multidisciplinary Optimization* 45 (5) (2012) 693–701.
- [45] J. Yoo, N. Kikuchi, J. L. Volakis, Structural optimization in magnetic devices by the homogenization design method, *IEEE Transactions on Magnetics* 36 (3) (2000) 574–580.
- [46] G. H. Yoon, J. S. Jensen, O. Sigmund, Topology optimization of acoustic-structure interaction problems using a mixed finite element formulation, *International Journal for Numerical Methods in Engineering* 70 (9) (2007) 1049–1075.
- [47] M. B. Dühring, J. S. Jensen, O. Sigmund, Acoustic design by topology optimization, *Journal of Sound and Vibration* 317 (3–5) (2008) 557–575.
- [48] T. Yamamoto, S. Maruyama, S. Nishiwaki, M. Yoshimura, Topology design of multi-material soundproof structures including poroelastic media to minimize sound pressure levels, *Computer Methods in Applied Mechanics and Engineering* 198 (17–20) (2009) 1439–1455.
- [49] G. Kiziltas, D. Psychoudakis, J. L. Volakis, N. Kikuchi, Topology design optimization of dielectric substrates for bandwidth improvement of a patch antenna, *IEEE Transactions on Antennas and Propagation* 51 (10) (2003) 2732–2743.

- [50] G. Kiziltas, N. Kikuchi, J. L. Volakis, J. Halloran, Topology optimization of dielectric substrates for filters and antennas using SIMP, *Archives of Computational Methods in Engineering* 11 (4) (2004) 355–388.
- [51] T. Nomura, K. Sato, K. Taguchi, T. Kashiwa, S. Nishiwaki, Structural topology optimization for the design of broadband dielectric resonator antennas using the finite difference time domain technique, *International Journal for Numerical Methods in Engineering* 71 (11) (2007) 1261–1296.
- [52] A. Erentok, O. Sigmund, Topology optimization of sub-wavelength antennas, *IEEE Transactions on Antennas and Propagation* 59 (1) (2011) 58–69.
- [53] N. Aage, N. A. Mortensen, O. Sigmund, Topology optimization of metallic devices for microwave applications, *International Journal for Numerical Methods in Engineering* 83 (2) (2010) 228–248.
- [54] J. S. Jensen, O. Sigmund, Systematic design of photonic crystal structures using topology optimization: Low-loss waveguide bends, *Applied Physics Letters* 84 (12) (2004) 2022–2024.
- [55] J. S. Jensen, O. Sigmund, Topology optimization of photonic crystal structures: a high-bandwidth low-loss T-junction waveguide, *Journal of the Optical Society of America B-Optical Physics* 22 (6) (2005) 1191–1198.
- [56] W. R. Frei, D. A. Tortorelli, H. T. Johnson, Topology optimization of a photonic crystal waveguide termination to maximize directional emission, *Applied Physics Letters* 86 (11) (2005) 111114.
- [57] J. S. Jensen, O. Sigmund, Topology optimization for nano-photonics, *Laser & Photonics Reviews* 5 (2) (2011) 308–321.
- [58] K. Hirayama, Y. Tsuji, T. Nomura, K. Sato, S. Nishiwaki, Application of topology optimization to H-plane waveguide component, *IEICE Transactions on Electronics E90-C* (2) (2007) 282–287.
- [59] S. Nishiwaki, T. Nomura, S. Kinoshita, K. Izui, M. Yoshimura, K. Sato, K. Hirayama, Topology optimization for cross-section designs of electromagnetic waveguides targeting guiding characteristics, *Finite Elements in Analysis and Design* 45 (12) (2009) 944–957.
- [60] J. Andkjær, S. Nishiwaki, T. Nomura, O. Sigmund, Topology optimization of grating couplers for the efficient excitation of surface plasmons, *Journal of the Optical Society of America B-Optical Physics* 27 (9) (2010) 1828–1832.
- [61] H. Soh, J. Yoo, D. Kim, Optimal design of the light absorbing layer in thin film silicon solar cells, *Solar Energy* 86 (7) (2012) 2095–2105.
- [62] H. Soh, J. Yoo, Texturing design for a light trapping system using topology optimization, *IEEE Transactions on Magnetics* 48 (2) (2012) 227–230.

- [63] A. R. Diaz, O. Sigmund, A topology optimization method for design of negative permeability metamaterials, *Structural and Multidisciplinary Optimization* 41 (2) (2010) 163–177.
- [64] O. Sigmund, Systematic design of metamaterials by topology optimization, *IUTAM Symposium on Modelling Nanomaterials and Nanosystems*, R. Pyrz and J. C. Rauhe (Eds.), Springer, Netherlands, 13 (2009) 151–159.
- [65] J. S. Choi, J. Yoo, Design and application of layered composites with the prescribed magnetic permeability, *International Journal for Numerical Methods in Engineering* 82 (1) (2010) 1–25.
- [66] O. Sigmund, Materials with prescribed constitutive parameters: an inverse homogenization problem, *International Journal of Solids and Structures* 31 (17) (1994) 2313–2329.
- [67] S. Zhou, W. Li, Q. Li, Design of 3-D periodic metamaterials for electromagnetic properties, *IEEE Transactions on Microwave Theory and Techniques* 58 (4) (2010) 910–916.
- [68] Y. El-Kahlout, G. Kiziltas, Inverse synthesis of electromagnetic materials using homogenization based topology optimization, *Progress in Electromagnetics Research* 115 (2011) 343–380.
- [69] P. Y. Chen, C. H. Chen, H. Wang, J. H. Tsai, W. X. Ni, Synthesis design of artificial magnetic metamaterials using a genetic algorithm, *Optics Express* 16 (17) (2008) 12806–12818.
- [70] J. A. Bossard, S. Yun, D. H. Werner, T. S. Mayer, Synthesizing low loss negative index metamaterial stacks for the mid-infrared using genetic algorithms, *Optics Express* 17 (17) (2009) 14771–14779.
- [71] W. Wang, W. K. Xu, H. Hai, An effective method for designing new structural left-handed material based on topology optimisation, *European Physical Journal-Applied Physics* 53 (2) (2011) 20401.
- [72] J. A. Sethian, A. Wiegmann, Structural boundary design via level set and immersed interface methods, *Journal of Computational Physics* 163 (2) (2000) 489–528.
- [73] M. Y. Wang, X. Wang, D. Guo, A level set method for structural topology optimization, *Computer Methods in Applied Mechanics and Engineering* 192 (1-2) (2003) 227–246.
- [74] G. Allaire, F. Jouve, A. M. Toader, Structural optimization using sensitivity analysis and a level-set method, *Journal of Computational Physics* 194 (1) (2004) 363–393.

- [75] M. Y. Wang, X. Wang, “Color” level sets: a multi-phase method for structural topology optimization with multiple materials, *Computer Methods in Applied Mechanics and Engineering* 193 (6–8) (2004) 469–496.
- [76] M. Y. Wang, S. Chen, X. Wang, Y. Mei, Design of multimaterial compliant mechanisms using level-set methods, *Journal of Mechanical Design* 127 (2005) 941–956.
- [77] G. Allaire, F. Jouve, Minimum stress optimal design with the level set method, *Engineering Analysis with Boundary Elements* 32 (11) (2008) 909–918.
- [78] S. Yamasaki, T. Yamada, T. Matsumoto, An immersed boundary element method for level-set based topology optimization, *International Journal for Numerical Methods in Engineering* DOI: 10.1002/nme.4417.
- [79] G. Allaire, F. de Gournay, F. Jouve, A. M. Toader, Structural optimization using topological and shape sensitivity via a level set method, *Control and Cybernetics* 34 (1) (2005) 59–80.
- [80] J. Sokolowski, A. Żochowski, On the topological derivative in shape optimization, *SIAM Journal on Control and Optimization* 37 (4) (1999) 1251–1272.
- [81] J. C ea, S. Garreau, P. Guillaume, M. Masmoudi, The shape and topological optimizations connection, *Computer Methods in Applied Mechanics and Engineering* 188 (4) (2000) 713–726.
- [82] M. Burger, B. Hackl, W. Ring, Incorporating topological derivatives into level set methods, *Journal of Computational Physics* 194 (1) (2004) 344–362.
- [83] L. He, C.-Y. Kao, S. Osher, Incorporating topological derivatives into shape derivatives based level set methods, *Journal of Computational Physics* 225 (1) (2007) 891–909.
- [84] S. Wang, M. Y. Wang, Radial basis functions and level set method for structural topology optimization, *International Journal for Numerical Methods in Engineering* 65 (12) (2006) 2060–2090.
- [85] Z. Luo, L. Tong, A level set method for shape and topology optimization of large-displacement compliant mechanisms, *International Journal for Numerical Methods in Engineering* 76 (6) (2008) 862–892.
- [86] P. Wei, M. Y. Wang, Piecewise constant level set method for structural topology optimization, *International Journal for Numerical Methods in Engineering* 78 (4) (2009) 379–402.
- [87] J. Lie, M. Lysaker, X.-C. Tai, A binary level set model and some applications to Mumford-Shah image segmentation, *IEEE Transactions on Image Processing* 15 (5) (2006) 1171–1181.

- [88] T. Lu, P. Neittaanmäki, X.-C. Tai, A parallel splitting up method and its application to navie-stokes equations, *Applied Mathematics Letters* 4 (2) (1991) 25–29.
- [89] J. Weickert, B. M. ter Haar Romeny, M. A. Viergever, Efficient and reliable schemes for nonlinear diffusion filtering, *IEEE Transactions on Image Processing* 7 (3) (1998) 398–410.
- [90] T. Yamada, K. Izui, S. Nishiwaki, A. Takezawa, A topology optimization method based on the level set method incorporating a fictitious interface energy, *Computer Methods in Applied Mechanics and Engineering* 199 (45-48) (2010) 2876–2891.
- [91] A. N. Tikhonov, V. Y. Arsenin, *Solutions of Ill-posed Problems*, Winston and Sons, Washington, D. C., 1977.
- [92] T. Yamada, K. Izui, S. Nishiwaki, A level set-based topology optimization method for maximizing thermal diffusivity in problems including design-dependent effects, *Journal of Mechanical Design* 133 (3) (2011) 031011.
- [93] S. Yamasaki, T. Nomura, A. Kawamoto, K. Sato, S. Nishiwaki, A level set-based topology optimization method targeting metallic waveguide design problems, *International Journal for Numerical Methods in Engineering* 87 (9) (2011) 844–868.
- [94] K. Hirayama, Y. Tsuji, S. Yamasaki, S. Nishiwaki, Design optimization of H-plane waveguide component by level set method, *IEICE Transactions on Electronics* E94-C (5) (2011) 874–881.
- [95] S. Zhou, W. Li, Q. Li, Level-set based topology optimization for electromagnetic dipole antenna design, *Journal of Computational Physics* 229 (19) (2010) 6915–6930.
- [96] S. Zhou, W. Li, G. Sun, Q. Li, A level-set procedure for the design of electromagnetic metamaterials, *Optics Express* 18 (7) (2010) 6693–6702.
- [97] S. Zhou, W. Li, Y. Chen, G. Sun, Q. Li, Topology optimization for negative permeability metamaterials using level-set algorithm, *Acta Materialia* 59 (7) (2011) 2624–2636.
- [98] S. Yamasaki, T. Nomura, K. Sato, N. Michishita, Y. Yamada, A. Kawamoto, Level set-based topology optimization targeting dielectric resonator-based composite right- and left-handed transmission lines, *International Journal for Numerical Methods in Engineering* 89 (10) (2012) 1272–1295.
- [99] K.-T. Cheng, N. Olhoff, An investigation concerning optimal design of solid elastic plates, *International Journal of Solids and Structures* 17 (3) (1981) 305–323.

- [100] M. Zhou, G. I. N. Rozvany, The COC algorithm, Part II: Topological, geometrical and generalized shape optimization, *Computer Methods in Applied Mechanics and Engineering* 89 (1–3) (1991) 309–336.
- [101] G. I. N. Rozvany, M. Zhou, T. Birker, Generalized shape optimization without homogenization, *Structural and Multidisciplinary Optimization* 4 (3–4) (1992) 250–252.
- [102] M. P. Bendsøe, O. Sigmund, Material interpolation schemes in topology optimization, *Archive of Applied Mechanics* 69 (9–10) (1999) 635–654.
- [103] A. Bensoussan, J. L. Lions, G. Papanicolau, *Asymptotic Analysis for Periodic Structures*, North-Holland Publishing Company, Amsterdam, 1978.
- [104] E. Sanchez-Palencia, *Non-Homogeneous Media and Vibration Theory*, Lecture Notes in Physics, Springer-Verlag, Berlin, 1980.
- [105] K. Matsui, K. Terada, Continuous approximation of material distribution for topology optimization, *International Journal for Numerical Methods in Engineering* 59 (14) (2004) 1925–1944.
- [106] Z. Hashin, S. Shtrikman, A variational approach to the theory of the effective magnetic permeability of multiphase materials, *Journal of Applied Physics* 33 (10) (1962) 3125–3131.
- [107] Z. Hashin, S. Shtrikman, A variational approach to the theory of the elastic behaviour of multiphase materials, *Journal of the Mechanics and Physics of Solids* 11 (2) (1963) 127–140.
- [108] C. C. Swan, I. Kosaka, Voigt–Reuss topology optimization for structures with linear elastic material behaviours, *International Journal for Numerical Methods in Engineering* 40 (16) (1997) 3033–3057.
- [109] C. Fleury, V. Braibant, Structural optimization: A new dual method using mixed variables, *International Journal for Numerical Methods in Engineering* 23 (3) (1986) 409–428.
- [110] K. Svanberg, The method of moving asymptotes - a new method for structural optimization, *International Journal for Numerical Methods in Engineering* 24 (2) (1987) 359–373.
- [111] K. Svanberg, A class of globally convergent optimization methods based on conservative convex separable approximations, *SIAM Journal of Optimization* 12 (2) (2002) 555–573.
- [112] Z.-D. Ma, N. Kikuchi, A new method of sequential approximate optimization for structural optimization problems, *Engineering Optimization* 25 (3) (1995) 231–253.

- [113] B. Samet, S. Amstutz, M. Masmoudi, The topological asymptotic for the Helmholtz equation, *SIAM Journal on Control and Optimization* 42 (5) (2003) 1523–1544.
- [114] M. Bonnet, N. Nemitz, FM-BEM and topological derivative applied to acoustic inverse scattering, In: *Boundary Element Analysis: Mathematical Aspects and Applications*, Springer Berlin Heidelberg 29 (2007) 187–212.
- [115] M. Bonnet, Topological sensitivity of energy cost functional for wave-based defect identification, *Comptes Rendus Mécanique* 338 (7–8) (2010) 377–389.
- [116] L. L. Howell, *Compliant Mechanisms*, John Wiley & Sons, Inc., 2001.
- [117] I. Her, A. Midha, A compliance number concept for compliant mechanisms, and type synthesis, *Journal of Mechanisms Transmissions and Automation in Design-Transactions of the ASME* 109 (3) (1987) 348–355.
- [118] P. Duysinx, M. P. Bendsøe, Topology optimization of continuum structures with local stress constraints, *International Journal for Numerical Methods in Engineering* 43 (8) (1998) 1453–1478.
- [119] J. R. R. A. Martins, N. M. K. Poon, On structural optimization using constraint aggregation, In: *Proceedings of the 6th World Congress on Structural and Multidisciplinary Optimization (WCSMO6)*, Rio de Janeiro, 2005.
- [120] J. París, F. Navarrina, I. Colominas, M. Casteleiro, Topology optimization of continuum structures with local and global stress constraints, *Structural and Multidisciplinary Optimization* 39 (4) (2009) 419–437.
- [121] J. París, F. Navarrina, I. Colominas, M. Casteleiro, Block aggregation of stress constraints in topology optimization of structures, *Advances in Engineering Software* 41 (3) (2010) 433–441.
- [122] J. París, F. Navarrina, I. Colominas, M. Casteleiro, Stress constraints sensitivity analysis in structural topology optimization, *Computer Methods in Applied Mechanics and Engineering* 199 (33–36) (2010) 2110–2122.
- [123] C. Le, J. Norato, T. Bruns, C. Ha, D. Tortorelli, Stress-based topology optimization for continua, *Structural and Multidisciplinary Optimization* 41 (4) (2010) 605–620.
- [124] X. Guo, W. S. Zhang, M. Y. Wang, Stress-related topology optimization via level set approach, In: *Proceedings of the 6th China-Japan-Korea Joint Symposium on Optimization of Structural and Mechanical Systems (CJK-OSM6)*, Kyoto, 2010.
- [125] Q. Xia, T. Shi, M. Y. Wang, A level set based method for topology optimization of continuum structures with stress constraint, In: *Proceedings of the 6th China-Japan-Korea Joint Symposium on Optimization of Structural and Mechanical Systems (CJK-OSM6)*, Kyoto, 2010.

- [126] M. Bruggi, P. Venini, A mixed FEM approach to stress-constrained topology optimization, *International Journal for Numerical Methods in Engineering* 73 (12) (2008) 1693–1714.
- [127] M. E. Gurtin, Generalized Ginzburg-Landau and Cahn-Hilliard equations based on a microforce balance, *Physica D* 92 (3–4) (1996) 178–192.
- [128] V. G. Veselago, The electrodynamics of substances with simultaneously negative values of ϵ and μ , *Soviet Physics Uspekhi* 10 (4) (1968) 509–514.
- [129] J. B. Pendry, A. J. Holden, W. J. Stewart, I. Youngs, Extremely low frequency plasmons in metallic mesostructures, *Physical Review Letters* 76 (25) (1996) 4773–4776.
- [130] J. B. Pendry, A. J. Holden, D. J. Robbins, W. J. Stewart, Magnetism from conductors and enhanced nonlinear phenomena, *IEEE Transactions on Microwave Theory and Techniques* 47 (11) (1999) 2075–2084.
- [131] D. R. Smith, W. J. Padilla, D. C. Vier, S. C. Nemat-Nasser, S. Schultz, Composite medium with simultaneously negative permeability and permittivity, *Physical Review Letters* 84 (18) (2000) 4184–4187.
- [132] D. Schurig, J. J. Mock, B. J. Justice, S. A. Cummer, J. B. Pendry, A. F. Starr, D. R. Smith, Metamaterial electromagnetic cloak at microwave frequencies, *Science* 314 (5801) (2006) 977–980.
- [133] S. Hrbar, J. Bartolic, Z. Sipus, Waveguide miniaturization using uniaxial negative permeability metamaterial, *IEEE Transactions on Antennas and Propagation* 53 (1) (2005) 110–119.
- [134] W. Cai, D. A. Genov, V. M. Shalaev, Superlens based on metal-dielectric composites, *Physical Review B* 72 (19) (2005) 193101.
- [135] C. Caloz, T. Itoh, A. Rennings, CRLH metamaterial leaky-wave and resonant antennas, *IEEE Antennas and Propagation Magazine* 50 (5) (2008) 25–39.
- [136] E. E. Narimanov, A. V. Kildishev, Optical black hole: Broadband omnidirectional light absorber, *Applied Physics Letters* 95 (4) (2009) 041106.
- [137] Q. Cheng, T. J. Cui, W. X. Jiang, B. G. Cai, An omnidirectional electromagnetic absorber made of metamaterials, *New Journal of Physics* 12 (2010) 063006.
- [138] S. A. Ramakrishna, Physics of negative refractive index materials, *Reports on Progress in Physics* 68 (2) (2005) 449–521.
- [139] A. K. Sarychev, V. M. Shalaev, *Electrodynamics of Metamaterials*, World Scientific Publishing Co. Pte. Ltd., 2007.

- [140] C. M. Krowne, Y. Zhang, (Eds.), Physics of Negative Refraction and Negative Index Materials, Springer Series in Materials Science, Vol. 98, 2007.
- [141] R. Marqués, F. Martín, M. Sorolla, Metamaterials with Negative Parameters: Theory, Design and Microwave Applications, Wiley-Interscience, A John Wiler & Sons. Inc.. Publication, 2008.
- [142] L. Solymar, E. Shamonina, Waves in Metamaterials, Oxford University Press, 2009.
- [143] T. J. Cui, D. R. Smith, R. Liu, (Eds.), Metamaterials Theory, Design, and Applications, Springer-Verlag, New York, 2009.
- [144] Q. Zhao, J. Zhou, F. Zhang, D. Lippens, Mie resonance-based dielectric metamaterials, Materials Today 12 (12) (2009) 60–69.
- [145] C. L. Holloway, E. F. Kuester, J. Baker-Jarvis, P. Kabos, A double negative (DNG) composite medium composed of magnetodielectric spherical particles embedded in a matrix, IEEE Transactions on Antennas and Propagation 51 (10) (2003) 2596–2603.
- [146] O. G. Vendik, M. S. Gashinova, Artificial double negative (DNG) media composed by two different dielectric sphere lattices embedded in a dielectric matrix, 34th European Microwave Conference, Amsterdam (2004) 1209–1212.
- [147] A. Ahmadi, H. Mosallaei, Physical configuration and performance modeling of all-dielectric metamaterials, Physical Review B 77 (4) (2008) 045104.
- [148] E. A. Semouchkina, G. B. Semouchkin, M. Lanagan, C. A. Randall, FDTD study of resonance processes in metamaterials, IEEE Transactions on Microwave Theory and Techniques 53 (4) (2005) 1477–1487.
- [149] Q. Zhao, L. Kang, B. Du, H. Zhao, Q. Xie, X. Huang, B. Li, J. Zhou, L. Li, Experimental demonstration of isotropic negative permeability in a three-dimensional dielectric composite, Physical Review Letters 101 (2) (2008) 027402.
- [150] L. Peng, L. Ran, H. Chen, H. Zhang, J. A. Kong, T. M. Grzegorzcyk, Experimental observation of left-handed behavior in an array of standard dielectric resonators, Physical Review Letters 98 (15) (2007) 157403.
- [151] K. Shibuya, K. Takano, N. Matsumoto, K. Izumi, H. Miyazaki, Y. Jimba, M. Hangyo, Terahertz metamaterials composed of TiO_2 cube arrays, Proceedings of the 2nd International Congress on Advanced Electromagnetic Materials in Microwaves and Optics (Metamaterials' 2008), Pamplona, 2008.
- [152] D. P. Gaillot, C. Croënne, D. Lippens, An all-dielectric route for terahertz cloaking, Optics Express 16 (6) (2008) 3986–3992.

- [153] W. Cai, U. K. Chettiar, A. V. Kildishev, V. M. Shalaev, Designs for optical cloaking with high-order transformations, *Optics Express* 16 (8) (2008) 5444–5452.
- [154] T. Ueda, A. Lai, T. Itoh, Demonstration of negative refraction in a cutoff parallel-plate waveguide loaded with 2-D square lattice of dielectric resonators, *IEEE Transactions on Microwave Theory and Techniques* 55 (6) (2007) 1280–1287.
- [155] T. Ueda, N. Michishita, M. Akiyama, T. Itoh, Dielectric-resonator-based composite right/left-handed transmission lines and their application to leaky wave antenna, *IEEE Transactions on Microwave Theory and Techniques* 56 (10) (2008) 2259–2269.
- [156] R. X. Wu, Effective negative refraction index in periodic metal-ferrite-metal film composite, *Journal of Applied Physics* 97 (7) (2005) 076105.
- [157] T. Ueda, M. Tsutsumi, Left-handed transmission characteristics of rectangular waveguides periodically loaded with ferrite, *IEEE Transactions on Magnetics* 41 (10) (2005) 3532–3537.
- [158] R.-X. Wu, X.-Y. Ji, Wave polarization and left-handed materials in metallic magnetic composites, *Applied Physics A - Materials Science & Processing* 87 (2) (2007) 205–208.
- [159] D.-Y. Zou, A.-M. Jiang, R.-X. Wu, Ferromagnetic metamaterial with tunable negative index of refraction, *Journal of Applied Physics* 107 (1) (2010) 013507.
- [160] H. Zhao, J. Zhou, Q. Zhao, B. Li, L. Kang, Y. Bai, Magnetotunable left-handed material consisting of yttrium iron garnet slab and metallic wires, *Applied Physics Letters* 91 (13) (2007) 131107.
- [161] H. García-Miquel, J. Carbonell, J. Sánchez-Dehesa, Left handed material based on amorphous ferromagnetic microwires tunable by dc current, *Applied Physics Letters* 97 (9) (2010) 094102.
- [162] J. Carbonell, H. García-Miquel, J. Sánchez-Dehesa, Double negative metamaterials based on ferromagnetic microwires, *Physical Review B* 81 (2) (2010) 024401.
- [163] A. A. Zharov, V. V. Kurin, Giant resonant magneto-optic kerr effect in nanostructured ferromagnetic metamaterials, *Journal of Applied Physics* 102 (12) (2007) 123514.
- [164] S. Engelbrecht, A. M. Shuvaev, Y. Luo, V. Moshnyaga, A. Pimenov, Negative refraction in natural ferromagnetic metals, *Europhysics Letters* 95 (3) (2011) 37005.

- [165] L.-P. Carignan, A. Yelon, D. Ménard, C. Caloz, Ferromagnetic nanowire metamaterials: Theory and applications, *IEEE Transactions on Microwave Theory and Techniques* 59 (10) (2011) 2568–2586.
- [166] O. Acher, M. Ledieu, A. Bardaine, F. Levassort, Piezoelectric disks used as metamaterial inclusions, *Applied Physics Letters* 93 (3) (2008) 032501.
- [167] O. Sigmund, S. Torquato, Design of materials with extreme thermal expansion using a three-phase topology optimization method, *Journal of the Mechanics and Physics of Solids* 45 (6) (1997) 1037–1067.
- [168] U. D. Larsen, O. Sigmund, S. Bouwstra, Design and fabrication of compliant micromechanisms and structures with negative poisson’s ratio, *Journal of Microelectromechanical Systems* 6 (2) (1997) 99–106.
- [169] N. Fang, D. Xi, J. Xu, M. Ambati, W. Srituravanich, C. Sun, X. Zhang, Ultrasonic metamaterials with negative modulus, *Nature Materials* 5 (6) (2006) 452–456.
- [170] S. H. Lee, C. M. Park, Y. M. Seo, Z. G. Wang, C. K. Kim, Acoustic metamaterial with negative modulus, *Journal of Physics: Condensed Matter* 21 (17) (2009) 175704.
- [171] H. H. Huang, C. T. Sun, G. L. Huang, On the negative effective mass density in acoustic metamaterials, *International Journal of Engineering Science* 47 (4) (2009) 610–617.
- [172] S. H. Lee, C. M. Park, Y. M. Seo, Z. G. Wang, C. K. Kim, Acoustic metamaterial with negative density, *Physics Letters A* 373 (48) (2009) 4464–4469.
- [173] Z. Liu, X. Zhang, Y. Mao, Y. Y. Zhu, Z. Yang, C. T. Chan, P. Sheng, Locally resonant sonic materials, *Science* 289 (5485) (2000) 1734–1736.
- [174] M. Hirsekorn, P. P. Delsanto, N. K. Batra, P. Matic, Modelling and simulation of acoustic wave propagation in locally resonant sonic materials, *Ultrasonics* 42 (1–9) (2004) 231–235.
- [175] J. Li, C. T. Chan, Double-negative acoustic metamaterial, *Physical Review E* 70 (5) (2004) 055602.
- [176] Y. Ding, Z. Liu, C. Qiu, J. Shi, Metamaterial with simultaneously negative bulk modulus and mass density, *Physical Review Letters* 99 (9) (2007) 093904.
- [177] H. Chen, C. T. Chan, Acoustic cloaking in three dimensions using acoustic metamaterials, *Applied Physics Letters* 91 (18) (2007) 183518.
- [178] J. Hu, X. Zhou, G. Hu, A numerical method for designing acoustic cloak with arbitrary shapes, *Computational Materials Science* 46 (3) (2009) 708–712.

- [179] S. Zhang, C. Xia, N. Fang, Broadband acoustic cloak for ultrasound waves, *Physical Review Letters* 106 (2) (2011) 024301.
- [180] M. Ambati, N. Fang, C. Sun, X. Zhang, Surface resonant states and superlensing in acoustic metamaterials, *Physical Review B* 75 (19) (2007) 195447.
- [181] J. Li, L. Fok, X. Yin, G. Bartal, X. Zhang, Experimental demonstration of an acoustic magnifying hyperlens, *Nature Materials* 8 (12) (2009) 931–934.
- [182] C. M. Soukoulis, S. Linden, M. Wegener, Negative refractive index at optical wavelengths, *Science* 315 (5808) (2007) 47–49.
- [183] C. M. Soukoulis, M. Wegener, Past achievements and future challenges in the development of three-dimensional photonic metamaterials, *Nature Photonics* 5 (9) (2011) 523–530.
- [184] O. C. Zienkiewicz, D. Kelly, P. Bettess, The sommerfeld (radiation) condition on infinite domains and its modelling in numerical procedures, *Computing Methods in Applied Sciences and Engineering, 1977, I, Lecture Notes in Mathematics* 704 (1979) 169–203.
- [185] J. M. Jin, D. J. Riley, *Finite Element Analysis of Antennas and Arrays, Vol. 127*, Wiley-IEEE Press, New Jersey, 2008.
- [186] O. Ouchetto, C. W. Qiu, S. Zouhdi, L. W. Li, A. Razek, Homogenization of 3-D periodic bianisotropic metamaterials, *IEEE Transactions on Microwave Theory and Techniques* 54 (11) (2006) 3893–3898.
- [187] Z. Hashin, Analysis of composite materials – a survey, *Journal of Applied Mechanics* 50 (3) (1983) 481–505.
- [188] D. R. Smith, J. B. Pendry, Homogenization of metamaterials by field averaging, *Journal of the Optical Society of America B-Optical Physics* 23 (3) (2006) 391–403.
- [189] D. R. Smith, S. Schultz, P. Markoš, C. M. Soukoulis, Determination of effective permittivity and permeability of metamaterials from reflection and transmission coefficients, *Physical Review B* 65 (19) (2002) 195104.
- [190] X. Chen, T. M. Grzegorzczak, B. I. Wu, J. Pacheco, Jr., J. A. Kong, Robust method to retrieve the constitutive effective parameters of metamaterials, *Physical Review E* 70 (1) (2004) 016608.
- [191] G. Lubkowski, R. Schuhmann, T. Weiland, Extraction of effective metamaterial parameters by parameter fitting of dispersive models, *Microwave and Optical Technology Letters* 49 (2) (2007) 285–288.
- [192] D. R. Smith, D. C. Vier, T. Koschny, C. M. Soukoulis, Electromagnetic parameter retrieval from inhomogeneous metamaterials, *Physical Review E* 71 (3) (2005) 036617.

- [193] D. J. Bergman, The dielectric constant of a composite material - a problem in classical physics, *Physics Reports* 43 (9) (1978) 377–407.
- [194] R. T. Rockafellar, The multiplier method of Hestenes and Powell applied to convex programming, *Journal of Optimization Theory and Applications* 12 (6) (1973) 555–562.
- [195] A. D. Belegundu, T. R. Chandrupatla, *Optimization Concepts and Applications in Engineering*, Second Edition, Vol. 194, Cambridge University Press, New York, 2011.
- [196] A. Sihvola, *Electromagnetic Mixing Formulas and Applications*, The Institution of Engineering and Technology, London, 1999.
- [197] G. W. Milton, *The Theory of Composites*, Cambridge University Press, Cambridge, 2001.
- [198] O. Sigmund, On the usefulness of non-gradient approaches in topology optimization, *Structural and Multidisciplinary Optimization* 43 (5) (2011) 589–596.
- [199] G. W. Milton, Bounds on the complex permittivity of a two-component composite material, *Journal of Applied Physics* 52 (8) (1981) 5286–5293.
- [200] G. A. Francfort, F. Murat, Homogenization and optimal bounds in linear elasticity, *Archive for Rational Mechanics and Analysis* 94 (4) (1986) 307–334.
- [201] K. A. Lurie, A. V. Cherkaev, Optimization of properties of multicomponent isotropic composites, *Journal of Optimization Theory and Applications* 46 (4) (1985) 571–580.
- [202] G. W. Milton, Modelling the Properties of Composites by laminates In: *Homogenization and Effective Moduli of Materials and Media*, The IMA Volumes in Mathematics and its Applications, Vol. 1, 150–174, Springer-Verlag, New York, 1986.
- [203] A. N. Norris, A differential scheme for the effective moduli of composites, *Mechanics of Materials* 4 (1) (1985) 1–16.
- [204] O. Sigmund, A new class of extremal composites, *Journal of the Mechanics and Physics of Solids* 48 (2) (2000) 397–428.
- [205] Y. Grabovsky, R. V. Kohn, Microstructures minimizing the energy of a two phase elastic composite in two space dimensions. I: the confocal ellipse construction, *Journal of the Mechanics and Physics of Solids* 43 (6) (1995) 933–947.
- [206] Y. Grabovsky, R. V. Kohn, Microstructures minimizing the energy of a two phase elastic composite in two space dimensions. II: the Vigdergauz microstructure, *Journal of the Mechanics and Physics of Solids* 43 (6) (1995) 949–972.

- [207] S. Vigdergauz, Energy-minimizing inclusions in a planar elastic structure with macroisotropy, *Structural Optimization* 17 (2–3) (1999) 104–112.
- [208] L. Rayleigh, On the influence of obstacles arranged in rectangular order upon the properties of a medium, *Philosophical Magazine* 34 (211) (1892) 481–502.
- [209] H. Wallén, H. Kettunen, A. Sihvola, Composite near-field superlens design using mixing formulas and simulations, *Metamaterials* 3 (3–4) (2009) 129–139.
- [210] J. Andkjær, N. A. Mortensen, O. Sigmund, Towards all-dielectric, polarization-independent optical cloaks, *Applied Physics Letters* 100 (10) (2012) 101106.
- [211] B. Lax, K. J. Button, *Microwave Ferrites and Ferrimagnetics*, McGraw-Hill, New York, 1962.
- [212] Z. D. Ma, N. Kikuchi, H. C. Cheng, Topological design for vibrating structures, *Computer Methods in Applied Mechanics and Engineering* 121 (1–4) (1995) 259–280.
- [213] J. Li, J. B. Pendry, Hiding under the carpet: A new strategy for cloaking, *Physical Review Letters* 101 (20) (2008) 203901.
- [214] T. Ergin, N. Stenger, P. Brenner, J. B. Pendry, M. Wegener, Three-dimensional invisibility cloak at optical wavelengths, *Science* 328 (5976) (2010) 337–339.
- [215] J. Zhang, L. Liu, Y. Luo, S. Zhang, N. A. Mortensen, Homogeneous optical cloak constructed with uniform layered structures, *Optics Express* 19 (9) (2011) 8625–8631.
- [216] J.-M. Jin, *The Finite Element Method in Electromagnetics*, Wiley-IEEE Press; Second Edition, 2002.

List of Publications

International Journal Papers

- [1] Masaki Otomori, Takayuki Yamada, Kazuhiro Izui and Nishiwaki Shinji, Level set-based topology optimisation of a compliant mechanism design using mathematical programming, *Mechanical Science*, Vol.2 (2011), pp.91-98.
- [2] Masaki Otomori, Jacob Andkjær, Ole Sigmund, Kazuhiro Izui, Shinji Nishiwaki, Inverse design of dielectric materials by topology optimization, *Progress in Electromagnetics Research*, Vol.127 (2012), pp.93-120.
- [3] Masaki Otomori, Takayuki Yamada, Kazuhiro Izui, Shinji Nishiwaki, Jacob Andkjær, A topology optimization method based on the level set method for the design of negative permeability dielectric metamaterials, *Computer Methods in Applied Mechanics and Engineering*, Vol. 237-240 (2012), pp.192-211.
- [4] Masaki Otomori, Takayuki Yamada, Kazuhiro Izui, Shinji Nishiwaki, Nozomu Kogiso, Level set-based topology optimization for the design of a ferromagnetic waveguide, *IEEE Transactions on Magnetics*, Vol. 48, No. 11 (2012), pp.3072-3075.
- [5] Masaki Otomori, Takayuki Yamada, Jacob Andkjær, Kazuhiro Izui, Shinji Nishiwaki, Nozomu Kogiso, Level set-based topology optimization for the design of an electromagnetic cloak with ferrite material, *IEEE Transactions on Magnetics*, Vol. 49, No. 5 (2013), *in press*.
- [6] Lirong Lu, Takashi Yamamoto, Masaki Otomori, Takayuki Yamada, Kazuhiro Izui, Shinji Nishiwaki, Topology optimization of an acoustic metamaterial with negative bulk modulus using local resonance, *Finite Elements in Analysis and Design*, *submitted*.
- [7] Keiichi Ueda, Masaki Otomori, Kogiso Nozomu, Takayuki Yamada, Shinji Nishiwaki, Level set-based robust topology optimization considering the spatial uncertainty of design parameters, *Structural and Multidisciplinary Optimization*, *submitted*.

Domestic Journal Papers (in Japanese)

- [1] 乙守正樹, 泉井一浩, 西脇眞二, マルチプルフェイズプロジェクション法によるトポロジー最適化 (設計変数の低減のための新しいプロジェクション関数の定式化), 日本機械学会論文集 (C編), 77巻 775号 (2011), pp.269-279.
- [2] 乙守正樹, 山田崇恭, 泉井一浩, 西脇眞二, 数理計画法を用いたレベルセット法に基づくトポロジー最適化, 日本機械学会論文集 (C編), 77巻 783号 (2011), pp.41-54.

- [3] 乙守正樹, 山田崇恭, 泉井一浩, 西脇眞二, Jacob Andkjær, Ole Sigmund, レベルセット法に基づく誘電体メタマテリアルのトポロジー最適化, 日本計算工学会論文集, Vol.2011, (2011), No.20110012.
- [4] 植田圭一, 乙守正樹, 小木曾望, 山田崇恭, 西脇眞二, 定常確率過程による不確定性表現を用いたレベルセット法に基づくロバストトポロジー最適設計, 日本機械学会論文集 (C編), 78 巻第 787 号 (2012), pp. 928-942.
- [5] 塚本翔太, 泉井一浩, 乙守正樹, 大門真, 野村壮史, 西脇眞二, トポロジー最適化に基づく金属パッチアンテナの最適設計法, 日本計算工学会論文集, Vol.2012, (2012), No.20120015.
- [6] 乙守正樹, 山田崇恭, 泉井一浩, 西脇眞二, 小木曾望, フェライトを用いた導波管のトポロジー最適化, 日本計算工学会論文集, *submitted*.
- [7] 小木曾望, 堀尾仁志, 乙守正樹, 山田崇恭, 西脇眞二, レベルセット法に基づくロバストトポロジー最適設計のパラメータがロバスト最適形態におよぼす影響について, 日本機械学会論文集 (C編), *submitted*.
- [8] 乙守正樹, 陸麗蓉, 山田崇恭, 山本崇史, 泉井一浩, 西脇眞二, レベルセット法による形状表現を用いた音響メタマテリアルのトポロジー最適化, 日本機械学会論文集 (C編), *submitted*.

Refereed International Proceedings

- [1] Masaki Otomori, Kazuhiro Izui, Shinji Nishiwaki, Reducing design variables in a multiple phase projection method, *Proceedings of 6th China-Japan-Korea Joint Symposium on Optimization of Structural and Mechanical Systems (CJK-OSM6)* June 22-25, 2010, Kyoto, Japan, J-17.
- [2] Masaki Otomori, Takayuki Yamada, Kazuhiro Izui, Shinji Nishiwaki, Level set-based topology optimisation of a compliant mechanism design using mathematical programming, *IFTToMM/ASME Second International Symposium on Compliant Mechanisms (CoMe2011)* May 19-20, 2011, Delft, The Netherlands, CoMe2011-3.
- [3] Masaki Otomori, Takayuki Yamada, Kazuhiro Izui, Shinji Nishiwaki, Level set-based topology optimization of negative permeability metamaterials, *Proceedings of 9th World Congress on Structural and Multidisciplinary Optimization (WCSMO-9)* June 13-17, 2011, Shizuoka, Japan, No.111.
- [4] Keiichi Ueda, Masaki Otomori, Nozomu Kogiso, Takayuki Yamada, Shinji Nishiwaki, Level set-based robust topology optimization using stochastic process model, *Proceedings of 9th World Congress on Structural and Multidisciplinary Optimization (WCSMO-9)* June 13-17, 2011, Shizuoka, Japan, No.347.
- [5] Masaki Otomori, Takayuki Yamada, Kazuhiro Izui, Shinji Nishiwaki, A level set-based topology optimization for mechanical structures, *EUROMECH Colloquium 522 - "Recent Trends in Optimisation for Computational Solid Mechanics"* October 10-13, 2011, Erlangen, Germany, pp. 44-46.

- [6] Masaki Otomori, Takayuki Yamada, Kazuhiro Izui, Shinji Nishiwaki, Nozomu Kogiso, Level set-based topology optimization for the design of a ferromagnetic waveguide, *IEEE International Magnetics Conference (Intermag 2012)* May 7-11, 2012, Vancouver, Canada, BE-08.
- [7] Masaki Otomori, Jacob Andkjær, Ole Sigmund, Kazuhiro Izui, Shinji Nishiwaki, Topology optimization for the microstructure design of dielectric materials, *Proceedings of 7th China-Japan-Korea Joint Symposium on Optimization of Structural and Mechanical Systems (CJK-OSM7)* June 18-21, 2012, Huangshan, China, J-39.
- [8] Lirong Lu, Takashi Yamamoto, Takayuki Yamada, Masaki Otomori, Kazuhiro Izui, Shinji Nishiwaki, Level set-based topology optimization method for the design of acoustic metamaterial with negative bulk modulus, *Proceedings of 7th China-Japan-Korea Joint Symposium on Optimization of Structural and Mechanical Systems (CJK-OSM7)* June 18-21, 2012, Huangshan, China, J-98.
- [9] Masaki Otomori, Takayuki Yamada, Kazuhiro Izui, Shinji Nishiwaki and Nozomu Kogiso, Level set-based structural topology optimization of a metallic waveguide loaded with ferrite, *Proceedings of 14th AIAA/ISSMO Multidisciplinary Analysis and Optimization Conference (2012MAO)* September 17-19, 2012, Indianapolis, USA, AIAA 2012-5477.
- [10] Keiichi Ueda, Masaki Otomori, Nozomu Kogiso, Takayuki Yamada and Shinji Nishiwaki, Level Set-Based Robust Topology Design Considering Spatial Uncertainty, *Proceedings of 14th AIAA/ISSMO Multidisciplinary Analysis and Optimization Conference (2012MAO)* September 17-19, 2012, Indianapolis, USA, AIAA 2012-5565.
- [11] Masaki Otomori, Takayuki Yamada, Jacob Andkjær, Kazuhiro Izui, Shinji Nishiwaki and Nozomu Kogiso, Level set-based topology optimization for the design of an electromagnetic cloak with ferrite material, *The 15th Biennial IEEE Conference on Electromagnetic Field Computation (CEFC2012)* November 11-14, 2012, Oita, Japan, (accepted).

Non refereed International Proceedings

- [1] Masaki Otomori, Kazuhiro Izui, Shinji Nishiwaki, A Shape and Topology Optimization Method with Minimum Length Scale Constraints, *The 7th MicRO Alliance Symposium*, November 22, 2010, Kyoto Japan, Group C, No. 39.
- [2] Masaki Otomori, Takayuki Yamada, Kazuhiro Izui, Shinji Nishiwaki, Nozomu Kogiso, Level set-based topology optimization for the design of a left-handed waveguide using ferromagnetic inclusions, *Proceedings of The 10th World Congress on Computational Mechanics (WCCM10)*, July 8- 13, 2012, Sao Paulo, Brazil, pp.206-207 (19015).
- [3] Masaki Otomori, Takayuki Yamada, Kazuhiro Izui and Shinji Nishiwaki, Level set-based topology optimization for the design of negative permeability dielectric metamaterials, *KSME-JSME Joint Symposium on CM & CAE 2012*, September 12, 2012, Kanazawa, Japan, CO-JP-3, pp.147–156.

- [4] Masaki Otomori, Jacob Andkjær, Ole Sigmund, Kazuhiro Izui and Shinji Nishiwaki, Design of dielectric materials with prescribed effective permittivity by topology optimization, *JSME-CMD International Computational Mechanics Symposium 2012 (JSME-CMD ICMS2012)*, October 9-11, 2012, Kobe, Japan, MS11-2-1(63).
- [5] Lirong Lu, Takayshi Yamamoto, Takayuki Yamada, Masaki Otomori, Kazuhiro Izui and Shinji Nishiwaki, Optimal design of acoustic metamaterials by topology optimization, *JSME-CMD International Computational Mechanics Symposium 2012 (JSME-CMD ICMS2012)*, October 9-11, 2012, Kobe, Japan, MS11-2-3(66).

Domestic Conferences (in Japanese)

- [1] 乙守正樹, 泉井一浩, 西脇眞二, 最小寸法制約を考慮したトポロジー最適化, 第23回計算力学講演会, 日本機械学会, 2010年9月23日-25日, 北見, 北海道, pp.395-396 (817).
- [2] 乙守正樹, 山田崇恭, 泉井一浩, 西脇眞二, 数理計画法を用いたレベルセット法に基づくトポロジー最適化, 第20回設計工学・システム部門講演会, 日本機械学会, 2010年10月27日-29日, 東京, pp.119-122 (2103).
- [3] 乙守正樹, 山田崇恭, 泉井一浩, 西脇眞二, レベルセット法に基づく機械構造物の構造最適設計法における数理計画法の適用, 最適化シンポジウム2010 (OPTIS2010), 日本機械学会, 2010年12月9日-10日, 名古屋, pp. 241-244 (115).
- [4] 乙守正樹, 山田崇恭, 泉井一浩, 西脇眞二, Jacob Andkjær, Ole Sigmund, トポロジー最適化手法を用いた誘電体メタマテリアルの最適設計, 2011年電子情報通信学会ソサイエティ大会, 2011年9月13日-16日, 札幌, 北海道, p.19 (C-1-19).
- [5] 乙守正樹, 山田崇恭, 泉井一浩, 西脇眞二, Jacob Andkjær, Ole Sigmund, レベルセット法に基づくトポロジー最適化を用いた誘電体メタマテリアルの最適設計法, 第21回設計工学・システム部門講演会, 日本機械学会, 2011年10月21日-23日, 山形, pp.332-335 (2311).
- [6] 植田圭一, 乙守正樹, 小木曾望, 山田崇恭, 西脇眞二, 確率過程を利用したロバストトポロジー最適設計, 第7回構造物の安全性・信頼性に関する国内シンポジウム, 日本学術会議, 2011年10月12日-14日, 東京, (全文査読有).
- [7] 乙守正樹, 山田崇恭, 泉井一浩, 西脇眞二, 小木曾望, トポロジー最適化手法を用いたフェライト導波管の最適設計, 2012年電子情報通信学会総合大会, 2012年3月20日-23日, 岡山, p.324 (C-15-17).
- [8] 乙守正樹, Jacob Andkjær, Ole Sigmund, 泉井一浩, 西脇眞二, 有効誘電率の設計を目的とした誘電体マイクロ構造のトポロジー最適化, 第17回計算工学講演会, 日本計算工学会, 2012年5月29日-31日, 京都, G10-1.
- [9] 乙守正樹, 山田崇恭, Jacob Andkjær, 泉井一浩, 西脇眞二, 小木曾望, トポロジー最適化手法によるフェライトを用いたクローキング装置の構造最適設計に関する一考察, 2012年電子情報通信学会ソサイエティ大会, 2012年9月11日-14日, 富山, p.273 (C-15-19).
- [10] 乙守正樹, 山田崇恭, 泉井一浩, 西脇眞二, 小木曾望, レベルセット法に基づくトポロジー最適化を用いたフェライトを装荷した導波管の最適設計法, 第22回設計工学・システム部門講演会, 日本機械学会, 2012年9月26日-28日, 広島, pp.468-472 (2210).

- [11] 大門真, 乙守正樹, 塚本翔太, 泉井一浩, 西脇眞二, 金属パッチアンテナの構造最適化, 第22回設計工学・システム部門講演会, 日本機械学会, 2012年9月26日-28日, 広島, pp.473-479 (2211).
- [12] 塚本翔太, 泉井一浩, 乙守正樹, 大門真, 野村壮史, 西脇眞二, 表皮効果を考慮した金属パッチアンテナのトポロジー最適化, Design シンポジウム 2012, 日本建築学会, 2012年10月16日-17日, 京都, pp.349-352.
- [13] 植田圭一, 小木曾望, 乙守正樹, 山田崇恭, 西脇眞二, パラメータの空間的な変動を考慮したロバストトポロジー最適設計, 第49回日本航空宇宙学会中部・関西合同秋季大会, 日本航空宇宙学会, 2012年11月30日, 愛知, A3.